

UNIVERSIDAD DE GRANADA



Tesis Doctoral

Subcell FDTD techniques for electromagnetic compatibility assessment in aeronautics

Memoria presentada por

Miguel David Ruiz-Cabello Núñez

para optar al grado de Doctor por la Universidad de Granada

realizada en la

Facultad de Ciencias

Departamento de Electromagnetismo y Física de la Materia

Grupo de Electromagnetismo de Granada

en el programa de doctorado de

Física y Matemáticas

Declaración de Autoría

El doctorando / The doctoral candidate Miguel David Ruiz-Cabello Núñez y los directores de la tesis / and the thesis supervisors D. Salvador González García y D. Luis Díaz Angulo.

Garantizamos, al firmar esta tesis doctoral, que el trabajo ha sido realizado por el doctorando bajo la dirección de los directores de la tesis y hasta donde nuestro conocimiento alcanza, en la realización del trabajo, se han respetado los derechos de otros autores a ser citados, cuando se han utilizado sus resultados o publicaciones.

/

Guarantee, by signing this doctoral thesis, that the work has been done by the doctoral candidate under the direction of the thesis supervisor/s and, as far as our knowledge reaches, in the performance of the work, the rights of other authors to be cited (when their results or publications have been used) have been respected.

Granada, 29 de Mayo de dos mil diecisiete

Director/es de la Tesis

Doctorando

Fdo. Salvador González García

Fdo. Miguel David Ruiz-Cabello Núñez

Fdo. Luis Díaz Angulo

D. Salvador González García, Doctor en Ciencias Físicas, Catedrático de Electromagnetismo en el Departamento de Electromagnetismo y Física de la Materia de la Facultad de Ciencias de la Universidad de Granada,

y

D. Luis Díaz Angulo, Doctor en Ciencias Físicas, Profesor sustituto interino en el departamento de de Electromagnetismo y Física de la Materia de la Facultad de Ciencias de la Universidad de Granada,

CERTIFICAN

Que el trabajo de investigación que se presenta en esta Memoria, titulada SUBCELL FDTD TECHNIQUES FOR ELECTROMAGNETIC COMPATIBILITY ASSESSMENT IN AERONAUTICS, ha sido realizado en este Departamento por el Licenciado en Física D. Miguel David Ruiz-Cabello Núñez bajo nuestra dirección, y constituye su Tesis Doctoral.

Con esta fecha autorizamos su presentación ante la Comisión de Doctorado de la Universidad de Granada.

Granada, 29 de Mayo de dos mil diecisiete

Fdo. Salvador González García

Fdo. Luis Díaz Angulo

A mi mujer Ester y mis hijos.

A mis padres, hermanos y abuelos.

Agradecimientos

Esta página es al mismo tiempo, el comienzo una obra y también el final de una etapa. En esta página me gustaría dedicarla a todos los que han estado presentes, apoyándome y sacrificándose de muchas formas diferentes, y que han hecho posible la realización de este trabajo.

En primer agradecimiento es a mi mujer Ester por dedicarme su apoyo incondicional.

Por supuesto, nada de esto hubiera sido posible sin las personas que conforman el Grupo de Electromagnetismo de Granada, por acogerme y facilitarme todos los medios necesarios; su labor ha sido indispensable para que trabajo haya sido posible. En primer lugar a Rafael por haberme dado la oportunidad de desarrollar mi labor en el GEG; él ha sido uno de los padres de este trabajo. A Amelia y Mario por el tiempo y cariño que ha dedicado en todos los aspectos formales. A Luis y Dani por haber compartido muchas de las frustraciones y alegrías con las que nos hemos encontrado a lo largo de estos años.

Agradecer especialmente a Salvador y Luis por labor en la dirección de todo este trabajo. En particular me gustaría extender este agradecimiento a Salvador no solo por aceptarme como doctorando sino por todo su trabajo, paciencia y dedicación personal. Su guía, consejos y aportaciones han sido, sin duda, esenciales, en mi aprendizaje, ha sido y es para mi una gran referencia, espero haya disfrutado tanto como yo en el desarrollo de este trabajo.

También agradecer al equipo de Airbus, Jesús, Enrique, Guadalupe, por todo lo que hay de su experiencia en esta tesis doctoral.

A todos, sinceramente,
Gracias.

Muy especialmente queremos agradecer la confianza de AIRBUS, INTA y UPC, compañeros de proyectos y contratos, sin cuya realimentación esto no hubiera podido llegar tan lejos. Específicamente, este trabajo ha sido parcialmente financiado por:

El Ministerio de Ciencia e Innovación en el proyecto TEC2010-20841-C04-04 y bajo la beca FPI BES-2011-048814 (EEBB-I-2015-10007) asociada al mismo.

La Comisión Europea a través del proyecto del 7PM "HIRF-SE" bajo el acuerdo de subvención núm. 205294.

AIRBUS a través del contrato LOU art. 83 EADS-FEUGR 3713-00 "A-UGRFDTD".

INTA a través del contrato LOU art. 83 C-3801 "OTS - UGRFDTD-MN".

La Junta de Andalucía a través del Proyecto de Excelencia P12-TIC-1442.

Los proyectos del MINECO TEC2013-48414-C3-01, TEC2016-79214-C3-3-R, and TEC2015-68766-REDC.

Resumen

Esta tesis doctoral se ha desarrollado en el marco de diversos proyectos y contratos nacionales e internacionales en colaboración con AIRBUS, INTA y UPC, entre otros. Estos proyectos surgen por la necesidad de evaluar el impacto del entorno electromagnético en la capacidad operativa de equipos, sistemas y plataformas aeronáuticas en particular, y de un modo genérico lo que se da en llamar efectos ambientales electromagnéticos. La relevancia de estos efectos es cada vez más importante en las plataformas aéreas modernas debido al aumento de los sistemas fly-by-wire en sustitución de las opciones mecánicas tradicionales. Los métodos numéricos permiten evaluar los efectos electromagnéticos con la intención encontrar vulnerabilidades y mitigarlas en la etapa de diseño previo a la etapa de fabricación del dispositivo.

Desde el punto de vista de la compatibilidad electromagnética, las principales amenazas de una aeronave pueden resumirse en:

- Efectos indirectos de rayos: estos son causados por la corriente eléctrica que fluye a través de la estructura interna y externa de del avión, como resultado del impacto de un rayo.
- Emisiones Radio frecuencia de alta intensidad: estas pueden ser intencionadas o no, y producidas tanto por fuentes internas como externas (TV, telefonía móvil, 3G, 4G, 5G, radares modernos, GNSS, etc, ...).
- Pulsos EM no nucleares: Este tipo de amenaza destructiva e intencionada, es producida por las denominadas bombas electromagnéticas. Estas en general no tiene suficiente energía como para producir daños permanentes, pero generan pulsos extremadamente de corta duración que causan el reinicio y/o paralización de los sistemas de abordó.

El resultado de la exposición a esta amenazas, es la inducción de corrientes que interfieren en los sistemas de abordó y en la comunicación entre estos. Actualmente debido al incremento de equipos y dispositivos electrónicos de abordó junto con el aumento de materiales electromagnéticamente más penetrables, vuelven a los aviones más vulnerables ante los efectos de electromagnéticos. Por esta razón las guías de certificación

aeronáutica proponen los test que han de superar las aeronaves para encontrar y mitigar las vulnerabilidades electromagnéticas (Capítulo 5).

Los métodos numéricos permiten evaluar los efectos electromagnéticos con la intención encontrar estas vulnerabilidades y mitigarlas en la etapa de diseño previamente a la etapa de fabricación del dispositivo lo que permite ahorrar costes en el desarrollo. Además en aplicaciones aeroespaciales los métodos numéricos permiten diseñar entornos que reproducen mejor las condiciones de vuelo, por ejemplo evitan los efectos de suelo de los resultados experimentales.

El principal objetivo de esta tesis ha sido el desarrollo de técnicas numéricas de alta eficiencia computacional para el análisis de problemas electromagnéticos reales de interés industrial. De un modo particular, nos hemos centrado en el método de diferencias finitas en el dominio del tiempo (FDTD), que es uno de los más conocidos para resolver numéricamente las ecuaciones de Maxwell. Este método fue propuesto en 1966 por Kane Yee, y hoy en día cuenta con una vasta bibliografía. Es uno de los más potentes en el estudio de compatibilidad electromagnética (EMC) e interferencias electromagnéticas (EMI) de vehículos aéreos.

El método FDTD tiene las siguientes características: permite una formulación explícita de las ecuaciones de Maxwell, lo que significa que se pueden aplicar técnicas de paralelización OpenMP y MPI, usadas fundamentales para resolver problemas grandes de forma eficiente; es un método condicionalmente estable, el criterio de estabilidad esta dado por una relación de causalidad espacio-tiempo conocida como criterio de Courant, que relaciona el incremento temporal máximo con el incremento espacial; el método FDTD permite implementar condiciones ideales de truncamiento como condiciones absorbentes que simulan el espacio libre indefinido, condiciones periódicas, regiones de iluminación para la generación de ondas planas ideales, etc.

Sin embargo, la formulación clásica del método FDTD tiene ciertas carencias, como la baja adaptación geométrica de objetos curvos, lo que se traduce en una reducción del orden de convergencia, además de la escasa eficiencia de los generadores usuales de mallas estructuradas, a menudo con defectos en las conexiones topológicas entre objetos, incluso generando aperturas que no aparecen en la geometría original. Además, salvo recurriendo a mallas inmanejables por ser extremadamente densas, el método FDTD no puede tratar directamente al mismo tiempo, sistemas de distintas escalas geométricas: microscópicos (composición interna de materiales complejos como materiales multicapas, fibras, materiales compuestos con armaduras metálicas, etc), y macroscópicos (p.e. el fuselaje de un avión).

Esta tesis trata de dar respuesta a algunos de estos retos y se han realizado avances en tres líneas complementarias de investigación:

1. Generación de modelos subcelda para el tratamiento de materiales de interés aeronáutico. En la actualidad hay un incremento, en el sector industrial (automóvil, aeroespacial), del uso de materiales más resistentes y ligeros y con mejores propiedades mecánicas (aleaciones, materiales reforzados con armaduras y/o fibra carbono, ...), sin embargo desde el punto de vista electromagnético estos materiales son más permeables al campo electromagnético, y, por tanto, presentan un peor apantallamiento frente a los metales clásicos.

Para tratar materiales cuya complejidad interna no puede ser tratada directamente mediante el algoritmo FDTD de Yee, se toma un material homogéneo equivalente con las mismas propiedades electromagnéticas que el material físico. Para su tratamiento numérico, se pueden utilizar métodos basados en impedancias superficiales, que en FDTD requieren de extrapolaciones no causales, y que son con frecuencia culpables de inestabilidades tardías. Con la intención de solventar esto, en el Capítulo 2 de esta tesis, se propone un método alternativo denominado *SGBC*, basado en una propagación FDTD de los campos electromagnéticos en el interior del material mediante una discretización espacial más densa, que permite muestrear la longitud de onda mínima y la atenuación adecuadamente. Este método es además incondicionalmente estable gracias al uso de técnicas híbridas explícitas-implícitas HIE. Además el método *SGBC* se ha extendido al tratamiento de materiales dispersivos arbitrarios usando métodos de ecuaciones diferenciales auxiliares (ADE).

2. Generación de algoritmos de adaptación conforme estables basados en los de Dey-Mittra. Estos algoritmos utilizan técnicas intracelda para tratar superficies curvas mediante la distorsión de las celdas clásicas de Yee. Se ha demostrado que estos algoritmos adaptativos son mucho más precisos que los puramente estructurados, tienen un orden de convergencia mayor, permiten determinar con mayor precisión las frecuencias resonantes, mitigan e incluso eliminan muchas de las frecuencias espúreas propia de las mallas escalonadas. Sin embargo los algoritmos conformes presentan criterios de estabilidad más rigurosos que el criterio usual de FDTD. En el Capítulo 3 se describe una técnica eficiente para obtener mallas conformes que garantizan la estabilidad en función del grado de adaptación. Esta técnica se basa en la relajación ó filtrado de las celdas que producen la inestabilidades.

Al final del Capítulo 3, los algoritmos conforme anteriormente formulados para conductores eléctricos perfectos, son extendidos para tratar materiales delgados.

3. Generación de malladores para superficies conformes y estructuradas mediante una

nueva técnica basada en representación discreta de contornos, que se generan mediante la intersección entre las celdas estructuradas y la geometría original, usualmente dada en forma de una malla de triángulos. La versión estructurada de esta técnica ha demostrado ser más precisa y eficiente que las basadas en trazado de rayos, y permite mantener las conexiones topológicas de la geometría original de un modo natural.

Finalmente, todos los algoritmos propuestos han sido validados en dos niveles. Primero, en casos controlados utilizando resultados analíticos (superficies planas y esferas) ó geometrías muy controladas (almendra NASA), y, finalmente, mediante casos reales completos representativos de test típicos propuestos en las guías de certificación: evaluación de los efectos indirectos de rayos de un unmmanned air vehicle (UAV), función de transferencia sobre cables dentro un avión ante emisiones externas en espacio abierto, y en la evaluación de la eficiencia apantallamiento en cámara reverberante. Aunque sólo se presentan resultados para 3 plataformas concretas (el avión EV55, el UAV SIVA y una Nacelle de un F7X), los métodos han sido validados ampliamente por AIRBUS en multitud de casos reales, que por protección industrial no pueden ser diseminados.

Los algoritmos desarrollados han sido implementados empleando técnicas híbridas de paralelización basadas en OMP-MPI.

Del resultado directo de este trabajo se han realizado varias publicaciones en revistas y en congresos nacionales e internacionales (ver CV).

Contents

Declaración de Autoría	I
Resumen	XI
1 Introduction and state-of-the-art	3
1.1 Motivation	3
1.2 Computational Electromagnetics overview	6
1.3 State-of-the-art	9
1.4 Fundamentals of FDTD	12
1.4.1 Discretization	12
1.4.2 Stability	16
1.4.3 Dispersion	17
1.5 FDTD for electric and magnetic dispersive media	19
1.6 Contributions to the state-of-the-art	21
2 FDTD modeling of lossy thin-panels	23
2.1 Introduction	24
2.2 Starting assumption	24
2.3 Macroscopic models of thin-panels	25
2.4 Thin-panel equations: as LTI system	26
2.4.1 LTI-to-FDTD Coupling	27
2.5 Network Impedance Boundary Conditions	29
2.5.1 Time-domain implementation	30
2.5.2 Passivity, stability and causality	32
2.6 Subgridding boundary condition	34
2.6.1 Hybrid 1D FDTD - 3D FDTD	36
2.6.2 Hybrid 1D CNTD - 3D FDTD	37
2.6.3 Extension to arbitrarily dispersive panels	39
2.6.4 Stability of SGBC	40
2.6.5 Accuracy	44
2.7 subgridding boundary conditions (SGBC) and NIBC computer requirements	47
2.8 Conclusions	48

3	Robust and Stable Conformal Methods	51
3.1	Introduction	51
3.2	Improving stability in conformal methods	55
3.2.1	The Conformal Relaxed Dey-Mitra (CRDM) method	56
3.2.2	Locally Enlarged Cell Technique (LECT)	58
3.3	Conformal thin-panels	59
3.3.1	Staircased subgridding methods	59
3.3.2	Conformal bulk methods	60
3.3.3	Conformal Thin-Panels	62
4	Validation	65
4.1	RCS computation results for PEC targets	65
4.1.1	perfect electric conductor (PEC) sphere	65
4.1.2	Anisotropic mesh effects	68
4.1.3	PEC Nasa-Almond	70
4.1.4	Conclusion	72
4.2	SGBC and NIBC for lossy thin slabs	72
4.2.1	Shielding effectiveness of planar thin-panels	73
4.2.2	Shielding effectiveness of dispersive panels	78
4.2.3	Shielding effectiveness of a sphere	79
4.2.4	Resistance of thin strips	81
5	Aeronautical applications	85
5.1	EV55: a numerical test-case to assess HIRF effects	87
5.1.1	Simulation approach and results	87
5.1.2	Discussion	89
5.2	SIVA: a DCI test-case to assess LIE effects	92
5.2.1	Experimental setup	92
5.2.2	Numerical approach	93
5.2.3	FSV validation	99
5.3	Falcon 7X nacelle in a reverberation chamber	101
5.3.1	Modeling and simulation approaches	102
5.3.2	Simulation results	105
6	CAD/CAE implementation notes	109
6.1	SEMBA	110
6.2	UGRFDTD	110
6.3	Meshing techniques for FDTD	113
	Conclusions and future work	118
	Glossary	123

List of Figures	132
List of Tables	137
Bibliography	139
Curriculum Vitae	155

INTRODUCTION AND STATE-OF-THE-ART

This PhD is the result of the research work at the GEG, performed during 6 years in the framework of several public funded projects and private contracts with aeronautic companies. A common topic to all of them has been the development of high performance computing (HPC) tools for computational electromagnetic (CEM), especially applied to electromagnetic compatibility (EMC) assessment of air vehicles (AVs).

Its main contributions are centered in the development of novel adaptive-mesh sub-cell techniques for curved surfaces for the finite-difference time-domain (FDTD) method to treat multilayered lossy thin-panels. In this chapter, we revise the state-of-the-art of previous approaches and provide a basic introduction to the fundamentals of FDTD.

1.1 Motivation

The increasing complexity of on-board electronic systems in modern fly-by-wire AV has made the topic of EMC assessment and protection a major concern for aircraft safety. Furthermore, the increased use of composite materials worsens the situation due to their poorer screening and conductive capabilities compared to metallic ones. This is especially problematic in low frequency (LF), under 400 MHz, and in very low frequency (VLF), under 10 kHz. Ensuring a high level of immunity under electromagnetic (EM) hazards plays a key role for the safety of current aircrafts.

Before a newly developed AV model is permitted to operate, it must be certified by the responsible aviation regulatory authority. Since 2003, european aviation safety agency (EASA) is responsible to guaranty the civil certification of AV in the EU. This certificate testifies that the type of aircraft meets the safety requirements set by the EU. The EMC certification methods of air vehicles has predominantly been based on experimental testing, these methods are usually standardized in documents and certification guides defined in IEEE, American national standards institute (ANSI), society of automotive engineers (SAE),

European Organization for Civil Aviation Equipment (EUROCAE) (ED20105, ED20107) United States defense standard (U.S. MIL-STD) (MIL-STD-202, MIL-STD-461) and many others industry and company standards and specifications.

The experimental tests involve costly measurement techniques and high rework costs associated to EM weakness and vulnerabilities detection. To alleviate this, the use of numerical solvers is increasingly considered in order to complement and support experimental means, appearing in EUROCAE certification guides, such as [ED–2010]. Numerical simulators enable the engineer to address the full complexity of the problem and to better understand the impact of changing key parameters. Several validation processes, such as HIRF-SE, have demonstrated that the EM solvers can successfully mimic experimental setups for AVs. Modeling supports the decision-making process throughout the design stages considering the variability of parameters that influence EMC risks (such as cable rerouting, shielding, material replacement, etc.), thus leading to shortened design times and reduced overall costs. Additionally, it permits the analysis and quantification of situations that cannot be tested experimentally, for instance fully in-flight scenarios, or the applicability of new devices or materials for aeronautic use [Gutierrez-2016], speeding up their time to market.

Numerical methods provide evident advantages to be used as a complement measurement campaigns:

- Experimental tests are not always meaningful in flight conditions because of ground effects (considered in the norm [ED–2010]).
- Experimental tests involve difficulties in reproducing the real far-field conditions in laboratory; indeed, a lot of types of test demand a reverberant or anechoic chamber, so it is not always possible to verify the coupling of the complete system for the case of large aircrafts.
- Numerical methods allow to assess EM effect during the design phase, minimizing the rework activities in order to find weaknesses and mitigate EM vulnerabilities. This reduces the cost of development and keep time and costs associated to testing “under control”.

Traditionally, the EMC assessment of electromagnetic interference (EMI) in the aeronautic industry, has relied on experimental campaigns at late stages of the aircraft manufacturing, where correction and redesign costs due to unforeseen EMI issues are prohibitive. However, the current computing power of modern clusters is making it possible to apply numerical simulations to predict EMC issues at early stages of the aircraft design, allowing the engineer to take decisions in alternative cable routings, shielding, bonding, material replacement, structural network addition [Gutierrez-2016], etc. For this purpose, a wide variety of CEM algorithms and methods exists, increasingly more capable of addressing

the electrical sizes and complexity often encountered in the aircraft industry, and suitable to be employed during the whole life-cycle of an aircraft.

Though the certification phase continues to be encompassed by experimental setups, it is becoming more and more difficult to only rely on measurements to deal with EMC aspects, especially by the increasing complexity level added by materials and electronic equipment, thus targeting CEM tools to be used as complementary means for certification. Actually, the use of numerical solvers is already considered by the certification standard EUROCAE [ED-2010], as a complementary means to support the classical experimental EMC essays, since they permit to have a better understanding of the key EM parameters, and to take decisions on EMC leading to cost reductions and increased safety levels. They also provide feedback to understand and improve the classical test-setups by reducing their complexity. Furthermore, the effects of the measurement equipment can be taken into account, and results found in ground setups, can be extrapolated to realistic in-flight conditions [J.Boissin-2012].

There is a large experience acquired through decades of research [Parmantier-2013, M.Apra-2001, M. Apra-2008, E.Perrin-2010, Sherman-1995], and several projects devoted to this topic: FULMEN, ILDAS, EMHAZ, MOVEA, STRUCTURES, GENIAL, ARROW, SAFETEL, GEMCAR, SARITSU, UAVEMI. Among them, we stress the FP7 European project HIRF-SE (2008-2013) where the UGR participated in a 44-partner consortium, involving all major European Airframers and research institutions. During this time, the UGRFDTD simulation tool, based in the FDTD method, was endowed with state-of-the-art capabilities to deal with cable bundles [Berenger-2000] and lossy thin-panels [Sarto-1999] using MPI and OpenMP HPC parallelization paradigms. UGRFDTD was one of the time-domain tools that passed all validation and verification stages performed by external airframers with test-cases based on full AVs.

Of course, there exist also lots of commercial EM solvers available in the market: ANSYS HFSS, FEKO, CST, SEMCAD, IE3D, XFDTD, GEMS, etc. All of them constitute valuable tools for the analysis and design of EM scenarios, but their general-purpose nature makes them difficult to be successfully employed in specific situations found in aeronautics, where the complexity cannot be simply managed by brute-force methods. This fact makes it necessary to find trade-offs to model accurately the intricate details (slots, junctions, thin-panels, cable bundles,...) by equivalent simplified models that do not jeopardize the physics of the real AV, while obtaining computationally affordable models.

Among all the CEM methods, the time-domain (TD) ones are especially suited to deal with EMC problems. Mainly because of the transient ultra wide band (UWB) nature of the excitation sources (electromagnetic pulses (EMPs), lightning, etc.) and because TD allows the engineer to get a better insight to interpret the results, by taking into account their causality to isolate interactions appearing at different time instants. In turn, among TD methods, the FDTD method [Yee-1966, Taflove-2005, Garcia-2003], based on a the

discretization of Maxwell's curl equations by using centered finite differences, has become the most widely employed in EMC [Kantartzis-2008a, Kantartzis-2008b]. FDTD is a highly flexible method, capable of analyzing electrically large complex objects including all the complexity both in material behavior (dispersive, anisotropic, non-linear,...) and in geometry [T.Hubing-2008], with the sole limitation imposed by the number of points required to sample space/time field variations (apart from stability considerations, as described below). Lots of books [Taflove-1995, Taflove-2005, Yu-2006] and thousands of papers contribute to its constant improvement since early 80s.

The FDTD method is particularly suited for complex EMC studies because of its simplicity and versatility to accurately analyze inhomogeneous bodies with arbitrary material properties, and its ability to get the desired broadband response in a single run [Taflove-2005]. However, numerically assessing the EMC of air vehicles is a challenging task that involves many parameters to accurately describe the geometry and material properties, which must be properly handled and simplified to achieve efficient simulation scenarios.

This PhD dissertation contributes to the development of HPC algorithms based in FDTD, specifically proposing new sub-cell models to treat composite materials, including conformal adaptive methods to handle their curvature. Several EM scenarios have been considered to validate these techniques: propagation, shielding, radiation... As an integration platform, the wide band electromagnetic simulator (SEMBA) tool developed by the UGR research group has been employed.

1.2 Computational Electromagnetics overview

Before computers became broadly available, analytical methods were the usual choice to find closed-form or series solutions of Maxwell equations. After 1960 computing facilities gave birth to the CEM discipline which has grown exponentially since then. However, no universal numerical method has been devised to be applicable for all kind of EM problems found in current engineering scenarios, such as antennas, microwave, millimeter-wave, terahertz devices, RADAR, nanophotonics, imaging, bioelectromagnetics, EMC... As a result, a plethora of numerical methods currently co-exist, whose range of applicability strongly depends on the frequency band and the problem complexity, including trade-offs between accuracy and computational requirements.

Several classifications exist in literature [Miller-1997]. Let us briefly adopt the one shown Fig. 1.1 which includes the most relevant methods. A general division of them can be made attending to:

- **Solution Domain:** Time-domain (TD) and frequency-domain (FD).
- **Field Propagator:** Full-Wave method (integral operator, differential operator) and asymptotic methods.

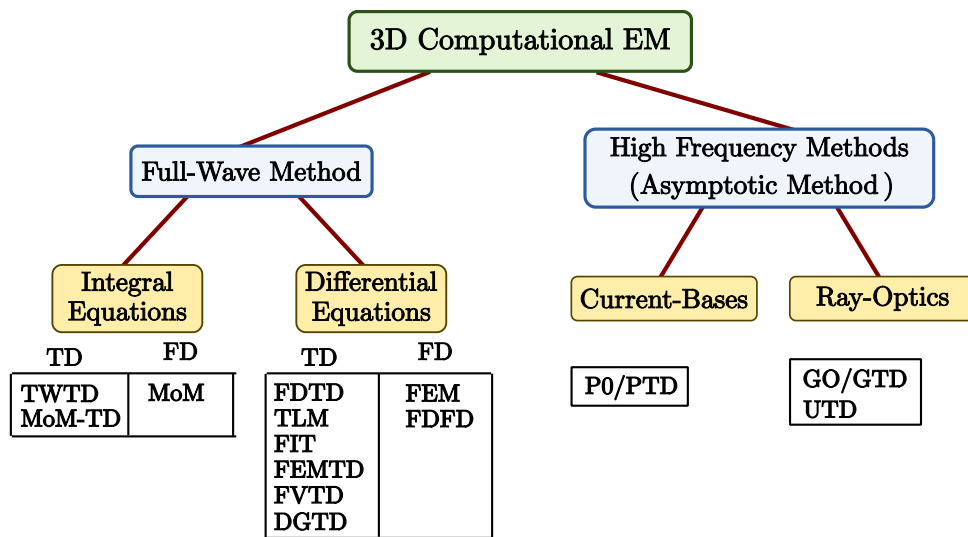


Figure 1.1: Classification of purely numerical 3D computational electromagnetic methods.

Asymptotic methods: Asymptotic methods find numerical solutions with low computational cost in the frequency-domain (FD), converging to the physical ones as frequency increases (optical approximations). They can be formulated as a simplified version of Maxwell's equations at high-frequencies, where the fields are propagated employing optical concepts thus ray-tracing (ray tubes), shadowing, and refraction/diffraction. There are lots of publications about the different techniques. A complete understanding of the mathematical formulation can be found [Bouche-2012].

- **Ray-Optic:** These methods are useful and improve when increasing frequency. Geometrical optics (GO) are fundamentally based on the refraction and reflection laws, using ray-tracing techniques without diffractions assumptions. This limitation does not let them predict fields at the shadow regions and to reproduce experimental observations such as Young's interference. To alleviate this, Geometric theory of diffraction (GTD) and Uniform theory of diffraction (UTD) methods were introduced. GTD method was formulated by J. B. Keller [Keller-1962]; it involves a more complicated ray-tracing, in order to take into account the contribution of diffracted rays from each diffracting object-source, specially those diffracted by corners, edges, shadow zones. It was applicable for objects with electric sizes around $ka > 5$. Another interesting extension of GTD was the UTD method presented in [Lewis-1969, Kouyoumjian-1974, Thiele-1975].
- The **Current-Based** methods such as physical optics (PO) and physical theory of diffraction (PTD), are an interesting family of asymptotic techniques [Bouche-2012, ch. 7]. PO employs GO for calculating the places of *lit* and shadow-zones, and finds the tangential field on surfaces from the currents, assuming that the incident field is

known. The tangential fields are subsequently propagated using Green's functions. These methods have employed with success in reflector antennas for main-lobe region calculation, for radar cross section (RCS) of large and complex objects (aircrafts, missiles). PTD was proposed by Ufimtsev [Ufimtsev-1971, Ufimtsev-1991, Ufimtsev-2007], it combines GO and GTD with algorithms for edge-current corrections.

Full-Wave methods: On the other hand, full-wave methods directly find the solution of Maxwell's equations by employing some kind of discretization, which ideally converge to the analytical one when refining the discretization. They can be classified, in turn, into integral and differential, attending to the starting form of Maxwell's equations. Depending on this, they also employ different discretization setups: structured (typical in pure differential methods), unstructured (in variational formulations of differential equations) or just boundary elements (in integral equation techniques).

Compared to volumetric differential equation methods, integral equation ones present the advantage of being boundary-element techniques. They only find the solution at surfaces, lines, interfaces where boundary conditions are known,... not requiring to propagate the solution across free-space. In turn, the propagator is provided by the knowledge of the problem Green's function, which is the kernel of the integral equations. The typical numerical technique to solve the integral equations is the well-known method of moments (MoM). It is characterized by its high accuracy, at the cost of high computer requirements due to the need to solve a system of equations (or matrix inversions). These may become prohibitive for electrically large problems, since the condition number of the system grows with the number of unknowns. Another drawback of integral equation methods is their lack of the generality to deal with bulk materials including anisotropy, dispersion, etc.

On the other hand, full-wave differential methods can handle complex bulk materials in a natural manner, at the cost of requiring the discretization of free-space between material objects. They include those directly solving Maxwell equations either in time or in frequency domain, using a direct discretization, and those solving them in a variational manner. The first ones typically employ structured meshes: Finite Difference in time-domain (FDTD) and Finite Difference in frequency-domain (FDFD), finite integration technique (FIT), transmission-line-matrix (TLM) method. Variational methods, both in FD and in TD, however, are usually formulated in unstructured meshes: finite volume (FV), finite element (FE), discontinuous galerkin (DG) methods. An advantage of variational methods is the possibility of employing geometric adaptivity combined with higher-order basis functions to achieve high accuracies, at the cost, compared to pure differential ones, of larger computer requirements.

Full-wave Frequency-domain (FD) methods, typically MoM and finite element method (FEM), are efficient to solve large structures with electrically small details in a narrow

frequency band. Their requirement to solve large system of equations (or to invert matrices), makes them inefficient for wideband analysis, for which TD methods are a natural alternative. However, structured-mesh TD methods impose severe constraints on the geometrical discretization of curved objects with direct impact on their accuracy. To overcome these limitations, conformal sub-cell techniques, like those presented in this dissertation, can be combined to be used locally the surface/line integral formulation of Ampère and Faraday’s laws to accurately model the object curvature. Finite-element time-domain (FETD) methods also constitute an alternative attracting an increasing attention. Especially those based on discontinuous galerkin time domain (DGTD) methods which retain most of the advantages of FDTD, FIT and TLM (explicit algorithm, simplicity, easy parallelization, low computational cost), combined with the advantages of classical finite element methods: geometrical adaptivity of the unstructured meshes and higher order convergences.

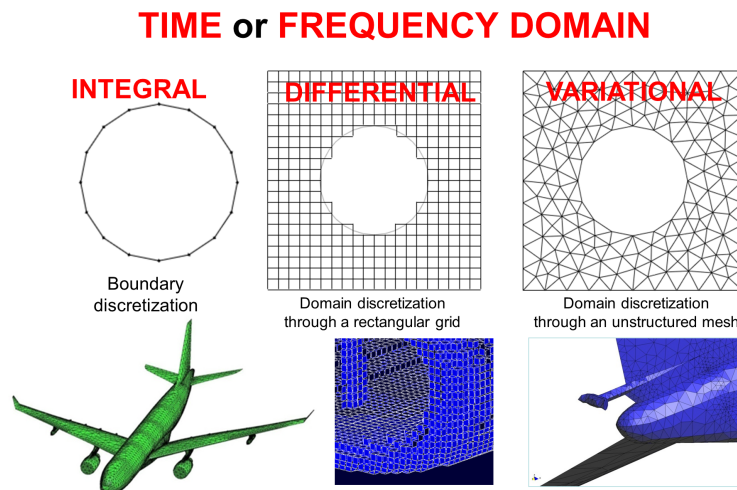


Figure 1.2: Typical discretizations depending on the numerical method.

In short, it should be noted that it is not possible to say that one or other method (FDTD, MoM, DGTD, FEM) or integration domain (TD, FD) is better or worse. This strongly depends on the range, precision, efficiency and specific needs of the application.

1.3 State-of-the-art

FDTD was introduced to the CEM community by Kane Yee in 1966 in the seminal paper [Yee-1966]. A huge bibliographic background exists describing its fundamentals and state-of-the-art. It is currently part of most syllabus of graduate courses in physics, electrical engineering and computer science. We are not going to review the existing bibliography in

this dissertation. Let us only mention the books of Allen Taflove [Taflove-2005, Taflove-2013] as excellent sources of information. Hence, we will focus ourselves solely in the review of antecedents directly relevant for the topics of this dissertation.

As mentioned in the previous section, a well-known major drawback of the FDTD method is its inherent staircasing approximation to model structures not aligned with the Cartesian mesh, which reduces the spatial error convergence from second to first order [Zagorodnov-2003, Nieter-2009]. To mitigate this effect, several alternatives have been proposed, being among the most popular ones those based on geometrically conformal approaches. Some of these make use of non-orthogonal coordinate systems or fully unstructured grids [Holland-1993]. Simpler approaches are based on integral forms of Ampère and Faraday laws, and give rise to the well-known contour path FDTD (CPFDTD) methods [Jurgens-1993, Gonzalez-1996]. CPFDTD have become popular for their accuracy, though the first formulations suffered from late-time instabilities, which limited their applicability [Railton-1995].

A modification of classical CPFDTD appeared in [Dey-1997] (Dey-Mitra (DM) method) with provable stability and second-order spatial convergence [Zagorodnov-2007]. A flaw of the DM method is that, the global time-step needs to be considerably reduced in order to ensure stability with respect to the usual FDTD Courant Friedrichs Lewy (CFL) conditions, thus degrading its computational performance. Since this seminal work was published, much effort has been dedicated to study new methods to overcome this time-step restriction.

In [Yu-2000] a variant of the DM method (Yu-Mitra (YM) method) was proposed to remove the time-step restriction by neglecting the differences in the areas of all irregular zones, which are taken as equal to that of the original Yee cell. This approach enables the authors to use the usual FDTD CFL stability criterion. The YM method is equivalent to introducing an artificial magnetic medium in conformal cells, which reduces its accuracy to first-order in space. This issue was overcome in [Benkler-2006] by employing an effective permeability for the magnetic field update and an electric permittivity for the electric field update (Benkler-Chavannes-Kuster method). A trade-off between the time-step and the accuracy, through a closed-form expression, can be found for the Benkler-Chavannes-Kuster method, which converges to that of the YM method at the usual CFL stability limit. Another technique, the enlarged cell techniques (ECT) proposed in [Xiao-2008], is based on enlarging the irregular cells and intruding on their neighbors. Although this method improves the stability constraints for all the cases presented therein, the requirement of enlarging the problematic cells is not straightforwardly applicable in complex geometries, since intruded cells cannot be intruders concurrently. Moreover, the ECT method requires a larger stencil, which is a significant change to be included in a already-existing traditional FDTD codes. In [Zagorodnov-2007], a technique called Uniformly Stable Conformal is proposed in the context of the FIT, claimed to be geometrically equivalent to ECT for FDTD. The authors

study two alternative methods consisting of modifying the area or the lengths of the irregular cells. They demonstrate an improvement in the time-step constraints without the need of enlarging the stencil. The authors also show that for certain cases they are able to achieve second-order accuracy.

The accurate and computationally affordable simulation of lossy thin-panels is another challenge in FDTD. This feature is necessary in electromagnetic simulation tools, as modern vehicle enclosures make use of them for electromagnetic or structural reasons. Examples include: multilayered carbon fiber composites [Holloway-2005], metal-mesh reinforcements [Sarto-2014], carbon nanotubes [Rosa-2008], graphene loaded composites [Nayyeri-2013], metalised coatings [Avloni-2007]. The main problem for FDTD to include them in its formulation, is the requirement of a dense discretization to properly sample the panel thickness, as well as to resolve the wavelength and skin-depth of waves propagating inside. In general, brute-force 3D meshing of thin-panels, joints, apertures and any small detail, is usually avoided for being unaffordable in terms of computational cost, making sub-cell equivalent models the preferred alternative. Three main techniques are found for approaching this: i) effective-parameter models; ii) Leontovich-based Impedance Boundary Conditions; and iii) fine-mesh discretization.

- i) Effective parameters (EP) models [Maloney-1992] have been demonstrated to accurately predict the conductive properties of electrically thin-panels at LF. These models are based on the definition of average constitutive parameters used to update the E-field components on the panel. They can model arbitrary dispersive behavior [Karkkainen-2003], and use extra degrees-of-freedom, to handle the discontinuity in the normal components, which are directly implemented in FDTD. These models are accurate for frequencies where the thin-panel thickness is smaller than, or comparable to, the skin depth.
- ii) Leontovich-based [Leontovich-1948] network impedance boundary conditions (NIBC) constitute a widely used alternative [Sarto-1999, Holloway-2005] also valid at high frequency (HF) where the EP approximation fails. NIBC techniques assume plane-wave propagation inside the thin-panel, along the direction normal to its surface, which is a reasonable hypothesis for highly conductive media with a refractive index much higher than that of the surrounding media. In this manner, NIBC does not need to take into account field components that are normal to the thin-panel, and only finds the tangential electric and magnetic fields at each thin-panel interface by using a frequency-domain matrix impedance relationships. The TD implementation in FDTD can be made in a number of ways: piecewise linear recursive convolution (PLRC) [Feliziani-1999, Sarto-1999], auxiliary differential equation (ADE) algorithms [Li-2015], circuital equivalents [Flintoft-2012, Feliziani-2012], etc. A drawback of

NIBC methods usually reported in literature for FDTD resides in the appearance of late-time instabilities [Kobidze-2010, Nayyeri-2013], often attributed to the upwind extrapolation used to co-locate the electric and magnetic fields at the interface [Cabello-2017a].

- iii) Finally, a natural alternative to EP and NIBC is to sub-grid with a dense spatial discretization inside the panel to properly resolve the wavelength and skin-depth attenuation inside it, thus allowing us to accurately deal with LF and HF regimes. However, the maximum allowable time-step for stability of classical FDTD depends on the minimum global mesh size, which is severely reduced for such dense discretizations, requiring unaffordable simulation times, even for modern computers.

In this dissertation we provide novel approaches to deal with the two challenges identified above. In a nutshell: robust methods to achieve mesh adaptivity for curved objects in general, and in particular for lossy thin-panels.

1.4 Fundamentals of FDTD

Let us briefly describe in this section the FDTD fundamentals and its main numerical characteristics: accuracy, stability, and dispersion. All of them are well studied in the FDTD literature, and we will only make here a simplified description. Other aspects, like the perfectly matched layer (PML) truncation conditions, total field (TF)/scattered field (SF) zoning, far-field and RCS calculation, thin-wire sub-cell approaches..., all of them already implemented in the simulator SEMBA-UGRFDTD used as a plug-in framework of this dissertation developments are not addressed in this document, since they are widely treated elsewhere [Taflove-2005, Yu-2006, Sullivan-2000, Kunz-1993, Schneider-2010].

1.4.1 Discretization

The classical FDTD method [Yee-1966] employs second-order centered operators to solve symmetric Maxwell's curl equations in time domain

$$-\nabla \times \vec{E} = \vec{M}_T + \mu_0 \frac{\partial \vec{H}}{\partial t} \quad (1.1a)$$

$$\nabla \times \vec{H} = \vec{J}_T + \epsilon_0 \frac{\partial \vec{E}}{\partial t} \quad (1.1b)$$

where \vec{J}_T, \vec{M}_T are the the total electric and magnetic current densities, \vec{E} and \vec{H} the electric and magnetic field vectors; all of them function of time and space (\vec{r}, t) . The total current densities include: the independent source current densities $J_{\text{source}}, M_{\text{source}}$; the polarization current densities J_p, M_p , in general dispersive and anisotropic; and the ohmic conduction

current density terms $J_c = \sigma E$, $M_c = \sigma_M H$,

$$\vec{M}_T = \vec{M}_{\text{source}} + \vec{M}_c + \vec{M}_p \quad (1.2a)$$

$$\vec{J}_T = \vec{J}_{\text{source}} + \vec{J}_c + \vec{J}_p \quad (1.2b)$$

The space and time discretization of the derivatives is performed by means of centered finite differences which can easily be proven to be a second-order approach to them

$$\frac{df(v)}{dv} \simeq \frac{f(v + \frac{\Delta v}{2}) - f(v - \frac{\Delta v}{2})}{\Delta v} \quad (1.3)$$

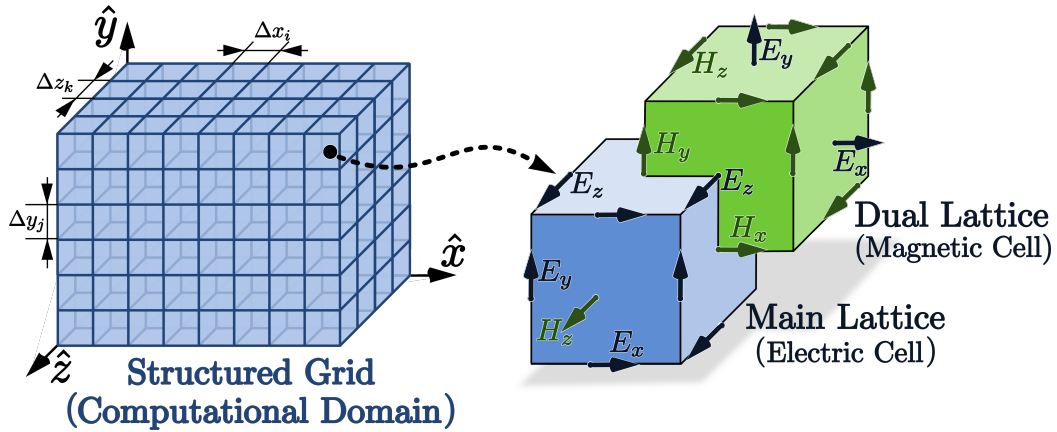


Figure 1.3: Position of the EM fields in Yee's cell.

This kind of discretization yields an explicit marching-on-in-time algorithm where the Cartesian components of the EM fields are naturally placed in the well-known Yee's cube staggered arrangement (Fig.1.3), and the E-field and H-field components evaluated at time instants shifted by a $\Delta t/2$ factor (it should be reminded that no one of the FDTD fields components are co-located at the same time-space point).

For instance, for the 1D source-free equations in free space we find

$$E_i^{n+1} = C_{a,i} E_i^n + C_{b,i} \left(H_{i-1/2}^{n+1/2} - H_{i+1/2}^{n+1/2} \right) \quad (1.4a)$$

$$H_{i+1/2}^{n+1/2} = D_{a,i+1/2} H_{i+1/2}^{n-1/2} + D_{b,i+1/2} \left(E_i^n - E_{i+1}^n \right) \quad (1.4b)$$

The subscript i denoted the space position ($i\Delta$), and the superscript n the time instant ($n\Delta t$). The evolution constants C_a, C_b, D_a, D_b take the value:

$$C_a = 1.0, \quad C_b = \frac{\Delta t}{\epsilon_0 \Delta} \quad (1.5a)$$

$$D_a = 1.0, \quad D_b = \frac{\Delta t}{\mu_0 \Delta} \quad (1.5b)$$

When ohmic currents exist, the evolution constants C_a, C_b, D_a and D_b of (1.4) must be modified, since a direct sampling of these terms would involve field components mixing for the same advancing equation the same field component evaluated both at integer and semi-integer time steps. Several approaches exist, depending on the time-integration scheme employed [Schuster-2000]. Common approaches are: time-backward, time-forward, time-average, and ETD. All of them lead to the same formal expression of (1.4) but making use of different evolution constants, and thus yielding different stability constraints (as shown below). Let us restrict ourselves to the two most common schemes: TA and ETD.

Time average (TA)

Time average (TA) employs a time-averaging procedure to co-locate in time all the E-fields (and H-fields) when ohmic terms are discretized. The resulting scheme is coherent with the space-time sampling, and preserves the second-order accuracy in time [Yee-1966] [Taflove-1995]. The evolution constants found after TA in 1D are:

$$C_{a,i} = \frac{2\tau_i - \Delta t}{2\tau_i + \Delta t} \quad (1.6a)$$

$$C_{b,i} = \frac{2\Delta t \tau_i}{\epsilon_i \Delta_i (2\tau_i + \Delta t)}$$

$$D_{a,i+1/2} = \frac{2\tau_{M,i+1/2} - \Delta t}{2\tau_{M,i+1/2} + \Delta t} \quad (1.6b)$$

$$D_{b,i+1/2} = \frac{2\Delta t \tau_{M,i+1/2}}{\mu_{i+1/2} \Delta_{i+1/2} (2\tau_{M,i+1/2} + \Delta t)}$$

where Δ_i is the cell size at the space position i , and $\Delta_{i+1/2}$ is the cell-size of the dual mesh defined by $\Delta_{i+1/2} = (\Delta_i + \Delta_{i+1})/2$. τ is the relaxation time given by:

$$\tau = \epsilon / \sigma \quad (1.7)$$

$$\tau_M = \mu / \sigma_M \quad (1.8)$$

Exponential time differencing (ETD)

Exponential time differencing (ETD) starts from a different assumption. Maxwell's equations can be expressed in terms of the superposition of a linear operator \mathcal{L} , and a non-homogeneous one \mathcal{N} . For instance for Ampère's law

$$\frac{\partial E(x,t)}{\partial t} - \mathcal{L}E(x,t) = \mathcal{N}(t) \quad (1.9)$$

where both $\mathcal{L} = -1/\tau$ and $\mathcal{N}(x,t) = \nabla \times H(x,t)/\varepsilon$ are continuous function.

Assuming a Cauchy initial-value problem, the solution of (1.9) can be expressed by

$$E(x,t) = e^{-(t-t_0)/\tau} E(x,t_0) + \frac{1}{\varepsilon} \int_{t_0}^t e^{-(t-t')/\tau} \nabla \times H(x,t') dt' \quad (1.10)$$

with the initial condition $E(x,t_0)$ assumed to be known. Sampling (1.10) [Beylkin-1998] in $t = (n+1)\Delta t$, $t_0 = n\Delta t$, and replacing the curl operator by its usual finite-centered approximation

$$\nabla \times H_i^{n+1/2} \sim \frac{H_{i-1/2}^{n+1/2} - H_{i+1/2}^{n+1/2}}{\Delta_{i-1/2}}$$

we find

$$E_i^{n+1} = e^{-\Delta t/\tau} E_i^n + \frac{1 - e^{-\Delta t/\tau}}{\sigma \Delta_{i-1/2}} \left(H_{i-1/2}^{n+1/2} - H_{i+1/2}^{n+1/2} \right) \quad (1.11)$$

and similarly

$$H_{i+1/2}^{n+1/2} = e^{-\Delta t/\tau_M} H_{i-1/2}^{n+1/2} + \frac{1 - e^{-\Delta t/\tau_M}}{\sigma_M \Delta_i} (E_i^n - E_{i+1}^n) \quad (1.12)$$

The expression found so far is formally identical to Yee's one (1.4a) except for the values of the evolution constants, which now become

$$C_a = e^{-\Delta t/\tau} \quad , \quad C_b = \frac{1 - e^{-\Delta t/\tau}}{\sigma \Delta x} \quad (1.13a)$$

$$D_a = e^{-\Delta t/\tau_M} \quad , \quad D_b = \frac{1 - e^{-\Delta t/\tau_M}}{\sigma_M \Delta x} \quad (1.13b)$$

It should be note that ETD can be seen in practice as a TA formulation with an enlarged permittivity/permeability. Since the updating equations TA y ETD are fully identical to (1.4), we can relate (1.6a) and (1.13a) by

$$\begin{aligned} C_{a,i}^{\text{TA}}(\sigma, \varepsilon) &= C_{a,i}^{\text{ETD}}(\sigma, \varepsilon_0) \\ C_{b,i}^{\text{TA}}(\sigma, \varepsilon) &= C_{b,i}^{\text{ETD}}(\sigma, \varepsilon_0) \end{aligned} \quad (1.14)$$

to find the following expression for the equivalent permittivity

$$\epsilon = \frac{\Delta t \sigma}{2} \frac{1 + e^{-\Delta t \sigma / \epsilon_0}}{1 - e^{-\Delta t \sigma / \epsilon_0}} \quad (1.15)$$

and, similarly, for the equivalent permeability

$$\mu = \frac{\Delta t \sigma_M}{2} \frac{1 + e^{-\Delta t \sigma_M / \mu_0}}{1 - e^{-\Delta t \sigma_M / \mu_0}} \quad (1.16)$$

Indeed, both the equivalent permittivity and permeability of ETD are larger than those of free-space, and converge to these in the limit of null conductivities. This fact presents, as later described, advantages of the ETD scheme over TA in terms of maximum allowable time step for stability.

1.4.2 Stability

The stability analysis of a numerical scheme aims at deriving the analytical conditions to yield bounded solutions when the excitation sources are also bounded. There are different techniques to deal with this problem [Sewell-2005, Kunz-1993, Taflove-1995, Remis-2000]. Let us mention three of them: the Von-Neumann criterion [VonNeumann-1950, Richtmyer-1967] requiring numerical plane-waves to propagate in a energy-conservative manner (or even dissipative); the Courant-Friedrich-Lewy [Courant-1967] criterion that make use of the causality of Maxwell's equations to require the numerical solution to include at least the causal light-cone of dependency of the analytical solutions; and the spectral criteria requiring the eigenvalues of the numerical time operator to be bounded [Gottlieb-1987] [Gottlieb-1987] [Morton-2005, Pg 241]. All of them can be proven to be equivalent, thanks to the Lax theorem [Lax-1956].

Whatever the method employed, the stability criterion enforces an upper limit to the time-step used for the discretization. In 3D, the following restriction is found [Taflove-2005]

$$c\Delta t \sqrt{\sum_v \frac{1}{\Delta_v^2}} \leq 1 \quad (1.17)$$

where v stands for the Cartesian directions $v = x, y, z$ and c is the phase speed of the light in the underlying medium. Note that the maximum time-step enforced by (1.17) decreases with the minimum cell size used for the spatial discretization.

The equation (1.17) is often referred to in literature as the CFL criterion, which serves to define the Courant Friedrichs Lewy number (CFLN)

$$\text{CFLN} = c\Delta t \sqrt{\sum_v \frac{1}{\Delta_v^2}} \quad (1.18)$$

which must fulfill $\text{CFLN} \leq 1$ for stability.

There are significant differences between the stability criteria when ohmic materials ($\sigma > 0$ or $\sigma_M > 0$) are treated either by ETD or by TA. Whereas TA requires the same stability limit than the lossless case (e.g. in 1D)

$$\text{CFLN}_{\text{TA}} = \frac{\Delta t}{\sqrt{\mu \epsilon}} \sqrt{\sum_v \frac{1}{\Delta_v^2}} \quad (1.19)$$

ETD is less restrictive than TA, as expected, since the phase speed in the equivalent media is slower than that of free-space. Replacing (1.15) and (1.16) in (1.19) we find

$$\text{CFLN}_{\text{ETD}} = \frac{2}{\sqrt{\sigma \sigma_M}} \sqrt{\frac{1 - e^{-\Delta t \sigma / \epsilon_0}}{1 + e^{-\Delta t \sigma / \epsilon_0}}} \sqrt{\frac{1 - e^{-\Delta t \sigma_M / \mu_0}}{1 + e^{-\Delta t \sigma_M / \mu_0}}} \sqrt{\sum_v \frac{1}{\Delta_v^2}} \quad (1.20)$$

1.4.3 Dispersion

It is a proven fact that FDTD is divergence-free and energy-preserving if it is stable, however it suffers from phase dispersion errors. Finding the numerical second-order wave equations from the numerical FDTD Ampère and Faraday's first-order equations, and searching for plane-wave solutions, we find the numerical dispersion relationship, that relates the numerical wavenumber to the angular frequency ω

$$\left(\frac{1}{c_0 \Delta t} \sin \left(\frac{\Delta t \omega}{2} \right) \right)^2 = \sum_{i=x,y,z} \left(\frac{1}{\Delta_i} \sin \left(\frac{k_i \Delta_i}{2} \right) \right)^2 \quad (1.21)$$

which is clearly different from the analytical one $\omega^2 = c_0^2 \sum_{i=x,y,z} k_i^2$. That is to say, there exists an artificial numerical dispersion due to the fact that the numerical phase speed in the discrete space does not coincide with that in the physical continuum space. Note that this error is actually anisotropic in 3D. Further details on this are well known in literature [Taflove-2005] and will not be reproduced here.

However, let us get some further insight in the numerical dispersion phenomena by resorting to the 1D case, for which (1.21) simplifies to

$$\sin^2 \left(\frac{\Delta t \omega}{2} \right) = \left(\frac{c_0 \Delta t}{\Delta} \right)^2 \sin^2 \left(\frac{k \Delta}{2} \right) \quad (1.22)$$

Employing (1.22) we find the numerical phase speed as a function of the Courant Number (1.19), and the space resolution point per wave length (PPW):

$$v_{\text{ph, num}} = \frac{\omega}{k} = \frac{\pi c_0}{\text{PPW} \arcsin \left(\frac{1}{\text{CFLN}} \sin \left(\frac{\pi \text{CFLN}}{\text{PPW}} \right) \right)} \quad (1.23)$$

where $\text{CFLN} = c_0 \Delta t / \Delta$ and PPW is the number of points per wavelength taken to sample the analytical wavelength.

$$\text{PPW} = \frac{\lambda}{\Delta} = \frac{2\pi c_0}{\omega \Delta} \quad (1.24)$$

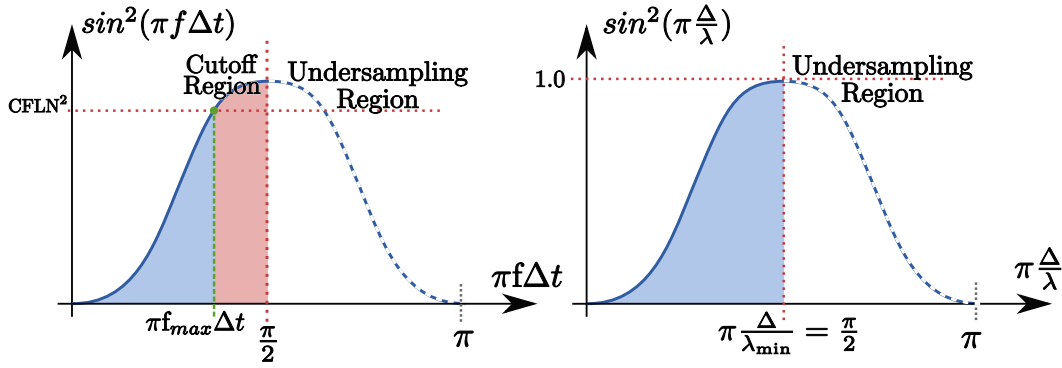


Figure 1.4: Wavenumber and frequency domain allowable solutions for a fixed CFLN in 1D.

Fig.1.5 shows the numerical phase speed (normalized to c_0) for a plane wave propagating in free-space, which converges to 1 when $\text{CFLN} \rightarrow 1$, decreases for $\text{CFLN} < 1$, and increases with the space resolution

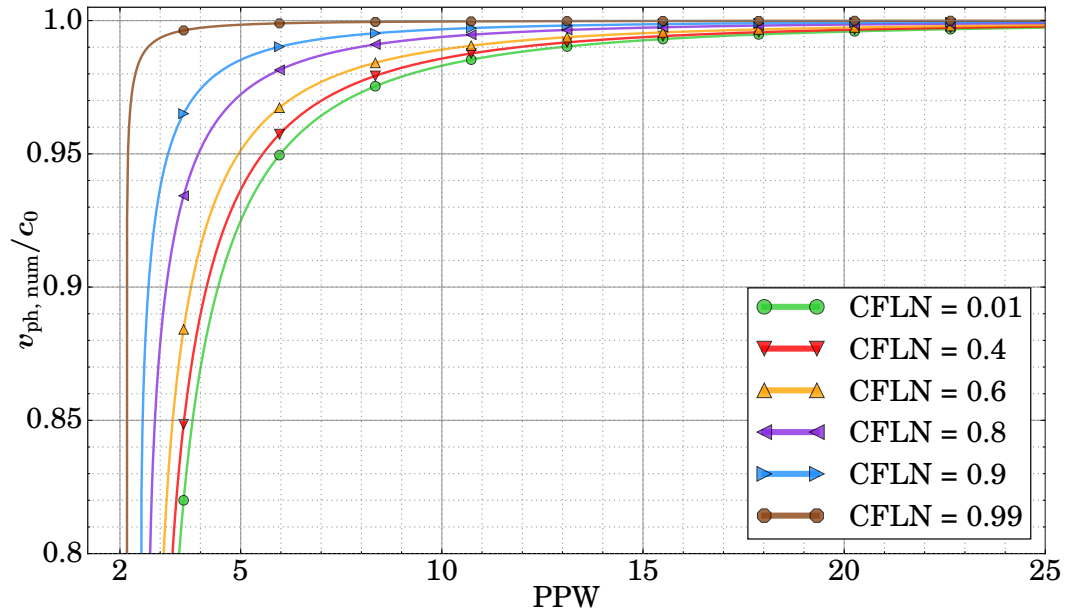


Figure 1.5: Numerical phase speed normalized to c_0 as a function of PPW for different CFLN in 1D.

The left-hand-side term of (1.22) allows us to obtain the maximum frequency as a function of the CFLN and the Nyquist sampling limit $f_0 = 1/(2\Delta t)$:

$$\sin^2(\pi f_{\max} \Delta t) = \text{CFLN}^2 \Rightarrow f_{\max} = f_0 \frac{2 \arcsin(\text{CFLN})}{\pi} \quad (1.25)$$

Using the space term in the right-hand-side of (1.22) we find the numerical wavelength as a function of the frequency

$$\lambda_{\text{num}}(f) = \frac{\pi\Delta}{\arcsin\left(\frac{\sin(\pi f\Delta t)}{\text{CFLN}}\right)} \quad (1.26)$$

1.5 FDTD for electric and magnetic dispersive media

Finally let us briefly describe in this Section the treatment used to deal with arbitrary frequency dispersive dielectric and magnetic materials, for its relevance for the algorithms presented in Section 2.6.3 to deal with multilayered thin-panels.

A typical way, found in literature, to treat dispersive materials assumes some type of dispersion (Debye, Lorentz, Drude, etc.) and produce a particular algorithm to include the constitutive relationships in TD and in FDTD. Different formulations are also found by using either the time-domain relationships between the electric/magnetic polarization currents and the E/H fields, or by directly using the D/B-E/H ones, either in convolutional or auxiliary differential equation (ADE) form [Taflove-2005, Pg. 361], [Okoniewski-1997].

Without entering in further discussions of the equivalence of the different approaches (see [Ramadan-2015] for instance), we will next describe the one taken in this dissertation which employs the ADE TD formulation given in [Han-2006]. This technique does not make distinction on the order of the dispersive model, and uses a general methodology which can be applied for all kind of dispersive materials, as far as their complex electric permittivity (permeability) can be expressed in a partial fraction expansion, as the sum of non-degenerate complex-conjugate pole-residue-pair fractions, found by a vector-fitting (VF) algorithm [Gustavsen-1999]

$$\epsilon_{\text{eff}}(\omega) = \sum_{k=1}^{N_{\epsilon,0}} \frac{R_{\epsilon,k}}{j\omega - p_{\epsilon,k}} \quad \mu_{\text{eff}}(\omega) = \sum_{k=1}^{N_{\mu,0}} \frac{R_{\mu,k}}{j\omega - p_{\mu,k}} \quad (1.27)$$

Maxwell's equations (1.1) in frequency domain, including the polarization current densities (1.2) can be written as

$$\epsilon_{\infty} j\omega \vec{E}(\omega) + \sigma \vec{E} + \vec{J}_p(\omega) = \nabla \times \vec{H}(\omega) \quad (1.28a)$$

$$\mu_{\infty} j\omega \vec{H}(\omega) + \sigma_M \vec{H} + \vec{M}_p(\omega) = -\nabla \times \vec{E}(\omega) \quad (1.28b)$$

where the constitutive relationships

$$\vec{J}_p(\omega) = j\omega \epsilon_{\text{eff}}(\omega) \vec{E}(\omega)$$

$$\vec{M}_p(\omega) = j\omega \mu_{\text{eff}}(\omega) \vec{H}(\omega)$$

Using the expansion (1.27) the currents can be decomposed into $\vec{J}_p(\omega) = \sum_k^{N_{e,0}} \vec{J}_{p,k}(\omega)$ and $\vec{M}_p(\omega) = \sum_k^{N_{h,0}} \vec{M}_{p,k}(\omega)$, with

$$\vec{J}_{p,k}(\omega) = \frac{R_{\varepsilon,k}}{j\omega - p_{\varepsilon,k}} j\omega \vec{E}(\omega) \quad (1.29a)$$

$$\vec{M}_{p,k}(\omega) = \frac{R_{\mu,k}}{j\omega - p_{\mu,k}} j\omega \vec{H}(\omega) \quad (1.29b)$$

Each term of the expansion is naturally causal (complies with Kramers-Kronig) and stable by requiring the VF procedure to produce poles in the left complex semi-plane. As a result, the polarization currents equations can be coupled to Maxwell's equations straightforwardly through the electric and magnetic fields found after solving the TD auxiliary differential equations arising from the FD equations (1.29)

$$\frac{d\vec{J}_{p,k}}{dt} - p_{e,k} \vec{J}_{p,k} = R_{e,k} \frac{d\vec{E}}{dt} \quad (1.30a)$$

$$\frac{d\vec{M}_{p,k}}{dt} - p_{h,k} \vec{M}_{p,k} = R_{h,k} \frac{d\vec{H}}{dt} \quad (1.30b)$$

Following the usual replacement of derivatives by centered differences, and using TA to evaluate the fields non-located in time, a FDTD consistent and explicit algorithm is found [Han-2006]

$$J_{p,i,k}^n = k_{\varepsilon,i,k} J_{i,k}^{n-1} + \beta_{\varepsilon,i,k} (E_i^n - E_i^{n-1}) \quad (1.31a)$$

$$M_{p,i+1/2,k}^{n+1/2} = k_{\mu,i+1/2,k} M_{i+1/2,k}^{n-1/2} + \beta_{\mu,i+1/2,k} (H_{i+1/2}^{n+1/2} - H_{i+1/2}^{n-1/2}) \quad (1.31b)$$

$$E_i^{n+1} = C_{a,i} E_i^n + C_{J,i} (2\nabla \times H_i^{n+1/2} - J_{p,i}^n) \quad (1.32a)$$

$$H_{i+1/2}^{n+1/2} = D_{a,i+1/2} H_{i+1/2}^{n-1/2} + D_{M,i+1/2} (2\nabla \times E_{i+1/2}^n - M_{p,i+1/2}^{n-1/2}) \quad (1.32b)$$

where the updating constants $C_{a,i}, D_{a,i+1/2}, C_{J,i}, D_{M,i+1/2}$ for the TA scheme are

$$J_{p,i}^n = \text{Re} \sum_{k=1}^{N_{\varepsilon,0}} (1 + \kappa_{\varepsilon,i,k}) J_{p,i,k}^n \quad (1.33a)$$

$$M_{p,i+1/2}^{n+1/2} = \text{Re} \sum_{k=1}^{N_{\mu,0}} (1 + \kappa_{\mu,i+1/2,k}) M_{p,i+1/2,k}^{n+1/2} \quad (1.33b)$$

$$C_{a,i} = \frac{2\varepsilon_\infty + \Lambda_{\varepsilon,i} - \sigma_i \Delta t}{2\varepsilon_\infty + \Lambda_{\varepsilon,i} + \sigma_i \Delta t} \quad (1.34a)$$

$$C_{J,i} = \frac{\Delta t}{2\varepsilon_\infty + \Lambda_{\varepsilon,i} + \sigma_i \Delta t}$$

$$D_{a,i+1/2} = \frac{2\mu_\infty + \Lambda_{\mu,i+1/2} - \sigma_{M,i+1/2} \Delta t}{2\mu_\infty + \Lambda_{\mu,i+1/2} + \sigma_{M,i+1/2} \Delta t} \quad (1.34b)$$

$$D_{M,i+1/2} = \frac{\Delta t}{2\mu_\infty + \Lambda_{\mu,i+1/2} + \sigma_{M,i+1/2} \Delta t}$$

And κ and β

$$\kappa_{v,\xi,k} = \frac{1 + p_{v,\xi,k} \Delta t / 2}{1 - p_{v,\xi,k} \Delta t / 2} \quad \beta_{v,\xi,k} = \frac{R_{v,\xi,k}}{1 - p_{v,\xi,k} \Delta t / 2} \quad (1.35)$$

$$\Lambda_{v,\xi} = \text{Re} \sum_{k=1}^{N_{v,0}} \beta_{v,\xi,k} \Delta t$$

Just for reference (1.32) becomes in 1D

$$E_i^{n+1} = C_{a,i} E_i^n + C_{b,i} \left(H_{i+1/2}^{n+1/2} - H_{i-1/2}^{n+1/2} \right) - C_{J,i} J_{p,i}^n \quad (1.36a)$$

$$H_{i+1/2}^{n+1/2} = D_{a,i+1/2} H_{i+1/2}^{n-1/2} + D_{b,i+1/2} \left(E_{i+1/2}^n - E_{i-1/2}^n \right) \quad (1.36b)$$

$$- D_{M,i+1/2} M_{p,i+1/2}^{n-1/2}$$

with $C_{b,i}$ and $D_{b,i+1/2}$

$$C_{b,i} = \frac{2\Delta t / \Delta_i}{2\varepsilon_\infty + \Lambda_{\varepsilon,i} + \sigma_i \Delta t} \quad D_{b,i+1/2} = \frac{\Delta t / \Lambda_{i+1/2}}{2\mu_\infty + \Lambda_{\mu,i+1/2} + \sigma_{M,i+1/2} \Delta t} \quad (1.37)$$

1.6 Contributions to the state-of-the-art

The rest of this manuscript presents contributions to the FDTD method carried on during this thesis. It is organized as follows: Chapter 2 illustrates two different techniques for the modeling of lossy *thin-panel* in FDTD called *subgridding boundary conditions (SGBC)* and *network impedance boundary conditions (NIBC)*. These are extended to conformal methods in Chapter 3. The same chapter introduces two different techniques for the treatment of 3D conformal meshes based on DM methods in order to obtain a global stability criterion, these techniques are called *conformal relaxed Dey-Mitra (CRDM)* and *locally enlarged cell technique (LECT)*. The validation results for challenging test-cases are presented in Chapter 4. In the Chapter 5 the numerical methods described in this thesis are applied to three typical test-cases presented in aeronautical certification guides as [ED–2010]. Finally,

Chapter 6 describes the implementation details of the software developed for this thesis and its usefulness and applicability for different design stages in industrial contexts.

FDTD MODELING OF LOSSY THIN-PANELS

This chapter presents a novel technique for the modeling of lossy thin-panels in FDTD schemes, with the main advantage of overcoming the instability problems of classical impedance boundary conditions techniques. Thin-panels can be understood as bodies whose thicknesses are very small with respect to the cell size of the FDTD grid. This fact makes them unaffordable to be solved by the usual methods and therefore special sub-cell techniques are required to simulate them. The method presented starts from the same physical hypothesis of the traditional methods, *i.e.* transversal electromagnetic (TEM) propagation normal to the panel, but instead of it, this technique employs a subgridding method inside the material in order to take the wave propagation into account. Therefore, the lossy thin-panel is meshed along its normal direction with a space step much finer than the one used in the surrounding medium. The tangential E-field components lying at the boundaries between the 1D and the 3D domain are updated by using weighted average conductivities and permittivities.

We discuss three techniques that may be used to update the fields in the subgridded zone. The first two are usual FDTD time-integration methods: TA and ETD. TA becomes rapidly unaffordable, requiring dramatic reductions in the maximum time-step in order to retain stability, whereas ETD still permits moderate reductions that can be feasible for some problems. For this reason, we present an alternative based on the unconditionally stable tridiagonally implicit CN-FDTD method which removes the restrictions on the maximum time-step. A hybrid implicit-explicit (HIE) algorithm is employed to connect the subgridded zone with the outer 3D-Yee FDTD space. The HIE algorithm preserves the usual stability of FDTD for the full problem. The stability of the different SGBC algorithms is analyzed and their accuracy is studied. The combination of this techniques results in a robust alternative to the NIBC methods with the advantages of having a low computational cost and not exhibiting late-time instabilities.

2.1 Introduction

The accurate simulation of lossy thin-panels is a classical challenge of the FDTD method. Lossy thin-panels provide a convenient way to model the EM behavior of modern vehicle enclosures, where carbon fiber based materials and composites are being pervasively used [Holloway-2005, Sarto-2014, Rosa-2008, Nayyeri-2013, Avloni-2007]. The brute-force discretization of the panel thickness, often multilayered, to sample waves propagating inside it, becomes computationally expensive, as shown in this chapter, and efficient alternatives are required.

A classical approach are Leontovich-based NIBC. NIBC is a general technique that enables the handling of arbitrarily multi-layered thin-panel, including their anisotropic dispersive behavior. NIBC relates the electric and magnetic fields on either side of the thin-panel by an impedance matrix in a two/four-port network model [Sarto-1999, Flintoft-2007, Li-2015]. A main drawback of NIBC resides in the appearance of late-time instabilities with an origin that is still not well known. Let us just mention that these have often been attributed [Kobidze-2010, Nayyeri-2013] to the H-node space-time upwind extrapolation required in classical FDTD in order to co-locate the tangential components of the electric and magnetic fields on the thin-panel surface. In our experience, even if canonical problems do not suffer from late-time instabilities, large and complex ones may exhibit them.

In this chapter we revisit the NIBC fundamentals, and propose a novel alternative overcoming the stability issues of NIBC based on a 1D subgridding of the thin-panel only along its perpendicular direction. We describe in detail this new approach, henceforth referred to as SGBC method, paying attention to its stability and its accuracy. In order to prevent reductions in the maximum time step for stability, the SGBC is combined with an unconditionally stable Crank-Nicolson time-domain (CNTD) [Salvador G. Garcia-2005], and a stable HIE algorithm [Wang-2014] to connect the CNTD method inside the thin-panel with the usual 3D Yee-FDTD method used outside it.

2.2 Starting assumption

Both NIBC and SGBC start from a common hypothesis which assumes that a plane wave impinging on a conductive planar thin-panel with oblique incidence will refract at a close-to-normal angle $\theta_t \rightarrow 0$ regardless of the actual angle of incidence θ_i , if the refractive index is much higher inside the thin-panel than outside. Indeed, for instance, for a lossy medium with free-space permittivity, embedded in free-space, Snell's law can be written as:

$$\sin(\theta_t) = \frac{\sin(\theta_i)}{\sqrt{1 - j/Q}}, \quad Q = 2\pi f\tau, \quad \tau = \frac{\epsilon}{\sigma} \quad (2.1)$$

where Q is the quality factor, τ is the relaxation time constant, and σ is the conductivity of the medium. For instance, for grazing incidence $\theta_i \rightarrow \pi/2$ (the worst-case), we find that $|\theta_r| < 10^{-2}$ if

$$f [\text{GHz}] < 1.8 \sigma [\text{kS/m}] \quad (2.2)$$

For instance, for conductivities of $\sigma > 10^4$ S/m, the applicability of the model is up to 18 GHz, regardless of the thickness of the thin-panel. Therefore, the transverse plane-wave assumption enables us to make a general analysis of most common thin-panel conductive materials in automotive or aeronautics applications.

Hence, both NIBC and SGBC only require the knowledge of the tangential field components on each side of the thin-panel. The main difference between them resides in the way that these are assessed: from surface impedance relationships, or from a 1D time-stepping algorithm which explicitly propagates the E and H fields inside the thin-panel. We will show that the latter does not require the time-space extrapolations of NIBC, suspicious of the stability issues of the former, preserving the natural non-colocated staggering of the usual FDTD method, and hence providing a robustly stable alternative.

2.3 Macroscopic models of thin-panels

Whatever technique is used for simulation, it will require information of its general frequency-dependent behavior. This information is often available from analytical models [Wait-1955, Holloway-2005, Sarto-2014] derived from its microscopic structure (e.g. a wire mesh of known geometry), from experimental measurements, provided by the material manufacturer, or even from simulation of its microscopic structure [Volski-2009]. This information is typically specified in terms of S-parameters or constitutive parameters equivalent detailed for each panel layer. The typical workflow (Fig. 2.1) to plug this information into the FDTD solver, depends on the method to be employed, NIBC or SGBC.

Since NIBC requires impedance relationships, S-parameters must be transformed into Z-parameters [Frickey-1994]; alternatively if the constitutive relationships are known, S-parameters can be analytically derived. For multilayered structures, the cascading of ABCD-parameters found from the S ones, permits to find the total Z-parameters in a simple manner.

However SGBC requires the constitutive parameters and its thickness layer-by-layer (or equivalent ones for the whole multilayer). When only S-parameters are available (typically coming from measurements), a set of effective constitutive parameters (ϵ_{eff} , μ_{eff}) need to be found by using parameter extraction homogenization techniques [Chen-2004, Hu-2010]. This poses an added difficulty for being this inverse problem non-uniquely determined [Arslanagić-2013].

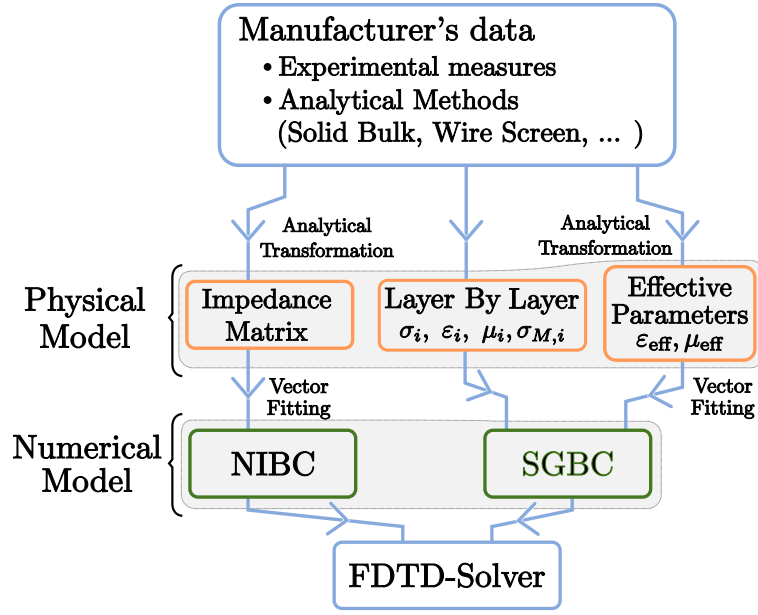


Figure 2.1: Typical workflow for the thin-panel FDTD simulation.

2.4 Thin-panel equations: as LTI system

The TEM plane-wave propagation through the conductive layer allows us to use an equivalent transmission line, 2-port network for isotropic media or 4-port network for anisotropic media, relating the electric and magnetic field tangential components at either of its sides Fig. 2.2. In this manner, the thin-panel can be regarded as a linear time invariant (LTI) system, formally described by introducing an integro-differential linear time operator \mathcal{Z}_t

$$[E_S](t) = \mathcal{Z}_t ([H_S](t)) \quad (2.3)$$

where $[H_S](t)$ and $[E_S](t)$ are the vector variables at the input and the output of the LTI system.

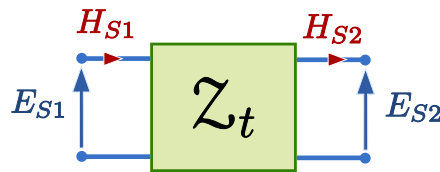


Figure 2.2: Two-port linear network equivalent to a planar thin-panel.

2.4.1 LTI-to-FDTD Coupling

The LTI relationships can be combined with the usual 3D Yee-FDTD scheme by duplicating the tangential electric fields $E_{Yee,1}^n, E_{Yee,2}^n$ at either side of the thin-panel Fig. 2.3. Assuming that these are found by the LTI equations, they are simply coupled from LTI to the 3D FDTD scheme by using them as boundary conditions (BC). The other way coupling, 3D Yee FDTD-to-LTI, is not so straightforward for the NIBC version of the LTI, and it needs some additional time-domain extrapolations as later described in Section 2.5.1, whereas it is natural for the LTI version SGBC, as described in Section 2.6.1.

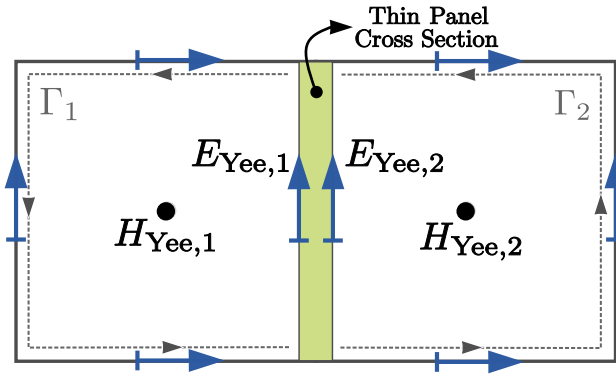


Figure 2.3: Coupling the LTI with FDTD.

So, focusing on the one-way LTI-to-FDTD coupling, and assuming that $E_{Yee,1}^n$ and $E_{Yee,2}^n$ is found by the LTI equations, the H-fields at the adjacent cells $H_{Yee,1}^{n+1/2}$ and $H_{Yee,2}^{n+1/2}$, employ the usual update algorithm by making use of these in Ampere's law, evaluated along a reduced loop to account for the thin-panel thickness

$$\begin{aligned} H_{Yee,1}^{n+1/2} &= H_{Yee,1}^{n-1/2} - \frac{\Delta t}{\mu_0 A_1} \left(\Gamma_1^n + \Delta_{\text{coarse}} E_{Yee,1}^n \right) \\ H_{Yee,2}^{n+1/2} &= H_{Yee,2}^{n-1/2} - \frac{\Delta t}{\mu_0 A_2} \left(\Gamma_2^n - \Delta_{\text{coarse}} E_{Yee,2}^n \right) \end{aligned} \quad (2.4)$$

Where $\Gamma_j^n = \sum_{\text{cell}_j} \Delta_i E_i^n$ is the usual discrete line integral of the E-field components along the 3 non-boundary edges. The surfaces used for the flux of the H-field are corrected to take into account the thin-panel thickness $A_{1,2} = \Delta_{\text{coarse}} \left(\Delta_{\text{coarse}} - \frac{th}{2} \right)$.

However, in a typical 3D FDTD problem we rarely find pure planar thin-panels aligned with the Cartesian grid. Typically the model is a staircase with a large number of 90-degree edges, along which the tangential E and H fields assume the TEM relationship, which serves as starting hypothesis of either NIBC or SGBC. The uncertainty of the normal to the thin-panel at each edge, makes it necessary to provide some methodology to prevent inaccuracies. Two techniques are found in the literature: the classical edge centered (EC) one [Sarto-1999], and a new face-centered approach [Flintoft-2012, J. F. Dawson-2017].

1. **Edge centered (EC) technique:** This technique leaves unaltered the usual Yee distribution of fields, therefore the electric fields along the edges are related by their LTI equation

$$[E]_{\text{Yee}} = \mathcal{Z}_r ([H]_{\text{Yee}}) \quad (2.5)$$

and the magnetic field components H_{Yee} at each side are found by the usual Yee-FDTD algorithm (2.4). For E-fields laying in a 90-degree edge, an average of the two ones is made, using each of the H-fields along the two normals of the planes intersecting at that edge.

2. **Face centered (FC) technique:** A major drawback of EC is essentially caused by the ambiguity of the normal vector of the surfaces intersecting at each edge. This is worsened in case of anisotropy, since the staggering of Yee distribution of E/H fields prevents to simultaneously have two tangential polarizations in an edge.

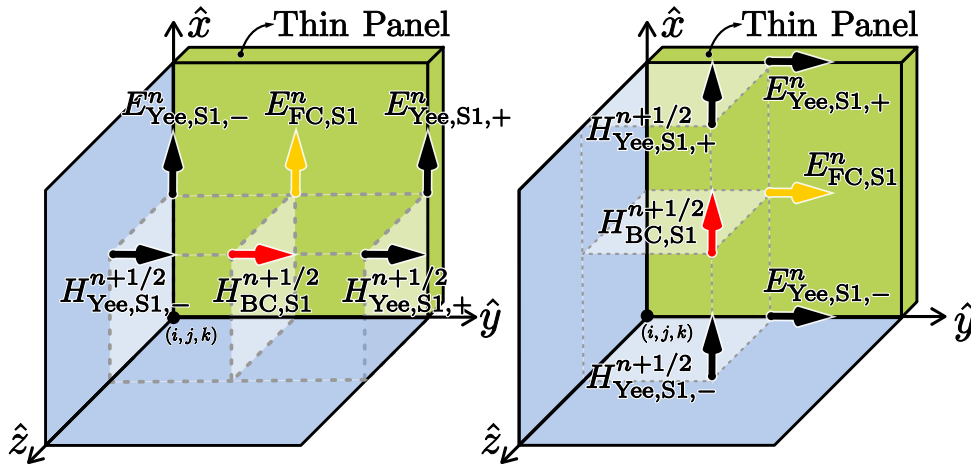


Figure 2.4: Spatial collocation of the tangential EM-Fields in the face centered (FC) approach.

FC addresses this issue by locating the fields found by LTI at the center of each cell, instead of along the edges. Proper interpolations are subsequently employed to find the fields at the actual Yee positions for the usual FDTD algorithm to continue. We can summarize, with the help of Fig. 2.4, the FC algorithm as follows:

- 1) The magnetic field components H_{BC} at the center of the volume cells are found by interpolating the known ones at the usual Yee positions at each side of the thin-panel (S1, S2):

$$H_{\text{BC},S1}^{n+1/2} = \frac{1}{2} \left(H_{\text{Yee},S1,-}^{n+1/2} + H_{\text{Yee},S1,+}^{n+1/2} \right)$$

$$H_{\text{BC},S2}^{n+1/2} = \frac{1}{2} \left(H_{\text{Yee},S2,-}^{n+1/2} + H_{\text{Yee},S2,+}^{n+1/2} \right)$$

2) Eq. (2.3) is used to find the E_{FC} from the H_{BC}

$$[E]_{\text{FC}} = \mathcal{Z}_t ([H]_{\text{BC}})$$

3) The usual E-fields at the edges are found from those at the center of the faces:

$$E_{\text{Yee},S1}^n = \frac{1}{2} \left(E_{\text{FC},S1,+}^n + E_{\text{FC},S1,-}^n \right)$$

$$E_{\text{Yee},S2}^n = \frac{1}{2} \left(E_{\text{FC},S2,+}^n + E_{\text{FC},S2,-}^n \right)$$

4) The usual H-fields are found by the usual FDTD scheme by (2.4).

2.5 Network Impedance Boundary Conditions

The LTI operator for the well-known NIBC [Sarto-1999, Holloway-2005] is straightforwardly yielded by translating the frequency-domain Z parameters into time domain. These can be found analytically, either from the S-parameters, or from the constitutive relationships. For instance, for an isotropic thin-panel, the fields E_S, H_S on each side are related by (Fig. 2.5)

$$\begin{bmatrix} E_{S1} \\ E_{S2} \end{bmatrix} = \underbrace{\begin{bmatrix} Z_{11} & Z_{12} \\ Z_{21} & Z_{22} \end{bmatrix}}_{Z_\omega} \begin{bmatrix} H_{S1} \\ -H_{S2} \end{bmatrix} \quad (2.6)$$

where E_{S1} and H_{S1} are the fields on one side of the thin-panel and E_{S2} and H_{S2} are the fields on the other. Note that $Z_{12} = Z_{21}$ for reciprocal media, and $Z_{11} = Z_{22}$ for left-to-right symmetric media. A similar algorithm is independently formulated for the other pair of E/H field components also tangential to the thin-panel surface. It can be generalized for anisotropic media [Sarto-1999, Holloway-2005] by using a fully coupled model similar to (2.6).

$$\begin{pmatrix} E_{S1\parallel} \\ E_{S1\parallel} \\ E_{S1\perp} \\ E_{S1\perp} \end{pmatrix} = Z_\omega \begin{pmatrix} H_{S1\parallel} \\ H_{S1\parallel} \\ H_{S1\perp} \\ H_{S1\perp} \end{pmatrix} \quad (2.7)$$

where the \perp and \parallel subscripts serve to distinguish the 2 different sets of tangential fields mutually coupled.

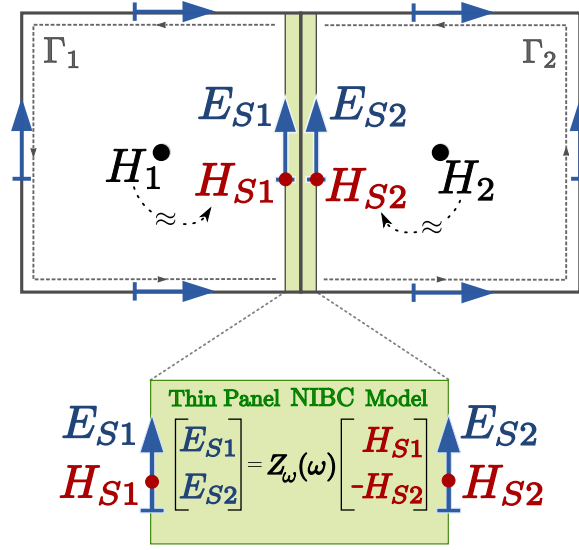


Figure 2.5: Cross section of a FDTDcell with a NIBC boundary.

2.5.1 Time-domain implementation

The FD relationship (2.6) is typically cast into the TD by first expanding each term of matrix Z_ω into a sum of partial fractions found by a VF procedure [Gustavsen-1999]

$$Z_{ij}(\omega) = Z_{\infty,ij} + \sum_{k=1}^{N_{ij}} \frac{R_{ij,k}}{j\omega - p_{ij,k}} \quad (2.8)$$

Next, a TD numerical version can be found in several ways: convolutional, by auxiliary differential equations, by solving equivalent digital filter models, etc. [Sarto-1999, Flintoft-2012, Feliziani-2012]. Let us briefly summarize the convolutional approach used by the PLRC algorithm.

Performing the inverse Fourier transform of (2.6), and taking into account (2.8), we find

$$\begin{aligned} E_{S1}(t) &= \sum_{k=1}^{N_{11}} z_{11,k}(t) * H_{S1}(t) - \sum_{k=1}^{N_{12}} z_{12,k}(t) * H_{S2}(t) \\ E_{S2}(t) &= - \sum_{k=1}^{N_{21}} z_{21,k}(t) * H_{S1}(t) + \sum_{k=1}^{N_{22}} z_{22,k}(t) * H_{S2}(t) \end{aligned} \quad (2.9)$$

where the $*$ operator denotes time convolution. Each term of this sum can be evaluated by

$$\zeta_{ij,k}^{n+1} = \int_0^{(n+1)\Delta t} z_{ij,k}((n+1)\Delta t - t) H_{Sj}(t) dt \quad (2.10)$$

where $\zeta_{ij,k}(t) = z_{ij,k}(t) * H_{Sj}(t)$, and $z_{ij}(t)$ is the impedance in time domain.

The convolution integrals (2.10) are computed numerically by applying the PLRC

formulation proposed in [Oh-1995], assuming that for a given instant $n\Delta t < t < (n+1)\Delta t$ the value of H_{Sj} can be approximated linearly by

$$H_{Sj}(t) = H_{Sj}^n + \left(\frac{t}{\Delta t} - n\right) (H_{Sj}^{n+1} - H_{Sj}^n)$$

which yields an explicit recursive relationship for $\zeta_{ij,k}$ for each term of (2.8) ¹

$$\zeta_{ij,k}^{n+1} = q_{a,ij,k} H_{Sj}^{n+1} + q_{b,ij,k} H_{Sj}^n + q_{c,ij,k} \zeta_{ij,k}^n \quad (2.11)$$

Where $q_{a,b,c}$ are

$$\begin{aligned} q_{a,ij,k} &= \frac{R_{ij,k}}{p_{ij,k}^2 \Delta t} (e^{p_{ij,k} \Delta t} - 1 - p_{ij,k} \Delta t) \\ q_{b,ij,k} &= \frac{R_{ij,k}}{p_{ij,k}^2 \Delta t} (1 + e^{p_{ij,k} \Delta t} (p_{ij,k} \Delta t - 1)) \\ q_{c,ij,k} &= e^{p_{ij,k} \Delta t} \end{aligned} \quad (2.12)$$

Finally

$$\begin{aligned} E_{S1}^{n+1} &= Z_{\infty,11} H_{S1}^{n+1} + \sum_{k=1}^{N_0} \zeta_{11,k}^{n+1} - \sum_{k=1}^{N_t} \zeta_{12,k}^{n+1} \\ E_{S2}^{n+1} &= -Z_{\infty,22} H_{S2}^{n+1} - \sum_{k=1}^{N_0} \zeta_{22,k}^{n+1} + \sum_{k=1}^{N_t} \zeta_{21,k}^{n+1} \end{aligned} \quad (2.13)$$

It should be noted that NIBC equations (2.13) present a difficulty when they are coupled with the usual Yee-FDTD, since they require to simultaneously know both the E and H -fields at the same time, and the same location on the interface. However, the Yee-FDTD method does not presents the electric and magnetic fields co-located, neither in time nor in space, but staggered by semi-integer time and space increments. Since NIBC requires them to be co-located, some extrapolation is to be done.

To yield a causal extrapolation formula, let us employ one idea inspired in the one used by Mur [Mur-1998, Engquist-1977] for one of the first absorbing boundary conditions (ABCs) used in the FDTD method. Let us assume that the waves traveling in both directions towards each side of the flat panel fulfill the one-way wave equations

$$\frac{\partial H}{\partial t} = \pm c_0 \frac{\partial H}{\partial r} \quad (2.14)$$

For instance for waves travelling along the normal direction of the panel, using centered

¹ $\mathcal{F}^{-1} \left(\frac{R_{ij,k}}{j\omega - p_{ij,k}} \right) = R_{ij,k} e^{p_{ij,k} t} u(t)$ with $u(t)$ the Heaviside step function.

averages and differences, we can write the 2^{nd} order formula

$$\frac{1}{2\Delta t} \begin{pmatrix} H_{S1}^{n+1/2} + H_1^{n+1/2} \\ -H_{S1}^{n-1/2} - H_1^{n-1/2} \end{pmatrix} = -\frac{c_0}{\Delta} \begin{pmatrix} H_{S1}^{n+1/2} + H_{S1}^{n-1/2} \\ -H_1^{n+1/2} - H_1^{n-1/2} \end{pmatrix} \quad (2.15a)$$

$$\frac{1}{2\Delta t} \begin{pmatrix} H_{S2}^{n+1/2} + H_2^{n+1/2} \\ -H_{S2}^{n-1/2} - H_2^{n-1/2} \end{pmatrix} = \frac{c_0}{\Delta} \begin{pmatrix} H_{S2}^{n+1/2} + H_{S2}^{n-1/2} \\ -H_2^{n+1/2} - H_2^{n-1/2} \end{pmatrix} \quad (2.15b)$$

This solution can be reduced to the special case, through a simple interpolation: $H_{S1,S2}^{n+1} = \frac{1}{2} (H_{S1,S2}^{n+1/2} + H_{S1,S2}^{n-1/2})$

$$\begin{aligned} H_{S1}^{n+1} &\simeq H_1^{n+1/2} \\ H_{S2}^{n+1} &\simeq H_2^{n+1/2} \end{aligned} \quad (2.16)$$

this is a 0^{th} -order upwind approximation used in [Beggs-1992, Feliziani-1999, Sarto-1999], which is only true if the numerical wave travels at the analytical free-space light-speed,

$$\frac{c_0\Delta t}{\Delta} = 1$$

which is unfeasible for stable FDTD 3D schemes fulfilling the Courant condition for a homogeneous grid,

$$\frac{c_0\Delta t}{\Delta} = \sqrt{3}$$

2.5.2 Passivity, stability and causality

The response of a LTI system physically represents a propagation phenomenon if it is passive, stable and causal [Zemanian-1963, Triverio-2007]. The LTI interpretation of thin-panel equations, permits us to make use of the well-known criteria of passivity, stability and causality, usual in LTI to also assess them in fully coupled scheme.

It is apparent that a necessary condition for stability of the coupled system, requires both the LTI and the 3D Yee-FDTD scheme to be stable by themselves. This analysis is beyond the scope of this dissertation, and we will restrict ourselves to the analysis of each system separately. For that, let us assume that the 3D Yee-FDTD method complies with the CFL stability condition (Chapter 1), and we will analyze the stability conditions for LTI used at the core of NIBC. This can be analyzed either in time by studying its impulse response, or in frequency domain by Fourier-transforming (2.3) the transfer function. In this case, an

impedance is found as a quotient of two polynomials of $j\omega$,

$$Z_\omega(\omega) = \frac{[E_S](\omega)}{[H_S](\omega)} = \frac{\sum_{k=1}^N a_k(j\omega)^k}{\sum_{k=1}^M b_k(j\omega)^k} \quad (2.17)$$

where Z_ω represents the operator \mathcal{Z}_t in frequency domain. Now, we can calculate the impulse response of the system by finding the inverse Fourier transform of (2.8):

$$z_{ij}(t) = \mathcal{F}^{-1}(Z_{ij}(\omega)) = Z_{\infty,ij} \delta(t) + u(t) \sum_{k=1}^{N_{ij}} R_{ij,k} e^{p_{ij,k}t} \quad (2.18)$$

where $z_{ij}(t)$ stands for the impulse function of each term of (2.6) and $u(t)$ is the Heaviside step function.

- i) **Causality:** In a physical system the response cannot precede its cause. This is equivalent to require the impulse response² $h(t)$ of the LTI to fulfill,

$$h(t) = 0 \text{ for } t < 0 \quad (2.19)$$

It is immediate to realize that $z_{ij}(t)$ (2.18) automatically fulfills the causality condition (2.19).

- ii) **Passivity:** A physical system is said to be passive when, it is unable to generate energy. In frequency-domain, this requires that

- The impedance must not have negative resistance $\text{Re}\{Z_\omega(\omega)\} \geq 0$.
- The Hermitian part of the impedance matrix $1/2(Z_\omega^H(\omega) + Z_\omega(\omega))$ must³ be nonnegative-definite⁴. A sufficient condition for this to occur is that the eigenvalues of the Hermitian part of the impedance must be real:

$$\lambda(\omega) = \text{Eigenvalues}\{Z_\omega(\omega) + Z_\omega^H(\omega)\} \in \mathbb{R} \quad (2.20)$$

and $\lambda(\omega) > 0$

- The impulse response (inverse Fourier transform of Z_ω) must be real⁵ and hence $Z_\omega^*(\omega) = Z_\omega(-\omega)$.

The passivity of (2.8) can be assessed in frequency domain by requiring that the

²The impulse response $h(t) = \int h(\tau)\delta(t-\tau)d\tau$ permits us to find $E(t) = h(t) * H(t)$

³The $()^H$ superscript denote the transpose conjugate also name self-adjoint.

⁴Equivalent to $a^H A a \geq 0 \forall a > 0$.

⁵The superscript * denote the complex conjugate.

Hermitian part of $Z(\omega)$ to be positive semi-definite. A necessary condition for this is $Z_{ii}(\omega) \geq 0, \forall \omega > 0, \forall i$, and a sufficient and necessary condition is (2.20).

- iii) **Stability:** The concept of stability is related to the boundedness of the system response. Several definitions of stability exist. We will consider the so-called bounded-input bounded-output (BIBO) definition of stability. If a system is BIBO-stable, then the output will be bounded for every bounded input. A necessary and sufficient condition for this is,

$$\int_{-\infty}^{\infty} |h(t)| < \infty \quad (2.21)$$

and in frequency domain by requiring that the poles of the impedance (2.17) to lay in the left complex semi-plane,

$$\text{Re}(p_{i,j,k}) < 0$$

In summary, the VF impedance expansion of the material in the frequency domain, must be done with care to guarantee the stability, causality and passivity (see also [Zemnian-1963, Angulo-2012]). In short, VF [Gustavsen-1999] is automatically causal and stable. However passivity must be enforced [Gustavsen-2001], by adding extra constraints to the original fitting procedure.

However, as stated earlier, even if both systems are stable when analyzed separately, the coupled system may be unstable. Indeed, the extrapolation described at the beginning of Section 2.4.1 is often blamed in literature as a source of late-time instabilities, and several efforts to overcome it have been published [Kobidze-2010, Nayyeri-2013]. Even further, from our experience, even if canonical problems do not suffer from late-time instabilities, large and complex ones may exhibit them. A typical workaround to remove instabilities is the reduction of the time-step in an iterative heuristic way hopefully concluding with a computationally affordable model. This issue limits the applicability of the NIBC method. For this reason, in the next section we present a novel technique aimed to overcome this limitation.

2.6 Subgridding boundary condition

Subgridding techniques are widely employed in FDTD [White-1997, Taflove-2005], also to treat composite materials [D'Amore-1997]. Subgridding is typically considered a brute-force method, yielding restrictive stability conditions that may become prohibitive. In this section, is presented a new HIE SGBC, inspired in the NIBC described above. It combines a 1D FDTD scheme to deal with fields inside the thin-panel, with the usual 3D Yee-FDTD scheme

for the rest of the problem. For this, the same starting principle used for NIBC is considered: thin-panel with a planar shape and plane waves propagating inside it at a normal angle.

However, instead of the impedance relationships (2.6) used by NIBC to find the fields on both faces of the panel, SGBC finds them after a full-wave 1D simulation inside the thin-panel, which is meshed into a fine spatial mesh, only along the direction normal to the panel. A high enough number of cells is used for it, to properly resolve the wavelength and the skin-depth at the maximum frequency of interest inside the thin-panel.

To overcome the shortcoming posed by the reduced time-step required for the stability of the overall FDTD scheme, a novel approach based on a CNTD unconditionally stable scheme is employed. The E and H fields inside the thin-panel are advanced by the 1D second-order CNTD method, which is just tridiagonally implicit in 1D [Garcia-2002] and has a negligible computational overhead, compared with the usual leap-frog FDTD. This is broadly compensated for by its unconditionally stable nature, which allows us not to reduce the time step inside the fine-mesh region, as if a classical 1D Yee-FDTD were applied.

We will next illustrate the CNTD and SGBC algorithms with the geometry depicted in Fig. 2.6. In this case, the thin-panel has been sub-gridded into N 1D-cells of size Δ_{fine} , with $N + 1$ E-field N H-field components inside. For simplicity the surrounding medium is assumed to be free space with a 3D cell size Δ_{coarse} , and a thin-panel with constant conductivity.

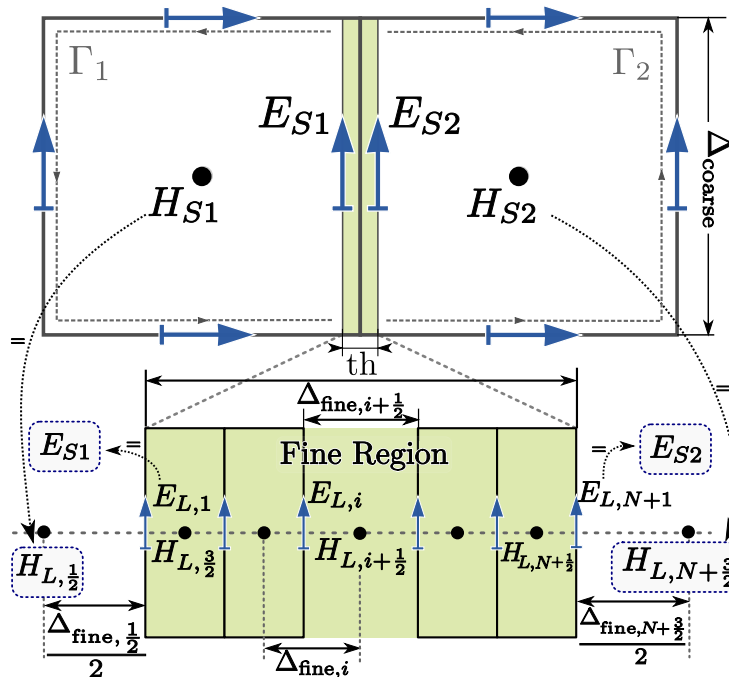


Figure 2.6: Cross section of a FDTD cell with a SGBC boundary.

As in NIBC, SGBC duplicates the tangential E-fields on the thin-panel surface E_{S1} , E_{S2} to account for each face value (Fig. 2.6). They are located at the usual staggered space-time

indexes of the Yee-FDTD cell. Also, as usual, the H-fields are located at the center of the adjacent 3D cells H_{S1} , H_{S2} . The SGBC algorithm proves to be as follows:

1. The fields inside the panel domain denoted by $E_{L,i}^n$, $H_{L,i+1/2}^n$ see Fig. 2.6 are updated by the usual 1D CNTD described above.
2. E-fields outside the thin-panel are advanced \vec{E}^n in the usual 3D Yee-FDTD manner.
3. H-fields outside the thin-panel are advanced $\vec{H}^{n+1/2}$ in the usual 3D Yee-FDTD manner.
4. H-fields at the adjacent cells $H_{S1}^{n+1/2}$ and $H_{S2}^{n+1/2}$, employ the usual 3D algorithm (2.4) with $E_{S1}^n = E_{L,1}^n$ and $E_{S2}^n = E_{L,N+1}^n$.
5. The connection between the coarse and fine mesh is made through the tangential electric field on the thin-panel surface, which is found by the HIE algorithm described next.

2.6.1 Hybrid 1D FDTD - 3D FDTD

An alternative to the CNTD scheme used inside the thin-panel is to use a classical one-dimensional Yee-FDTD scheme to deal with the field propagation, using either a TA or an ETD method, the latter to partially palliate the stability constraints of TA. These schemes within the panel would read

$$H_{L,i+1/2}^{n+1/2} = D_{a,i+1/2} H_{L,i+1/2}^{n-1/2} + D_{b,i+1/2} (E_{L,i}^n - E_{L,i+1}^n) \quad (2.22)$$

$$E_{L,i}^{n+1} = C_{a,i} E_{L,i}^n + C_{b,i} (H_{L,i-1/2}^{n+1/2} - H_{L,i+1/2}^{n+1/2}) \quad (2.23)$$

with the $C_{a,i}$, $C_{b,i}$, $D_{a,i+1/2}$, $D_{b,i+1/2}$ given in (1.4) for TA and in (1.13a) and (1.13b) for ETD.

The connection between the 1D and 3D domains is performed in a straightforward manner by using a non-centered finite difference approximation to find the tangential electric field at the interface from the magnetic fields inside and outside it, with an average of the constitutive parameters to account for the jump from free-space to the thin-panel.

A simple extension to treat multilayered materials would just require the tangential electric field components (remember that the normal components are not required) to be located at integer locations coinciding with each layer interfase Fig. 2.6. Assuming that each σ and ε are known at semi-integer positions $i + 1/2$, effective parameters can be found to update the electric field in a simple manner. The constants $C_{a,i}$, $C_{b,i}$ given in (1.6a) are found

from the effective constitutive parameters ε_i and σ_i by weighted averages [Taflove-2005]

$$\begin{aligned}\sigma_i &= \frac{\sigma_{i-1/2}\Delta_{\text{fine},i-1/2} + \sigma_{i+1/2}\Delta_{\text{fine},i+1/2}}{\Delta_{\text{fine},i-1/2} + \Delta_{\text{fine},i+1/2}} \\ \varepsilon_i &= \frac{\varepsilon_{i-1/2}\Delta_{\text{fine},i-1/2} + \varepsilon_{i+1/2}\Delta_{\text{fine},i+1/2}}{\Delta_{\text{fine},i-1/2} + \Delta_{\text{fine},i+1/2}}\end{aligned}\quad (2.24)$$

where actually $\Delta_{\text{fine},1/2} = \Delta_{\text{coarse}}$ and $\Delta_{\text{fine},N+3/2} = \Delta_{\text{coarse}}$.

2.6.2 Hybrid 1D CNTD - 3D FDTD

Let first describe the 1D CNTD used inside the thin-panel shown in Fig. 2.6 (further details of CNTD can be found in several places, e.g., [Crank-1947, Pg. 50–67] [Rouf-2009]). For this, we start from the usual Yee-FDTD equations for the Ampere-Maxwell law, assuming that H-fields are located at integer time-steps and using a time average for the right-hand-side E-fields to also co-locate them in time with the H-field components

$$\begin{aligned}H_{L,i+1/2}^{n+1} &= D_{a,i+1/2}H_{L,i+1/2}^n + \\ &\quad \frac{D_{b,i+1/2}}{2} \left(E_{L,i}^n - E_{L,i+1}^n + E_{L,i}^{n+1} - E_{L,i+1}^{n+1} \right)\end{aligned}\quad (2.25)$$

Using the same method for the Faraday law, we find

$$\begin{aligned}E_{L,i}^{n+1} &= C_{a,i}E_{L,i}^n + \\ &\quad \frac{C_{b,i}}{2} \left(H_{L,i-1/2}^{n+1} - H_{L,i+1/2}^{n+1} + H_{L,i-1/2}^n - H_{L,i+1/2}^n \right)\end{aligned}\quad (2.26)$$

with the $C_{a,i}$, $C_{b,i}$, $D_{a,i+1/2}$, $D_{b,i+1/2}$ given in (1.4) for TA and in (1.13a) and (1.13b) for ETD.

Now extracting H^{n+1} from (2.25) and inserting it into (2.26), a fully consistent algorithm with the space positions of E and H staggered in space as in the usual Yee-Scheme is yielded, but evaluated at co-located integer time-steps. After some algebra, a tridiagonal system of equations is found for the E-fields for $i = 2, \dots, N$

$$a_i E_{L,i-1}^{n+1} + b_i E_{L,i}^{n+1} + c_i E_{L,i+1}^{n+1} = d_i^n \quad (2.27)$$

Next, a proper HIE scheme is devised to connect the solutions found by CNTD (inside the thin-panel) and by Yee-FDTD (outside the thin-panel). For this, we assume that the CNTD-domain is terminated in the E-field components E_{S1} and E_{S2} , and we modify the CNTD procedure found after (2.26), so that only the H-fields inside the CNTD-domain are averaged in time, while those outside have been previously found by the usual Yee-FDTD at semi-integer time-steps, thus playing the role of external source terms. Hence, for the $(L, 1)$,

$(L, N + 1)$ boundaries, we find

$$E_{L,1}^{n+1} = C_{a,1}E_{L,1}^n + C_{b,1} \left(H_{S1}^{n+1/2} - \frac{H_{L,3/2}^n + H_{L,3/2}^{n+1}}{2} \right) \quad (2.28a)$$

$$E_{L,N+1}^{n+1} = C_{a,N+1}E_{L,N+1}^n + C_{b,N+1} \left(\frac{H_{L,N+1/2}^n + H_{L,N+1/2}^{n+1}}{2} - H_{S2}^{n+1/2} \right) \quad (2.28b)$$

Inserting the magnetic fields inside the thin-panel found by CNTD by (2.25), into (2.28), we get two implicit equations that must be solved together with (2.27) for the interior E-fields

$$b_1 E_{L,1}^{n+1} + c_1 E_{L,2}^{n+1} = d_1^n \quad (2.29a)$$

$$a_{N+1} E_{L,N}^{n+1} + b_{N+1} E_{L,N+1}^{n+1} = d_{N+1}^n \quad (2.29b)$$

where coefficients a_i, b_i, c_i, d_i are given after some algebra by

$$\begin{aligned} a_i &= \left(-\frac{C_{b,i} D_{b,i-1/2}}{4} \right) \\ c_i &= \left(-\frac{C_{b,i} D_{b,i+1/2}}{4} \right) \\ b_i &= (1 - a_i - c_i) \\ a_0 &= 0 \\ c_{N+1} &= 0 \end{aligned} \quad (2.30a)$$

$$\begin{aligned} d_i^n &= \left(\frac{C_{b,i}}{2} \right) (1 + D_{a,i-1/2}) H_{CN,i-1/2}^n \\ &\quad - \left(\frac{C_{b,i}}{2} \right) (1 + D_{a,i+1/2}) H_{CN,i+1/2}^n \\ &\quad - a_i E_{CN,i-1}^n + (C_{a,i} + a_i + c_i) E_{CN,i}^n - c_i E_{CN,i+1}^n \end{aligned} \quad (2.30b)$$

All E-fields $E_{L,i}^{n+1}$ are assessed solving the tridiagonal system (2.31), which can be efficiently solved with a linear complexity $\mathcal{O}(n)$ using the back-substitution algorithm [Thomas-1949], the magnetic field components can be finally found in an explicit inserting $E_{L,i}^{n+1}$ into (2.25) manner.

$$\begin{pmatrix} E_{L,1}^{n+1} \\ \vdots \\ E_{L,i}^{n+1} \\ \vdots \\ E_{L,(N+1)}^{n+1} \end{pmatrix} = \begin{pmatrix} b_1 & c_1 & 0 & \cdots & \cdots & 0 \\ a_2 & b_2 & c_2 & \ddots & & \vdots \\ 0 & a_i & b_i & c_i & \ddots & \vdots \\ \vdots & \ddots & & \ddots & & 0 \\ \vdots & & \ddots & a_N & b_N & c_N \\ 0 & \cdots & \cdots & 0 & a_{(N+1)} & b_{(N+1)} \end{pmatrix} \begin{pmatrix} d_1^n \\ \vdots \\ d_i^n \\ \vdots \\ d_{N+1}^n \end{pmatrix} \quad (2.31)$$

This procedure permits us a consistent connection between CNTD and Yee-FDTD in such a way that the CNTD algorithm employs only the 3D Yee-FDTD H-fields as source terms, and hence without degrading its unconditional stability.

2.6.3 Extension to arbitrarily dispersive panels

The method previously described can be extended to deal with arbitrarily dispersive thin panels in a similar way. For this, let us assume that the bulk equivalent dispersive constitutive parameters are known, and that a VF procedure has been performed to express them as partial fraction expansion. The constitutive parameters can be retrieved from its scattering parameters by using a parameter extraction method, like that described in Section 2.3. In this manner, if the internal structure is not known, or cannot be expressed in terms of simple multilayered bulk parameters, SGBC can be still applied as an alternative to NIBC.

The whole procedure used for simply lossy media can be applied now, just by endowing the CNTD method with the capability to treat arbitrarily frequency dispersive electric and magnetic media. For instance using an extension of the ADE method proposed in [Han-2006] and described in the Section 1.5 [M. R. Cabello-2017].

Starting from the usual Yee-FDTD-ADE equations (1.36) for the Faraday-Maxwell law (1.36b), and assuming that H-fields are located at integer time-steps, we can write

$$H_{L,i+1/2}^{n+1} = D_{a,i+1/2} H_{L,i+1/2}^n + \frac{D_{b,i+1/2}}{2} \left(E_{L,i}^n - E_{L,i+1}^n + E_{L,i}^{n+1} - E_{L,i+1}^{n+1} \right) - D_{M,i+1/2} M_{L,i+1/2}^n \quad (2.32)$$

where a plain TA scheme has been taken for simplicity in the right-hand-side of to co-locate E-fields in time with H-fields. Now, using the same way for the Ampère-Maxwell law (1.36a), we find:

$$E_{L,i}^{n+1} = C_{a,i} E_{L,i}^n + \frac{C_{b,i}}{2} \left(H_{L,i-1/2}^{n+1} - H_{L,i+1/2}^{n+1} + H_{L,i-1/2}^n - H_{L,i+1/2}^n \right) - \frac{C_{b,i}}{2} J_{L,i}^n \quad (2.33)$$

where the coefficients C_a, C_b, D_a, D_b are given by (1.34).

Now extracting H^{n+1} from (2.32) and plugging it into (2.33), a fully consistent algorithm with the space positions of E and H, staggered in space as in the usual Yee-Scheme, is yielded, but evaluated at co-located integer time-steps, as required by CNTD. After some algebra, a tridiagonal system of equations is again found for the E-fields for $i = 2, \dots, N$

$$a_i E_{L,i-1}^{n+1} + b_i E_{L,i}^{n+1} + c_i E_{L,i+1}^{n+1} = d_i^n - C_{J,i} J_{L,i}^n - \frac{C_{b,i}}{2} \left(D_{M,i-1/2} M_{L,i-1/2}^n - D_{M,i+1/2} M_{L,i+1/2}^n \right) \quad (2.34)$$

with a_i, b_i, c_i, d_i given by (2.30).

The connection between the solution found by ADE-CNTD (inside the thin-panel) and by Yee-FDTD (outside the thin-panel) is found in a similar manner to the one used for the non-dispersive case. For the $(L, 1)$, $(L, N + 1)$ boundaries we find

$$\begin{aligned} E_{L,1}^{n+1} &= C_{a,1} E_{L,1}^n + C_{b,1} \left(H_{S1}^{n+1/2} - \frac{H_{L,3/2}^n + H_{L,3/2}^{n+1}}{2} \right) \\ &+ C_{J,1} J_{L,1}^n - \frac{C_{b,1}}{2} \left(D_{M,3/2} M_{L,3/2}^n \right) \end{aligned} \quad (2.35a)$$

$$\begin{aligned} E_{L,N+1}^{n+1} &= C_{a,N+1} E_{L,N+1}^n + C_{b,N+1} \left(\frac{H_{L,N+1/2}^n + H_{L,N+1/2}^{n+1}}{2} - H_{S2}^{n+1/2} \right) \\ &+ C_{J,N+1} J_{L,N+1}^n + \frac{C_{b,N+1}}{2} \left(D_{M,N+1/2} M_{L,N+1/2}^n \right) \end{aligned} \quad (2.35b)$$

Plugging the magnetic fields inside the thin-panel found by ADE-CNTD by (2.32) into (2.35), we obtain two implicit equations that must be solved together with (2.34) for the interior E-fields

$$b_1 E_{L,1}^{n+1} + c_1 E_{L,2}^{n+1} = d_1^n - C_{J,1} J_{L,1}^n + \frac{C_{b,1}}{2} \left(D_{M,3/2} M_{L,3/2}^n \right) \quad (2.36a)$$

$$\begin{aligned} a_{N+1} E_{L,N}^{n+1} + b_{N+1} E_{L,N+1}^{n+1} &= d_{N+1}^n - C_{J,N+1} J_{L,N+1}^n \\ &- \frac{C_{b,N+1}}{2} \left(D_{M,N+1/2} M_{L,N+1/2}^n \right) \end{aligned} \quad (2.36b)$$

where the coefficients $a_1, c_1, a_{N+1}, b_{N+1}, d_1^n, d_{N+1}^n$ are also given by (2.30).

2.6.4 Stability of SGBC

A rigorous study of the coupled system formed by the coarse region (usual 3D Yee-FDTD) and the 1D SGBC fine region would require to analyze the spectral properties of the whole algorithm [Pereda-1998, Remis-2000, Sewell-2005]. However a simplified analysis can still be done by assuming that the 1D-SGBC fine and the 3D-Yee coarse region are independent. A heuristic study will serve to demonstrate the validity of this assumption. For this, let us define

$$\text{CFLN} = \min(\text{CFLN}_{\text{sgbc}}, 1.0) \quad (2.37)$$

where $\text{CFLN}_{\text{sgbc}}$ is given by the ratio between the time-steps required for stability at each zone

$$\text{CFLN}_{\text{sgbc}} = \frac{\Delta t_{\text{fine}}}{\Delta t_{\text{coarse}}} \quad (2.38)$$

We have kept the notation CFLN for this coefficient as a measure of the reduction required by the hybrid scheme with respect to the one used in the 3D coarse zone.

Assuming for the coarse zone an uniform isotropic structured mesh with a cell size Δ_{coarse} , the maximum time step therein is provided by the usual Courant criterion (1.19)

$$\Delta t_{\text{coarse}} = \frac{\Delta_{\text{coarse}}}{\sqrt{N_D} c_0} = \frac{\lambda_{\text{air}} / \text{PPW}_{\text{coarse}}}{\sqrt{N_D} c_0}$$

where N_D is the space dimensionality where the coarse system is laid ($N_D = 3$ in 3D), the mesh size has been expressed as the free-space wavelength divided by the PPW used to sample it. (2.37) can be further written as

$$\text{CFLN}_{\text{sgbc}} = \sqrt{N_D} \frac{c_0 \text{PPW}_{\text{coarse}}}{\lambda_{\text{air}}} \Delta t_{\text{fine}} \quad (2.39)$$

The fine mesh resolution Δ_{fine} , can be determined from the accuracy required for the wavelength λ_{fine} inside the SGBC zone. Since this is a function of the frequency and the material constants, we can find a simpler formulation by working with the material quality factor instead $Q = \omega \varepsilon / \sigma$

$$\lambda_{\text{fine}} = \lambda_{\text{air}} \Upsilon_Q, \quad \Upsilon_Q = \frac{1}{\sqrt{\frac{1}{2} (\sqrt{1 + Q^{-2}} + 1)}} \quad (2.40)$$

hence, the space step inside the fine region as a function of the resolution PPW_{fine} is

$$\Delta_{\text{fine}} = \frac{\lambda_{\text{air}} \Upsilon_Q}{\text{PPW}_{\text{fine}}} \quad (2.41)$$

With this notation, we can find the following stability criterion depending on the time-integration scheme used in the fine region: Yee-FDTD TA, Yee-FDTD ETD and CNTD.

- **Yee-FDTD TA:** The maximum Δt_{fine} for stability is given by (1.19), using in it (2.41) we obtain,

$$\Delta t_{\text{fine}} = \frac{\lambda_{\text{air}} \Upsilon_Q}{\text{PPW}_{\text{fine}} c_0}$$

using Δt_{fine} in (2.39)

$$\text{CFLN}_{\text{sgbc}} = \sqrt{N_D} \frac{\text{PPW}_{\text{coarse}}}{\text{PPW}_{\text{fine}}} \Upsilon_Q \quad (2.42)$$

Note that for a lossless case $\Upsilon_Q > 1/\sqrt{N_D}$, and using the same resolution in the coarse and in the fine region, the $\text{CFLN}_{\text{sgbc}} > 1$, which means that the SGBC region (or fine region) has a criterion of stability less restrictive than that at the coarse region .

- **Yee-FDTD ETD:** The maximum Δt_{fine} for stability is given by (1.20)

$$1 = \frac{2}{\sqrt{\sigma \sigma_M}} \sqrt{\frac{1 - e^{-\Delta t_{\text{fine}} \sigma / \varepsilon}}{1 + e^{-\Delta t_{\text{fine}} \sigma / \varepsilon}}} \sqrt{\frac{1 - e^{-\Delta t_{\text{fine}} \sigma_M / \mu}}{1 + e^{-\Delta t_{\text{fine}} \sigma_M / \mu}}} \frac{1}{\Delta t_{\text{fine}}} \quad (2.43)$$

in this way using (2.39) in the last equation an implicit relation is found for $\text{CFLN}_{\text{sgbc}}$ as a function of the space resolution and the Q -factor. If assuming null magnetic conductivity,

$$1 = \frac{\text{CFLN}_{\text{sgbc}} Q}{\sqrt{N_D} \text{PPW}_{\text{coarse}} \pi} \frac{1 - e^{-\text{CFLN}_{\text{sgbc}} \frac{2\pi}{\sqrt{N_D} \text{PPW}_{\text{coarse}} Q}}}{1 + e^{-\text{CFLN}_{\text{sgbc}} \frac{2\pi}{\sqrt{N_D} \text{PPW}_{\text{coarse}} Q}}} \frac{\text{PPW}_{\text{fine}}^2}{\Upsilon_Q^2} \quad (2.44)$$

- **CNTD-FDTD:** The CNTD method is well known for being unconditionally stable [Garcia-2006] and hence the stability condition is kept unaltered with respect to the usual one in the coarse region: $\text{CFLN}_{\text{sgbc}} > 1$.

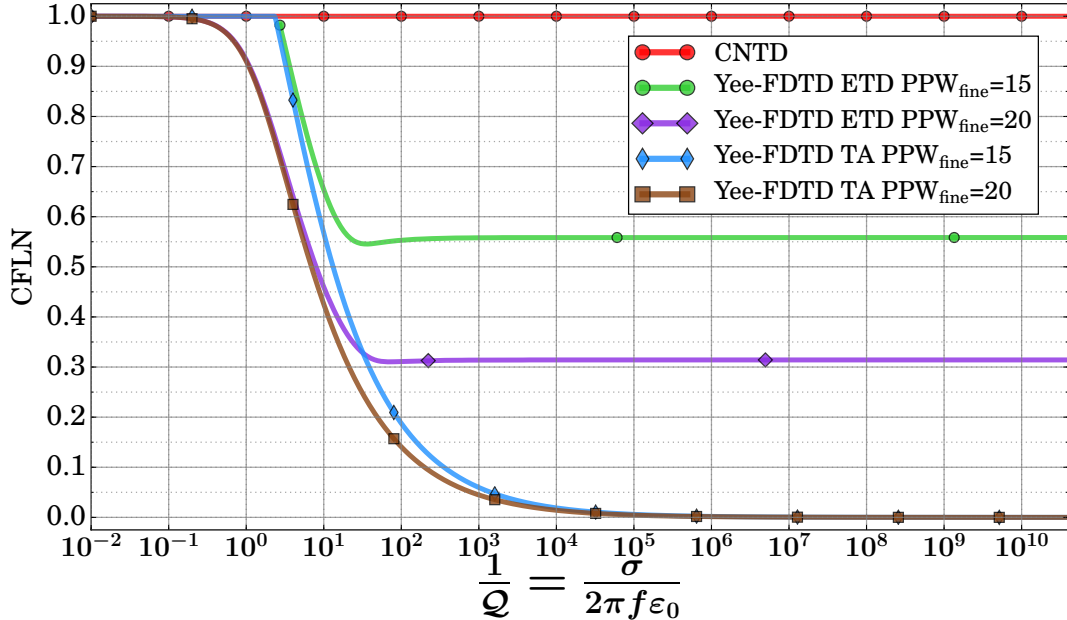


Figure 2.7: CFLN as a function of Q for a fixed mesh resolution $\text{PPW}_{\text{coarse}} = 20$ and $N_D = 1$

From the equations (2.42) and (2.44), it easy follows that the value of CFLN depends on the dimension of the coarse region N_D , the Q -factor, and the resolutions for both the fine and coarse regions. Fig. 2.7 for 1D and Fig. 2.8 for 3D, show the value at the maximum CFLN in order to guarantee stability. The plots maintain a fixed value for the resolutions

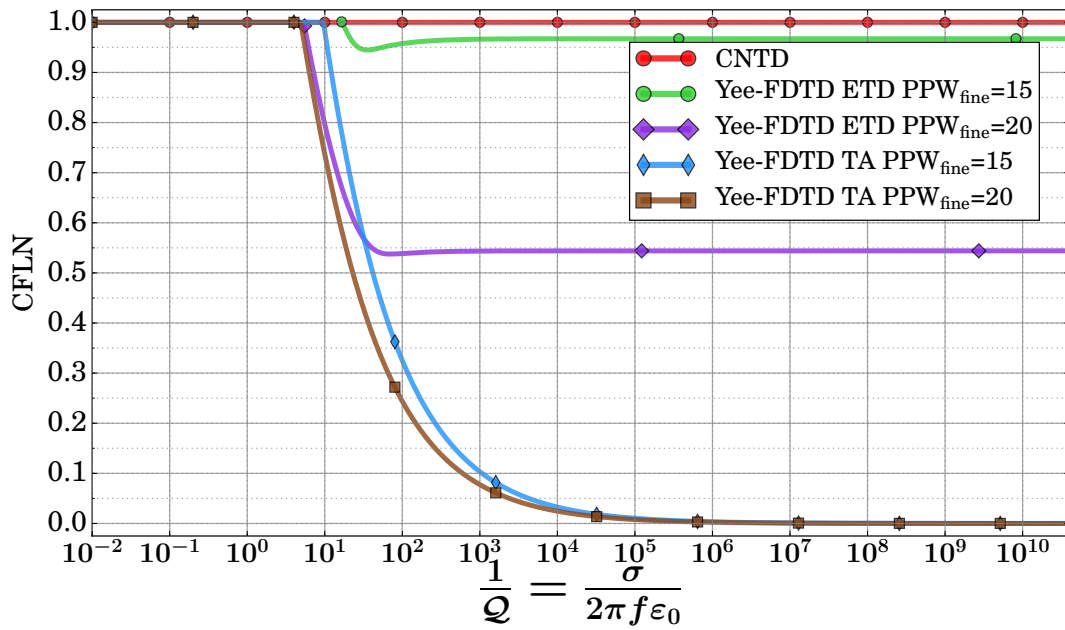


Figure 2.8: CFLN as a function of Q for a fixed mesh resolution $PPW_{\text{coarse}} = 20$ and $N_D = 3$

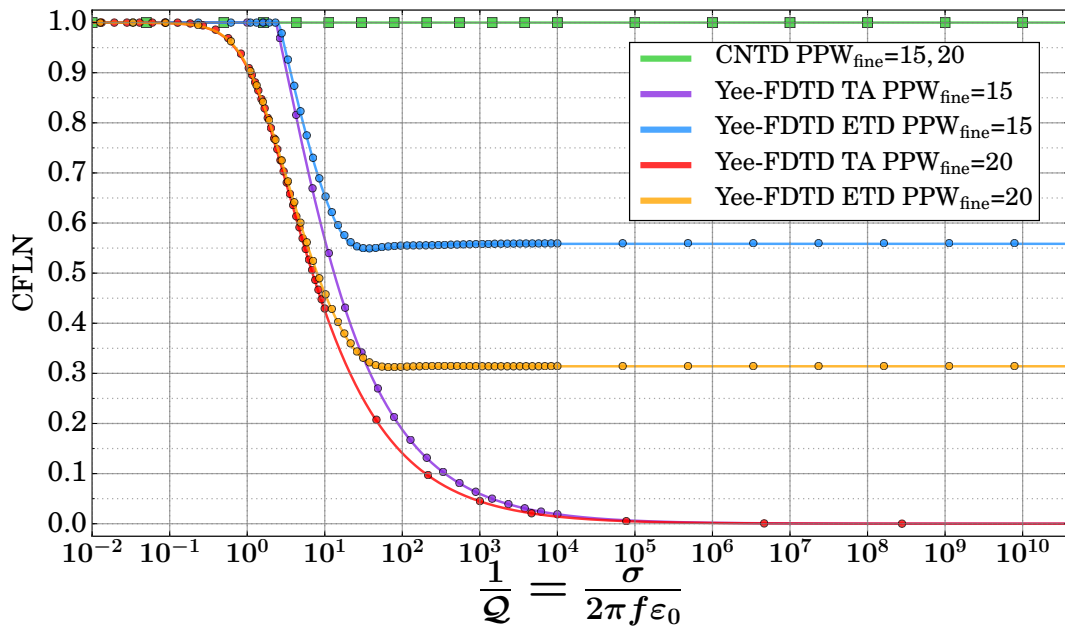


Figure 2.9: Comparison between heuristically and theoretical CFLN for a fixed mesh resolution $PPW_{\text{coarse}} = 20$ and $N_D = 1$

$PPW_{\text{coarse}} = 20$ and vary the quality factor Q , which is also given for two set of curves by fixing $PPW_{\text{fine}} = 15, 20$. The following conclusions can be drawn:

- When the conditions of the fine region ($PPW_{\text{fine}} < PPW_{\text{coarse}}$ and/or $N_d > 1$) are less restrictive than those at the coarse region, it may happen that stability criterion of the fine region defined by (2.38) is less restrictive than the coarse region, so the total stability criterion of the coupled system saturates at 1.0 according to (2.37).
- The curve for $PPW_{\text{fine}} = 15$ on Fig. 2.8 for LF-ETD shows a reasonable stability criterion $CFLN > 0.95$ for any Q-factor. This may mislead you to believe that the usage CN-TA method can be avoided in favor of the LF-ETD one. However, for multilayers, or for very thin materials, the thickness is the limiting factor for Δ_{fine} . So that we cannot always set the value of PPW_{fine} , which is imposed by the thickness, thus making of CN-TA the method of choice.
- We have verified the above criterions by assessing the stability curves also in a numerical heuristic manner (Fig. 2.9), confirming us that the initial hypothesis, assuming the coarse and fine schemes independent, is acceptable to study the stability of the hybrid method. A key point to further justify this assumption, is the fact that the HIE algorithm just connects the Yee-FDTD and the SGBC regions by means of boundary conditions, with no other interpolation/extrapolation procedure.

2.6.5 Accuracy

Non-physical reflections

Non-physical reflections are well known to appear at boundaries between regions treated with different numerical schemes [Wang-2002]. This is what happens in the boundary of two regions meshed with different space steps, as occurs in SGBC. A reason for this, is that the numerical phase velocities differ between both regions, indeed, they are a function of the frequency.

This phenomenon can be analytically studied by finding the reflection coefficient of a TEM plane wave propagating in a semi-infinite free-space region and impinging the interface with another semi-infinite free space region, both of them discretized with a different mesh size and treated with the same or different numerical schemes. The reflection coefficient can be expressed as a function of the phase speed at each medium by

$$R_{\text{num}} = \frac{v_{\text{coarse}} - v_{\text{fine}}}{v_{\text{coarse}} + v_{\text{fine}}} \quad (2.45)$$

where v_{coarse} , v_{fine} is the numerical phase speed inside each zone, which is found with the

numerical dispersion relationship in Chapter (1.23), here reproduced for convenience for the usual TA Yee-FDTD

$$v_{\text{ph, num}} = \frac{\omega}{k} = \frac{\pi c_0}{\text{PPW} \arcsin\left(\frac{1}{\text{CFLN}} \sin\left(\frac{\pi \text{CFLN}}{\text{PPW}}\right)\right)} \quad (2.46)$$

and the the numerical dispersion relationship of CNTD that can be easily proven to be

$$v_{\text{ph, num}} = \frac{\omega}{k} = \frac{\pi c_0}{\text{PPW} \arctan\left(\frac{1}{\text{CFLN}} \sin\left(\frac{\pi \text{CFLN}}{\text{PPW}}\right)\right)} \quad (2.47)$$

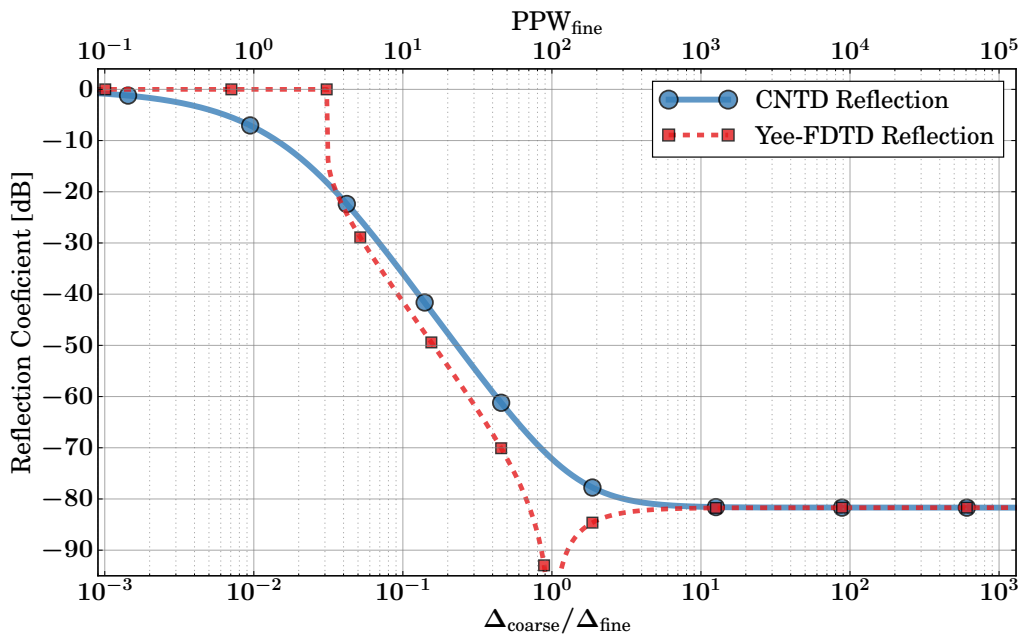


Figure 2.10: Unphysical reflection at by a semi-infinite free-space SGBC region as a function of the ratio between the space-steps. The coarse mesh is meshed with a fixed resolution $\text{PPW}_{\text{coarse}} = 100$.

Fig. 2.10 shows the analytical reflection coefficient as a function of the resolution in the fine region, keeping a constant $\text{PPW}_{\text{coarse}} = 100$, assuming that a 1D Yee-FDTD is used for the coarse region, and either a 1D Yee-FDTD or a 1D CNTD is used in the fine region. The setup of Fig. 2.12 has been employed to corroborate this claim numerically. Fig. 2.11 shows the reflection coefficient (ideally null) and transmission coefficient (ideally unity) for SGBC-CNTD and SGBC-Yee-FDTD as a function of $\Delta_{\text{coarse}}/\Delta_{\text{fine}}$. The number PPW in the thin-panel, PPW_{fine} , is also shown for reference in the upper x-axis. The coefficients have been computed using a resolution outside the thin-panel of $\text{PPW}_{\text{coarse}} = 100$ cells/wavelength. The effect of the numerically spurious backwards wave created by the impressed source is removed by subtracting it from a first simulation without the thin-panel. It bears noting that there is full reflection beneath the Nyquist limit $\text{PPW}_{\text{fine}} = 2$. Above the Nyquist limit the

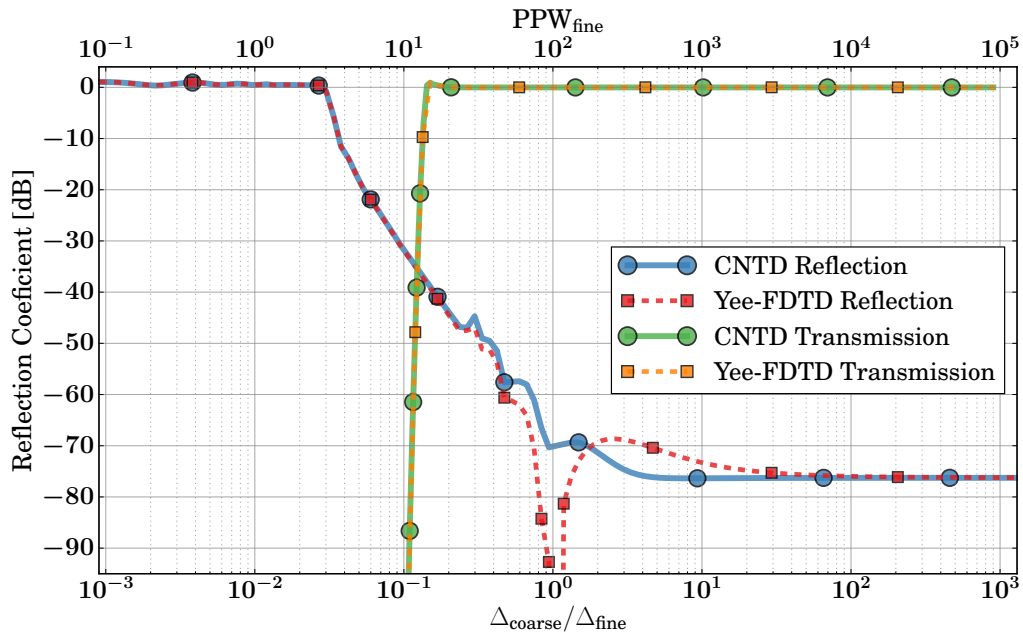


Figure 2.11: Reflection and transmission coefficients (S_{11} and S_{12}) for a uniform normally incident plane wave on a free-space thin-panel for $PPW_{\text{coarse}} = 100$ fixed. Note that we keep the convention of Δ_{fine} for the space step inside the thin-panel even for $\Delta_{\text{coarse}}/\Delta_{\text{fine}} < 1$ for which the discretization outside is actually finer than that inside.

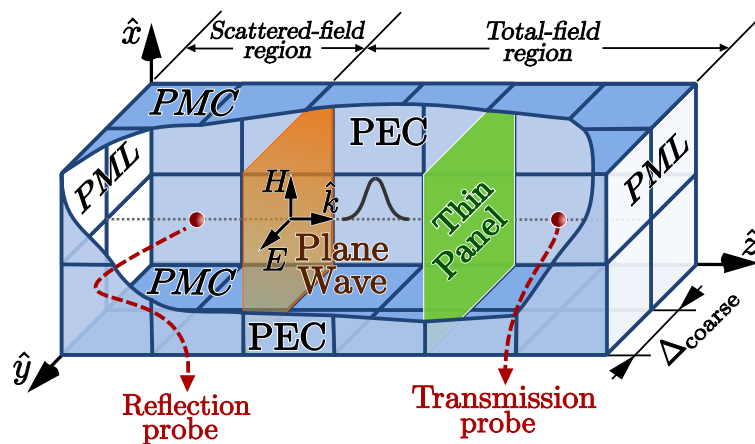


Figure 2.12: Details of the test-setup for a uniform normally incident plane wave on a thin-panel.

reflection coefficient decreases and, as expected, becomes zero as for the usual Yee-FDTD when there is no jump in the discretization ($\Delta_{\text{coarse}}/\Delta_{\text{fine}} = 1$). When SGBC-CNTD is used instead, the error is not zero since numerical reflections appear at the interface between the CNTD and the Yee-FDTD scheme. When the discretization inside and outside coincide, the error begins to become constant, even for finer discretizations inside the thin-panel, since it is dominated by the constant discretization outside it.

2.7 SGBC and NIBC computer requirements

The computational overburden of the subcell method employed to deal with thin-panels has been studied by Amdahl's law (2.48). For this, we take into account the number of floating point operations (FLOPs) added by the subcell algorithm and compute the next figure-of-merit to measure the computer speed reduction

$$S = \frac{1}{(1 - N_{\text{cells}}) + \frac{N_{\text{cells}}}{A^{\text{FLOP}}}} \quad (2.48)$$

where N_{cells} is the ratio of sub-cell special cells to the total number of cells, and A^{FLOP} is the ratio of the number of FLOPs required by the usual FDTD with and without cells affected by the sub-cell treatment

$$A^{\text{FLOP}} = \frac{A_{\text{FDTD}}^{\text{FLOP}}}{A_{\text{FDTD}}^{\text{FLOP}} + A_{\text{sub-cell}}^{\text{FLOP}}} \quad (2.49)$$

For FDTD $A_{\text{FDTD}}^{\text{FLOP}} = 14$ (8 additions/subtractions and 6 multiplications) and $A_{\text{sub-cell}}^{\text{FLOP}}$ depends on the number of new degrees-of-freedom added to the full problem: the number of layers for SGBC N_L , and the number of poles/residues N_p for NIBC (Table 2.1).

Method	+ and -	*	/
SGBC with Yee-FDTD	$5 + 6N_L$	$4 + 4N_L$	0
SGBC with CNTD	$2 + 7N_L$	$2 + 5N_L$	$2 + 2N_L$
NIBC	$6 + 4N_p$	$4 + 12N_p$	0

Table 2.1: $A_{\text{sub-cell}}^{\text{FLOP}}$ for the different sub-cell methods.

In Fig. 2.13, we show the parameter defined in (2.48) as a function of N_L , and N_p for two different ratios of cells requiring a sub-cell treatment. Though N_L , and N_p are not magnitudes that can be compared, Fig. 2.13 can be used to provide an idea of the computational cost of each model for a certain performance degradation. For instance a $N_L = 22$ layers SGBC CNTD model requires the same number of FLOPS as a $N_p = 19$ model with NIBC, with a

degradation in performance of $S = 0.9$ for 0.5% sub-cell cells and $S = 0.525$ for 4% sub-cell cells. These curves are ideal results which agree with data found after actual numerical simulations for small problems that can fit into memory caches. However, for large, problems the memory access time is actually dominant over the FLOP/second processor capabilities in the computational time of FDTD methods [Yu-2011], and the CNTD and NIBC curves tend to be closer. Finally let us also stress, that the apparent lower computer time requirement for the NIBC is obscured by its lack of robustness in stability, as mentioned in the introduction. This often requires reductions in the CFLN which are not necessary in the SGBC CNTD.

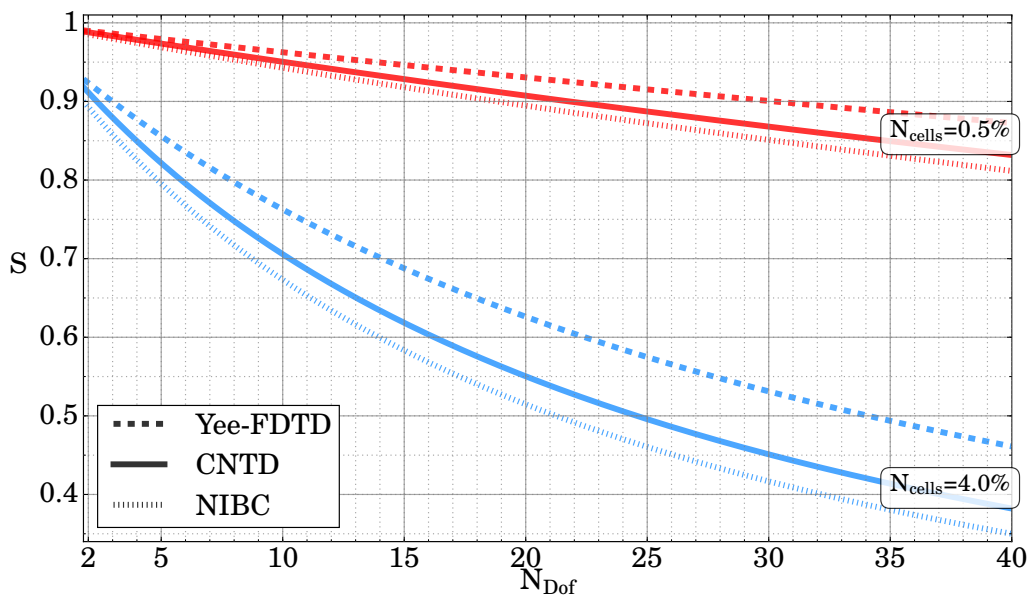


Figure 2.13: S figure of merit. N_{Dof} stands either for N_L or N_p depending on the technique used.

2.8 Conclusions

This chapter has presented a novel technique for the modeling of thin-panel lossy materials in a robustly stable and computationally affordable manner. We can summarize some advantages and disadvantages of the SGBC technique compared to the VF NIBC, when dealing with lossy thin-panel materials:

1. NIBC enables us to deal with thin-panel materials with arbitrary dispersive behavior, as long as the scattering parameters under plane-wave incidence are known either analytically, numerically, or experimentally. SGBC, in principle, requires knowledge of the internal structure of the thin-panel (thickness and bulk conductivity) in order to model wave propagation across it. However, the method can be easily extended for arbitrary frequency dispersion, by finding equivalent single-layer electric and magnetic

dispersive models [Chen-2004]. The CNTD method can also be easily extended to handle these media, for instance by employing the formulation of [Han-2006].

2. NIBC is reported to have late-time instabilities often difficult to control even by dramatic reductions of CFLN, this is often blamed on the non co-location of the electric and magnetic field components at the surface of the thin-panel. SGBC employs the natural co-location of Yee-FDTD and does not require reductions with respect to the usual stability limit thanks to the Crank Nicolson (CN) unconditional stability.
3. SGBC can also be combined with ETD with moderate constraints in the CFLN for stability. It can be used as far as lower mesh resolution requirements are acceptable inside the thin-panel (typically $PPW_{\text{fine}} = 10$) but becomes not affordable for higher resolutions (e.g. $PPW_{\text{fine}} = 20$) as shown in Fig. 2.8. This fact makes it not applicable, for instance, when dealing with multilayered materials embedding non-lossy layers (e.g. foams or honeycombs), as shown in the validation Section 4.2. SGBC-CNTD however does not present this restriction thanks to the unconditional stability of the CNTD method.
4. NIBC can handle either isotropic and anisotropic [Holloway-2005] panels, whereas SGBC is affordable only by the use of CNTD in 1D. Unconditionally stable, split-step methods could be used instead [Singh-2010] to build a 2D anisotropic SGBC. Another possibility would be to use a 2D SGBC and ETD, with the aforementioned precautions.

ROBUST AND STABLE CONFORMAL METHODS

In this chapter, we introduce different techniques for the treatment of 3D conformal meshes for their use with the DM formulation [Dey-1997]. In order to guarantee the stability, two new numerical algorithms are presented: the conformal relaxed Dey-Mittra (CRDM) [Cabello-2016] and the locally enlarged cell technique (LECT). The CRDM method is based on the relaxing and filtering of the conformal mesh by modifying the distorted cells which cause instability. On the other hand, the LECT algorithm, changes local and selectively the evolution constants of duplicated magnetic fields. These algorithms can also work with an extension of the NIBC and SGBC for thin layer modeling introduced in Ch. 2. In the last section of this chapter, these are formulated in the context of conformal methods.

3.1 Introduction

FDTD methods are typically formulated in an structured grid where all the geometrical features are transformed to regular hexahedra, rectangular faces, and straight edges. An advantage of this process is that it implies the filtering-out of small details while, if done correctly, the ohmic conductivities between structures are preserved. However, this comes at the cost of creating a staircasing effect [Cangellaris-1991, Holland-1993] which implies a reduction of the order of error convergence [Zagorodnov-2007, Nieter-2009, Cabello-2016]. Moreover, it introduces errors in the sizes of the meshed objects due to the lack of adaptivity to curved geometries to a shift in the resonance frequencies of the objects [Dey-1997], and an increase in their ohmic losses at low frequencies. These problems have been studied extensively in previous works and several solutions have been proposed, we classify them into two main groups: solutions that modify the global pattern of the grid, and solutions that imply a modification of the cells or the field-updating equations.

One example of introducing grid modifications is the non-uniform orthogonal grid

technique explained in [Taflove-2005, ch11]. This increases the grid resolution in the regions with more curvature. However, this method presents several problems. Firstly, it drives to a reduced order of error convergence, exhibiting spurious mode reflections between regions with different resolution. On top of that, it forces restrictions on stability conditions caused by the use of smaller cell sizes [Remis-2006]. Another grid-modifying technique is the use of global non-orthogonal curvilinear coordinates [Taflove-2005, ch.11] [Fusco-1990] [Fusco-1991] [Holland-1983] [Gedney-1996] [Hwang-1999] [Kantartzis-2000] [Kantartzis-2001] [Lee-2011], requiring the introduction of metric elements in the evolution equation. Moreover, non-orthogonal systems can not be easily generalized to any type of structure requiring a high grade symmetry in their geometry.

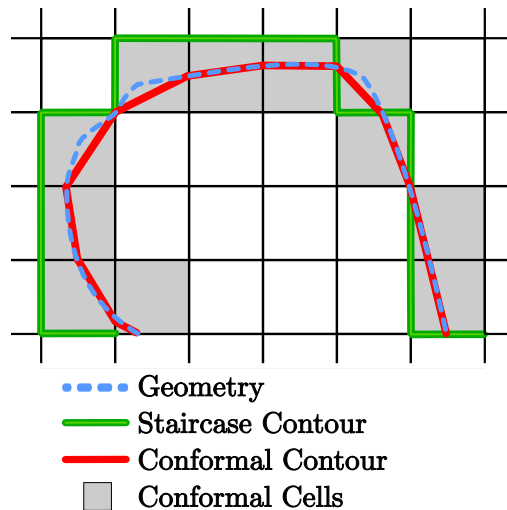


Figure 3.1: An schematic view of the mesh approximations needed in a given geometry (dashed blue) in order to apply staircased algorithm, a staircased mesh contour (green) has to be generated. Conformal algorithms allow for a closer to the original geometry mesh (red). Cells that require the use of the conformal algorithm are marked in gray, the rest are treated with the classical FDTD method.

In the second group, the Conformal FDTD (C-FDTD) methods are the most popular techniques for the treatment of curved objects. These improve the adaptation of the mesh to the original geometry without losing most of the benefits of the classic FDTD method (Fig. 3.1) which is unaltered within most part of the computational domain. In the cells wherever the C-FDTD method is applied, the cells are split in two zones using the so called conformal mesh contour. In these cells, the electric fields are edge-centered and the magnetic fields are face-centered. Therefore, at conformal cell faces, electric fields are always tangential and magnetic fields are always normal to that face. The magnetic field in each zone of the face is calculated, using Faraday's Law, by computing the electric field

circulation on the deformed contour (Fig. 3.2),

$$H_k^{n+1/2} = H_k^{n-1/2} - \sum_v D_{k,v} E_{k,v} \quad \text{with:} \quad D_{k,v} = \frac{\Delta t l_{k,v}}{\mu A_k} \quad (3.1)$$

with A_k representing the area of the distorted zone, $l_{k,v}$ the length of each segment v in the integration contour path, $E_{k,v}$ the electric field in segment l_v (Fig. 3.2). For conformal segments of PEC material, the tangential electric fields are zero, *e.g.* $E_{1,S}, E_{2,S} = 0$ in Fig. 3.2.

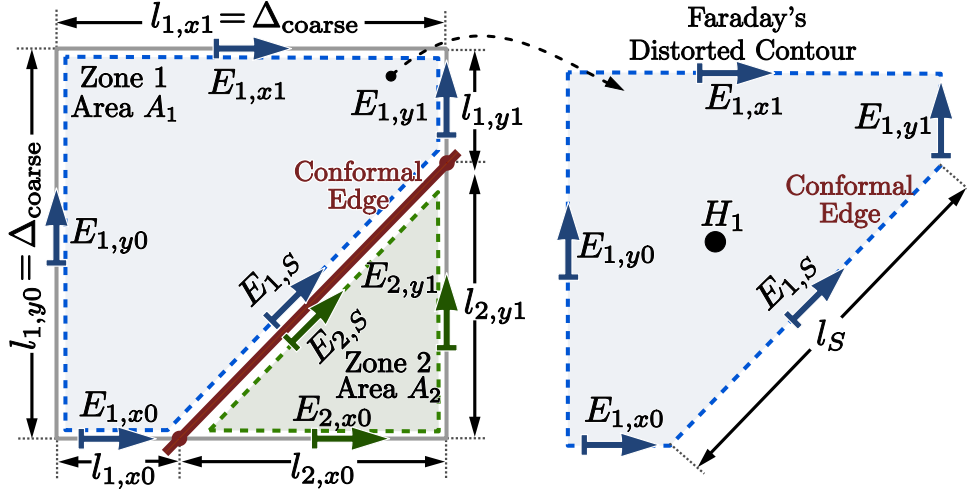
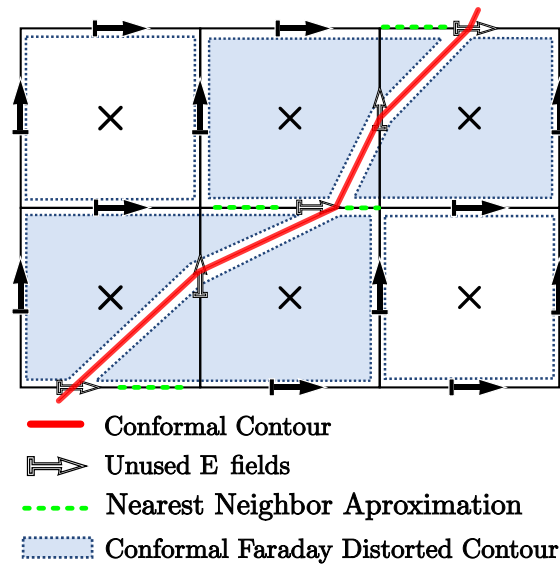


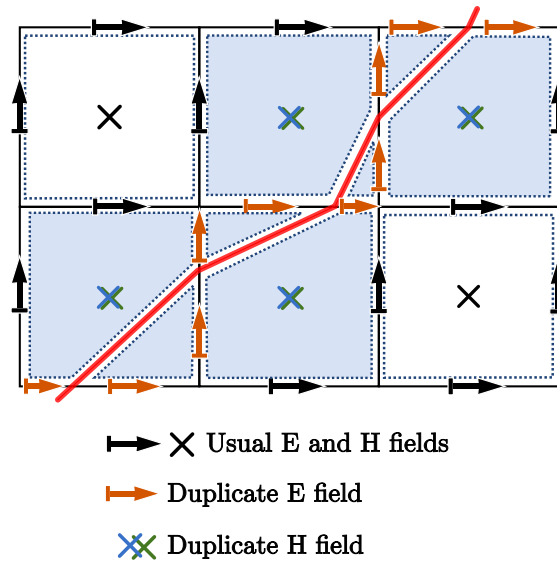
Figure 3.2: Located of the electric fields $E_{k,v}$ on the closed contour. The magnetic field is assumed to be constant inside the contour.

The distinct conformal methods differ in the way that the $D_{k,v}$ coefficients in (3.1) are chosen in order to update the magnetic field:

- In 1992s Jurgens-Taflove [Jurgens-1992] [Jurgens-1993] [Fang-1993] proposed a conformal method called Contour Path FDTD (CP-FDTD) in which the Maxwell's integral path equation is modified along each distorted cell and its neighbour (Fig.3.3a). This method uses the same fields as the classic FDTD but evaluated on wider contours. To do so, it interpolates H and E -field components of the collinear nearest neighbor to approximate the fields where it is needed. However, this produces a lack of causality and reciprocity during the field updating stage which may drive to instabilities [Garcia-1994, Railton-1995, Steeds-1996, Dey-1997].
- In [Mezzanotte-1995], a simple and accurate procedure to approximate a metal curved surface within a Cartesian grid is proposed. The method allows the conventional staircased approximation to be replaced with a slanted walls approximation. However, this method lacks adaptivity as it only allows for cell faces with a triangular shape.
- The Dey-Mitra (DM) method [Dey-1997, Yu-2000, Yu-2001, Yu-2005, Yu-2006, Yu-2011] consists on a explicit method for handling the intersection between a PEC



(a) Distorted cells stencil for Conformal Contour Path FDTD method.



(b) Distorted cells stencil for Conformal Dey-Mitra.

Figure 3.3: C-FDTD stencil.

volume and surface material within a Cartesian grid which results in an excellent geometrical adaptivity. The method is a simplification of the CP-FDTD which avoids the need of performing a contour path integral and subsequent field interpolations. Each zone has a magnetic fields H_1 , H_2 associated with it, these fields are updated by using the closed line integral of the tangential fields along their contour according to

(3.1). For instance, in the case of Fig. 3.2, the magnetic fields are updated as:

$$H_{1,z}^{n+1/2}(i, j, k) = H_{1,z}^{n-1/2}(i, j, k) - \frac{\Delta t}{\mu A_1} \begin{bmatrix} l_{1,x}(i, j, k) E_{1,x}^n(i, j, k) \\ +l_{1,y}(i+1, j, k) E_{1,y}^n(i+1, j, k) \\ -l_{1,x}(i, j+1, k) E_{1,x}^n(i, j+1, k) \\ -l_{1,y}(i, j, k) E_{1,y}^n(i, j, k) \end{bmatrix} \quad (3.2a)$$

$$H_{2,z}^{n+1/2}(i, j, k) = H_{2,z}^{n-1/2}(i, j, k) - \frac{\Delta t}{\mu A_2} \begin{bmatrix} l_{2,y}(i+1, j, k) E_{2,y}^n(i+1, j, k) \\ -l_{2,x}(i, j+1, k) E_{2,x}^n(i, j+1, k) \end{bmatrix} \quad (3.2b)$$

while the E-fields as updated by the usual FDTD algorithm.

- A conformal DM refinement is proposed in [Junkin-2007] for arbitrary geometries based on simple polygons for 3D PEC geometries. This implementation allows for the possibility of treating fine and sub-cell details which can be helpful in certain cases where objects geometries are in close proximity.

3.2 Improving stability in conformal methods

The main drawback of the DM scheme mentioned above, is that requires a significantly more restrictive time-step stability condition than that imposed by the classic FDTD CFL criterion. This restriction depends on the relative position of the conformal mesh with respect to the grid, the zone area A_k and the lengths of segments $l_{k,v}$. The DM stability condition, as reported in [Yu-2000, Zagorodnov-2003, Benkler-2006] and, as we will further confirm by the numerical experiments shown in Section 4.1, is

$$\Delta t_k = F_{\text{stb}} \sqrt{\frac{A_k \Delta}{A_{\text{FDTD}} \max_v(l_{k,v})}} \Delta t_{\text{CFL}} = \text{CFLN}_k \Delta t_{\text{CFL}} \quad (3.3)$$

with

$$\text{CFLN}_k = F_{\text{stb}} \sqrt{\frac{A_k^{\text{ratio}}}{\max_v(l_{k,v}^{\text{ratio}})}} \leq 1.0 \quad (3.4)$$

where A_{FDTD} and Δt_{CFL} are respectively, the area and time step in the CFL limit for the usual Yee algorithm, $l_{k,v}$ is the length of segment v for the zone k and F_{stb} is a constant heuristical factor valued $\sqrt{3}$.

To alleviate this restriction, Yu-Mitra (YM) [Yu-2000] proposed a variant of the DM

method which removes the time-steps restriction, neglecting the differences in the areas of all distorted zones, by making $A_{1,2} = A_{\text{FDTD}}$, and therefore using the original Yee cell face area. In practice, this correction is equivalent to introducing a fictitious magnetic medium and which will compromise precision,

$$D_{k,v}^{\text{Yu-Mittra}} = \frac{\Delta t l_{k,v}}{\mu_0 A_{\text{FDTD}}} \equiv \frac{\Delta t l_{k,v}}{\mu_0 \mu_{r,k} A_k} \quad \text{with} \quad \mu_{r,k} = \frac{A_{\text{FDTD}}}{A_k} \geq 1 \quad (3.5)$$

3.2.1 The Conformal Relaxed Dey-Mittra (CRDM) method

A novel strategy presented in this dissertation [Cabello-2016] has been devised to warrant the stability while allowing a trade-off between accuracy and computationally efficiency. This consists on fixing a value for CFLN in (3.4). Then, this value is used to automatically modify the mesh to allow only certain zones of the intersections over the edges (Fig. 3.4), modifying only the cells which would be responsible of causing instabilities in the DM method. This implies shifting the point of the original conformal intersection, l_c , to the closest point outside a region delimited by a *forbidden* length l_f , whose range is between 0 and $\Delta/2$. The new intersection will have a location defined by a relaxed length l_r

$$l_r = \begin{cases} 0.0 & \text{if } l_c \leq \frac{l_f}{2} \\ l_f & \text{if } l_f > l_c > \frac{l_f}{2} \\ l_c & \text{if } l_c > l_f \end{cases} \quad (3.6)$$

If we define the relaxation factor $F_{\text{rlx}} = l_f/\Delta$ as the relative distance over the edge of the Yee's cell which determines where the conformal intersections will be located, the stability criteria (3.3) now can be written as a function of, uniquely, the relaxing factor:

$$\Delta t = \min_{\text{All cells}} (\text{CFLN}_k) \Delta t_{\text{CFL}} \quad (3.7)$$

If we assume a conformal edge of PEC material, the worst case for (3.3) is given:

$$\Delta t = \sqrt{\frac{3 F_{\text{rlx}}}{2}} \Delta t_{\text{CFL}} \quad (3.8)$$

CRDM is therefore a selective technique which only modifies the unstable cells according to the relaxing criteria (3.6) in opposition to the global criteria imposed by the YM method (3.5). The relaxation factor provides also the degree of adaptation of the conformal mesh to the original geometry, being $F_{\text{rlx}} = 0.0$ the maximum adaptation and $F_{\text{rlx}} = 0.5$ the minimum as can be seen in Fig.3.5.

Finally, the relaxed mesh automatically erases negligible areas and edges having small l^k . This also improves the computational costs, by reducing the duplicated degrees of freedom

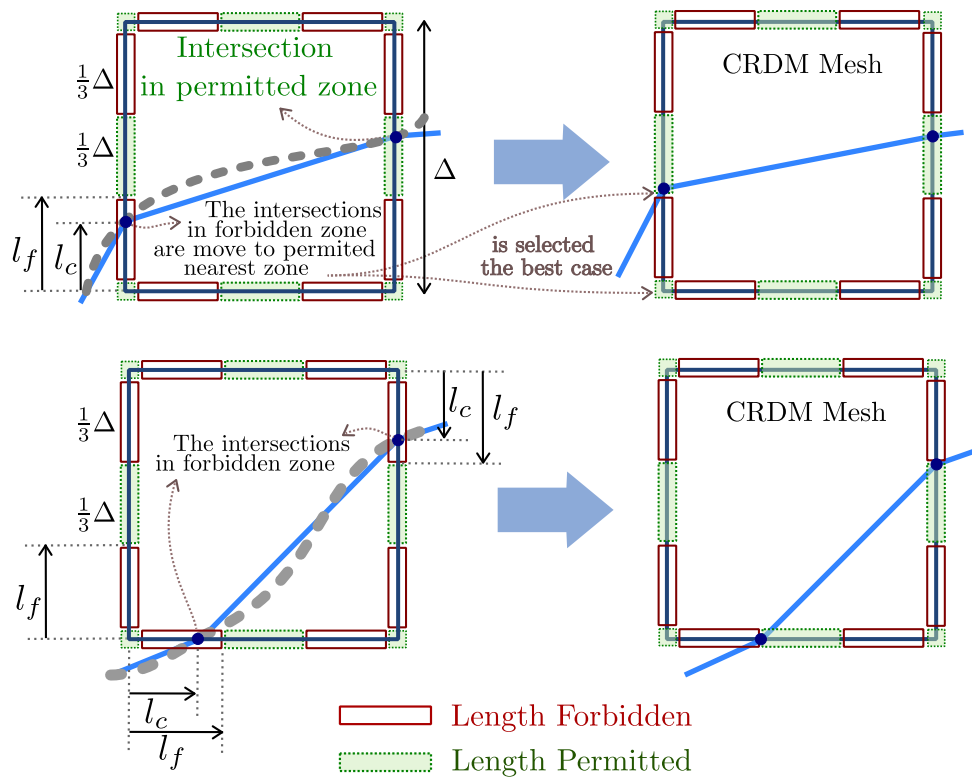


Figure 3.4: Examples of the CRDM relaxation for $F_{rlx} = 1/3$ in which the geometry (dashed line) intersects the left and right edges that will be used for the simulation, represented by a simplified surface (continuous line).

when l_r is zero (Fig. 3.6). Note also that, as opposite to the YM method, no artificial magnetic medium is introduced. Numerical experiments in Section 4.1 will demonstrate that this technique allows us to retain the second-order convergence of the classical FDTD method in free-space.

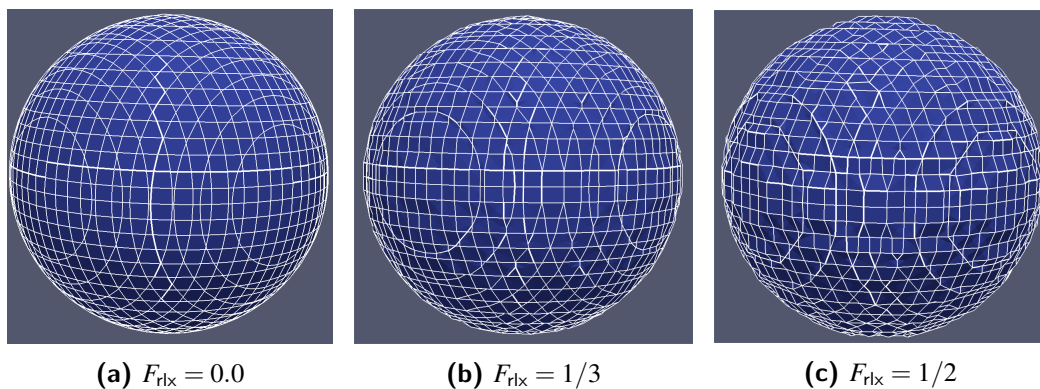


Figure 3.5: Surface model of a target sphere with different conformal relaxed factor meshing.

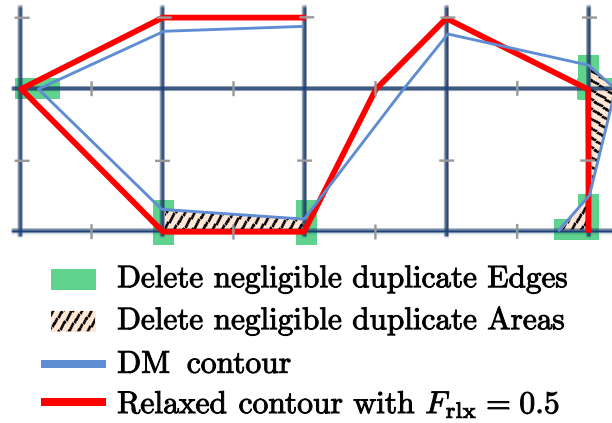


Figure 3.6: Examples of areas and edges deleted by the CRDM method.

3.2.2 Locally Enlarged Cell Technique (LECT)

The LECT is another novel approach consisting on a simplification of the enlarged cell techniques (ECT) presented in [Xiao-2004, Xiao-2008]. Contrary to ECT, the main advantage of LECT is that it avoids the need of modifying neighbor cells and the corresponding Faraday's Law contour path integral. This is, therefore, a selective method because we are modifying only the zones causing instability $A_{1,2}$ according to the minimum area criteria obtained in (3.3)

$$A_k^{\text{mod}} = \begin{cases} A_k & \text{if } A_k \geq A_{\min,k} \\ A_{\min,k} & \text{if } A_k < A_{\min,k} \end{cases} \quad \text{para } k = 1, 2 \quad (3.9)$$

where $A_{1,2}^{\text{mod}}$ represents the value of the modified area, $A_{\min,k}$ is the minimum value needed by the area of a zone k to satisfy the stability criteria (3.8) which depends on the fixed CFLN and the geometry of each conformal cell,

$$A_{\min,k} = A_{\text{FDTD}} \frac{\text{CFLN}^2}{F_{\text{stb}}^2 \Delta} \max_v (l_{k,v}) \quad (3.10)$$

This let us to redefine the area constant in (3.1), which can now be expressed as

$$D_{k,v} = \frac{\Delta t l_{k,v}}{(\mu A_k^{\text{mod}})} \quad (3.11)$$

where the rest of parameters are not changed.

The LECT and CRDM methods can be used simultaneously, trading accuracy for computational efficiency. We can choose to increase the CFLN over the stability criterion

(3.8). For a mesh relaxed by a factor F_{rlx} , the relative error in the area for the worst case is

$$\text{Err} = \frac{A_k^{\text{mod}}}{A_k} = \begin{cases} 0 & \text{if } A_k \geq A_{\text{min},k} \\ \frac{A_{\text{min},k}}{A_k} = \frac{\text{CFLN}^2/F_{\text{stb}}^2}{0.5F_{\text{rlx}}} - 1 & \text{if } A_k < A_{\text{min},k} \end{cases} \quad (3.12)$$

In case that just one of the distorted zones does not fulfill the minimum area criterion, the complementary area zone can be reduced so that the sum of both equals to the total face area,

$$A_1^{\text{mod}} + A_2^{\text{mod}} = (A_1^{\text{mod}} + A_{\text{min},1}) + (A_2^{\text{mod}} - A_{\text{min},1}) = A_{\text{FDTD}} \quad (3.13)$$

Which allows the modification of the updating field coefficients in a consistent way that warrants the coherence of the magnetic flux.

3.3 Conformal thin-panels

In the previous sections of this chapter we have introduced conformal methods capable of solving PEC objects. In this section, we will extend these techniques for the solution of materials with finite conductivity but that are still significantly thinner when compared with the grid spatial steps, and therefore they can not be modeled directly as volumes. Before entering to explain the approach that we have followed, let us review the problems associated with some of solutions that can be found in the literature. We will classify them into three groups: staircased subgridding [Wang-2002, Xiao-2005], effective average parameters, and conformal thin-panel methods [Dey-1997].

3.3.1 Staircased subgridding methods

Staircased subgridding methods allow the user to avoid filtering out small-scale geometrical details, and keeping the relevant ones, in an efficient and stable manner [Ritter-1997]. However, subgridding fails to properly model the physical size of objects because the rectilinear grid imposes a different metric, namely the Manhattan distance. The Manhattan distance is defined as the distance between two points measured in a grid along axes at right angles *e.g.* in a plane with p_1 at (x_1, y_1) and p_2 at (x_2, y_2) is equal to $|x_1 - x_2| + |y_1 - y_2|$. The problem with this metric is that the distance between two points along a non-aligned staircased line is always larger than the Euclidean one (Fig. 3.7). Specifically, the associated error is:

$$\text{err} = \frac{|d_{\text{manhattan}} - d_{\text{euclidean}}|}{d_{\text{euclidean}}} = \frac{\sum_k^{N_D} |p_{1,k} - p_{2,k}|}{\sqrt{\sum_k^{N_D} (p_{1,k} - p_{2,k})^2}} - 1 \quad (3.14)$$

where p_1 and p_2 represent two points located at Cartesian grid vertices and N_D is the spatial dimension. Note that the error is independent of the grid step size which. For the case of a diagonal line, the worst case, this associated error is:

$$\text{err} = \frac{N_D}{\sqrt{N_D}} - 1 \quad (3.15)$$

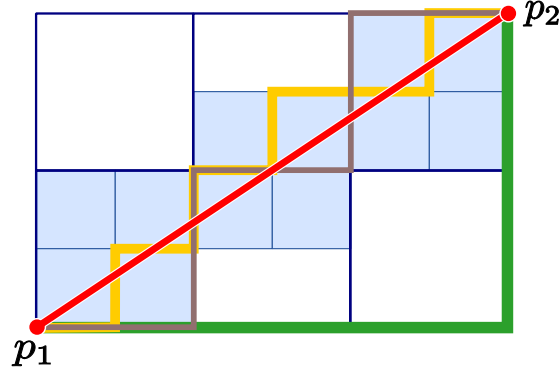


Figure 3.7: Red line represents the diagonal Euclidean distance between two points p_1, p_2 . Green, brown, and yellow lines have the same Manhattan distance even for different grid sizes.

3.3.2 Conformal bulk methods

Conformal methods for bulk method presented in [Kaneda-1997, Dey-1999, Yu-2001, Taflove-2005] are typically based on a use of effective constitutive relationships calculated as simple averages. To do so, different average estimations have been tested and reported for constant permittivities which can be straightforwardly extended to simply conductive or magnetic materials. The most representative are:

1. The homogeneous filled average methods consist on computing a fictitious material from the original materials present on each grid cell. Then the associated parameters to this material is used to compute the cell field unknowns, possibly varying on each direction. These parameters can be evaluated according to the filling ratio as

$$v_{\xi,av} = R_{\xi} v_{\xi} + (1 - R_{\xi}) v_{\xi,0}$$

with v_{ξ} being the corresponding EM constitutive parameter to be averaged evaluated at a specific position ξ . The filling ratio R_{ξ} can be computed using a variety of geometric criteria:

- Linear average [Yu-2001] (Fig. 3.8a),

$$R = L_{\text{filled}}/L_{\text{Total}}$$

- Surface average [Taflove-2005, Section 10.3.2] (Fig. 3.8b),

$$R = S_{\text{filled}}/S_{\text{Total}}$$

- Volumetric average [Dey-1999] (Fig. 3.8c),

$$R = V_{\text{filled}}/V_{\text{Total}}$$

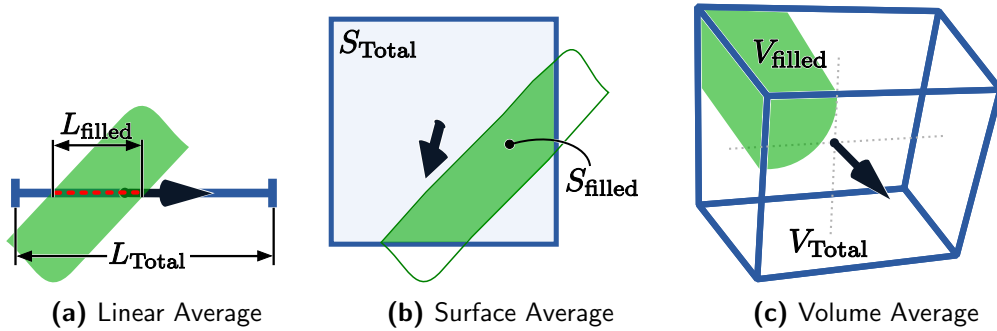


Figure 3.8: Surface model of a target sphere with different conformal relaxed factor meshing.

2. Integral averages [Kaneda-1997]. The average is numerically made through several slices normal to the field component. It attains better accuracy than the previous cases, but the computation of the parameters is more complex.

$$\epsilon_{z_{i,j,k+1/2}}^* = \left[\frac{1}{\Delta z} \int_z^{z+\Delta z} \frac{1}{\alpha(z) \epsilon_1 + (1 - \alpha(z)) \epsilon_0} dz \right]^{-1}$$

where $0 \leq \alpha(z) \leq 1$ is the fraction of the cell area embedded in the dielectric material.

3. A more accurate technique employs 3D tensor effective parameters based on the normal vector of the dielectric surface inside the cells [Nadobny-2003], with different effective parameters optimized for the normal and tangential components of the fields [Hwang-2001].

However, these methods present a potential problem consisting on the creation of unwanted ohmic contacts in regions where two different materials are close (Fig. 3.9). This is caused by the averaging of an electric field-component which overlaps with the averaging of the neighboring one. Proper pre-processing tools are needed to detect and correct these cases.

Moreover, effective parameter methods drive to a reduction in accuracy because the wavelength inside a material is shorter than in vacuum. In consequence, to keep the same spatial resolution we would need to reduce the cell size, but this is not possible for these

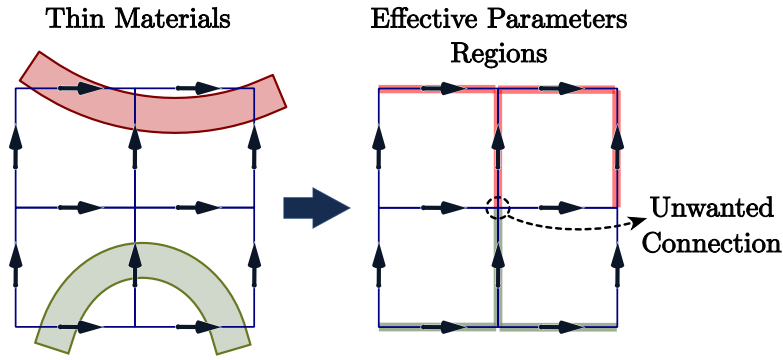


Figure 3.9: Unwanted connection conflict when using the length average method with separated thin materials.

methods. Assuming plane-wave propagation of the form $E(\xi) = E_0 e^{-\alpha\xi} e^{j(\omega t - \beta\xi)}$, for a good conductor approximation $\sigma/\omega\varepsilon \gg 1$, the propagation constants are $\alpha = \beta = \sqrt{\mu\sigma\omega/2}$, therefore, the relative error of it is $\text{err} = 1 - \sqrt{R}$, consequently, this implies an error in all the parameters that derive from the propagation constants, *e.g.* S -parameters, impedance, or shielding effectiveness. Therefore, a combination of subgridding and conformal methods can be optimal to deal with all the complexity in most general cases of thin-panel.

3.3.3 Conformal Thin-Panels

In this section we propose a novel algorithm than can be seen as a generalization of the conformal algorithm proposed by DM [Dey-1997] also to deal with lossy thin panels. In this section we extend the PEC described above, to the two-sided NIBC and SGBC presented in Chapter 2, which take into account both scattering and penetration. In [Junkin-2011] a one-sided classical surface impedance boundary conditions (SIBC) was presented to model bulk lossy objects capable of analyzing the scattering problem, while not handling the penetration (interior) problem.

To do so, we introduce two degrees of freedom, $E_{1,S}$ and $E_{2,S}$, to represent the tangential electric field at both sides of the thin layer. Besides of this difference, we will follow the same notation used in there. The resulting technique can be summarized as follows:

- 1) E-fields at usual cell edges outside the panel are advanced according to DM algorithm.
- 2) The tangential E-fields on the panel surface $E_{1,S}$, $E_{2,S}$ are advanced by the thin-panel algorithm, these method are extensively described in the Chapter 2,
 - (a) NIBC proposed in Section 2.5 using (2.13)
 - (b) SGBC ADE-CNTD proposed in Section 2.6.2 using (2.34) (2.32)
- 3) The conformal H-fields, H_1 and H_2 , are updated using the closed line integral of

tangential electric fields along their contour.

$$\begin{aligned} H_{1,S}^{n+1/2} &= H_{1,S}^{n-1/2} - \frac{\Delta t}{\mu_0 A_1} \left(\Gamma_1^n + l_S E_{1,S}^n \right) \\ H_{2,S}^{n+1/2} &= H_{2,S}^{n-1/2} - \frac{\Delta t}{\mu_0 A_2} \left(\Gamma_2^n - l_S E_{2,S}^n \right) \end{aligned} \quad (3.16)$$

Where $\Gamma_k^n = \sum_{\nu} l_{k,\nu} E_{k,\nu}^n$ is the usual discrete line integral of the E-field components for conformal PEC edges, where k denotes the side location, ν the geometrical position at the Cartesian grid, and l_S the conformal edge length on conformal cell.

All the procedures described for the staircased case to relate the fields at either side of the panel, can now be applied with no difference to the conformal case. For NIBC the setup is depicted in Fig. 3.10 and for SGBC that of Fig. 3.11.

The same CRDM and LECT strategies presented in Chapter 3, can be used to ensure the stability of the method. Taking (3.3), and considering a conformal edge of non-PEC material, the worst case for stability occurs when $\max_{\nu} (l_{k,\nu}) = \sqrt{2} \Delta$. Therefore, (3.8) now transforms into

$$\Delta t = \sqrt{\frac{3 F_{\text{rlx}}}{2\sqrt{2}}} \Delta t_{\text{CFL}} \quad (3.17)$$

which implies that the stability criterion can be written again as a function of, uniquely, the relaxing factor.

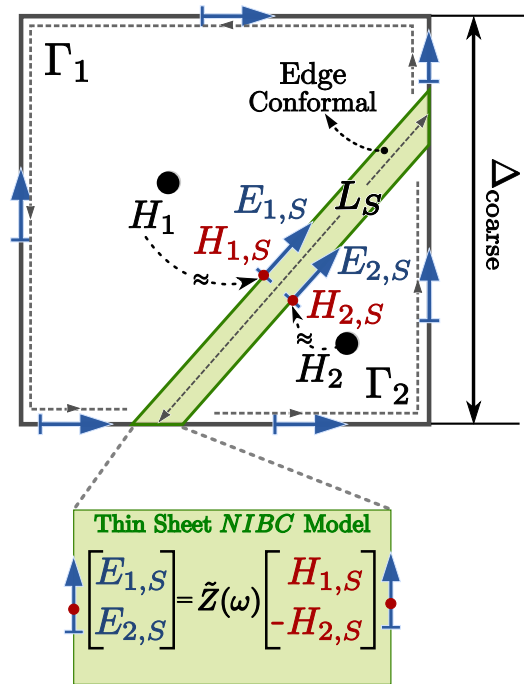


Figure 3.10: Cross section of a conformal Cell with NIBC layer.

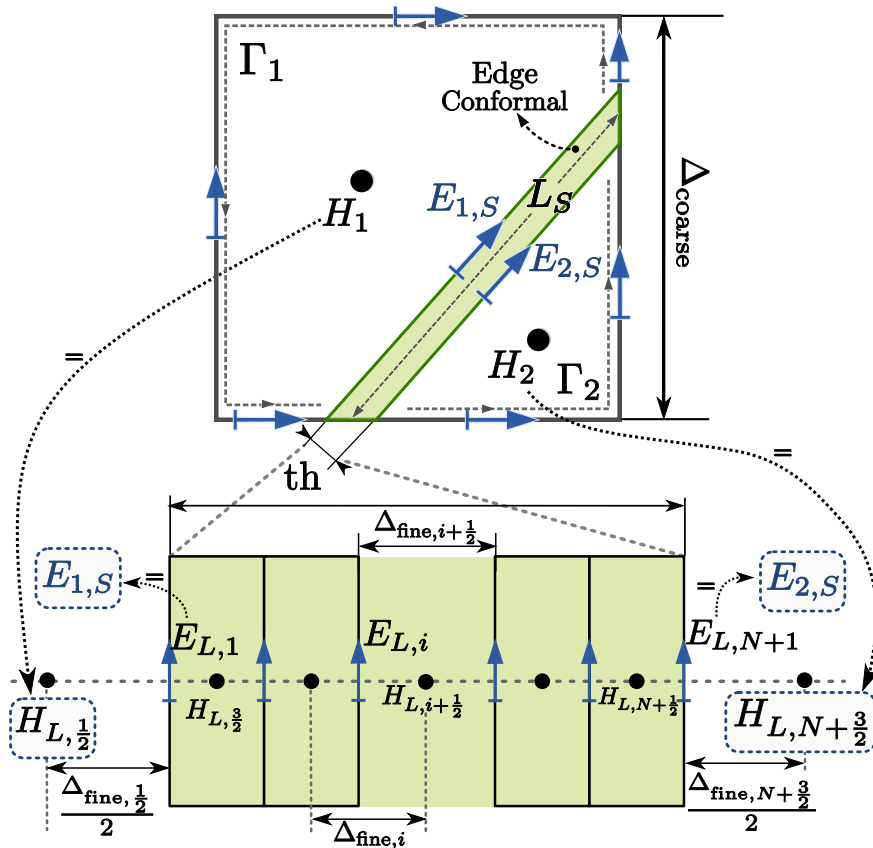


Figure 3.11: Cross section of a conformal Cell with SGBC layer.

VALIDATION

This chapter and the following one are devoted to the validation of the techniques described in previous chapters. We have split the results according to the complexity level and application scope. This chapter focuses on canonical and general-purpose test-cases, for which analytical or closed-form solution exist, whereas the following one is specifically devoted to EMC in aeronautical applications. We start here, by assessing the RCS of a PEC sphere and that of a NASA almond. Next, results for the attenuation due to planar slabs and spherical shells are analyzed. Finally, results for the low frequency ohmic resistance of thin slabs are also included, to show the validity of our approach not only under scattering conditions, but also in conductive problems.

4.1 RCS computation results for PEC targets

The monostatic RCS of a PEC sphere and a NASA almond have been calculated in order to assess the accuracy and computational performance of the proposed conformal method. We will follow the RCS definition given in [IEEE-1990],

$$\text{RCS} = \lim_{r \rightarrow \infty} 4\pi r^2 \frac{|\vec{E}_{\text{scat}}|^2}{|\vec{E}_{\text{inc}}|^2} = \lim_{r \rightarrow \infty} 4\pi r^2 \frac{E_{\phi, \text{scat}}^2 + E_{\theta, \text{scat}}^2}{|\vec{E}_{\text{inc}}|^2} \quad (4.1)$$

where \vec{E}_{scat} is the scattered electric field and \vec{E}_{inc} is the electric field illuminating the object. The scattered fields can be obtained by near-to-far-field transformations, [Taflove-1983, Luebbers-1991, Garcia-2000, Merewether-1980, Balanis-2012]. The near-to-far-field transformation has been computed using the geometric mean method [Schneider-2010].

4.1.1 PEC sphere

The monostatic RCS backscattering results for a PEC sphere with 3 m radius is first studied. The space is discretized using a regular grid of $\Delta = 3/14$ m. The model is illuminated

by a plane-wave with a Gaussian profile and a bandwidth of 0.2GHz with a propagation direction aligned with the grid axis. The conformal techniques proposed in the Chapter 3 (Section 3.2.1 and Section 3.2.2) have been used, with a CFLN = 0.9, and applying the LECT area modifications. Results of this setup are shown in Fig. 4.1 and Fig. 4.2, together with analytical Mie-series results. A study of convergence is shown in Fig. 4.3, where the error at each frequency, expressed as points per wavelength, $PPW = c_0/(f\Delta)$, is computed using the corresponding analytical result as reference.

The CRDM and LECT methods show a clear improvement of the results, when compared with the staircased and the conformal YM methods. The study of the convergence illustrated on Fig. 4.3 shows, as expected, a first order convergence for the staircased scheme compared with a close to second order behavior for the conformal methods. This holds even for simplified CRDM cases with low degree of adaption. Tab. 4.1 shows the dependence on the precision with the degrees of adaption of the conformal mesh to the original geometry as a function of F_{rlx} . The first four test-cases do not employ LECT, thus requiring a CFLN more restrictive with higher levels of adaption (smaller F_{rlx}). The second group of four test-cases employs a fixed CFLN and makes use of the LECT method for different F_{rlx} . Now, a high degree of adaptation (low F_{rlx}) requires a high number of cells to be modified by LECT in order to guarantee stability. We find that for a CFL fixed at 0.9 the trade-off for the optimal case is heuristically found at $F_{rlx} = 0.3$.

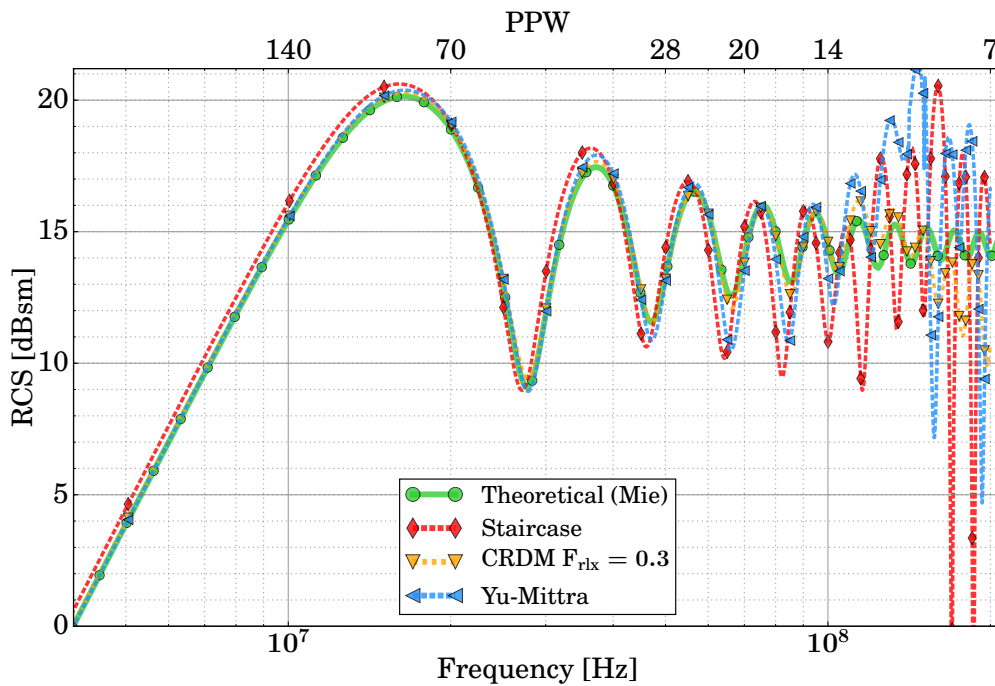


Figure 4.1: Comparison of the RCS for a sphere of radius 3 m with meshes for CRDM and structured with space resolution of $\Delta = 3/14$ m and CFLN = 0.9.

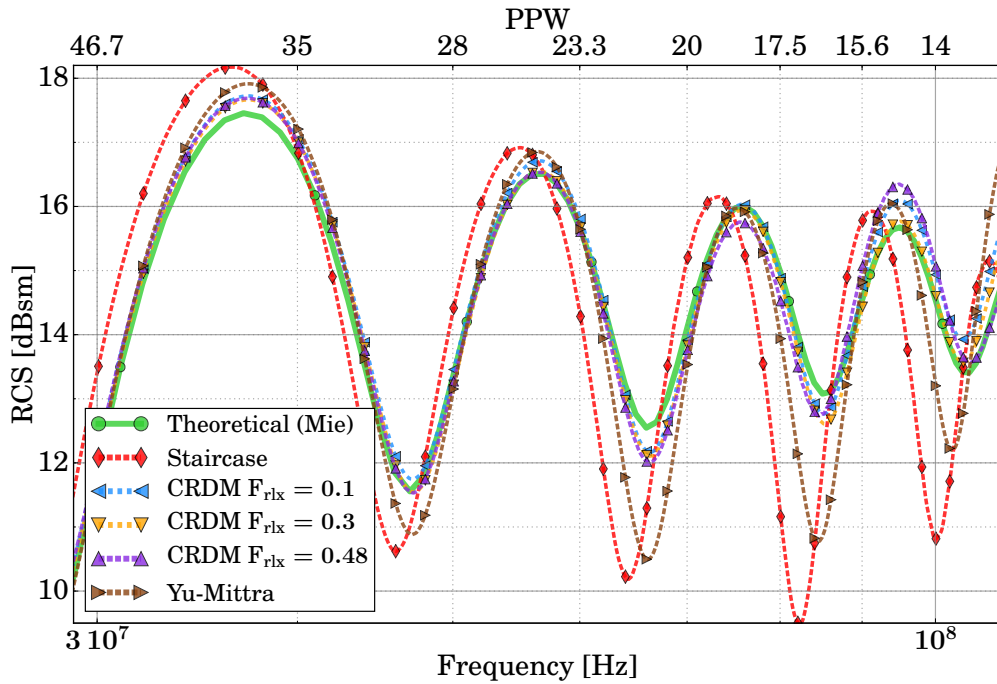


Figure 4.2: Comparison of the first resonances of the RCS

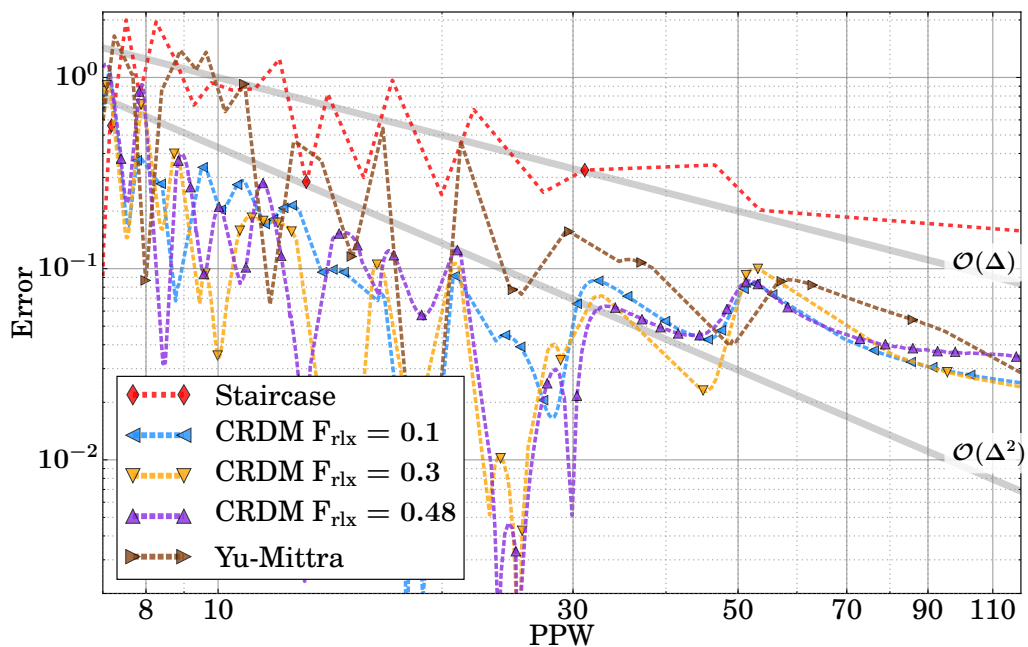


Figure 4.3: Relative error convergence of the RCS with respect to the analytical results. Figure shows results for the structured case and different conformal techniques as a function of the spatial resolution (PPW) and considering CFLN = 0.9.

Method		% LECT cells modified	Error RMS [dBsm]	CPU Time
CRDM $F_{rlx} = 0.05$	CFLN=0.273	0.0 %	0.198	3.32
CRDM $F_{rlx} = 0.1$	CFLN=0.39	0.0 %	0.201	2.44
CRDM $F_{rlx} = 0.3$	CFLN=0.67	0.0 %	0.225	1.40
CRDM $F_{rlx} = 0.48$	CFLN=0.85	0.0 %	0.278	1.10
CRDM $F_{rlx} = 0.05$	CFLN=0.9	43 %	0.243	1.05
CRDM $F_{rlx} = 0.1$	CFLN=0.9	28 %	0.226	1.05
CRDM $F_{rlx} = 0.3$	CFLN=0.9	19 %	0.225	1.04
CRDM $F_{rlx} = 0.48$	CFLN=0.9	0.5 %	0.278	1.04
Yu-Mittra	CFLN=0.9	100 %	0.595	1.05
Staircase	CFLN=0.9	N/A	1.201	1.0

Table 4.1: RMS error [dBsm] in the interval [10,100]MHz, and the percentage of cells modified by the LECT for different F_{rlx} values of the conformal method. A cell is considered to have been modified when it is changed by a factor 0.1 or more from its original area value. The CPU time is shown as the number of times employed by the structured case.

4.1.2 Anisotropic mesh effects

A well-known source of error in classical FDTD schemes comes from the fact that the simulation mesh may present different degrees of adaption to the original geometry depending on its orientation with respect to the grid. This, in effect, leads to an anisotropic error.

In order to assess the effects of this error, we computed the mono-static RCS of an object by varying the propagation direction of an incident plane wave with respect to one of the grid axis. To this aim, we used the spherical target described in Section 4.1.1 with the same spatial discretization.

The results, shown in Fig. 4.4, represent the variation of the RCS, as a function of the propagation direction, at 100MHz. In Fig. 4.5 we also show the maximum variation of the RCS for angles of incidence in the interval $[0^\circ, 45^\circ]$, as a function of frequency. It can be noticed that the particular orientation of the geometry has a severe impact in the precision of the which is significantly improved by the use of the CRDM technique.

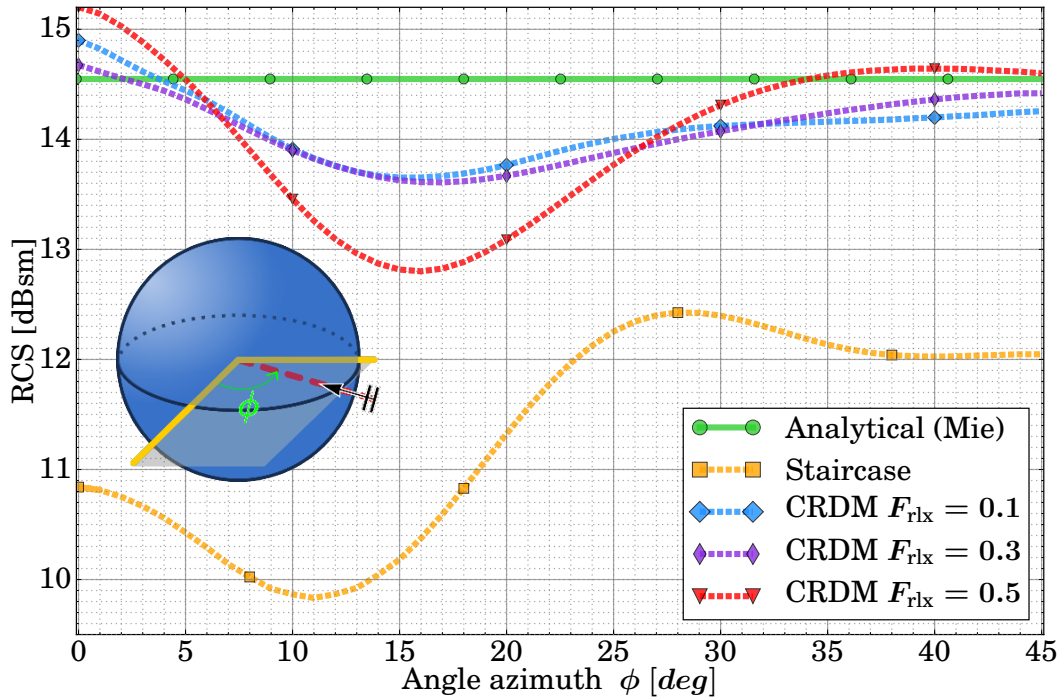


Figure 4.4: Comparison of the variation of the RCS at 100 MHz as a function of the plane-wave angle of incidence with respect to one the grid axis for a sphere of radius 3 m.

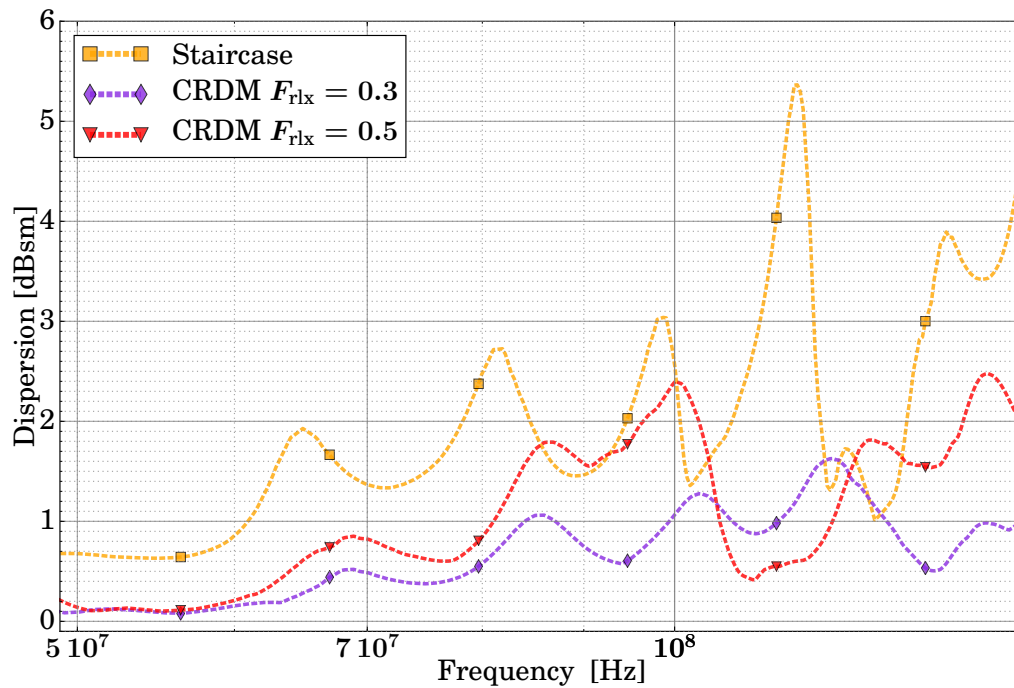


Figure 4.5: A comparison of the maximum variation (dispersion) of the computed RCS for the computed angles of incidence as a function of the frequency.

4.1.3 PEC Nasa-Almond

The NASA almond, and ogives in general [Woo-1993, A. C. Woo-1993], are particularly demanding cases due to the highly variations in curvature of their geometries. In order to obtain good results, a high precision is required during the meshing process. For this reason, these are ideal to illustrate the capabilities of the conformal CRDM and LECT with respect to the structured case.

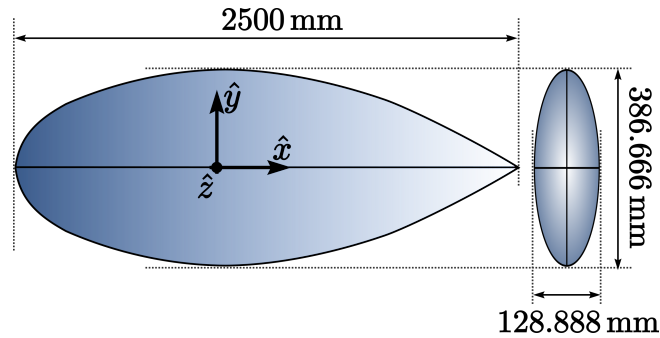


Figure 4.6: The dimensions of the Flamme model in millimeters

For these simulations, the NASA almond model used is the one described in [Alvarez-2014] using the sizes and system of reference shown in Fig. 4.6. For the structured case, a regular grid of $\Delta = 5\text{mm}$ is used. In order to obtain the monostatic RCS Fig. 4.7, the model is illuminated using a plane-wave with a Gaussian amplitude and a bandwidth of 3 GHz. The propagation direction is $-\hat{x}$ and the polarization is \hat{y} .

Method		% LECT cells modified	Error RMS [dBsm]	CPU Time
CRDM $F_{\text{rlx}} = 0.05$	CFLN=0.273	0 %	0.91	3.34
CRDM $F_{\text{rlx}} = 0.1$	CFLN=0.39	0 %	0.91	2.36
CRDM $F_{\text{rlx}} = 0.3$	CFLN=0.67	0 %	1.22	1.39
CRDM $F_{\text{rlx}} = 0.48$	CFLN=0.85	0 %	2.17	1.08
CRDM $F_{\text{rlx}} = 0.05$	CFLN=0.9	46 %	1.61	1.05
CRDM $F_{\text{rlx}} = 0.1$	CFLN=0.9	29 %	1.09	1.05
CRDM $F_{\text{rlx}} = 0.3$	CFLN=0.9	22 %	1.53	1.04
CRDM $F_{\text{rlx}} = 0.48$	CFLN=0.9	0.8 %	2.12	1.04
Yu-Mitra	CFLN=0.9	100 %	4.15	1.05
Structured	CFLN=0.9	N/A	5.87	1.00

Table 4.2: RMS error [dBsm] with respect to a MoM-computed reference solution for the monostatic RCS of the NASA Almond, in the interval $[0.5, 2]$ GHz. The third column shows the percentage of LECT-modified cells for the different conformal techniques. A cell is considered to have been modified if its original area is changed by a 10% or more. CPU time is expressed as a ratio with respect to the classic structured case.

In Tab. 4.2, the improvements in accuracy of the CRDM method with respect to the structured case are shown. We can note that, even for the cases with lesser adaptive relaxing

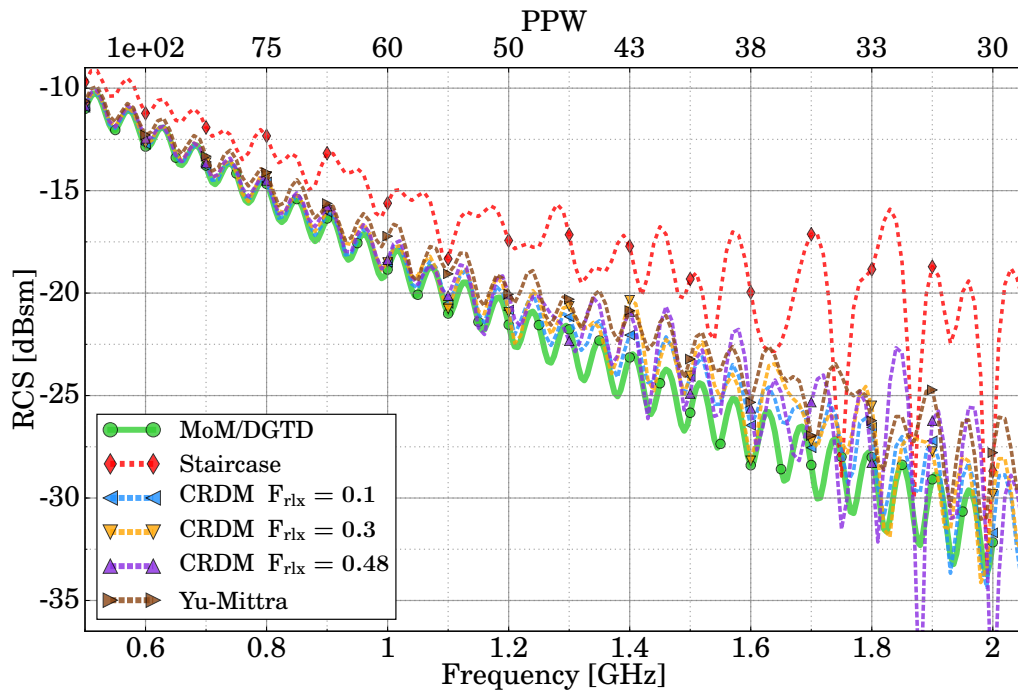


Figure 4.7: Comparison with the MoM of the RCS results for a NASA almond. The results have been obtained with different conformal techniques (LECT, Yu-Mittra) for a mesh with $\Delta = 5$ mm and a CFLN = 0.9.

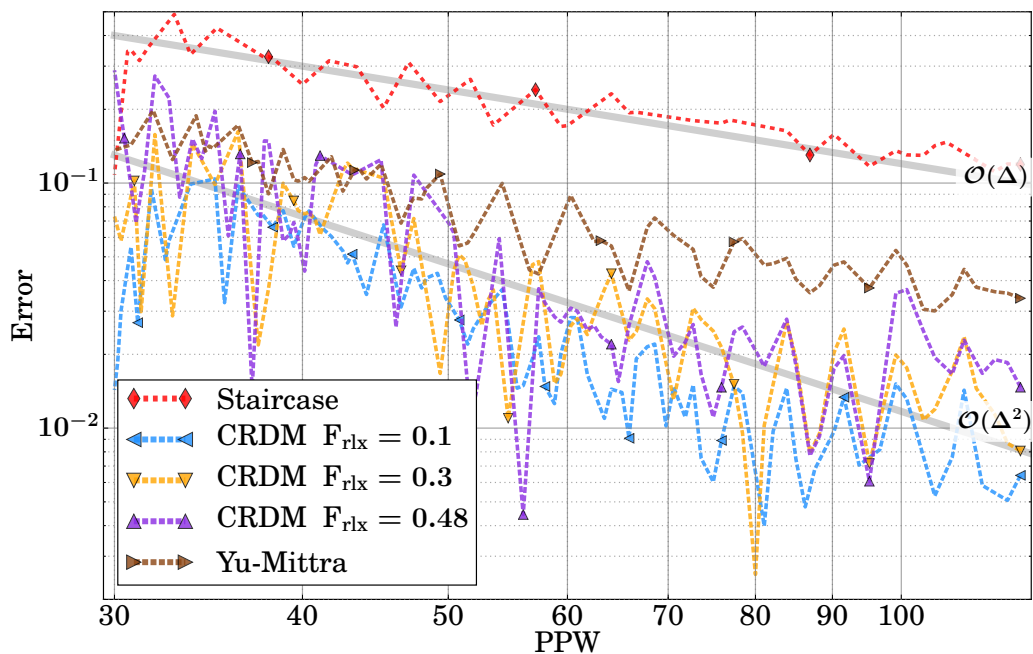


Figure 4.8: Relative error of the computed RCS with respect to MoM results for the structured case and for different conformal techniques: LECT and YM. Results are presented as a function of the spatial resolution measured in cells per wavelength and considering a fixed CFLN = 0.9.

factors, the error and convergence error improve the purely structured case. However, the CRDM techniques with smaller F_{rlx} are less stable and require smaller time steps for stability. We also show results using LECT and YM to keep a fixed CFLN. All the results are compared to the ones obtained with MoM [Alvarez-2014]. The RMS error norm with respect to MoM in frequency has also been used in Fig. 4.8, to study the convergence of the monostatic backscattered RCS as a function of the space resolution.

4.1.4 Conclusion

A new conformal CRDM and LECT strategy was proposed in chapter 3 as a way of mitigating the time-step constraint of the DM method while retaining a second-order spatial convergence. The results show a significant improvement in accuracy compared to classic FDTD with half the spatial resolution. For all test cases we find the CPU time to be approximately inversely proportional to the CFLN, implying a negligible cost on the additional operations needed in conformed cells.

The RMS error norm with respect to the exact case in a frequencies range has also been used to study the convergence of the backscattered monostatic RCS with respect to the spatial resolution. As shown in Fig. 4.3 and Fig. 4.8, the CRDM and LECT methods have a convergence of $\mathcal{O}(\Delta^2)$ while the FDTD has $\mathcal{O}(\Delta)$ as it is severely affected by the staircasing effect. These figures also shows that the method seems to have a similar order of convergence for all the relaxation factors studied.

As a figure of merit for the different methods, the error of the global RMS norm with respect to exact case was used (Tab. 4.1 and Tab. 4.2). These results confirm that the efficiency of the conformal method depends on the precision required. The precision of the conformal method is altered by the number of modified cells by LECT method and the grade of adaptivity given by relaxing factor CRDM, in this way, for a fixed CFL, a high degree of adaptation (low F_{rlx}) involves a high number of cells to be modified by LECT in order to guarantee the stability. In practice, it can be said that it is desirable to keep a high degree of adaptivity for complex geometries. For instance, for the NASA-Almond case (Tab. 4.2), the optimal value is $F_{\text{rlx}} \approx 0.1$. However, for smoother curvatures (Tab. 4.1) it is found that a relaxing factor $F_{\text{rlx}} = 0.3$ is the optimal.

4.2 SGBC and NIBC for lossy thin slabs

This section presents various applications for thin-panel techniques (SGBC, NIBC) which were presented in Chapter 2, illustrating the benefits of using geometry conforming meshes for thin-panel to alleviate the electrical size degradation inherent to the staircased meshes. In practice, the staircase approximation has several shortcomings for lossy conductive objects, like the overestimation of (4–6) dB in the shielding effectiveness (SE) of enclosures,

the shifting of their natural resonance frequencies, and the overestimation of their ohmic resistance.

4.2.1 Shielding effectiveness of planar thin-panels

In this section, we show results of the SGBC method for two canonical cases: the prediction of the shielding effectiveness of planar thin-panels; and the LF resistance, which is of interest in conduction problems. The shielding effectiveness of an infinite planar thin-panel illuminated by a plane-wave with normal incidence and embedded in a medium with intrinsic impedance η_0 can be expressed, from (2.6), as

$$SE = S_{12}^{-1} = \frac{(\eta_0 + Z_{11})(\eta_0 + Z_{22}) - Z_{12}^2}{2\eta_0 Z_{21}} \quad (4.2)$$

where η_0 denote the intrinsic impedance of free-space, and Z_{ij} are the terms of the matrix (2.6). For instance, for a thin-panel of thickness h and constant conductivity

$$\tilde{Z}(\omega) = \frac{\eta}{\sinh(\gamma h)} \begin{bmatrix} \cosh(\gamma h) & 1 \\ 1 & \cosh(\gamma h) \end{bmatrix} \quad (4.3)$$

with η the usual intrinsic impedance and γ the wave propagation constant inside. From this, the shielding effectiveness (4.2) can be expressed as

$$SE = \cosh(\gamma h) + \frac{1}{2} \left(\frac{\eta_0}{\eta} + \frac{\eta}{\eta_0} \right) \sinh(\gamma h) \quad (4.4)$$

The Z relationship (2.6) can also be used to find the resistance in the low-frequency limit for conductive media $Q \ll 1$

$$\tilde{Z}_{LF}(\omega) = \frac{\gamma}{\sigma \sinh(\gamma h)} \begin{bmatrix} 1 & 1 \\ 1 & 1 \end{bmatrix} \quad (4.5)$$

in the case of a strip with width w and length l (Fig. 4.20), assuming in (4.3) $\cosh(\gamma h) \simeq 1$ we can write

$$E_{S1} = E_{S2} = \gamma \frac{H_{S1} - H_{S2}}{\sigma \sinh(\gamma h)} \quad (4.6)$$

and using a square Ampère path around it, the low-frequency impedance for the strip Z_t is

$$Z_t = \frac{\int_0^l \vec{E} \cdot d\vec{l}}{\int_S \vec{J} \cdot d\vec{S}} = \frac{\int_0^l \vec{E} \cdot d\vec{l}}{\oint_L \vec{H} \cdot d\vec{l}} = \frac{E_{S1} l}{w(H_{S1} - H_{S2})} = \frac{\gamma h}{\sinh(\gamma h)} R_{DC} \quad (4.7)$$

with R_{DC} the resistance, usually found from Ohm's law

$$R_{DC} = \frac{l}{w\sigma h}$$

For highly conductive ($\eta \simeq \frac{\gamma}{\sigma} \ll \eta_0$) thin-panels $\gamma h \ll 1$, and at the DC limit ($\omega \rightarrow 0$), we can further simplify previous equation as

$$Z_t \simeq \frac{l\eta_0}{2w} \frac{1}{SE} \simeq R_{DC}, SE \simeq \eta_0 \frac{\sigma \sinh(\gamma h)}{2\gamma} \simeq 60\pi\sigma h \quad (4.8)$$

Using the test setup of Fig. 2.12, we have conducted numerical experiments to find the SE of indefinite conductive planar thin-panels. First, we compare the results of SGBC-CNTD with analytical results and the face-centered implementation of NIBC [Flintoft-2012] [Flintoft-2014, AEG Vulture], which also employs a digital filter (DigFilt) time-integration scheme to deal with LTI relation of the fields at each side of the panel.

First, the error of the SGBC-CNTD algorithm has been assessed in Fig. 4.9 which shows the relative error as a function of PPW_{fine} for several values of PPW_{coarse} . To accomplish this, the test-setup on Fig. 2.12 is used, the thin-panel is chosen with $1/Q = 10^3$ and a thickness of 1 wavelength (roughly 2π times the skin-depth). It can be noted that, the larger PPW_{fine} becomes (for a fixed frequency value) the smaller error of SE until it reaches a constant plateau when the PPW_{coarse} dominates over PPW_{fine} .

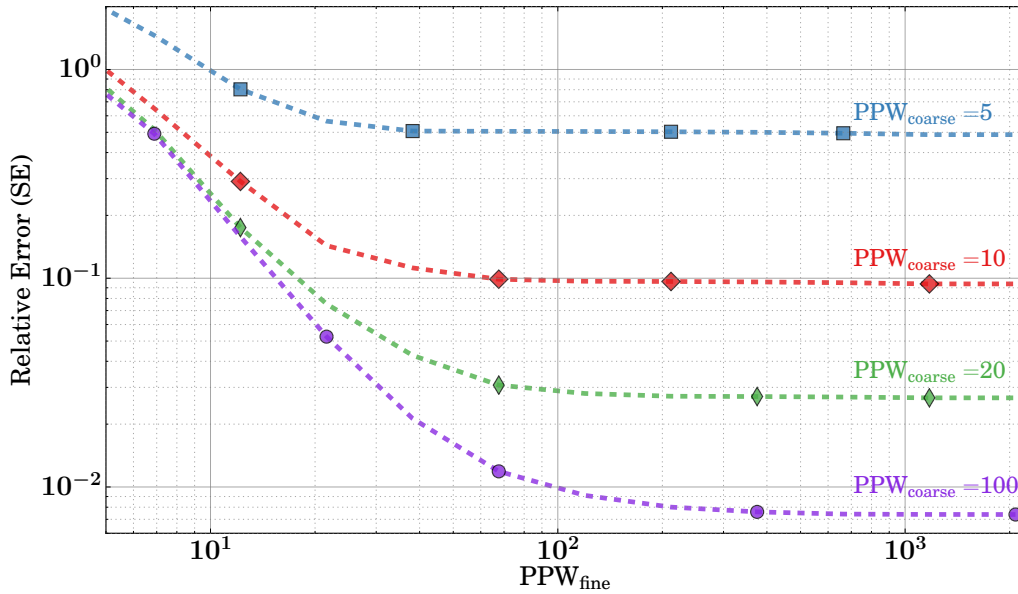


Figure 4.9: Error in the shielding effectiveness ($SE = S_{12}^{-1}$) for a uniform normally incident plane-wave on a conductive thin-panel for SGBC-CNTD using several coarse resolutions. This error is found by $|SE_{\text{sim}} - SE_{\text{teo}}|/SE_{\text{teo}}$, with SE_{sim} and SE_{teo} being the simulation and analytical values.

Now, we find the SE for an infinite aluminum planar panel with a conductivity $\sigma = 3.456 \cdot 10^7$ S/m and a thickness $th = 0.3$ mm under plane-wave incidence. A uniform spatial mesh with $\Delta = 2.5$ mm is used for the free space region, and the set-up is illuminated by a Gaussian pulse excitation with -3 dB decay in amplitude at 1GHz ($f(t) = e^{-(t-t_0)^2/w^2}$, $t_0 = 0.696$ ns, $w = 0.187$ ns.). Results for a 56th order DigFilt and several SGBC are shown

in Fig. 4.10. As expected, the stability condition, even for the 40-layers case does not need any time-step reduction compared to the usual 3D-FDTD one.

Another test case which is representative for low conductivity materials has been simulated, also under plane-wave normal incidence. The panel has a constant conductivity of 10^4 S/m and a thickness of 10 mm. The results are shown in Fig. 4.11. A three-layer slab has also been simulated, with outer layers having $\sigma = 10^4$ S/m and a thickness of 0.92 mm and the middle one being a lossless thick material of 10 mm (mimicking a low-density honeycomb). Results are shown in Fig. 4.12.

We have also included, for reference, results found with the classical Maloney approach [Maloney-1992], which can be regarded as a kind of 1-layer SGBC with extra degrees of freedom to account for the electric-field normal components at the interface, which do not have any influence on this problem due to the assumption of normal propagation inside the thin-panel. As expected, Maloney's method fails to catch the skin-depth effect, because of this assumption of constant field inside the thin-panel.

Lastly, another validation has been performed with the prediction of the shielding effectiveness (SE) of a planar thin-panel under normal plane-wave incidence (Fig. 4.13). A constant conductivity of 10^4 S/m and a width of 0.92 mm has been assumed. Results for a 4th-order vector-fitted NIBC model and a 4-layer SGBC are shown. Note that $\Delta_{\text{fine}} = 0.92/4$ mm yields more than 10 cells/wavelength resolution inside the thin-panel for $f < 200$ MHz, which is the maximum frequency of interest, and that the skin-depth at that frequency is 0.36 mm (smaller than the thin-panel thickness). However, results in Fig. 4.13 show that this limit can be pushed further and continue to be accurate even up to 1 GHz.

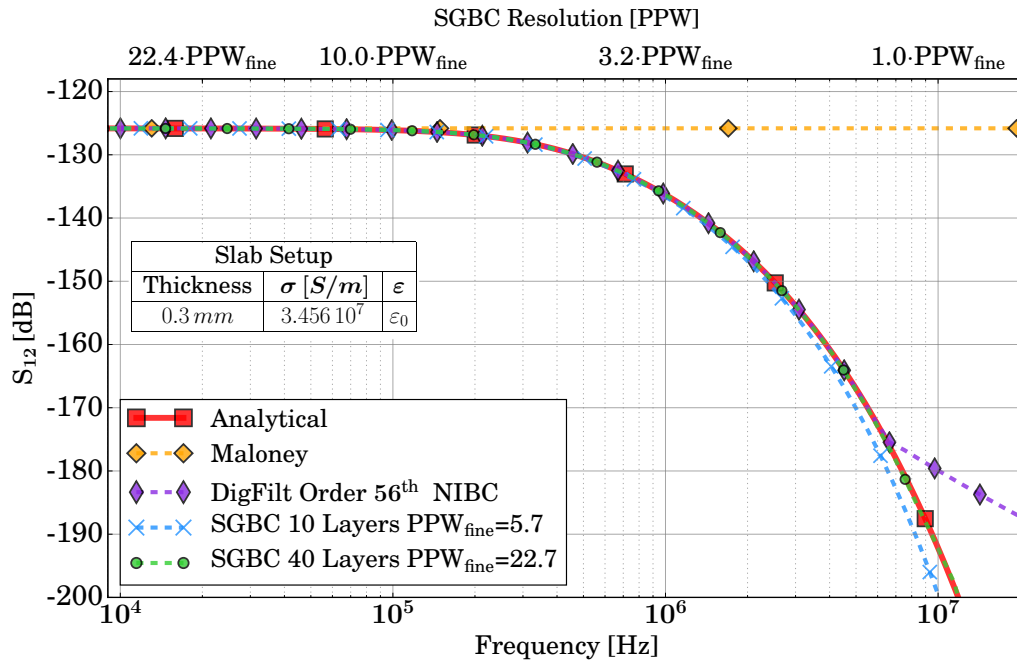


Figure 4.10: $S_{12} = SE^{-1}$ for an aluminum planar thin-panel with a conductivity $\sigma = 3.456 \cdot 10^7$ S/m and a thickness $th = 0.3$ mm. Space step $\Delta_{\text{coarse}} = 2.5$ mm. Moved to put in citation order

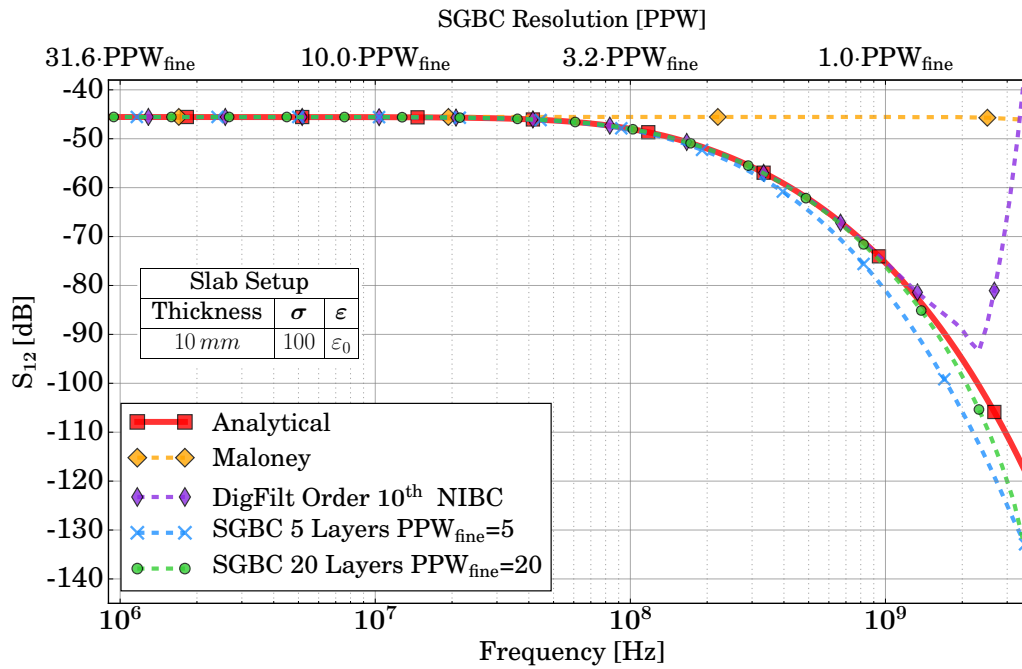


Figure 4.11: $S_{12} = SE^{-1}$ for an infinite homogeneous planar thin-panel, with $\sigma = 100$ S/m, and thickness $th = 10$ mm. Space step $\Delta_{\text{coarse}} = 20$ mm.

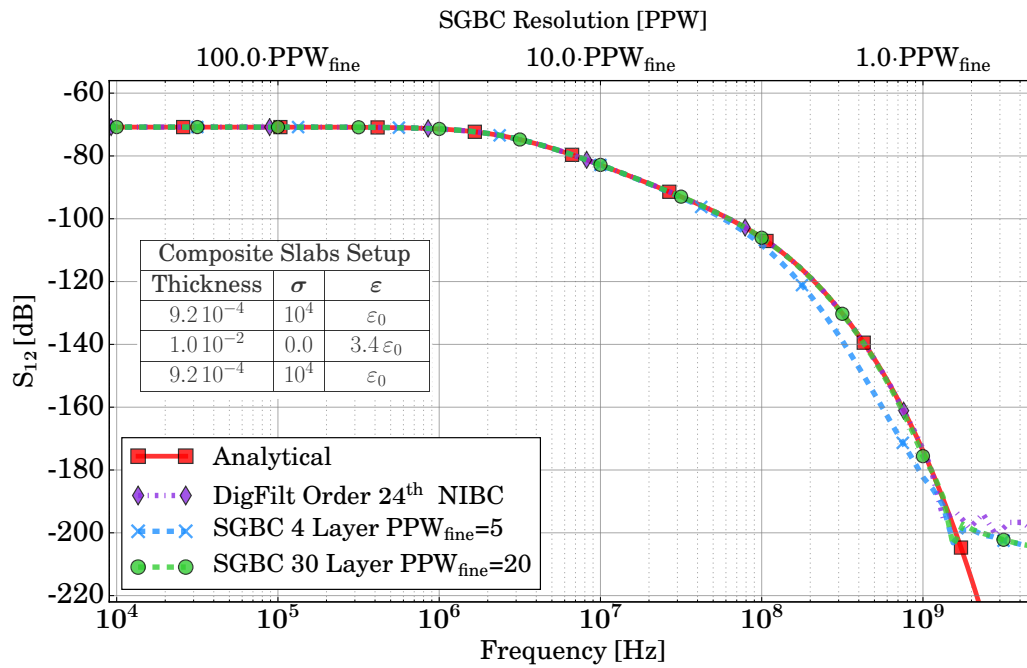


Figure 4.12: $S_{12} = SE^{-1}$ for an infinite 3-layer planar thin-panel. Space step $\Delta_{\text{coarse}} = 20$ mm.

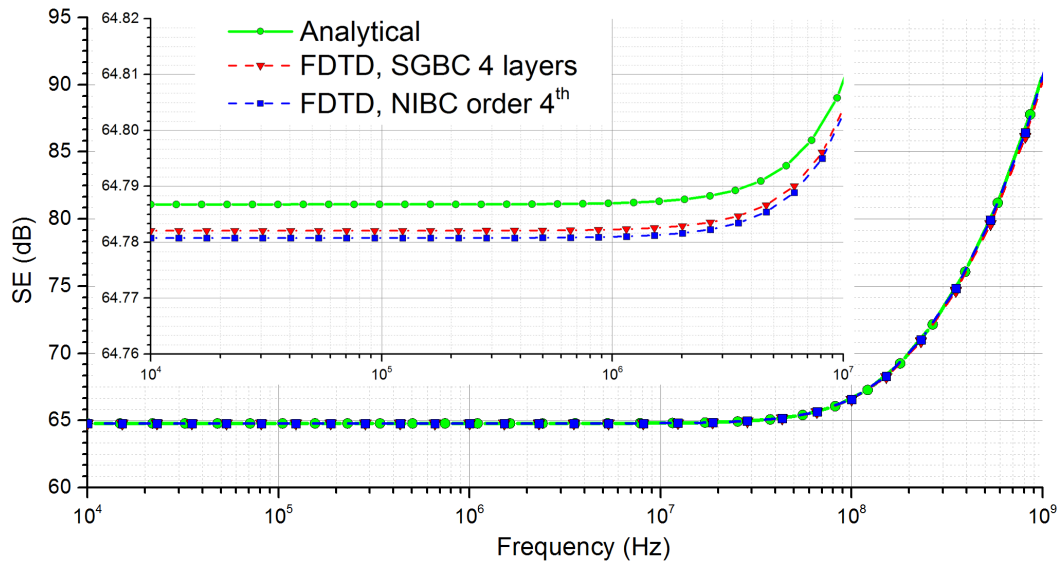


Figure 4.13: SE of an indefinite planar thin-panel with a constant conductivity of 10^4 S/m and a width of 0.92 mm. The inset shows a zoom of the planar part. The mesh sizes are $\Delta_{\text{fine}} = 6$ mm, $\Delta_{\text{fine}} = 0.92/4$ mm.

4.2.2 Shielding effectiveness of dispersive panels

A validation of for arbitrarily dispersive thin panels is shown in this section. For this, we use an indefinite panel of prepreg copper mesh Fig. 4.14, proposed in [Sarto-2014, S1 test-case], and whose S-parameters have been found by the approximate formulation derived of its microscopic structure [Wait-1955] [Sarto-2014]. It has been modeled using the procedure in the Section 2.6.3. The constitutive parameters of the equivalent homogeneous material have been vector-fitted with a 10th order pole-residue expansion Fig. 4.15. We have simulated a thin-panel of this material under plane-wave TE incidence, taking 10 cells for its 100 μm thickness. Results for SE are shown in Fig. 4.16, simulated both with CNTD-ADE and FDTD-ADE. They perfectly match the analytical ones, and reasonably agree with experimental measurements from [Sarto-2014].

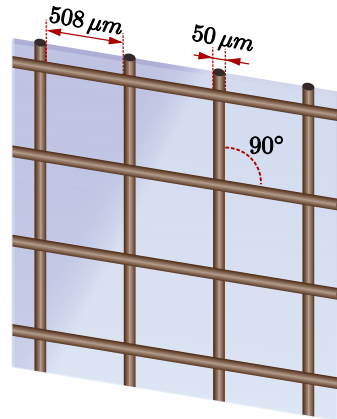


Figure 4.14: Microscopic structure of prepreg copper mesh.

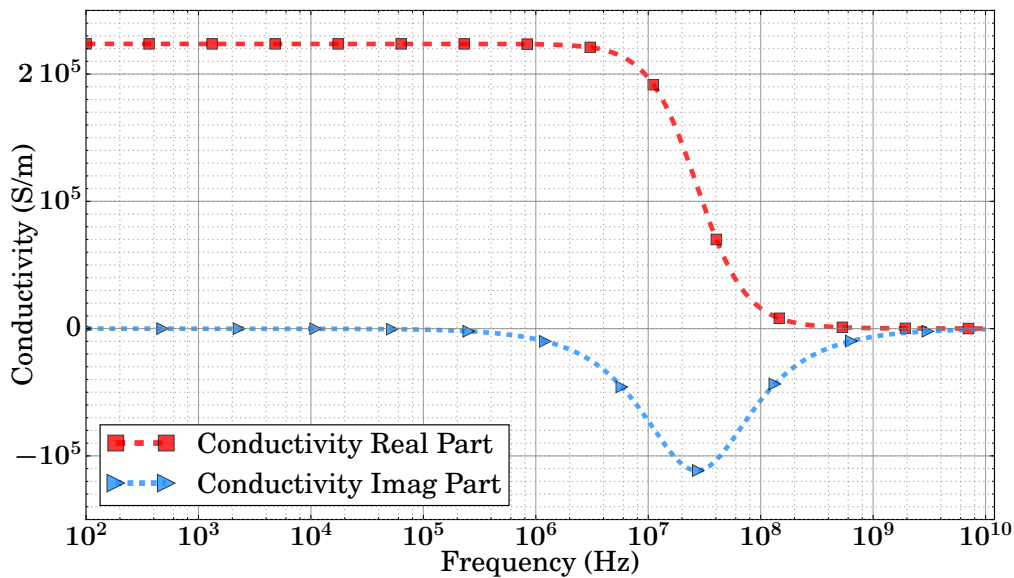


Figure 4.15: Estimated real and imaginary part of the conductivity for an homogeneous equivalent panel of the prepreg copper mesh panel.

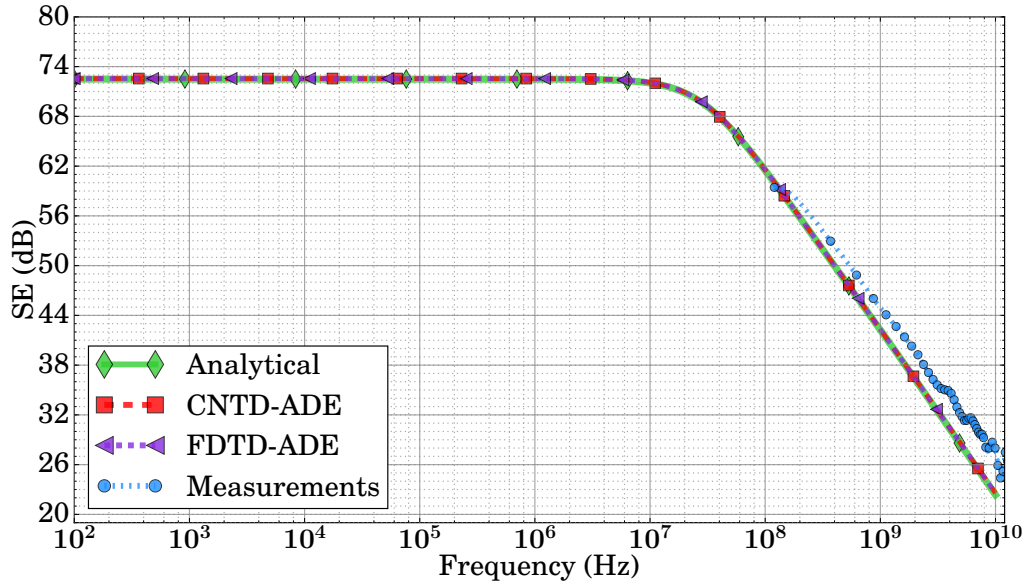


Figure 4.16: Simulated and measurement TE-SE for the equivalent thin panel of thickness of $100 \mu\text{m}$.

4.2.3 Shielding effectiveness of a sphere

One important topic within EMC concerns the study of the SE of enclosures. In this section, the thin-panel methods proposed earlier in this dissertation (SGBC, NIBC) are applied to the study of the SE at the center of a conductive spherical shell. For this purpose, a sphere of 1 meter radius is used with two configurations of conductivity and thickness, as illustrated in Tab. 4.3

	Conductivity	Thickness
Test Case 1 (Low skin-depth)	200 S/m	5 mm
Test Case 2 (High skin-depth)	10^3 S/m	1 mm

Table 4.3: Configuration proposed for evaluating the SE of a spherical shell.

The grid consists on cubic cells with $\Delta = 20$ mm of length. The time-step corresponds to CFLN = 0.9. PML are used as ABC, and a uniform plane-wave with grid-aligned incidence and Gaussian profile is employed. The value of SE is obtained at the center of the sphere:

$$SE_{\text{dB}}(f) = 20 \log \frac{\sqrt{E_x(f)E_x(f)^* + E_y(f)E_y(f)^* + E_z(f)E_z(f)^*}}{\sqrt{E_{\text{inc}}(f)E_{\text{inc}}(f)^*}} \quad (4.9)$$

where (*) denotes the complex conjugate, E_{inc} is the amplitude of the incident field, and $E_{x,y,z}$ are the field-components measured at the center of the sphere.

The results for each configuration of Tab. 4.3 are shown in Fig. 4.17 and Fig. 4.18. The RMS error as a figure of merit for the different methods, is illustrated in Tab. 4.4 and Tab. 4.5. An excellent agreement between NIBC and SGBC is found, with the mismatch between the

Mesh type	Thin-Panel method	Error RMS [$10^6, 10^8$] Hz	Error RMS [$10^8, 5 \cdot 10^9$] Hz	Error [dB] at 70 MHz
CRDM ($F_{rlx} = 0.2$)	SGBC (PPW=1)	2.3	25.4	2.6
CRDM ($F_{rlx} = 0.2$)	SGBC (PPW=8)	1.2	8.2	1.3
CRDM ($F_{rlx} = 0.2$)	NIBC (4 th order)	1.1	18.7	1.0
Staircase	SGBC (PPW=8)	5.2	9.23	5.3

Table 4.4: Error RMS estimate for a spherical shell with, $\sigma = 200\text{S/m}$, $Th = 5\text{mm}$, $F_{rlx} = 0.2$, $CFLN = 0.9$

Mesh type	Thin-Panel method	Error RMS [$10^6, 10^8$] Hz	Error RMS [$10^8, 10^9$] Hz	Error [dB] at 70 MHz
CRDM ($F_{rlx} = 0.2$)	SGBC (PPW=3)	1.3	1.7	1.2
CRDM ($F_{rlx} = 0.2$)	NIBC (8 th order)	1.1	1.8	1.0
Staircase	SGBC (PPW=8)	5.1	5.8	5.2

Table 4.5: Error RMS estimate for a spherical shell with, $\sigma = 10^3\text{S/m}$, $Th = 1\text{mm}$, $F_{rlx} = 0.2$, $CFLN = 0.9$

analytical and staircase results fully attributable to staircasing effects. This staircasing effect typically appears as a constant offset level in the results of (4 – 6) dB. As can be appreciated, when using a conformal approach, this offset level is lessened up to 1 dB. Analytical results from [Tesche-2008, Ansarizadeh-2013] are used for comparison.

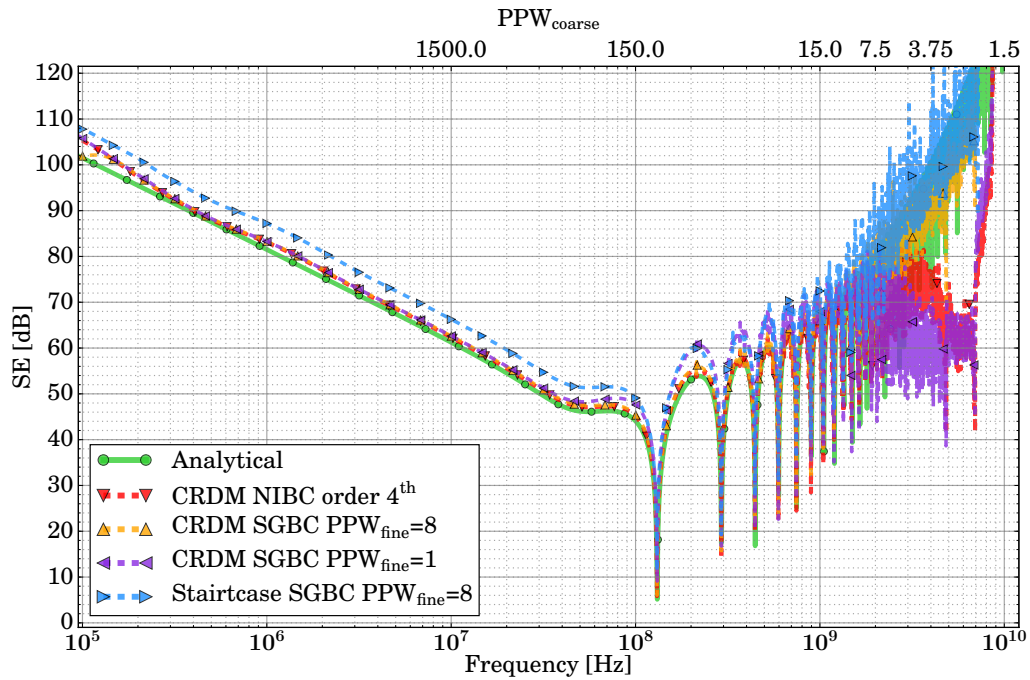


Figure 4.17: SE for an sphere of radius 1m, 200 S/m conductivity and 5 mm thickness (Low skin-depth).

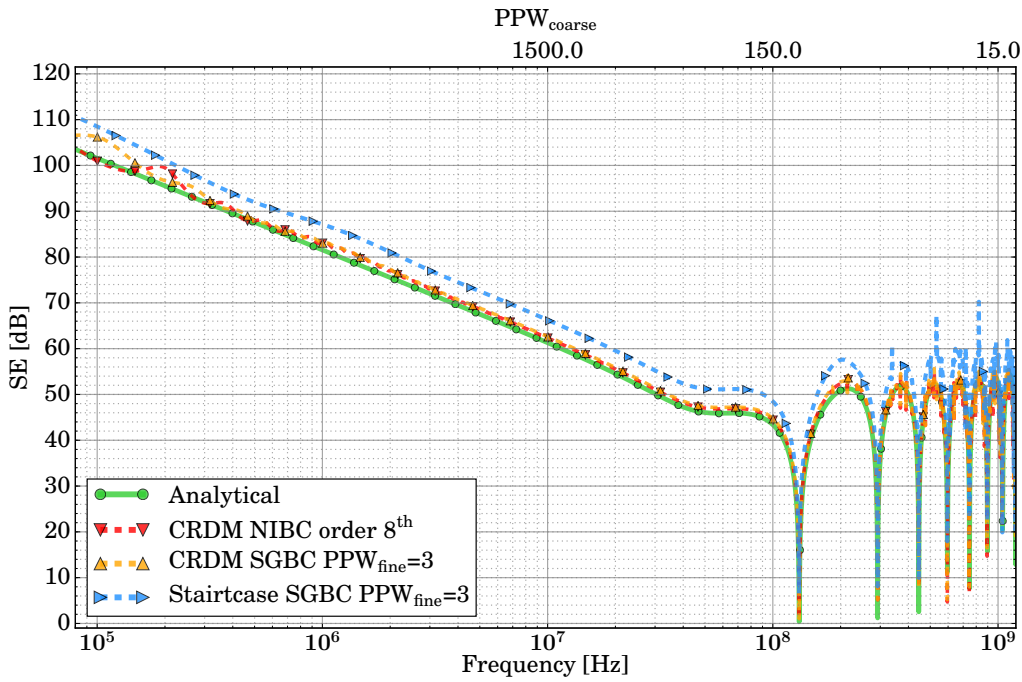


Figure 4.18: SE for an sphere of radius 1m, 10^3 S/m conductivity and 1 mm thickness (High skin-depth).

4.2.4 Resistance of thin strips

The accuracy of the SGBC and NIBC method in the prediction of low-frequency (DC) resistance of low-conductivity strips has also been assessed with the test-setup Fig. 4.19, and compared to an analytical value

$$R_{DC,teo} = \frac{1}{\sigma} \frac{L_S}{w \text{th}} \quad (4.10)$$

where L_S , is the length, w is the width and th is the thickness of a conductor strip.

The conductor strip under test is connected at each end to an external U-shaped set of PEC strips excited by a set of hard electric nodal sources at the gap, see Fig. 4.19. The conductor is modeled using the SGBC and NIBC methods.

The source is modeled with a quasi-DC profile, with a very low frequency transient part. The resistance is computed by dividing the value of the gap-voltage and the bulk current I_{BC} computed by a line integral around patch enclosing the lossy strip $I_{BC} = \oint H \cdot dl$. The whole setup can be enclosed with no error inside a PEC cage, to speed up the calculations, since no error of reflections are introduced by these at the DC limit.

$$R_{DC,sim} = \frac{V_{\text{gap}}}{I_{BC}} = \frac{E_{\text{gap}} d_{\text{gap}}}{\oint H \cdot dl} \quad (4.11)$$

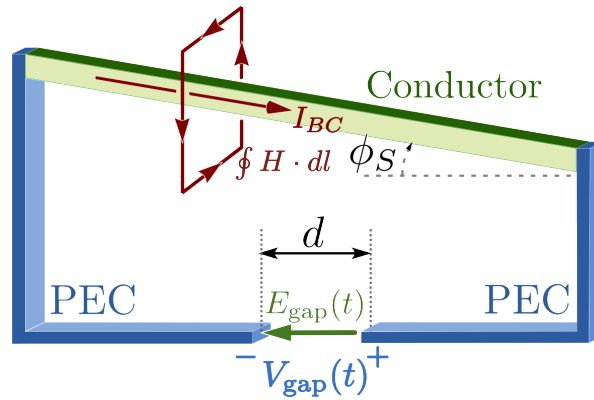


Figure 4.19: Test case for estimating the resistance.

Strip aligned with the grid

Here the methods for thin-panel (SGBC, NIBC, EP) are compared by using a straight strip aligned along one of the grid axis (Fig. 4.20), in order to avoid the staircasing effect of the structured mesh. A low-conductivity strip with $\sigma = 20\text{S/m}$, length $L_S = 216\text{mm}$, width $w = 120\text{mm}$, and thickness $\text{th} = 2\text{mm}$ has been used. A uniform spatial mesh with $\Delta = 6\text{mm}$ is used for the free space, and a quasi-DC source for the excitation. The current flowing across the material has been measured, for estimating the LF ohmic DC resistance by using (4.11). This is compared with an analytical value using (4.10)

$$R_{DC} = 45\Omega$$

The vector fitting procedure accurately yields the expected analytical value at direct current (DC)

$$Z = Z_\infty + \lim_{\omega \rightarrow 0} \sum_{k=1}^P \frac{r_k}{j\omega - p_k} = \frac{1}{\sigma \text{th}} = 25.0\Omega$$

for all the elements Z_{ij} of the Z -matrix (2.6). However, an error in R_{DC} around of 5% was found by DigFilt, whereas for SGBC the error was always under $10^{-3}\%$ as reflected in Table 4.6. The reason for this can be attributed to the more accurate manner in which SGBC handles material interfaces by means of the integral versions of Maxwell's equations, by the use of effective values (2.24) at the interfaces with the coarse mesh.

Strip not aligned with the grid

Issues derived by the use of staircased meshes can be revealed with objects which are curved or are not aligned with the grid axis. The irremediable degradation of the material lengths will ultimately affect the value of the resistance. The use of conformal methods solves these issues because they approximate better the physical lengths. To assess this, a conductive thin strip slanted by an angle ϕ_s respect to the grid axis has been used (Fig. 4.21).

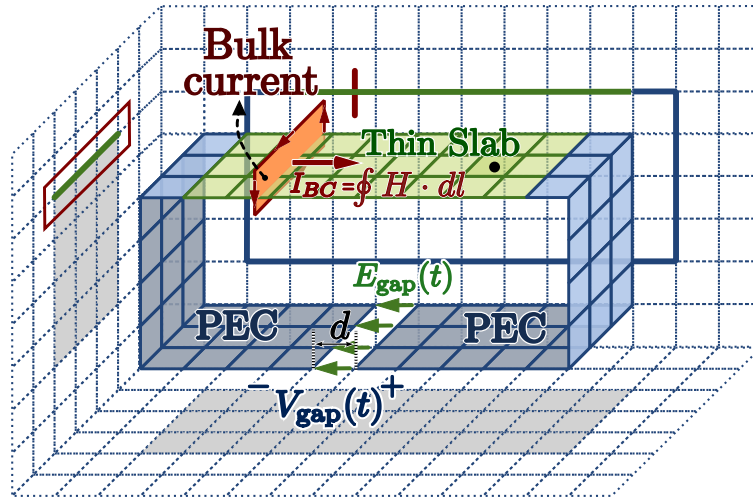


Figure 4.20: Test-setup to the computation of the resistance at LF for a conductive thin strip aligned with the grid.

Method	Error in R_{DC}
Pure Maloney	$< 10^{-3}\%$
SGBC 1 layers	$1.17 \cdot 10^{-4}\%$
SGBC 4 layers	$9.62 \cdot 10^{-5}\%$
DigFilt NIBC	5.294%

Table 4.6: Errors in DC prediction of a ($\sigma = 20S/m$), 216mm long \times 120 mm width \times 2 mm thick meshed with $\Delta_{\text{coarse}} = 6mm$.

It should be noted that the error committed in the size representations by the structured mesh of a non-aligned strip is inherent to the existence of the directions privileged by the grid and therefore is independent of the spatial resolution. The error measure, labeled as *Structured Theoretical* and shown on Fig. 4.22 is calculated by using in equation (4.10) with the notion of Manhattan distance, defined in (3.14), which is for the structured case on Fig. 4.21

$$L_{S,\text{str}} = L_S(\sin \phi_s + \cos \phi_s) \implies R_{DC,\text{str}} = \frac{1}{\sigma} \frac{L_S(\sin \phi_s + \cos \phi_s)}{W \text{ th}} \quad (4.12)$$

For each simulation, the scheme on Fig. 4.21 is utilized with a fixed angle; the voltage in the gap is imposed using a delta-gap source, the current is measured around the conductor using a bulk-current probe similarly to Fig. 4.20, finally the resistance at LF is found by (4.11). For the conductive thin strip we have chosen: $\sigma = 20S/m$ of conductivity, $L_S = (216\text{mm}/\cos \phi_s)$ of length, $w = 120\text{mm}$ of width, and thickness of $\text{th} = 2\text{mm}$.

The relative error of the resistance at LF as a function of the tilted angle is illustrated in Fig. 4.22 both for conformal and structured meshes. It is worth to note that the error for the structured mesh behaves similarly to its theoretical estimate (4.21), which does not

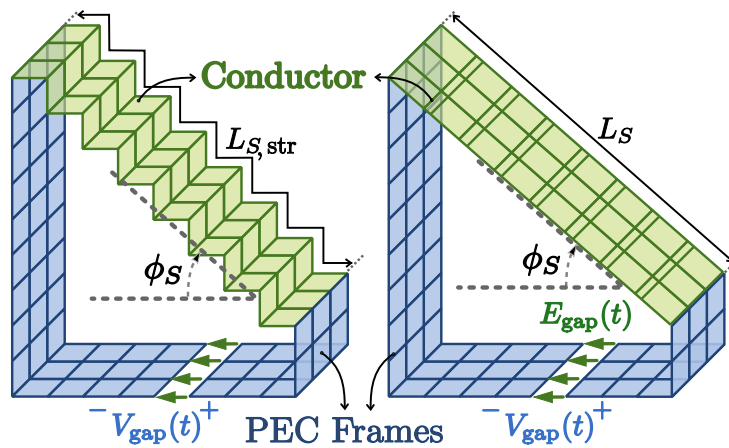


Figure 4.21: Test-setup to the computation of the resistance at LF for a conductive thin strip slanted a angle ϕ_S respect to the grid.

appear when a conformal mesh is used. This shows that this defect is dominated by the mesh adaptation and not because of the accuracy of thin-panel algorithms (NIBC and SGBC).

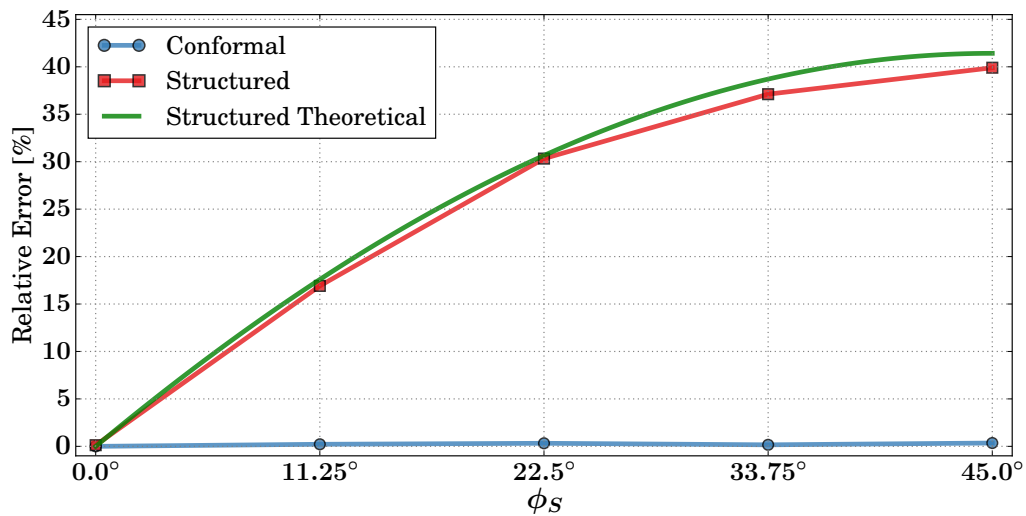


Figure 4.22: Error in the LF resistance as function of the tilted angle with respect to the grid. Conformal results were obtained with NIBC and SGBC algorithms which are identical.

AERONAUTICAL APPLICATIONS

Modern AVs fully rely on complex electronic systems for their functioning, thus making EMC assessment a major safety concern. As carbon fiber composite (CFC) materials are more used to meet strong, light-weight structural requirements, AVs become increasingly susceptible to EMI due to the poorer conductive capabilities of CFCs compared to conventional metallic materials. From the EMC point of view, the main EM threats for an aircraft can be summarized as follows:

- **Lightning indirect effects (LIE):** 0-50 MHz. These are caused by the electric current flowing through the structure and internal wiring as a result of the impact of lightning. Current trends in aircraft manufacturing industry to increase the use of CFC, carbon fiber reinforced composite (CFRC), composite fiber reinforced plastic (CFRP), have made harder for them to provide protection of critical avionic devices against LIE [Meyer-2008].
- **High intensity radiated field (HIRF):** 10 kHz-18 GHz. Due to artificial intentional or unintentional external/internal radio frequency (RF) sources such as TV, mobile, 3G, 4G, 5G, modern radar, GNSS, etc.. Nowadays, the on-board aircraft electrical and electronic equipment has become more vulnerable to adverse effects originating from these sources. Mainly because of their increasing role to perform and automatize flight/landing task, and the reduction in the electromagnetic shielding provided by new composite materials.
- **Non-nuclear electromagnetic pulse (NN-EMP):** 0-100 MHz. This is a type of intentional destructive electromagnetic hazard. Most low-level EMP generators do not pull enough energy to produce permanent damage. However, novel devices are able to involve much higher power levels, with extremely short durations, that can cause computers and networks to crash, hang, or reboot; thus yielding a temporary disruptive effect [Radasky-2004]. These modern weapons (also named E-bombs), are becoming

cheaper and susceptible of being used in terrorist acts. Low frequency E-bombs can have effects similar to those of a lightning strike.

In all these cases, as a result of the exposition to the EM hazard, transient currents flow along the aircraft surface creating an EM field which penetrates the fuselage through apertures such as windows, or by diffusion through parts made of composite materials. Inside the aircraft, these transients can overcome the immunity limits of the equipment, generating failures and/or damage, and compromising its safety.

A main role of certification authorities is to define the requirements of protection of civil and military aircrafts to prevent possible critical effects. For this, three types of aircraft test scenarios are considered for in the well-known [ED–2010] aircraft certification guide:

- **Low-level direct drive (LLDD):** In this test, a current injected directly on the fuselage plays the role of the EM source (Fig. 5.1). The fundamental aim is to find either the current coupled to the internal cables, or the internal RF fields, normalized to the injected current. This test, applied in Section 5.2 to the SIVA an UAV, is suited to deal both with HIRF and lightning, and is proposed in the certification guide [ED–2010, section 6.4.2].

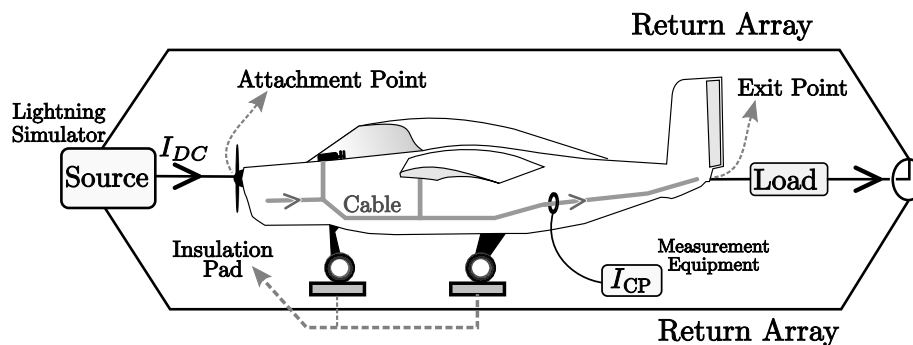


Figure 5.1: Typical direct current injection (DCI) test in nose/tail layout.

- **Radiated test :** In this test, the aircraft is illuminated by radiating antennas. The specific position and the number of antennas depend upon the aircraft widespread, apertures (entry points), and the position of the system under test. Regardless of these, the selected positions must be such that the system under interest is representative of the worst coupling case [ED–2010, section 6.3.5]. This type of test has been applied for a simplified model of an EV55-aircraft in Section 5.1, on which the transfer function of the currents along the cables, and the tangential magnetic fields on the fuselage at external points, are assessed.
- **Tests in a reverberation chamber:** The use of a reverberation chamber is considered by [ED–2010, section 6.3.6] as an alternative to the illumination by sequential antenna

positions. Also the reverberant chambers are used for system tests in order to yield a statistical EM environment, and to avoid deterministic results. In this chapter, this test is used in order to get the SE at several critical points around the FADEC of a nacelle (Section 5.3).

These tests are used to estimate the transfer function relating the external sources (RF fields or injected currents) to, either induced cable currents, or internal fields. The transfer functions are used to scale the internal effects when the aircraft is exposed to the appropriate external environment (high intensity radiated field (HIRF), lightning).

In this chapter, we show representative results found in these three scenarios, comparing experimental data (or data found with other numerical techniques), with results found with FDTD incorporating the techniques described in previous chapters of this dissertation to cope with materials and curvature in an accurate manner: SGBC, CRDM, LECT.

5.1 EV55: a numerical test-case to assess HIRF effects

In this section, the HIRF effects on an aircraft are studied by employing a numerical test-case based on a modified version of an EV55 aircraft¹ that was proposed as a cross-validation workbench in the HIRF-SE project.

5.1.1 Simulation approach and results

The dimensions of the model used for this aircraft are $16.5897 \times 4.4253 \times 16.1072$ m. The model also includes a generic part of the cabling inside (Fig. 5.2 and Fig. 5.3). The fuselage is assumed to be a PEC, and just the shield of the cable-enclosure has been modeled with a cylindrical cross section of 30 mm of radius, a per unit length (p.u.l.) resistance of $1.263 \cdot 10^{-3} \Omega/\text{m}$, and a thickness of 2 mm. The SGBC technique has been employed to deal with the coupling of the EM environment inside the lossy shield². The aircraft is radiated with a plane-wave with Gaussian amplitude decaying -3 dB at 3 GHz, and with propagation-direction and polarization with respect to the aircraft shown in Fig. 5.2.

Probes at two points (Fig. 5.3) have been selected to compare conformal and staircased simulations with results found using a DGTD method [Alvarez-2012b]. A bulk-current probe around the inner wire, tagged as *EK003*, close to the apertures on the fuselage, and a tangential magnetic field probe tagged as *STP4* placed on the external side of a wing. The time domain results for those probes are transformed in frequency domain, and normalized

¹The EV55-aircraft geometry presented in this thesis has been provided by EVEKTOR under the HIRF-SE project.

²The final objective of HIRF is to find the transfer function for each wire as the ratio of the induced current over the external field. However, we have just restricted ourselves in this test-case to the prediction of the currents flowing along the shield, though UGRFDTD also counts with wire models to find the transfer function at internal wire level.

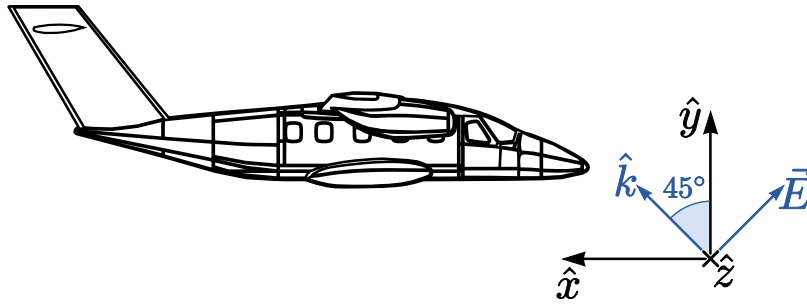


Figure 5.2: Plane-wave polarization and propagation direction.

to the incident plane-wave amplitude, in order to obtain the *transfer functions*³. For the simulation, a grid of cubic cells is used to create the simulation mesh, with a space-step of 12mm for the structured case, and 24mm with a relaxed factor of 0.3 for the conformal case. The time step is chosen for each case by fixing a value of 0.8 for the CFLN. The computation domain is truncated by PML absorbing boundary conditions.

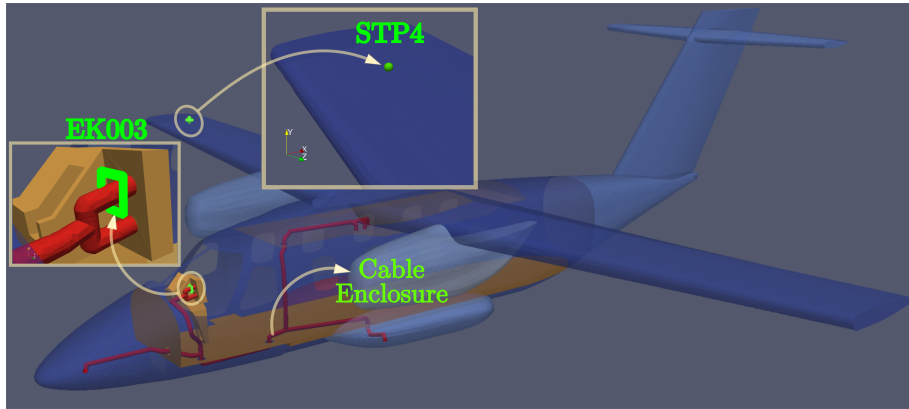


Figure 5.3: Location of the surface magnetic field-probes, and cable bulk current-probes.

The transfer function for the bulk current at EK003 is evaluated as

$$\text{TF}_{\text{EK003}}(f) = \frac{I_{\text{BC}}(f)}{E_{\text{PW}}(f)} \quad (5.1)$$

where E_{PW} is the plane-wave amplitude, and I_{BC} is the current induced in the bundle shield calculated with a closed-loop line-integral of the magnetic fields around its section

$$I_{\text{BC}} = \oint \vec{H} \cdot d\vec{l} \quad (5.2)$$

Similarly, the transfer function at STP4 is evaluated as

$$\text{TF}_{\text{STP4}}(f) = \frac{H_{\text{STP4,S}}(f)}{H_{\text{PW}}(f)} \quad (5.3)$$

³The Transfer function in dBs is in general defined as 20 times the decimal logarithm of the ratio of a electrical output of a system to the electrical input of a system in the frequency domain.

where $H_{\text{STP4,S}}(f)$ denotes the modulus of the tangential component of the magnetic field at STP4, and H_{PW} is the amplitude of the magnetic field of the plane-wave.

In Fig. 5.4, Fig. 5.5, and Fig. 5.6 we show results found by the conformal and SGBC methods presented in this dissertation, compared to results obtained by DGTD, well-known for its MoM-like accuracy [Alvarez-2012b]. Results obtained with a structured-FDTD popular commercial solver, are also shown for reference.

5.1.2 Discussion

Typically, the HIRF frequency-domain behavior is divided into three frequency bands, according to the usual electric size of an aircraft and its apertures. Each band produces different electromagnetic coupling effects inside and around the fuselage:

- **Low Frequency:** (10KHz, 50MHz). In this region, there are not resonances inside because field penetration into the fuselage is low, behaving as a cavity under its cut-off frequency, and the external radiated wave induces strong surface currents on its skin. This effect can be appreciated on the Fig. 5.4 for frequencies lower than 40MHz.

Actually, an aircraft at low-frequency can be considered as a simple LR series circuit driven by a voltage source [Rasek-2011, Schröder-2014, Rasek-2015], with a "cut-off" frequency provided by:

$$f_{\text{cut-off}} = \frac{R}{2\pi L} \quad (5.4)$$

The DC-voltage source level is given as a function of the incident-field amplitude, and the geometry and position with respect to the apertures of the aircraft, such as the windows. The resistance is given by the conductivity and dimensions (length and section) of the cable and its loads, and the inductance is given by the cable dimension (length and radius) and the distance of the cable to the current-return (e.g., the fuselage). Typically the inductive part is masked by low-resistive behavior (low-loss cables, or cables directly grounded to the fuselage). Hence, the cut-off frequency (5.4) is small, and only a planar trend in the transfer function is observed under the first resonance. On the other hand, high-loss cables, or cables grounded to the fuselage through lumped loads –e.g. 50 Ohms-, or even ungrounded, are dominated by the inductive behavior (linear increasing transfer function with a 20 dB/decade slope), before the constant resistive behavior eventually appears. Fig. 5.4 is representative of the first situation, since the cable has low losses and it is directly grounded to the fuselage.

It should be noted that, the results obtained by the conformal SGBC method are better, taking DGTD as a reference, than the structured-mesh ones, because the conformal

mesh is more precise reproducing the length and radius of the shield. This was already discussed in Section 4.2.4 in relation to the accuracy to the resistance estimation. This effect modify the plateau level of the transfer function at DC (Fig. 5.4).

- Medium Frequency: (10MHz, 100MHz) The apertures of the aircraft become more penetrable as frequency increases. The maximum coupling is reached at the first resonance of the aircraft structure or of the wiring. This normally occurs when the aircraft size or the wires length are a quarter or a half of the wavelength (Fig. 5.4).
- High Frequency: (100MHz, 20GHz), in this band, the penetration field into the fuselage is strong, and the surface current (jump between internal and external tangential magnetic field) on the fuselage-skin diminishes, as shown in Fig. 5.6. A large number of resonances are produced in the cable as shown in Fig. 5.5. The field that penetrates into the fuselage may create destructive and constructive interferences, as a reverberant chamber, that may even exceed the external field (very high peaks). This is a major potential risk of this band, which affects the aircraft electronics devices directly. Again, the conformal method proves to have better resolution in the position of the resonant frequencies, compared to the structured case, since they depend mainly on the geometrical fidelity of the mesh.

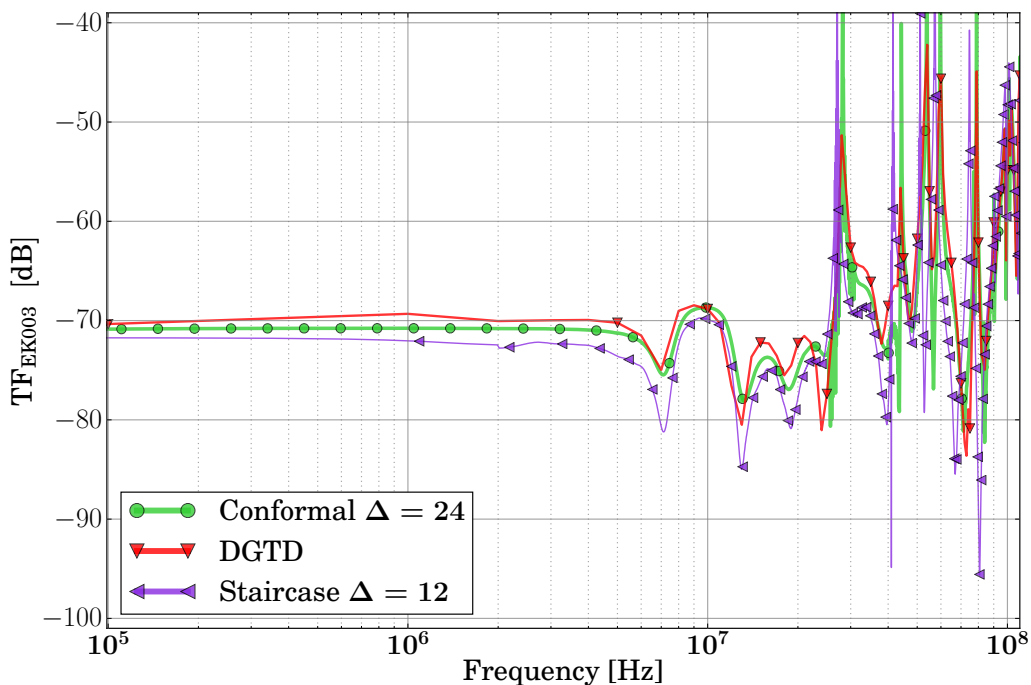


Figure 5.4: Transfer function at LF and MF, evaluated in EK0003 positions.

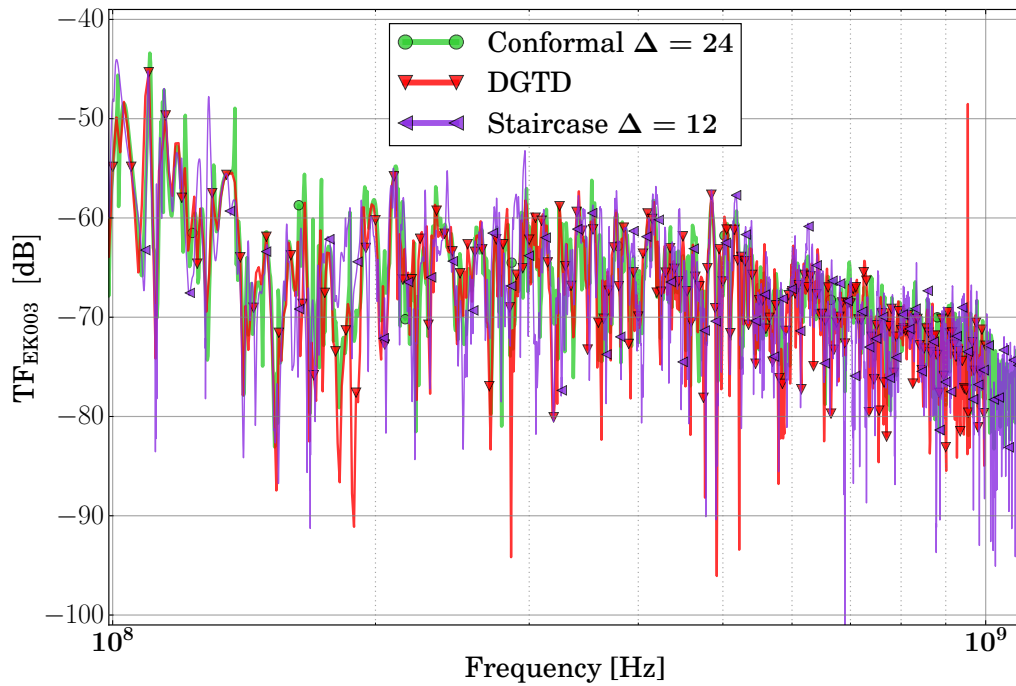


Figure 5.5: Transfer function at LF and MF, of the bulk current evaluated at EK0003.

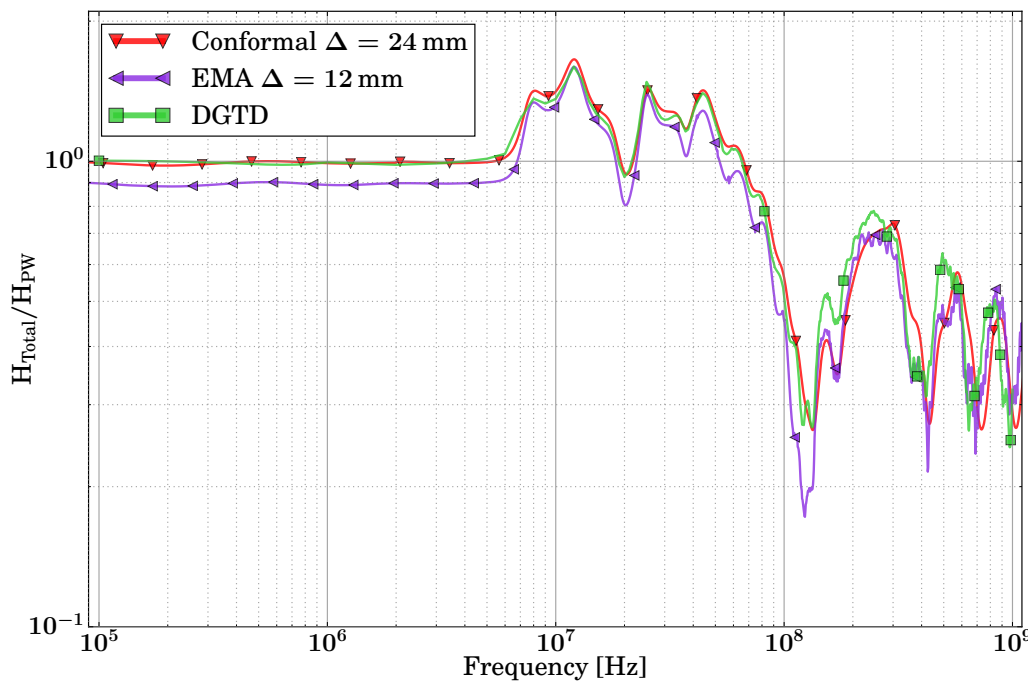


Figure 5.6: Transfer function evaluated of the magnetic field at STP4.

5.2 SIVA: a DCI test-case to assess LIE effects

This section presents the experimental arrangement for an integrated system of aerial vigilance (SIVA) UAV also described in [Cabello-2017b]. This set-up has been tested with the DCI procedure in a low-level direct drive (LLDD) setup [ED-2010] [Rasek-2008] (Fig. 5.1). Results are shown mainly for the lightning indirect effects (LIE) frequency band and compared to experimental data provided by INTA. The SIVA system consists on an UAV plus a ground-control station, which is made mostly of CFC and fiberglass, and has a wingspan of 5.81 m, a length of 4.025 m, and a height of 1.63 m Fig. 5.7.

For these UAVs, in the absence of large apertures, otherwise usual in typical aircrafts, the main mechanisms of EM energy entrance are due to apertures covered by fiberglass (radomes, fairings), hatches, joints, and hinges, and through the CFC materials themselves.

The process of building a numerical model computationally affordable, yet representative, of the full complexity, is described in this exercise. We complete it with a verification procedure based on the feature selective validation (FSV) IEEE standard implemented in the GVT tool of the Universitat Politècnica de Catalunya, which has been successfully employed in several scenarios for comparing sets of data [Gutierrez-2012, Alvarez-2012c, Alvarez-2012a, Romero-2012, Gutierrez-2014]. For these simulations, the SGBC and NIBC methods described in Chapter 3 have been employed to deal with the CFC skin in a structured-mesh model of the UAV.



Figure 5.7: DCI test setup using coaxial return of SIVA-UAV in INTA's Open Area Test Site (OATS).

5.2.1 Experimental setup

Experimental data for the DCI test setup of Fig. 5.1, Fig. 5.7 measured in INTA's Open Area Test Site (OATS) have been used for validation. The DCI test results are used to relate the bundle current to the surface current flowing along the aircraft skin, and it is one of the alternative tests used during the EMC certification process in the frequency range

from 10KHz to the first resonance frequency of the aircraft. In this case, we extended the measurement frequency range up to 200MHz. Concerning the test setup, the standard [ED–2010] recommends the design and construction of a coaxial return wire network where the UAV fuselage is considered the main conductor. The UAV was supported by polystyrene blocks. The distance between metal wires of the coaxial return was 30 cm and the distance from the UAV surface was 63 cm for the upper surface and 37 cm for the lower surface. The RF power was injected through 2 wires connected to the propeller screws. The injected current was measured and recorded for normalization of the surface currents, and the current induced on different cables installed inside the UAV. Most SIVA equipment was removed, keeping just four representative ones for our validation purposes: the flight termination control unit (FTCU), the power control unit (PCU), the Airbag Bottle and the wings lights, together with the three cable bundles routed among them.

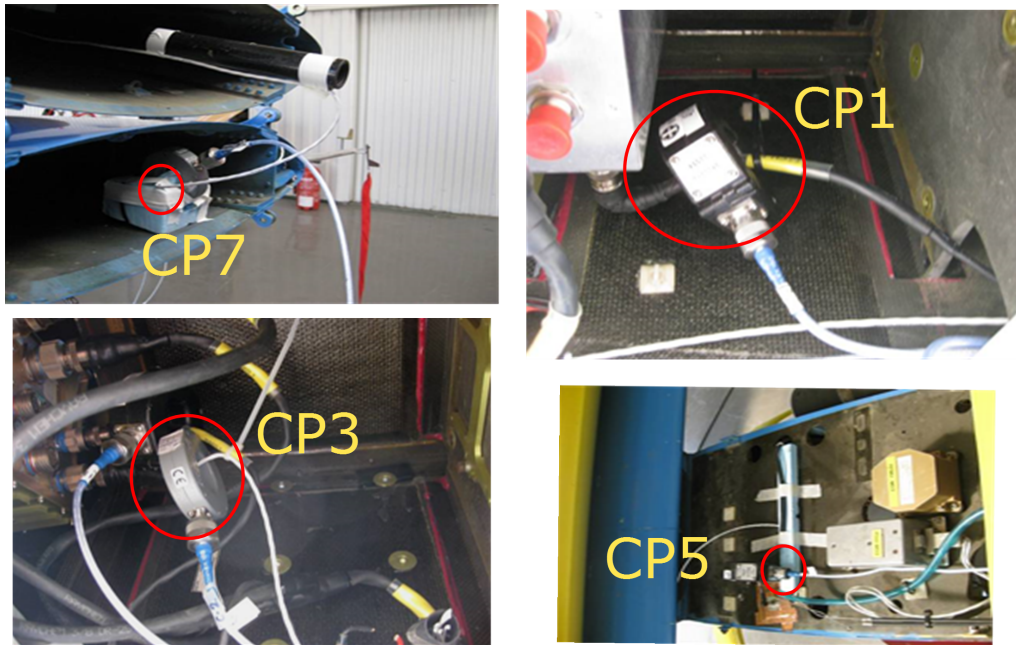


Figure 5.8: DCI probes: CP1, CP3, CP5, CP7.

5.2.2 Numerical approach

For the numerical procedures, a CATIA-V5 digital mock-up was taken as a starting point, including all the geometrical details and the whole test setup of Fig. 5.9a. However, the complexity of this original model is unnecessary for simulation purposes, and it was reduced by encompassing a de-featuring and simplification phase, to provide a model simple enough to be meshed and computed (Fig. 5.9b). A geometrical simplification is needed since the full digital mock-up cannot be directly treated by meshers or EM simulators. All the internal/external details representative from the EM viewpoint are kept, while very small

parts and details (holes, bolts, nuts) are removed. The complex surfaces are redefined by means of simpler ones [Gil-2011, Gutierrez-2012].

For this simplification procedure, mainly know-how and experience was used. In this case, the first step was to remove from the CATIA digital mock-up the SIVA equipment which had not been tested, and to apply the simplification procedure explained above. Secondly, from the simplified computer aided design (CAD) model, IGES files were generated and imported into the meshing tool. The structured-mesh cell-size must be small enough to represent properly the relevant details of the structure, and to solve the smallest wavelength (higher frequency) of interest, but large enough to yield a computationally affordable number of cells.

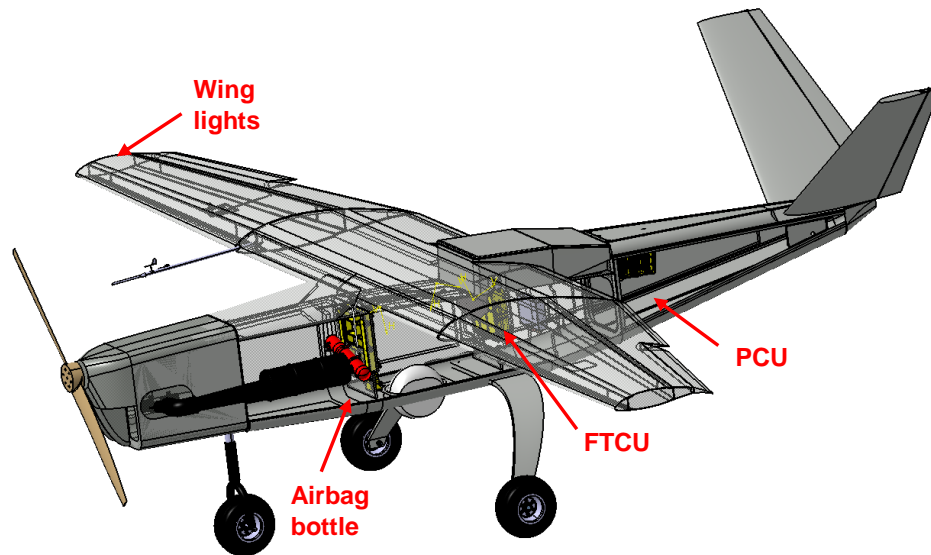
A model with 160 Mcells of size was finally yielded by using a uniform isotropic grid of 6 mm space-step, used to mesh the UAV, combined with a non-uniform one ending into a 20 mm space step at the convolutional perfectly matched layer (CPML) boundaries (some details of the mesh can be seen in Fig. 5.10). A maximum $CFLN = 0.75$ has been taken. This limit was actually imposed by the wire-bundle stability condition [Schmidt-2004]; a close-to-the-critical CFLN was shown to be stable by SGBC when cables were removed. CPML boundary conditions with 8 layers were employed. A total physical time of $20 \mu s$ (2.5 M-iterations) was simulated in the Alhambra-UGR Cluster in 32 CPUs at around 500 Mcells/second (around 10 days of CPU).

UAV Model

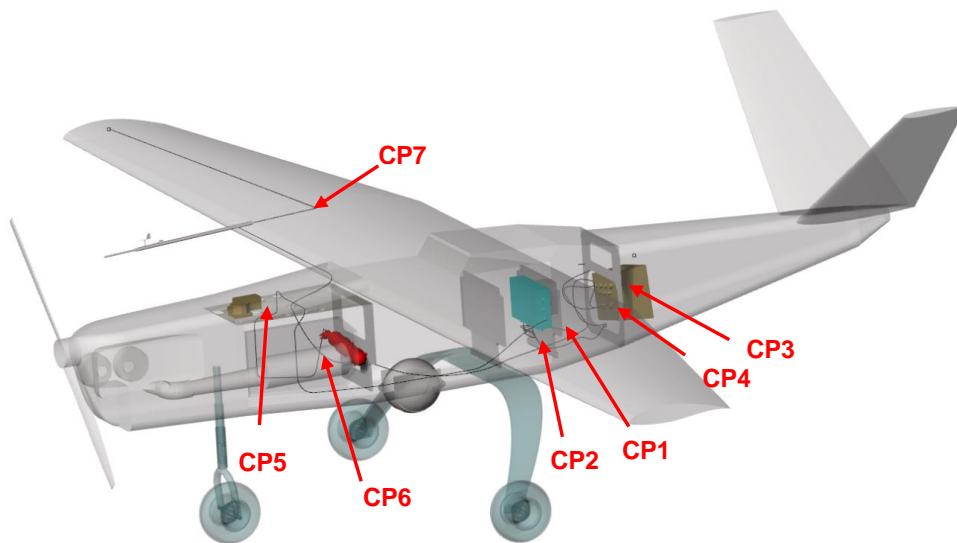
Regarding the materials, just CFC ones were maintained, while fiberglass ones were removed. The equipment PCU, FTCU, airbag bottle (fig.(5.9a)) have been modeled as PEC. The UAV skin is a CFC modeled with a constant conductivity of $10^4 S/m$, and an average thickness of 0.92 mm. The thin-panel models proposed in Chapter 2 have been employed to account for it. The SE of an indefinite panel of this material was already presented in Chapter 4.2 (shown in Fig. 4.13).

Simulations using both NIBC and SGBC were conducted. However, NIBC forced us to reduce the CFLN to 0.1 to get long-term stable results, and these were computed only until $2 \mu s$. Though they fully agree in time-domain with SGBC, they are not sufficiently converged to find correct frequency-domain results and, therefore they are not shown here.

In order to deal with cables and bundles inside the UAV, a multiconductor transmission line network (MTLN) thin-wire generalization [Berenger-2000] of the classical Holland's [Holland-1981] method, was used. The cables from the FTCU to igniter harness, and the cable from the wing light to the PCU were modeled in this way including resistive ending connectors.



(a) Original CAD model including all geometrical details.



(b) CAD model simplified after cleaning and including equipment and current probe locations.

Figure 5.9: Digital mock-up of the SIVA

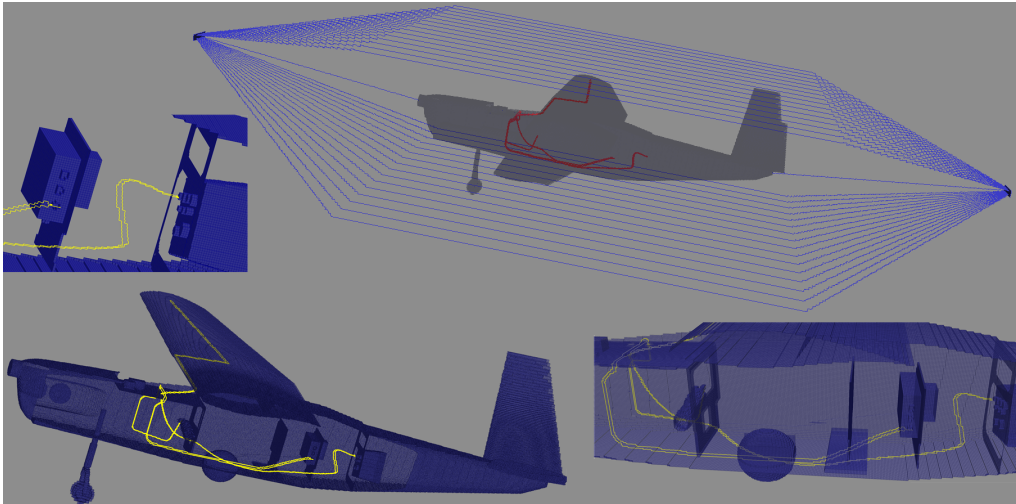


Figure 5.10: General and zoom views of final FDTD mesh. The upper right inset shows the DCI injection wires attached to the nose and tail of the UAV. In red the internal wire bundles.

DCI Layout approaches

For the numerical simulations of the DCI test, the current is directly injected through the cable at the attachment point Fig. 5.1. The cable at the exit point has a lumped resistance of 50Ω . A Gaussian signal with -3 dB decay at 400 MHz $f(t) = e^{-(t-t_0)^2/w^2}$, $t_0 = 10$ ns, $w = 46.8$ ns is fed as a voltage source in a thin wire located at the beginning of the coaxial return. The surfaces and lines of the coaxial return array had been modeled with PEC.

The ground effect is modeled by using a concrete dielectric insulation material in order to mimic the ground plane of the OATS facility [ED-2010, 6.4.3.2], though the results in this frequency range are insensitive to this, for being a DCI test-setup.

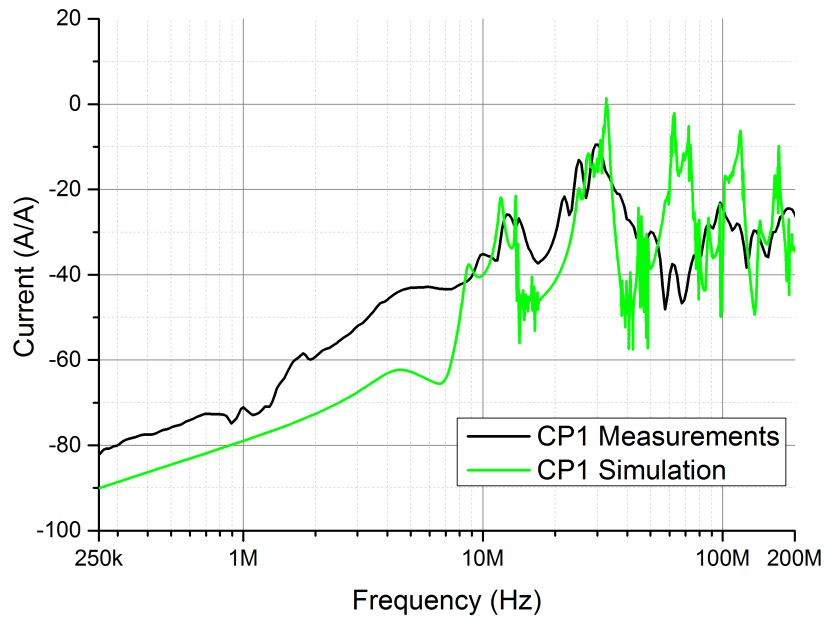
Results

The induced current at different probes (CP1, CP3, CP5, CP7) are evaluated (Fig. 5.9) and their values normalized in the frequency domain with respect to the injected current to find the transfer function:

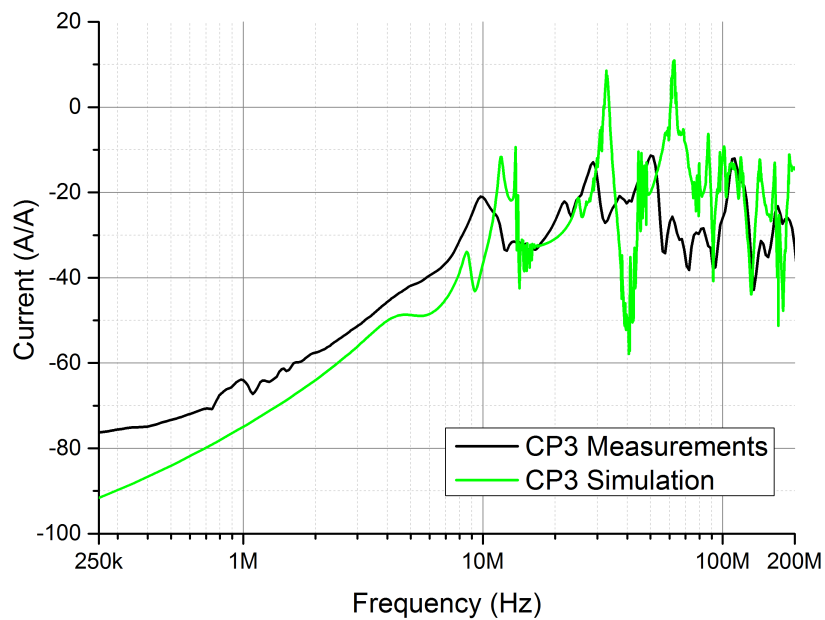
$$T_{CP1,3,5,7} = 20 \log \frac{|I_{CP1,3,5,7}|}{|I_{DC}|} \quad (5.5)$$

which are plot in Fig. 5.11.

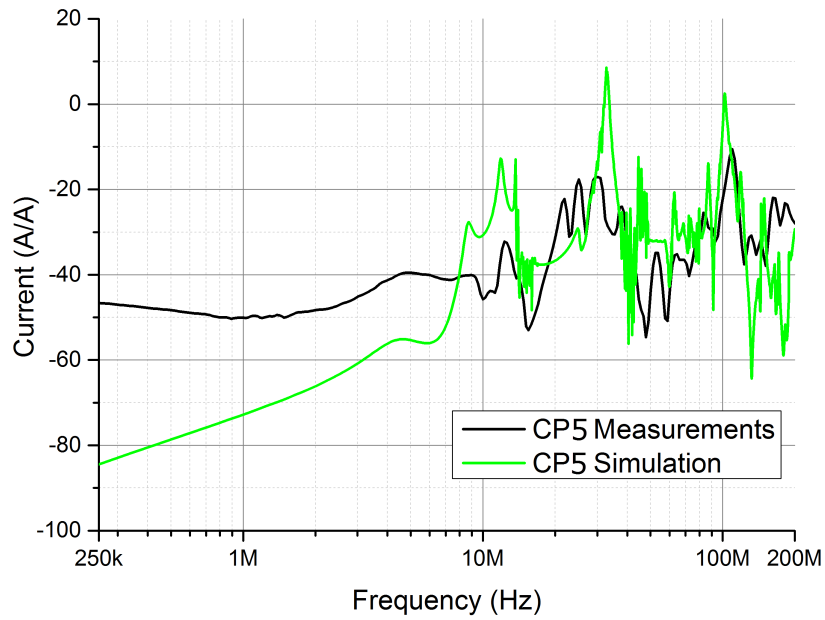
We can appreciate in low-frequency at the points CP1, CP3, CP7 an inductive behavior, since these cables are being grounded through a resistive connector to the fuselage. However CP5 was directly grounded in the experimental setup, but the numerical model made use mistakenly of a grounding resistance. This explains the constant trend in the experimental transfer function at low frequency, compared to the linear one found numerically



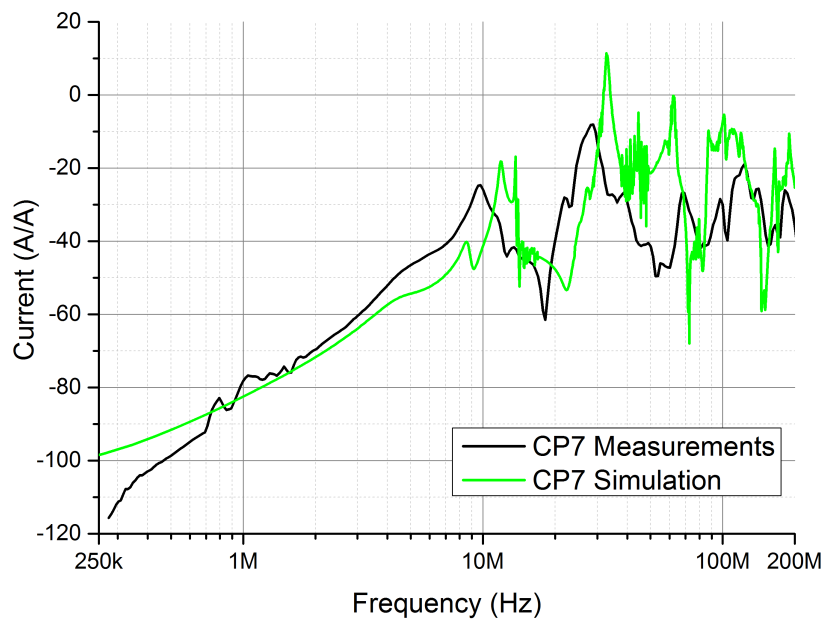
(a) Current in probes CP1.



(b) Current in probes CP3.



(c) Current in probes CP5.



(d) Current in probes CP7.

Figure 5.11: Transfer function of the current probes.

5.2.3 FSV validation

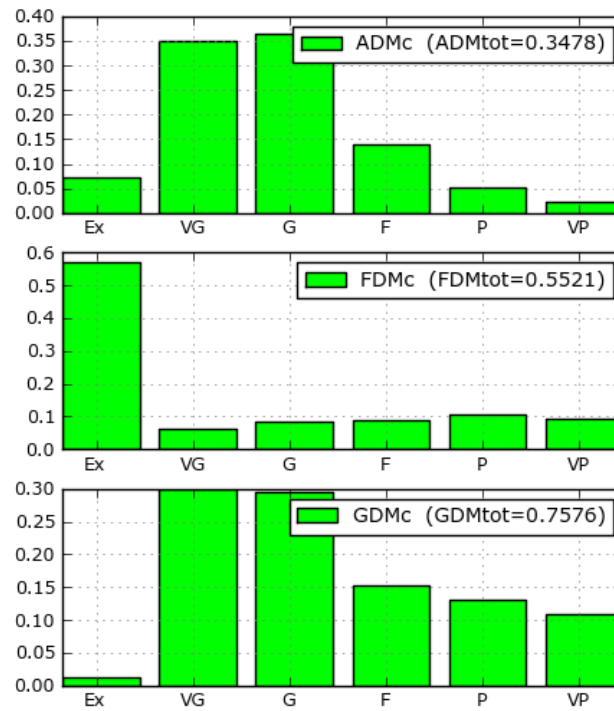
Validation methods are necessary to objectively evaluate the similarity between different datasets in a qualitative way imitating the opinion of EMC experts. Several methods are available for engineers to discuss whether the data satisfies a requirement. One of the most widely used ones in EMC is the FSV [Duffy-2006, Orlandi-2006b, Orlandi-2006a, Jauregui-2013], for its versatility and simplicity. FSV, which is incorporated into IEEE standard 1597.1 [IEE-5971], has the advantage of analyzing the two major aspects that are widely considered to be paramount in any validation: the magnitude levels and the shape of the dataset graphs.

Here, the GVT FSV tool from the UPC was used for this purpose. With the aim of considering the most relevant data of the measurements and the simulations, a previously developed weighting technique was also applied [Jauregui-2014]. A common scenario in EMC is to compare data with an extremely low level at certain frequencies which can be influenced by the noise of the measurement instrumentation. Therefore it is recommended to focus on the frequency range where the most energy is found by means of this weighting technique.

The FSV figure-of-merit indicators are the ADM, FDM, and GDM. They are associated with the difference in amplitude (Amplitude Difference Measure, ADM), the difference between the shape characteristics of the signal (Feature Difference Measure, FDM) and a Global Difference Measure (GDM), which is determined from the ADM and FDM indicators, providing a measurement of the overall difference [Duffy-2006]. The FSV validation methodology was applied to the results shown in Fig. 5.11 and reliable results were found. Tab. 5.1 summarizes the indicators of the FSV results, which correspond to a *good - very good* qualitative opinion of the experts, according to the threshold levels defined in the standard IEEE P1597.1 [IEE-5971], hence allowing us to state that the numerical model of the SIVA is representative of the real test setup. As a means of clarifying the implication of the GDM results presented in Table 5.1, a bar diagram of the FSV results comparing the measurements and simulations of the current probe CP3 is given in Fig. 5.12. The bar diagram shows the experts opinion for the amplitude, the shape and the global result when CP3 simulations and measurements are compared. From the diagram of the global indicator (GDM), it is shown that around the 30% of the experts will conclude that the similarity between the graphs is very good, another 30% will consider it a good agreement, around the 15% a fair agreement, around 12% a poor fitting, and finally less than 10% a very poor similarity. Elsewhere, the bar results for the amplitude indicator (ADM) and the shape indicator (FDM) are also shown, highlighting that the experts' opinion clearly assumes that the fitting is stronger in terms of shape than in agreement of amplitude.

Table 5.1: FSV results

Reference	ADM	FDM	GDM
CP1	0.20	0.53	0.62
CP3	0.35	0.55	0.76
CP5	0.27	0.61	0.74
CP7	0.26	0.53	0.67

**Figure 5.12:** Bar diagram FSV result considering the comparison between measurements and simulation of current probe CP3.

5.3 Falcon 7X nacelle in a reverberation chamber: a test-setup to assess HIRF effects

This case was conducted under the HIRF-SE project. It consists on the integrated power plant system (IPPS) of the Falcon-F7X, developed by Dassault Aviation. It includes the engine, the nacelle and the full authority digital engine control (FADEC). The FADEC is an attachment system between the engine and the aircraft, consisting of a digital computer (Fig. 5.13b), which manages accessories related with the control of all performance and monitoring aspects of the aircraft engine. The FADEC is usually classified as a system with the highest level of vulnerability, this is noted as level-A by certification guides [ED–2010, section 6.4.2]. The failure of systems in that level would prevent the safe flight and landing of the aircraft. Hence, this equipment require very high level of protection. The best solution is to home it within highly shielded enclosures. In a practice, the degradation of the shielding is mainly due to apertures, seams and low-conductivity materials. The use of light composite materials for this purpose, makes these enclosures more penetrable with worse shielding.

The aim of this test case is to evaluate the SE value from 200MHz up to 18GHz inside the nacelle, at three points around of the FADEC. The experimental data for the SE is taken inside a reverberation chamber. This kind of tests are usually adopted as alternative to radiation test [ED–2010, section 6.3.6] based on sequential changes in the antenna position. The reverberation chamber creates a good statistical EM distribution equivalent to illuminate the object with all directions and polarizations, thus allowing us to take into account the effect of all apertures (slot, holes and penetrable materials) at a whole.

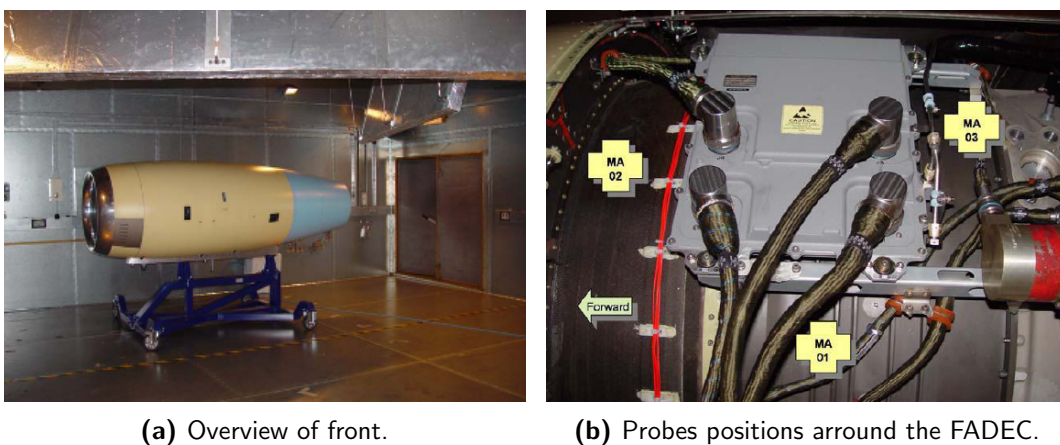


Figure 5.13: F7X nacelle.

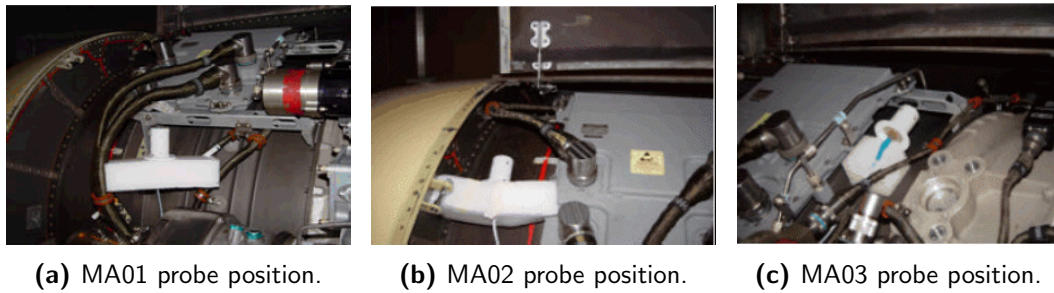


Figure 5.14: Probes location of a target nacelle.

5.3.1 Modeling and simulation approaches

The structured mesh was provided by Dassault Aviation⁴. The cubic-cell mesh has a space-step of 5 mm. The time step is calculated for a CFLN value fixed at 0.8. The materials, also given by Dassault Aviation, presented incertitudes which required a previous phase of tuning summarized below.

Modeling of the Materials

The nacelle incorporates several kinds of materials (see Table Tab. 5.2 for a summary). The main assumptions to deal with them have been:

- The materials with very low penetration, Shielding effectiveness over than 90 dB, within between (0.1, 10) GHz, have been assumed to be PEC Fig. 5.15.

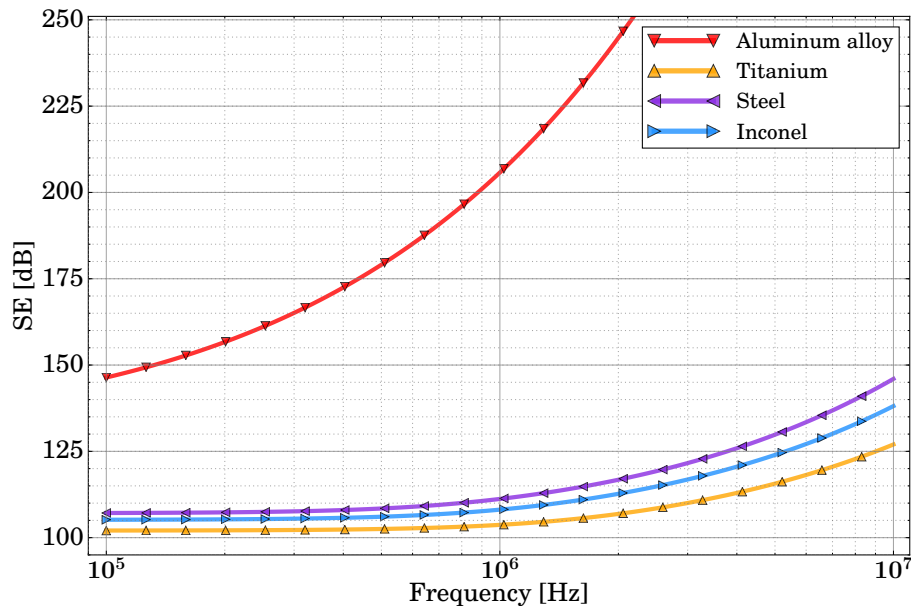


Figure 5.15: Shielding effectiveness of materials with a very low penetration (assuming PEC).

⁴For IPR reasons, just the structured mesh was made available

- The apertures such as: holes, thin slots and materials with low attenuation have been assumed to be free space, and removed from the model.
- The CFCs have been modeled using the NIBC thin-panel models proposed in⁵ Chapter 2. Proper vector fitting models from their microscopic composition were found with the tool URM-MAT provided by the Univ. of Rome La Sapienza under the HIRF-SE project.
 - Material CFC-0: Composed by a carbon fiber sheet. The fibers are woven at a perpendicular angle, each fiber has a conductivity of $8.7 \cdot 10^4 \text{ S/m}$, a $45 \mu\text{m}$ of diameter and the fibers are separated between them by $15 \mu\text{m}$ of distance. The carbon fibers are embedded in a non-conductive epoxy resin with 3.4 of relative permittivity. This panel has a total thickness of 0.3 mm.
 - Material CFC-1: Composed by 4 layer of CFC-1 with a total thickness of 1.2 mm.
 - Material CFC-2: Composed by a panel of CFC-1 with a reinforcement mesh embedded at its center. The reinforcement mesh has a density of 80 g/m^3 , and is composed by bronze wires braided to 90 degrees. Each of one has a conductivity of $\sigma = 2.5 \cdot 10^7 \text{ S/m}$, $42.3 \mu\text{m}$ of diameter and they are separated 1.25 mm each and other.
 - Material CFC-3: This material are composed by a panel of CFC-1 with a reinforcement mesh composed by steel wires braided to 90 degrees. Each of one has a conductivity of $\sigma = 1.4 \cdot 10^7 \text{ S/m}$, $76.0 \mu\text{m}$ of diameter and they are separated 1.25 mm each and other.

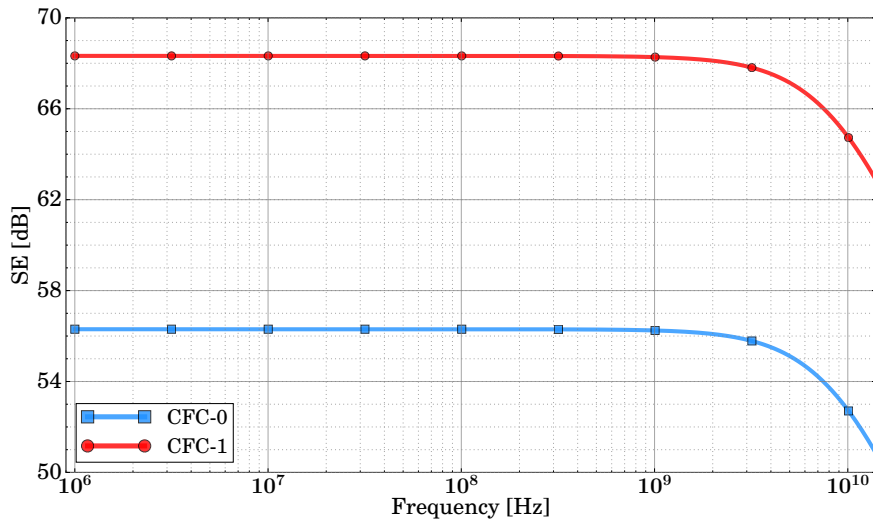
The Shielding effectiveness of each CFC are illustrated on Fig. 5.16, where the contribution of each layer is also shown.

Modeling the reverberation chamber

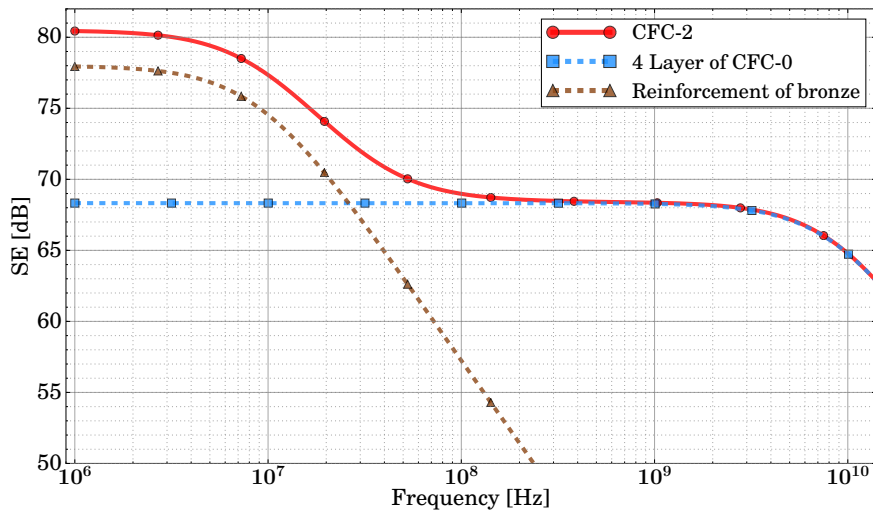
Reverberation chamber tests require to average the measurements over many stirrer positions in order to change the modal distribution inside the cavity. The cavity must be large enough in order to accumulate enough modes at low frequencies, for obtaining an average uniform field throughout on the volume occupied by the device under test. For instance, a cubic reverberation chamber must have at least 13 m of length, to accumulated 50 modes between 1 – 2 GHz.

The numerical simulation of several stirrer positions inside an electrically large highly-resonant cavity is unaffordable for a time-domain solver. However, a equivalent model can be used by employing a superposition set of plane waves with a random uniform statistical

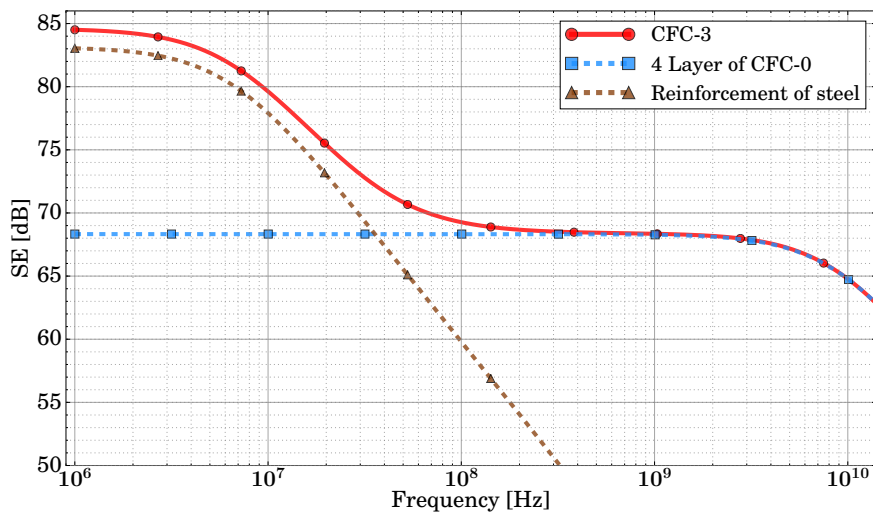
⁵No SGBC tools were available at that time



(a) Shielding effectiveness of CFC-1.



(b) Shielding effectiveness of CFC-2.



(c) Shielding effectiveness of CFC-3.

Figure 5.16: Shielding effectiveness of the CFCs materials used.

distribution on their polarization, delays and direction of incidence [Hill-1998, Moglie-2006]. Instead of a PEC cavity, the computational space can then be truncated by usual PML as ABC and affordable simulations can be done. In our case, a Gaussian-modulated plane-wave was used covering the frequency range 200 MHz – 10 GHz.

5.3.2 Simulation results

The transfer function was evaluated at several observation positions close to the FADEC Fig. 5.13b and Fig. 5.14. For this, the E-field $\vec{E}_{1,k}$ is recorded in time, transformed into frequency and normalized by the incident E-field measured at the same observation point (without the nacelle) $\vec{E}_{0,k}$:

$$T_{\text{dB},k} = 20 \log_{10} \frac{\sqrt{\vec{E}_{1,k} \cdot \vec{E}_{1,k}^*}}{\sqrt{\vec{E}_{0,k} \cdot \vec{E}_{0,k}^*}} \quad (5.6)$$

where (*) denote the complex conjugate, and k denote the probe positions labeled by (MA01, MA02, MA03) see Fig. 5.13b.

Results with SEMBA-UGRFDTD solver, a power balance (PWB) code from ONERA⁶ and a TLM code from University of Nottingham [Smartt-2013] are cross-compared together on Fig. 5.17 for each probe and on the Fig. 5.18 is shown the mean value between the three probes. The results show a good agreement at each probe position ⁷.

⁶The PWB method can solve EM problems into the frequency range where the device under test (DUT) is much larger than the wavelength. This method is based on a macroscopic and statistical analysis of transfer and dissipation of energy [Junqua-2007, Junqua-2011]

⁷For industrial property rights (IPR) reasons we cannot show experimental data, but we state that a good agreement was found.

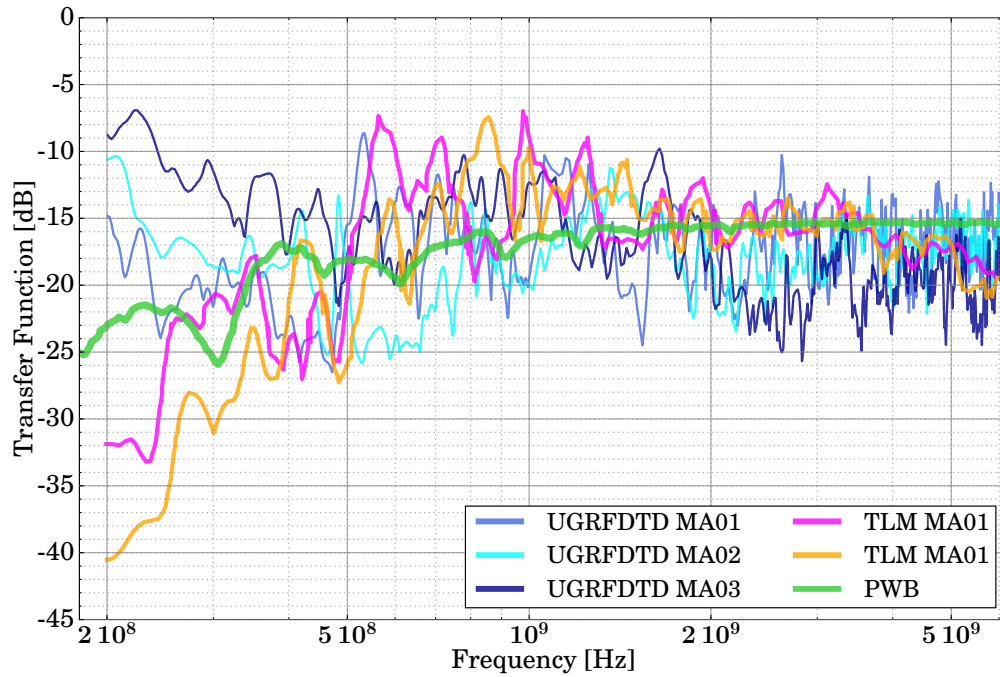


Figure 5.17: Transfer function of the nacelle-SS05.

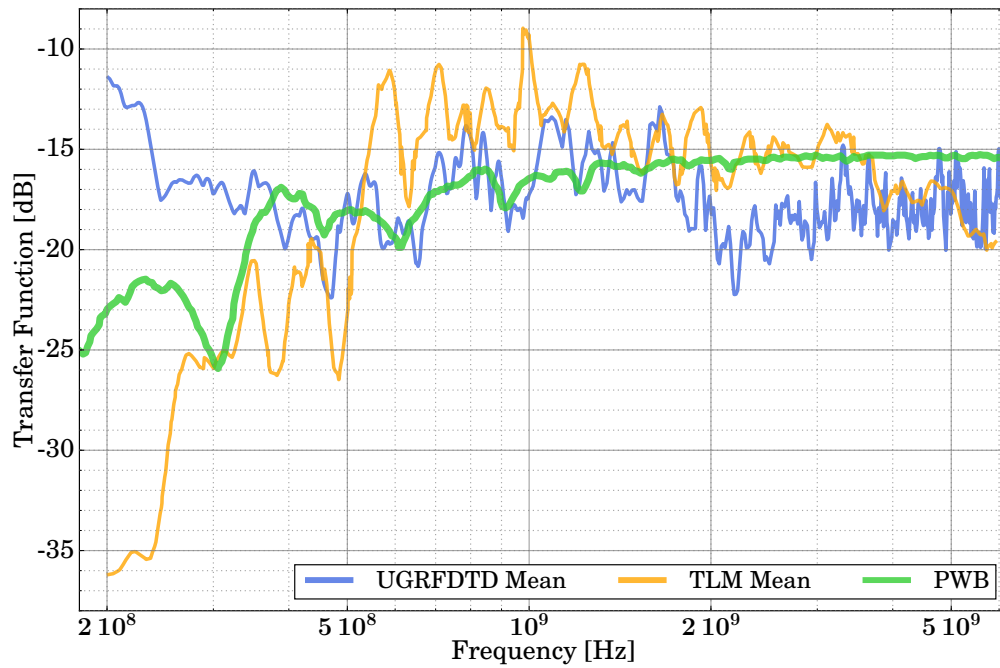


Figure 5.18: Transfer function of the nacelle-SS05.

Engine Part Name	Material	EM. Model
Inner barrel, Fan Cowl Door (int side), Internal of Inert Afterbody, Engine bypass, Rear Outboard Bypass Duct	CFC (Epoxy resin)	CFC-1
FCD-CFCBr (LFCDext, UFCDext)	CFC with Bronze Mesh	CFC-2
IAB-CFCBr	CFC with Bronze Mesh	CFC-2
INL-CFCBr (AiPanel, OutBarrel)	CFC with Bronze Mesh	CFC-2
INL-CFCSt-InBarrel	CFC with Steel Mesh	CFC-3
Inlet lib skin, plates and attachment angles, bonding strap in contact with FCD conductive gasket, ALU parts of Fan Cowl Doors-misc,engine bypass, miscellaneous ALU parts.	Aluminum alloy	PEC
After bulkhead, anti-ice exhaust panel, inlet flange, forward bulkhead, below AL exhaust panel, pylon firewall, parts of Fan Cowl doors-misc, Ti frame of IAB, engine compartments, miscellaneous TI parts, yoke	Titanium Ti6Al-4V	PEC
Dielectrics around TAI feeder, part of Fan cowl doors, miscellaneous electric parts	Dielectric	Air
Slot between FCD and other part	slots	Air
TAI feeder and little tubes, miscellaneous INCO parts	Inconel	PEC
Parts of fan cowl doors-misc, bonding plates and fingers	Steel	PEC
Engine Intermediate section, miscellaneous steel parts	Stainless-Steel	PEC
Pipes (Fuel, Hydraulic, Ice, Rain, AGB, air, oil Fire protection), Chanel wiring (A,B), FADEC wiring, PMA wiring, feeder, FADEC, engine mounts and exhaust	Metal, over-shield and wiring parts	PEC

Table 5.2: Engine parts and material definition.

CAD/CAE IMPLEMENTATION

NOTES

CAD tools like Catia, Rhinoceros 3D, FreeCad, etc. are pervasively used by the industry (mechanical, electrical, automotive, aerospace...) in the pre-manufacturing phases of a product. They allow the user to generate a geometrical model of any 3D object quickly and accurately. The modeling is typically based on parametrization techniques, in terms of non-uniform rational B-spline (NURBS), which are used to provide a geometrical form as close as possible to the original one. They allow the user to iterate over the CAD model, during the development stage, to reach a final design. In this way, the different verification and certification stages that influence the design of an object, are simplified and centralized, and the cost of the re-work procedures is consequently reduced.

With the same purpose computer aided engineering (CAE) tools come forth to provide a computational synthetic environment for the system under development, to obtain and/or optimize its physical behavior such as: structural analysis, shape optimization, assembly conflicts, thermal transfers, particle dynamics, fluid dynamics, electromagnetics, etc.. This yields a reduction in the development time, and economic savings in the production cost which has triggered a seminal interest for industry to research and develop simulators, meshers, post-processing techniques, graphical user interfaces (GUIs), etc..

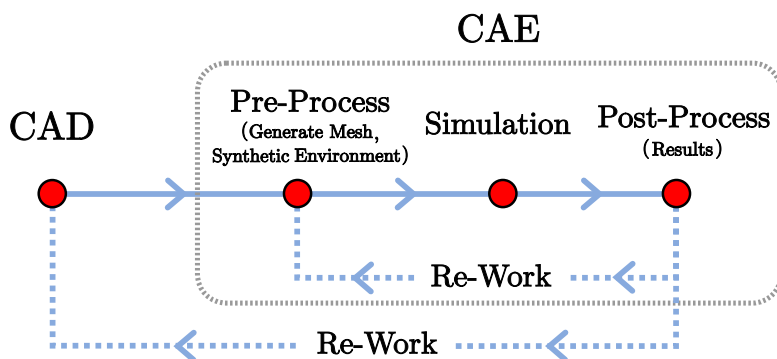


Figure 6.1: Computer aided CAD and CAE stages.

6.1 SEMBA

SEMBA (Wideband Electromagnetic Solver) is a CAE tool developed by GEG at the UGR. It is a framework envisaged for simulations in the field of CEM for EMC. EMC problems present important challenges from the simulation point of view since results need to be obtained for large bandwidths or for transient excitations, usually for extremely complex geometries. Moreover, many electrical scales can be simultaneously present, requiring appropriate non-brute-force sub-cell models, etc. SEMBA contains the necessary tools to manage the whole simulation chain for an EMC problem, starting from a CAD design, and ending into the calculation of the desired field and currents. It includes pre-processors, meshers, solvers and post-processors. It has a graphical interface based on the commercial CAE tool GiD, which permits the user to import CAD files, assign materials and generate meshes. It also comprises two simulators: one based in FDTD, and another one in DGTD.

6.2 UGRFDTD

The UGRFDTD solver, embedded into SEMBA, is based on the FDTD method, it implements state-of-the-art advances in FDTD methods, and it has been extensively used in a variety of extremely challenging problems of interest for the aircraft industry: HIRF-SE, RCS, lightning indirect effects, etc.. SEMBA is currently employed under licence by AIRBUS-DS, INTA, NUDT, ESPE. It has been thoroughly validated, under the frame of several projects and contracts, with analytical and experimental results of several aircrafts in HIRF and lightning scenarios: C295 [Gutierrez-2014], F7X, A400M, EV55, ATLANTE, SIVA [Cabello-2017b], MILANO, etc.. This thesis has been aimed to the implementation of new methods into the UGRFDTD solver. Namely, conformal meshing and solving algorithms DM [Dey-1997] for the adaptive modeling of curved geometries, and numerical models for the treatment of multilayered composite thin-panels.

The simulation stage is critical in the CAE process, typically requiring high computational resources to deal realistically with the problem complexity. As stated in Chapter 1, there are many numerical methods, among them, FDTD has been demonstrated to provide an optimum trade-off between accuracy and computational efficiency for broadband problems, which has made of it the method of choice of many commercial solvers in CEM for EMC. The FDTD with conformal method is able to achieve a second-order accuracy (Section 4.1). Additionally, it is explicit in time and hence just requires the evaluation of the fields at each space/time position as a function of their neighbor at earlier field values. This feature makes it a perfect candidate to be efficiently parallelized at different levels:

1. **Fine-grained parallelism:** The use of a structured grid yields a fixed scheme for the placement of the fields, which makes it possible to update the fields in the same order

in which they are stored in memory. Therefore the compiler can optimize the code using *vectorization* methodology based on single instruction multiple data (SIMD) techniques [Hwang-2011]. This scheme also allows the programmer to take profit of the *cache memory spatial locality*, and therefore to decrease the number of *cache failures*. Unfortunately this not straightforward for problems larger than the cache size, because not all the fields involved in the update fit in nearby memory addresses, and cache failures generate bottlenecks because of the continuous communication between the different levels of the memory. In consequence, the total simulation speed is limited by the *maximum memory bandwidth*¹ between cache and RAM [Cessenat-2013].

2. **Shared memory parallelism:** Current microprocessors have a large number of independent processing units (cores), with a common-address memory space. The explicit FDTD formulation implies that each field in each space position can be updated independently from the other ones. In this way, for a parallel execution, the computational space can be subdivided in subspaces, each of which is updated at the same time by different processing units. This kind of parallelization can be easily implemented by using *multi-threading* techniques based on *Fork-Join* procedures, such as OpenMP or C++11 threads. For FDTD, this multi-threading technique has a high degree of scalability for problem sizes smaller than the memory cache of the computer system. However for problems not fitting into the cache size, the multi-threading scalability is limited by the maximum bandwidth of the computer system, see Fig. 6.2

3. **Distributed memory parallelism:** When problems become larger than the shared-memory size, and/or the speedup is limited by the bandwidth of a single computer, we must resort to distributed-memory clusters of computers. For this, the computational space is divided into sub-domains and distributed in several independent *processes* assigned to different computers. Since, each process has a different memory space, the sub-domains are allocated so that the neighboring processes share a common overlapped boundary with tangential magnetic fields which are updated by both neighbors. After each time step, just the tangential H-fields need to be exchanged between the neighbors via network (ethernet, InfiniBand) to provide valid values for E-fields to perform the next time step. This kind of parallelization is implemented by using *message passing interface (MPI)* techniques which distribute and perform the communication of data between processes [Yu-2005].

¹The maximum rate at which data can be transferred into memory by the processor (in GB/s)

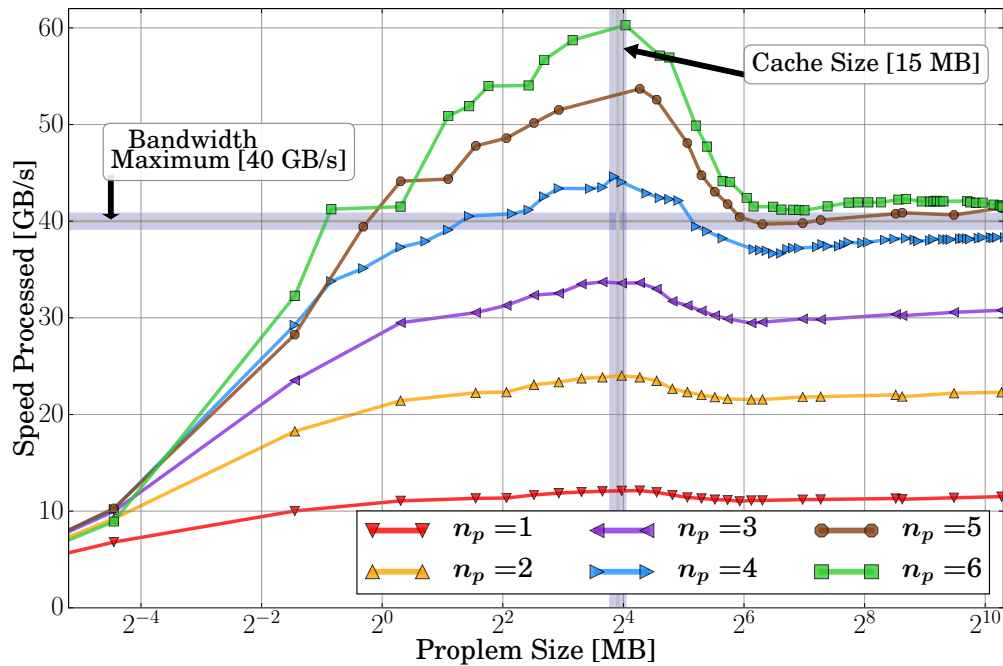


Figure 6.2: Speed measured in [GB/s] for UGRFDTD as function of the problem size in [MB], using a different number of threads in a machine based on an Intel-i7-3960X, whose bandwidth is 40GB/s. As expected, the processing speed saturates with the maximum bandwidth of the computer system.

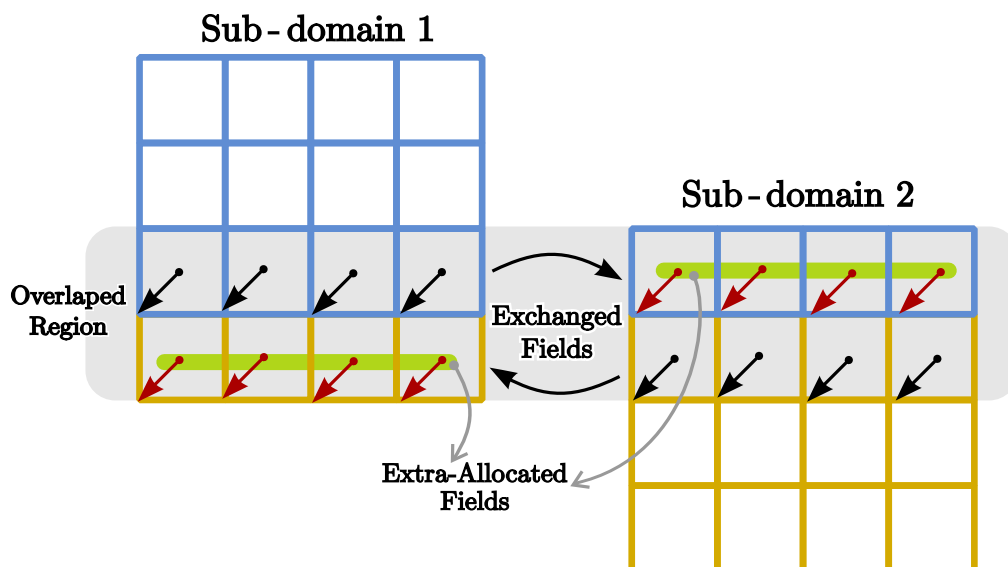


Figure 6.3: The computational domain is divided into sub-domains according to the number of available computer units. The H-fields in the overlapped region is exchanged between neighbor sub-domains.

6.3 Meshing techniques for FDTD

The achievement of precise and powerful meshing techniques has been an important line of research for the results of this thesis. The mesh is the ultimate geometric description used in the final simulation.

There is a vast description in literature of algorithms and techniques to generate and optimize structured meshes. The most usual ones are based on *Adaptive Mesh Refinement* pioneered by Berger in 1914 and *ray-tracing* algorithms. The basis of the ray-tracing method [Aftosmis-1998] is to cast rays over geometrical primitives (pixel, triangles, quad, polygons, etc), and collect elements reached by the rays. In fact, ray-tracing algorithms are also the most used ones in rendering applications. Usually, the order of complexity of ray-tracing algorithms is very high $O(N^3 \log(T))$. However, optimization methods borrowed from other disciplines (computer animation, collision detection, hierarchical data structures...) can also be used for ray-tracing in FDTD. These include the *AABB-Tree* and the *OBB-Tree* [Glassner-1989, chap. 6] which are used for lessening the number of unnecessary and expensive calls to exact intersection algorithms between primitives, so that a hierarchical tree is built by using a recursively partition of the bounded polygons, and from this, to bound the resulting groups with tight-fitting oriented bounding boxes. Those fast ray-tracing algorithms [Gottschalk-1996, Kim-2010] permits to obtain structured meshes in a more efficient manner.

The majority of ray-tracing meshers use a triangular mesh as starting point, which is found through the triangulation of the CAD surfaces. However, the connections and intersections between the different CAD surfaces may yield several type of flaws and defects in this triangular mesh (Fig. 6.4). Some of the defects that we may find are: isolated elements, gaps, gaps with partial overlaps, overlapped triangles, self-intersections, etc. Therefore, in order to obtain high-quality structured meshes for an EM FDTD simulator, a *clean* mesh of triangles is required. It should be noted that the simulation requirements, especially in EM, are more strict in regards to the quality of the meshes when compared to other areas such as: visualization, video games, modeling, computer animation [Attene-2013]. Usually those cleaning tasks involve a tedious work that must be manually performed on the CAD design phase.

A so-called *conformal-mesher (CMesh)*, has been developed in the framework of this thesis (under the A-UGRFDTD project funded by Airbus between 2013 and 2018) with the capacity to generate both structured and conformal meshes, and to automate many of the cleaning tasks [Bischoff-2005] aforementioned. This mesher, first transforms the original input triangle mesh into an intermediate mesh, that is composed by a wire-frame of lines, with each of these line placed on a structured cell. The intermediate-mesh maintains the topological connectivity of the original mesh, or it is even adapted, in order to avoid defects of the original mesh (see Fig. 6.5). In this way, the intermediate mesh is used to iterate and

simplify the non-suitable cells (cells non-supported by simulator), until a suitable conformal or structured mesh is attained [Lorensen-1987, Nielson-1991, Bischoff-2005]. This method achieves a very efficient order of convergence $O(N^2 T)$, and includes essential features avoid the costly readjustment work on the CAD to simplify frames.

Usually, the CAD design contains fine details that are irrelevant to the simulation because their electrical size is very small with respect to the minimum wavelength which is given in FDTD by the space resolution of the grid. Hence, FDTD meshers are naturally able to filter-out and perform processes of regularization automatically: the geometry must be reduced to vertices, edges or faces on the cell. As a result, fine details coming from the input mesh are automatically filtered out. CMesh includes this capability, with some others that can be summarized as follows:

- CMesh is capable of treating non-topologically connected input meshes of triangles Fig. 6.4a. It takes into account all objects, however small they are Fig. 6.4b.
- CMesh is able to repair unwanted sub-cell holes and thin gaps between surfaces (Fig. 6.4c), overlaps (Fig. 6.4d). For instance, it takes decisions on merging two surfaces (Fig. 6.5) if the distance between them is under a prescribed tolerance, usually specified as fraction of the cell size.
- The dimensional degeneration capacity is a very important feature in EM. This degeneration cases are applied on objects which one of its dimensions is very small with respect to the grid. In these cases, the object is collapsed in this direction. For instance, this is useful for the treatment of a thin-panel or thin object which is represented as a volume in the CAD design but that must be approached as a surface by the simulator (Fig. 6.12).

It should be stressed that the structured mesh found by Cmesh is not a classical one. A surface meshed with a classical structured mesher results in faces aligned with the grid axis (Fig. 6.7a) and therefore the four edges of each of these faces are automatically affected when updating the fields. The structured mesh given by CMesh is given by a wireframe-shaped composed by edges of the grid, this mesh permit us to separate both sides of a surface using the least number of edges when updating the fields. This kind of mesh is called as minimal-mesh (Fig. 6.7b).

To illustrate it, Fig. 6.12 show some details of the mesh for a PEC surface. The apparently open faces of cells might be appreciated in the resulting mesh, due to the concept of wireframe meshing. However, these are only geometrically open and they remain closed from the EM point of view. In Fig. 6.8, it can be appreciated that there are cells where the normal magnetic field (shown as surfaces) is not required to be PEC, since not all the

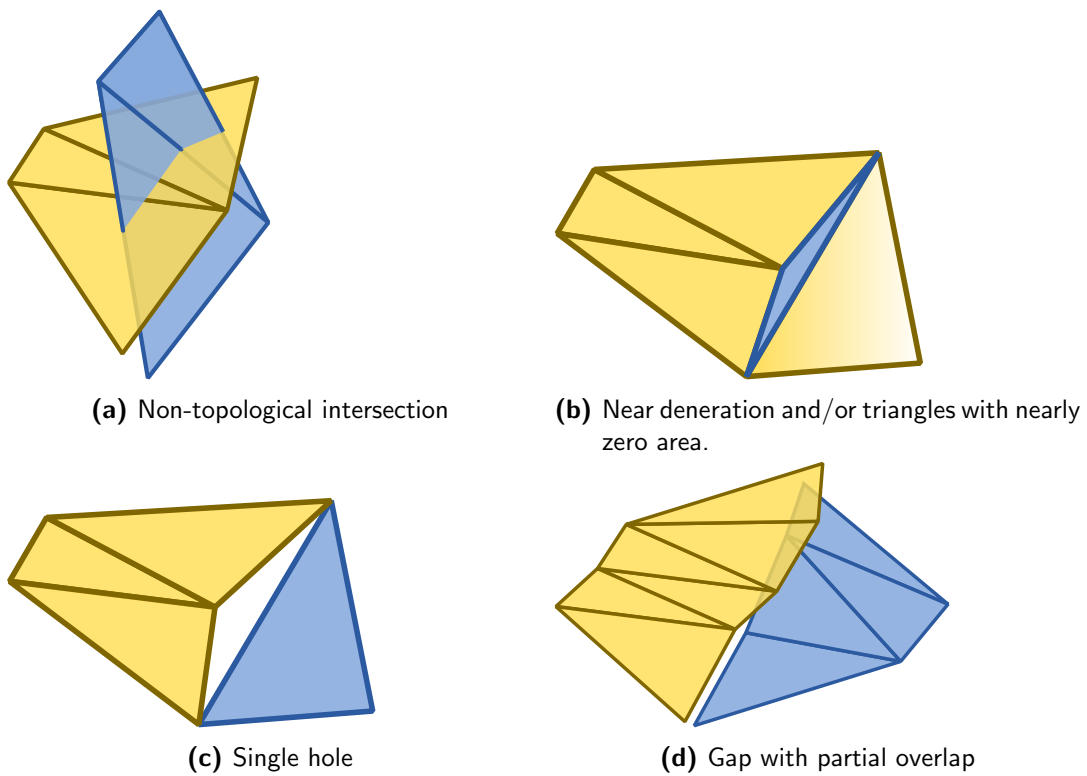


Figure 6.4: Types of defects and flaws, occurred in triangles meshes.

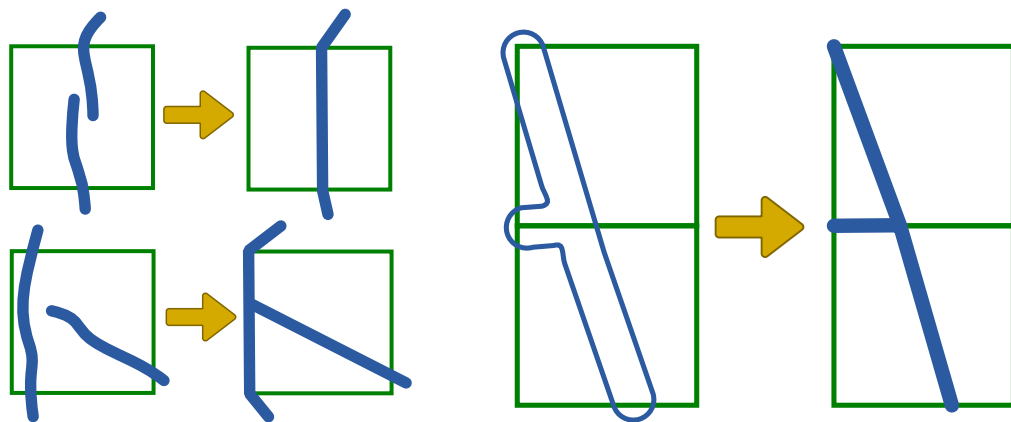


Figure 6.5: Topology repair: the objects not topologically connected are connected by the conformal mesher.

Figure 6.6: Dimension reduction.

surrounding tangential field components (shown as a wireframe) are PEC. However, no EM coupling can be seen to actually occur from side to side.

Some snapshots of the meshes found with this model are below, emphasizing the challenges addressed:

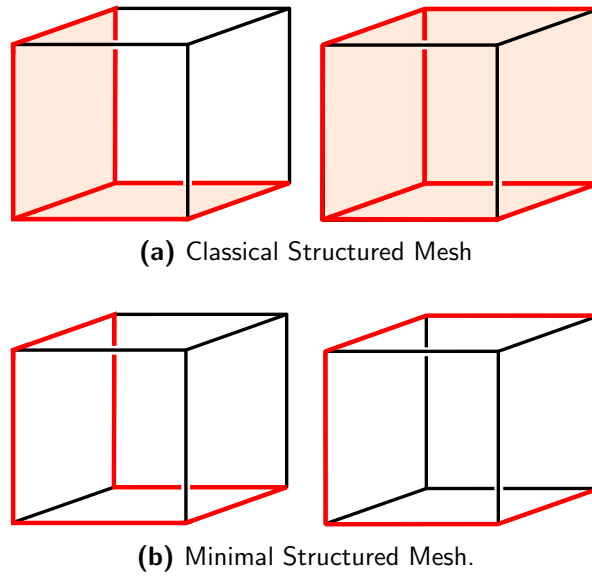


Figure 6.7: Classical structured mesh and minimal mesh comparison.

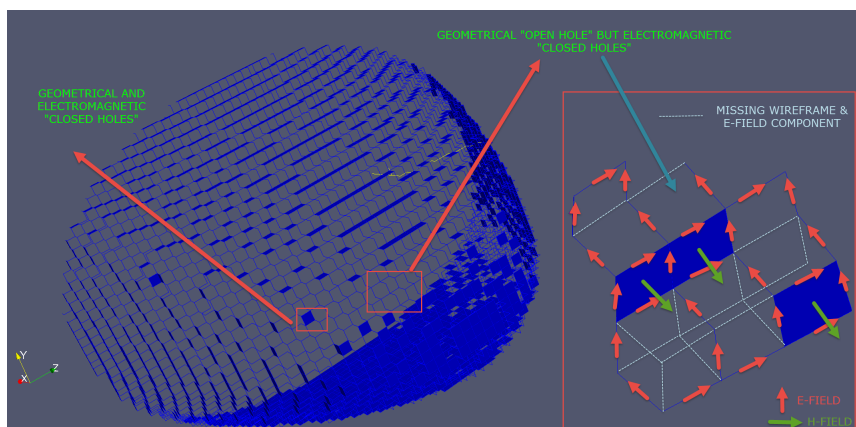


Figure 6.8: Details of minimal mesh for a curved surface.

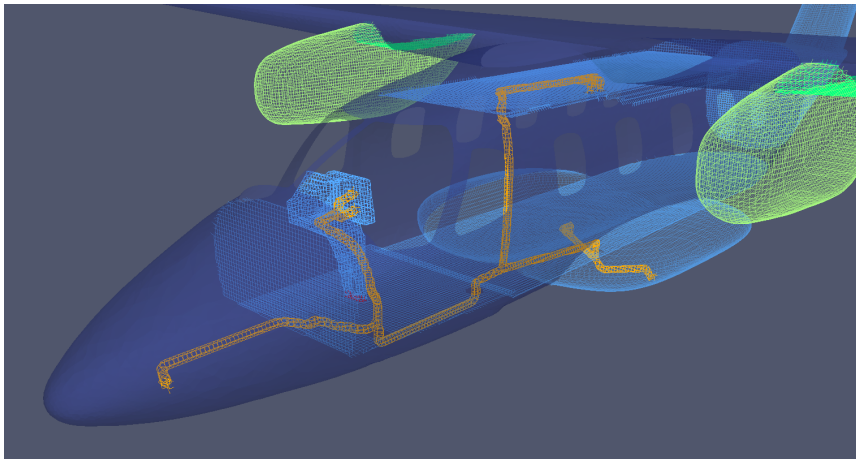


Figure 6.9: EV55 aircraft internal details meshing with conformal mesh.

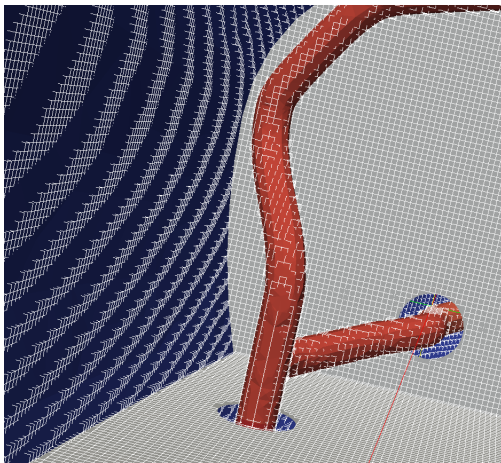


Figure 6.10: Structured minimal mesh of thick wires, the topological connections is preserved around the holes.

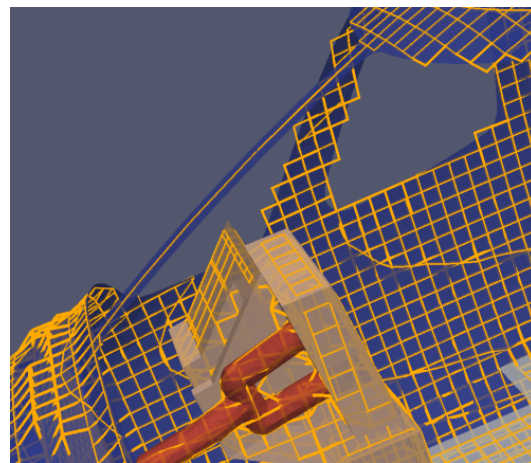


Figure 6.11: Conformal mesh: Dimension Reduction

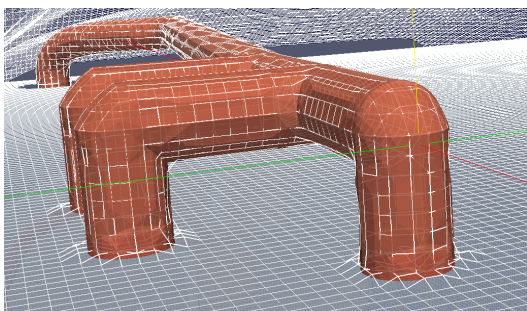


Figure 6.12: Conformal Mesh of intersection between structures. The mesh adapts itself to preserve the topological ohmic connections in the intersection area.

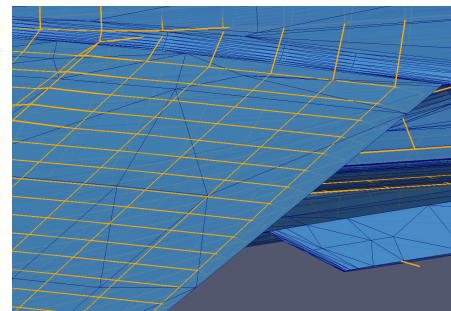


Figure 6.13: Conformal Mesh of sharp edge.

Conclusions and future work

This dissertation has been aimed at contributing to the development of efficient numerical tools for the analysis of aeronautical structures from the electromagnetic point of view. Its achievements can be summarized as follows:

1. The classical FDTD method has been improved with a stable conformal algorithm for PEC and lossy surface multilayered materials.

The stability of the conformal method is guaranteed by using the relaxation techniques proposed in the Chapter 3. We have demonstrated that this approach yields an order of convergence higher than the usual FDTD. It permits us to mitigate some of the well-known pitfalls of staircase meshing inherent to the Manhattan distance error, such as spurious resonances, shifting in the resonant frequencies of the structure, overestimation of ohmic losses and shielding effects (in low and in high frequency), and mesh anisotropy.

2. The modeling of complex materials has been one of the most important topics in this dissertation. To this end, the notion of two-sided thin-panel methods has been introduced in Chapter 2. These take into account both the scattering and wave penetration at each side of the material, in contrast with the one-sided classical SIBC, which just model bulk lossy objects from the scattering point of view, not handling the penetration (interior) problem. Namely the classical NIBC has been analyzed, and a novel robustly stable alternative called SGBC has been introduced.

As a result, we can state that:

- Thin-panel methods handle correctly a wide frequency range including skin-depth effects, at high frequencies, as well as ohmic losses at low frequency.
- Thin-panel methods are reliable both for far-field and near-field computations.
- The classical NIBC does not preserve the usual placement of the FDTD fields, requiring a non-causal upwind extrapolation, often blamed to cause late-time instabilities.

- The SGBC provides a robust stable alternative by using different temporal integration methods. Namely, the Crank-Nicolson scheme yields an unconditionally stable algorithm, and the stability constraints of the complete system (FDTD-3D with SGBC) is only conditioned by the usual FDTD-3D Courant criterion.
3. A complete workflow for the simulation of multilayered lossy thin-panels of arbitrary composition has been proposed in the Chapter 2, to account for modern composite materials used in the aeronautic industry. Usually, the internal microscopic structure of the material (layers, reinforcement internal meshes, fibers, ...), cannot be approached directly by subcell methods, and a equivalent homogeneous material with the same EM behavior is required. As a starting point, the electromagnetic parameters (constitutive, impedance, scattering, ...) are required. These can be found by measurements, analytically, or by approximate formulations derived from the microscopic structure. Next, those parameters are processed for yielding suitable physical models (impedance matrix for NIBC, or layer-by-layer definition or bulk constitutive parameters for SGBC), according to the thin-panel method used in the simulation Fig. 2.1.

Future work

During this work, several lines of future research have been identified. Some of them are the result of the feedback provided by airframers with whom we have collaborated for years. In direct relation to this dissertation topics, we next summarize some which are a natural continuation of this work.

1. In the aeronautical EMC sector, is fundamental to study and assess the shielding behavior of the aircraft. As stated along the manuscript, the shielding is worsened by penetrable materials, but this is not the only entry point of energy: apertures (joints, gasket, slot, holes), can be in fact even more critic from the EMC point of view. Large apertures are naturally handled by FDTD, however thin slots, or, in general, apertures much thinner than the FDTD space-step cannot be treated directly into FDTD, unless using unaffordable brute-force meshes. A line of work to tackle this is given below.
 - Several approaches exist in literature that can serve as a starting point: a promising one is that of [Edelvik-2004] which proposes a dual magnetic equivalent of Holland thin-wire model for thin slots. Its extension to conformal techniques will also permit us to also handle the slot curvature. We already count with experience in conformal meshing and treatment of metal thin wires. Though this topic has not been included in this dissertation, we can take profit of it.

2. Strictly speaking, conformal methods are not sub-cell algorithms, in the sense that sub-cell details (sharp edges of surfaces, holes, bolted junctions...) cannot be fitted in an accurate manner. A complementary solution is proposed based on the well-known subgridding techniques:
 - The combination of subgridding for sub-cell details, with the conformal algorithms for curved geometries, proposed here, will allow us to provide a full solution to this multi-scale problem. We count with mature meshing tools as a starting point that can be extended with subgridding capabilities. However, a well-known challenge of subgridding resides in its weak stability. A promising approach to overcome this, is the work of [Ritter-2015].
3. Aeronautic materials is a hectic field of research. Homogenization methods to find causal models of general materials are a must. The formulation to find the S-parameters assuming the thickness and constitutive parameters of a material sample, is rather simple, and uniquely determined. However, the inverse problem does not have a unique solution to provide the constitutive relationship from the S-parameters, and the direct analytical method does not supply a continuous solution in frequency. These discontinuities are given by the ambiguity in the choice of the branch of the complex logarithm of analytical relationships. The classical Nicolson-Ross-Weir (NRW) method is continuously revisited to provide a solutions for this problem [Arslanagić-2013]. However, this issue is not fully solved and, in time-domain, it is especially crucial to find stable models.
 - Our starting point employs a NRW method, that still needs enhancements, by combining it with evolutionary optimization techniques to find Kramers-Kronig compliant multilayer models from the measured S-parameters of structures whose internal layout is unknown. Non-deterministic alternatives to classical vector-fitting methods should also be investigated.
4. The computational performance of the conformal methods in particular, and of FDTD in general, is another topic of interest. Several improvements are envisaged:
 - The late-time convergence of resonant low-frequency responses can be accelerated by employing permittivity scaling methods. Already introduced in 1994 by Holland [Holland-1994], they are currently attracting attention [Hue-2005].
 - Computational speed is currently limited by the maximum bandwidth between the CPU and the main memory, as studied in Chapter 6. By using causal local time updating we can take profit of the fast speed of cache memory by optimizing the memory locality. A starting point for this, can be work of [Minami-2014].

- Last but not least, the appearance in the market of the novel Knight Landing Intel many-core processor, promises to fill the gap between high-speed limited-memory GPU codifications of FDTD, versus low-speed large-memory CPU ones. This architecture provides a dramatic increase in FDTD speed-up, for counting with up to 16 GB of ultrafast (GPU-like) memory, combined with the classical channels to access the main memory. The tuning of OpenMP capabilities for this novel architecture will definitely, in our opinion, lean the scale in favor of CPU implementations, allowing us to keep the current code sources with few modifications. We already count with preliminary results supporting this.

To conclude, our ultimate goal is to advance in the definition of a whole methodology to address EMC certification scenarios, combining numerical techniques with experimental ones, to be actually acceptable by EMC certification authorities. In this sense, there is a long way to go in order to achieve a good level of confidence in numerical solvers in a task classically relying just in experimental testing. The validation of any numerical model of physical features (subcell, material, junction, etc.) with experimental data is the only way to advance in this line. Also, the incertitude in the physical parameters must be addressed in a smart manner, e.g. by stochastic methods [Smith-2014]. Finally, literature often tiptoes over the role of nonlinearities, because of the complexity required to deal with them; further work is required.

Cables by themselves, together with their shielding and grounding, would still deserve more than a dissertation: they play a starring role in EMC. Though this has not been our topic, the UGRFDTD tool already counts with a Holland-based multiconductor transmission line method to treat thin-wire cable bundles [Berenger-2000]. Similarly new conformal techniques [Perrin-2013] for oblique wires are under development in UGRFDTD. The hybridization of conformal surface methods with oblique thin-wire methods still poses some challenges that require further work. The investigation of relaxed methods based on Agrawal's principle to deal with massive cable bundles is also a topic of interest [Rachidi-2012] to overcome Holland's thin-wire limitations.

Targeting certification authorities is an ambitious goal. It requires counting with them, and with the synergy of test houses, airframers and software providers. During this work, we have counted with these elements under several projects, some of them still running, and we hope to be able to continue growing in the same manner.

Glossaries

ABC absorbing boundary condition.

ADE auxiliary differential equation.

AV air vehicle.

BIBO bounded-input bounded-output.

CAD computer aided design.

CAE computer aided engineering.

CEM computational electromagnetic.

CFC carbon fiber composite.

CFL Courant Friedrichs Lewy.

CFLN Courant Friedrichs Lewy number.

CFRC carbon fiber reinforced composite.

CFRP composite fiber reinforced plastic.

CN Crank Nicolson.

CNTD Crank-Nicolson time-domain.

CPFDTD contour path FDTD.

CPML convolutional perfectly matched layer.

CRDM conformal relaxed Dey-Mitra.

DC direct current.

DCI direct current injection.

- DG** discontinuous galerkin.
- DGTD** discontinuous galerkin time domain.
- DM** Dey-Mittra.
- DUT** device under test.
- EC** edge centered.
- ECT** enlarged cell techniques.
- EM** electromagnetic.
- EMC** electromagnetic compatibility.
- EMI** electromagnetic interference.
- EMP** electromagnetic pulse.
- EP** effective parameters.
- ETD** exponential time differencing.
- FADEC** full authority digital engine control.
- FC** face centered.
- FD** frequency-domain.
- FDFD** finite-difference frequency-domain.
- FDTD** finite-difference time-domain.
- FE** finite element.
- FEM** finite element method.
- FETD** finite-element time-domain.
- FIT** finite integration technique.
- FSV** feature selective validation.
- FTCU** flight termination control unit.
- FV** finite volume.
- GNSS** global navigation satellite system.

-
- GO** geometrical optics.
- GTD** geometric theory of diffraction.
- GUI** graphical user interface.
- HF** high frequency.
- HIE** hybrid implicit-explicit.
- HIRF** high intensity radiated field.
- HPC** high performance computing.
- IPPS** integrated power plant system.
- IPR** industrial property rights.
- LECT** locally enlarged cell technique.
- LF** low frequency.
- LIE** lightning indirect effects.
- LLDD** low-level direct drive.
- LTI** linear time invariant.
- MoM** method of moments.
- MPI** message passing interface.
- MTLN** multiconductor transmission line network.
- NIBC** network impedance boundary conditions.
- NN-EMP** non-nuclear electromagnetic pulse.
- NRW** Nicolson-Ross-Weir.
- NURBS** non-uniform rational B-spline.
- OMP** open multi-processing.
- p.u.l.** per unit length.
- PCU** power control unit.

- PEC** perfect electric conductor.
- PLRC** piecewise linear recursive convolution.
- PML** perfectly matched layer.
- PO** physical optics.
- PPW** point per wave length.
- PTD** physical theory of diffraction.
- PWB** power balance.
- RCS** radar cross section.
- RF** radio frequency.
- RMS** root mean square.
- SE** shielding effectiveness.
- SEMBA** wide band electromagnetic simulator.
- SF** scattered field.
- SGBC** subgridding boundary conditions.
- SIBC** surface impedance boundary conditions.
- SIMD** single instruction multiple data.
- SIVA** integrated system of aerial vigilance.
- TA** time average.
- TD** time-domain.
- TE** transversal electric.
- TEM** transversal electromagnetic.
- TF** total field.
- TLM** transmission-line-matrix.
- UAV** unmmanned air vehicle.
- UTD** uniform theory of diffraction.

UWB ultra wide band.

VF vector-fitting.

VLF very low frequency.

YM Yu-Mittra.

Entities & Organizations

AEG Vulture AEG Vulture is a finite-difference time-domain solver for electromagnetic applications developed by University of York [Flintoft-2014].

Alhambra-UGR Cluster Alhambra Cluster alhambra.ugr.es.

ANSI American National Standards Institute, <http://www.sae.org/>.

EASA European Aviation Safety Agency, <https://www.easa.europa.eu/>.

ESPE The Army University of Ecuador.

EUROCAE European Organization for Civil Aviation Equipment, <https://www.eurocae.net/>.

GEG Electromagnetic group of Granada <http://www.geg.ugr.es/>.

GiD The personal pre and post processor, [http://www.gidhome.com/..](http://www.gidhome.com/)

GVT validation tools software developed by electromagnetic compatibility group (University of Catalunya) <http://www.upc.edu/web/gcem>.

INTA Instituto Nacional de Tecnica Aeroespacial, Organismo Público de Investigación especializado en la investigación y desarrollo tecnológico aeroespacial, <http://www.inta.es/>.

NUDT National University of Defense Technology of China, Hunan, Changsha,.

SAE Society of Automotive Engineers, <http://www.sae.org/>.

U.S. MIL-STD United States Defense Standard, <http://www.sae.org/>.

UGR University of Granada <http://www.ugr.es/>.

UPC Polytechnic University of Catalunya.

Aeronautical Projects & Descriptions

A-UGRFDTD Advanced UGRFDTD electromagnetic computer simulation tool (A-UGRFDTD) project consists on the development of a fully functional geometrically conforming FDTD simulator. It is being funded by the Airbus-DF Group and the University of Granada (2012-2016)..

ARROW Aircraft lightning threat Reduction, (EU FP7 CLEAN SKY).

EMHAZ Efficient methods and technologies to handle electromagnetic effects, inclusive lightning strikes to aircraft (EU FP5, 2000-2003).

FULMEN Analysis of Experimental Data and Models for Upgraded Lightning Protection Requirements (EUFP3, 1996-1999).

GEMCAR Guidelines for EM Compatibility Modelling for Automotive Requirements, (computational electromagnetics), Contract no. G3RD-CT-1999-00024.

GENIAL Optimizing Electrical Network In Airplane Composite Structures, (EU CLEAN SKY).

HIRF-SE The High Intensity Radiated Fields Synthetic Environment project aims to develop a computer framework to simulate electro-magnetic phenomena during the development phase. This project is funded by the European Commission and 44 other partners from the EU. The contribution by our group consisted in a fully functional FDTD volumic solver to be integrated within the framework. More information in: <http://www.hirf-se.eu>.

ILDAS In flight lightning sensor on board aircraft (EU FP6, 2006-2009).

MOVEA Statistical prediction of aircraft vulnerability to Electromagnetic threat (HIRF, Lightning, ESD) (French MoDN 2005-2008).

SAFETEL Safe Electromagnetic Telecommunication on Vehicle, Project Reference: IST-2002-506829..

SARITSU Smart Intelligent Aircraft Structures (FP7 Level 2, 2011-2015)..

STRUCTURES Strategies for the Improvement of Critical Infrastructure Resilience to Electromagnetic Attacks (EU FP7, 2012-2015).

UAVEMI This project analyses the electromagnetic immunity of Unmanned Air Vehicles (UAV) under the effect of lightning and High Intensity Radiated Fields (HIRF). It is being developed by a partnership between the Polytechnical University of Catalonia (UPC), the National Institute for Aerospace Technique (INTA) and the University of Granada. Granted by Secretariat of state for research, development and innovation. (January 2014 - December 2017).

List of Figures

1.1	Classification of purely numerical 3D computational electromagnetic methods.	7
1.2	Typical discretizations depending on the numerical method.	9
1.3	Position of the EM fields in Yee's cell.	13
1.4	Wavenumber and frequency domain allowable solutions for a fixed CFLN in 1D.	18
1.5	Numerical phase speed normalized to c_0 as a function of PPW for different CFLN in 1D.	18
2.1	Typical workflow for the thin-panel FDTD simulation.	26
2.2	Two-port linear network equivalent to a planar thin-panel.	26
2.3	Coupling the LTI with FDTD.	27
2.4	Spatial collocation of the tangential EM-Fields in the FC approach.	28
2.5	Cross section of a FDTDcell with a NIBC boundary.	30
2.6	Cross section of a FDTDcell with a SGBC boundary.	35
2.7	CFLN as a function of Q for a fixed mesh resolution $PPW_{\text{coarse}} = 20$ and $N_D = 1$	42
2.8	CFLN as a function of Q for a fixed mesh resolution $PPW_{\text{coarse}} = 20$ and $N_D = 3$	43
2.9	Comparison between heuristically and theoretical CFLNfor a fixed mesh resolution $PPW_{\text{coarse}} = 20$ and $N_D = 1$	43
2.10	Unphysical reflection at by a semi-infinite free-space SGBC region as a function of the ratio between the space-steps. The coarse mesh is meshed with a fixed resolution $PPW_{\text{coarse}} = 100$	45
2.11	Reflection and transmission coefficients (S_{11} and S_{12}) for a uniform normally incident plane wave on a free-space thin-panel for $PPW_{\text{coarse}} = 100$ fixed. Note that we keep the convention of Δ_{fine} for the space step inside the thin-panel even for $\Delta_{\text{coarse}}/\Delta_{\text{fine}} < 1$ for which the discretization outside is actually finer than that inside.	46
2.12	Details of the test-setup for a uniform normally incident plane wave on a thin-panel.	46
2.13	S figure of merit. N_{Dof} stands either for N_L or N_p depending on the technique used.	48

3.1	An schematic view of the mesh approximations needed in a given geometry (dashed blue) in order to apply staircased algorithm, an staircased mesh contour (green) has to be generated. Conformal algorithms allow for a closer to the original geometry mesh (red). Cells that require the use of the conformal algorithm are marked in gray, the rest are treated with the classical FDTD method.	52
3.2	Located of the electric fields $E_{k,v}$ on the closed contour. The magnetic field is assumed to be constant inside the contour.	53
3.3	C-FDTD stencil.	54
3.4	Examples of the CRDM relaxation for $F_{rlx} = 1/3$ in which the geometry (dashed line) intersects the left and right edges that will be used for the simulation, represented by a simplified surface (continuous line).	57
3.5	Surface model of a target sphere with deferents conformal relaxed factor meshing.	57
3.6	Examples of areas and edges deleted by the CRDM method.	58
3.7	Red line represents the diagonal Euclidean distance between two points $p1, p2$. Green, brown, and yellow lines have the same Manhattan distance even for different grid sizes.	60
3.8	Surface model of a target sphere with deferents conformal relaxed factor meshing.	61
3.9	Unwanted connection conflict when using the length average method with separated thin materials.	62
4.4	Comparison of the variation of the RCS at 100MHz as a function of the plane-wave angle of incidence with respect to one the grid axis for a sphere of radius 3 m.	69
4.5	A comparison of the maximum variation (dispersion) of the computed RCS for the computed angles of incidence as a function of the frequency.	69
4.9	Error in the shielding effectiveness ($SE = S_{12}^{-1}$) for a uniform normally incident plane-wave on a conductive thin-panel for SGBC-CNTD using several coarse resolutions. This error is found by $ SE_{sim} - SE_{teo} /SE_{teo}$, with SE_{sim} and SE_{teo} being the simulation and analytical values.	74
4.10	$S_{12} = SE^{-1}$ for an aluminum planar thin-panel with a conductivity $\sigma = 3.456 \cdot 10^7$ S/m and a thickness $th = 0.3$ mm. Space step $\Delta_{coarse} = 2.5$ mm. Moved to put in citation order	76
4.11	$S_{12} = SE^{-1}$ for an infinite homogeneous planar thin-panel, with $\sigma = 100$ S/m, and thickness $th = 10$ mm. Space step $\Delta_{coarse} = 20$ mm.	76
4.12	$S_{12} = SE^{-1}$ for an infinite 3-layer planar thin-panel. Space step $\Delta_{coarse} = 20$ mm.	77
4.13	SE of an indefinite planar thin-panel with a constant conductivity of 10^4 S/m and a width of 0.92 mm. The inset shows a zoom of the planar part. The mesh sizes are $\Delta_{fine} = 6$ mm, $\Delta_{fine} = 0.92/4$ mm.	77
4.14	Microscopic structure of prepreg copper mesh.	78
4.15	Estimated real and imaginary part of the conductivity for an homogeneous equivalent panel of the prepreg copper mesh panel.	78
4.16	Simulated and measurement TE-SE for the equivalent thin panel of thickness of 100 μ m.	79
4.17	SE for an sphere of radius 1m, 200 S/m conductivity and 5 mm thickness (Low skin-depth).	80

4.18	SE for an sphere of radius 1m, 10^3 S/m conductivity and 1 mm thickness (High skin-depth).	81
4.19	Test case for estimating the resistance.	82
4.20	Test-setup to the computation of the resistance at LF for a conductive thin strip aligned with the grid.	83
4.21	Test-setup to the computation of the resistance at LF for a conductive thin strip slated a angle ϕ_S respect to the grid.	84
4.22	Error in the LF resistance as function of the tilted angle with respect to the grid. Conformal results were obtained with NIBC and SGBC algorithms which are identical.	84
5.1	Typical DCI test in nose/tail layout.	86
5.2	Plane-wave polarization and propagation direction.	88
5.3	Location of the surface magnetic field-probes, and cable bulk current-probes.	88
5.4	Transfer function at LF and MF, evaluated in EK0003 positions.	90
5.5	Transfer function at LF and MF, of the bulk current evaluated at EK0003.	91
5.6	Transfer function evaluated of the magnetic field at STP4.	91
5.7	DCI test setup using coaxial return of SIVA-UAV in INTA's Open Area Test Site (OATS).	92
5.8	DCI probes: CP1, CP3, CP5, CP7.	93
5.9	Digital mock-up of of the SIVA	95
5.10	General and zoom views of final FDTD mesh. The upper right inset shows the DCI injection wires attached to the nose and tail of the UAV. In red the internal wire bundles.	96
5.11	Transfer fuction of the current probes.	98
5.12	Bar diagram FSV result considering the comparison between measurements and simulation of current probe CP3.	100
5.13	F7X nacelle.	101
5.14	Probes location of a target nacelle.	102
5.15	Shielding effectiveness of materials with a very low penetration (assuming PEC).	102
5.16	Shielding effectiveness of the CFCs materials used.	104
5.17	Transfer function of the nacelle-SS05.	106
5.18	Transfer function of the nacelle-SS05.	106
6.1	Computer aided CAD and CAE stages.	109
6.2	Speed measured in [GB/s] for UGRFDTD as function of the problem size in [MB], using a different number of threads in a machine based on an Intel-i7-3960X, whose bandwidth is 40GB/s. As expected, the processing speed saturates with the maximum bandwidth of the computer system.	112
6.3	The computational domain is divided into sub-domains according to the number of available computer units. The H-fields in the overlapped region is exchanged between neighbor sub-domains.	112
6.4	Types of defects and flaws, occurred in triangles meshes.	115
6.5	Topology repair: the objects not topologically connected are connected by the conformal mesher.	115
6.6	Dimension reduction.	115

6.7	Classical structured mesh and minimal mesh comparison.	116
6.8	Details of minimal mesh for a curved surface.	116
6.9	EV55 aircraft internal details meshing with conformal mesh.	117
6.10	Structured minimal mesh of thick wires, the topological connections is preserved around the holes.	117
6.11	Conformal mesh: Dimension Reduction	117
6.12	Conformal Mesh of intersection between structures. The mesh adapts itself to preserve the topological ohmic connections in the intersection area.	117
6.13	Conformal Mesh of sharp edge.	117

List of Tables

2.1	$A_{\text{sub-cell}}^{\text{FLOP}}$ for the different sub-cell methods.	47
4.1	RMS error [dBsm] in the interval [10, 100] MHz, and the percentage of cells modified by the LECT for different F_{rlx} values of the conformal method. A cell is considered to have been modified when it is changed by a factor 0.1 or more from its original area value. The CPU time is shown as the number of times employed by the structured case.	68
4.2	RMS error [dBsm] with respect to a MoM-computed reference solution for the monostatic RCS of the NASA Almond, in the interval [0.5, 2] GHz. The third column shows the percentage of LECT-modified cells for the different conformal techniques. A cell is considered to have been modified if its original area is changed by a 10% or more. CPU time is expressed as a ratio with respect to the classic structured case.	70
4.3	Configuration proposed for evaluating the SE of a spherical shell.	79
4.4	Error RMS estimate for a spherical shell with, $\sigma = 200\text{S/m}$, $\text{Th} = 5\text{mm}$, $F_{\text{rlx}} = 0.2$, $\text{CFLN} = 0.9$	80
4.5	Error RMS estimate for a spherical shell with, $\sigma = 10^3\text{S/m}$, $\text{Th} = 1\text{mm}$, $F_{\text{rlx}} = 0.2$, $\text{CFLN} = 0.9$	80
4.6	Errors in DC prediction of a ($\sigma = 20\text{S/m}$), 216mm long x 120 mm width x 2 mm thick meshed with $\Delta_{\text{coarse}} = 6\text{mm}$	83
5.1	FSV results	100
5.2	Engine parts and material definition.	107

Bibliography

- [IEE-5971] (1597.1). Ieee 1597.1 "standard for validation of computational electromagnetics computer modeling and simulations".
- [ED-2010] (2010). Guide to certification of aircraft in a high-intensity radiated field (HIRF) environment, Eurocae ED-107A.
- [A. C. Woo-1993] A. C. Woo, H. T. G. W. and Schuh, M. J. (1993). Benchmark radar targets for the validation of computational electromagnetics programs. *IEEE Antennas and Propagation Magazine*, 35(1):84 – 89.
- [Aftosmis-1998] Aftosmis, M. J., Berger, M. J., and Melton, J. E. (1998). Robust and efficient cartesian mesh generation for component-based geometry. *AIAA journal*, 36(6):952–960.
- [Alvarez-2014] Alvarez, J., Alonso-Rodriguez, J. M., Carbajosa-Cobaleda, H., Cabello, M. R., Angulo, L. D., Gomez-Martin, R., and Garcia, S. G. (2014). DGTD for a class of low-observable targets: A comparison with mom and (2,2) FDTD. *IEEE Antennas and Wireless Propagation Letters*, 13:241–244.
- [Alvarez-2012a] Alvarez, J., Angulo, L., Bandinelli, M., Bruns, H., Francavilla, M., Garcia, S., Guidi, R., Gutierrez, G., Jones, C., Kunze, M., Martinaud, J., Munteanu, I., Panitz, M., Parmantier, J., Pirinoli, P., Reznicek, Z., Salin, G., Schroder, A., Tobola, P., and Vipiana, F. (2012a). EV55: A numerical workbench to test TD/FD codes in HIRF EMC assessment. In *Proc. EUROEM European Electromagnetic*, Toulouse (France).
- [Alvarez-2012b] Alvarez, J., Angulo, L. D., Bandinelli, M., Bruns, H., Francavilla, M., Garcia, S., Guidi, R., Gutierrez, G., Jones, C., Kunze, M., Martinaud, J., Munteanu, I., Panitz, M., Parmantier, J., Pirinoli, P., Reznicek, Z., Salin, G., Schroder, A., Tobola, P., and Vipiana, F. (2012b). HIRF interaction with metallic aircrafts. a comparison between TD and FD methods. In *Electromagnetic Compatibility (EMC EUROPE), 2012 International Symposium on*, pages 1–6.
- [Alvarez-2012c] Alvarez, J., Angulo, L. D., Rubio Bretones, A., and Garcia, S. (2012c). A spurious-free discontinuous Galerkin time-domain method for the accurate modeling of microwave filters. *IEEE Transactions on Microwave Theory and Techniques*, 60(8):2359–2369.

- [Angulo-2012] Angulo, L. D., Greco, S., Cabello, M. R., García, S. G., and Sarto, M. S. (2012). Fdtd techniques to simulate composite air vehicles for emc. In *Advanced Electromagnetics Symposium, AES*.
- [Ansarizadeh-2013] Ansarizadeh, M. (2013). *Calculation of ohe shielding effectiveness of carbon-fiber composite structures*. PhD thesis, The Department of Electrical and Computer Engineering, Montreal, Quebec, Canada.
- [Arslanagić-2013] Arslanagić, S., Hansen, T. V., Mortensen, N. A., Gregersen, A. H., Sigmund, O., Ziolkowski, R. W., and Breinbjerg, O. (2013). A review of the scattering-parameter extraction method with clarification of ambiguity issues in relation to metamaterial homogenization. *IEEE Antennas and Propagation Magazine*, 55(2):91–106.
- [Attene-2013] Attene, M., Campen, M., and Kobbelt, L. (2013). Polygon mesh repairing: An application perspective. *ACM Comput. Surv.*, 45(2):15:1–15:33.
- [Avloni-2007] Avloni, J., Ouyang, M., Florio, L., Henn, A. R., and Sparavigna, A. (2007). Shielding effectiveness evaluation of metallized and polypyrrole-coated fabrics. *Journal of Thermoplastic Composite Materials*, 20(3):241–254.
- [Balanis-2012] Balanis, C. A. (2012). *Advanced engineering electromagnetics*. John Wiley & Sons, Inc., second edition edition.
- [Beggs-1992] Beggs, J., Luebbers, R., Yee, K., and Kunz, K. S. (1992). Finite-difference time-domain implementation of surface impedance boundary conditions. *Antennas and Propagation, IEEE Transactions on*, 40(1):49–56.
- [Benkler-2006] Benkler, S., Chavannes, N., and Kuster, N. (2006). A new 3-D conformal PEC FDTD scheme with user-defined geometric precision and derived stability criterion. *Antennas and Propagation, IEEE Transactions on*, 54(6):1843–1849.
- [Berenger-2000] Berenger, J. P. (2000). A multiwire formalism for the FDTD method. *IEEE Transactions on Electromagnetic Compatibility*, 42(3):257–264.
- [Beylkin-1998] Beylkin, G., Keiser, J. M., and Vozovoi, L. (1998). A new class of time discretization schemes for the solution of nonlinear pdes. *Journal of Computational Physics*, 147(2):362–387.
- [Bischoff-2005] Bischoff, S. and Kobbelt, L. (2005). Structure preserving cad model repair. In *Computer Graphics Forum*, volume 24, pages 527–536. Wiley Online Library.
- [Bouche-2012] Bouche, D., Molinet, F., and Mittra, R. (2012). *Asymptotic methods in electromagnetics*. Springer Science & Business Media.
- [Cabello-2017a] Cabello, M., Angulo, L. D., Alvarez, J., Flintoft, I., Bourke, S., Dawson, J., Martin, R. G., and Garcia, S. G. (2017a). A hybrid crank-nicolson fdtd subgridding boundary condition for lossy thin-layer modeling. *IEEE Transactions on Microwave Theory and Techniques*. Accepted.

- [Cabello-2016] Cabello, M. R., Angulo, L. D., Alvarez, J., Bretones, A. R., Gutierrez, G. G., and Garcia, S. G. (2016). A new efficient and stable 3D conformal FDTD. *IEEE Microwave and Wireless Components Letters*, 26(8):553–555.
- [Cabello-2017b] Cabello, M. R., Fernández, S., Pous, M., Pascual-Gil, E., Angulo, L. D., López, P., Riu, P. J., Gutierrez, G. G., Mateos, D., Poyatos, D., Fernandez, M., Alvarez, J., Pantoja, M. F., Añón, M., Silva, F., Bretones, A. R., Trallero, R., Nuño, L., Escot, D., Martin, R. G., and Garcia, S. G. (2017b). Siva UAV: A case study for the EMC analysis of composite air vehicles. *IEEE Transactions on Electromagnetic Compatibility*, PP(99):1–11.
- [Cangellaris-1991] Cangellaris, A. and Wright, D. (1991). Analysis of the numerical error caused by the stair-stepped approximation of a conducting boundary in FDTD simulations of electromagnetic phenomena. *Antennas and Propagation, IEEE Transactions on*, 39(10):1518–1525.
- [Cessenat-2013] Cessenat, O. (2013). Sophie, an FDTD code on the way to multicore, getting rid of the memory bandwidth bottleneck better using cache. *arXiv preprint arXiv:1301.4539*.
- [Chen-2004] Chen, X., Grzegorzczak, T. M., Wu, B.-I., Pacheco, J., and Kong, J. A. (2004). Robust method to retrieve the constitutive effective parameters of metamaterials. *Phys. Rev. E*, 70:016608.
- [Courant-1967] Courant, R., Friedrichs, K., and Lewy, H. (1967). On the partial difference equations of mathematical physics. *IBM J. Res. Dev.*, 11:215–234.
- [Crank-1947] Crank, J. and Nicolson, P. (1947). A practical method for numerical evaluation of solutions of partial differential equations of the heat-conduction type. In *Mathematical Proceedings of the Cambridge Philosophical Society*, volume 43. Cambridge Univ Press.
- [D’Amore-1997] D’Amore, M. and Sarto, M. S. (1997). Time domain analysis of lightning interactions to aeronautical structures composite materials. In *IEEE Int. EMC Symp.*, pages 397–402, Austin, TX.
- [Dey-1997] Dey, S. and Mittra, R. (1997). A locally conformal finite-difference time-domain (FDTD) algorithm for modeling three-dimensional perfectly conducting objects. *Microwave and Guided Wave Letters, IEEE*, 7(9):273–275.
- [Dey-1999] Dey, S. and Mittra, R. (1999). A conformal finite-difference time-domain technique for modeling cylindrical dielectric resonators. *IEEE Transactions on Microwave Theory and Techniques*, 47(9):1737–1739.
- [Duffy-2006] Duffy, A. P., Martin, A. J. M., Orlandi, A., Antonini, G., Benson, T. M., and Woolfson, M. S. (2006). Feature selective validation (FSV) for validation of computational electromagnetics (CEM). Part I - the FSV method. *IEEE Transactions on Electromagnetic Compatibility*, 48(3):449–459.

- [Edelvik-2004] Edelvik, F. and Weiland, T. (2004). Stable modelling of arbitrary thin slots in the finite-element time-domain method. *International Journal of Numerical Modelling: Electronic Networks, Devices and Fields*, 17(4):365–383.
- [Engquist-1977] Engquist, B. and Majda, A. (1977). Absorbing boundary conditions for numerical simulation of waves. *Proceedings of the National Academy of Sciences*, 74(5):1765–1766.
- [E.Perrin-2010] E.Perrin (2010). *Modelisation des effets indirects de la foudre sur avion composite*. PhD thesis, Univ.Limoges.
- [Fang-1993] Fang, J. and Ren, J. (1993). A locally conformed finite-difference time-domain algorithm of modeling arbitrary shape planar metal strips. *Microwave Theory and Techniques, IEEE Transactions on*, 41(5):830–838.
- [Feliziani-2012] Feliziani, M. and Cruciani, S. (2012). FDTD modeling of impedance boundary conditions by equivalent Iti circuits. *Microwave Theory and Techniques, IEEE Transactions on*, 60(12):3656–3666.
- [Feliziani-1999] Feliziani, M., Maradei, F., and Tribellini, G. (1999). Field analysis of penetrable conductive shields by the finite-difference time-domain method with impedance network boundary conditions (inbcs). *IEEE transactions on electromagnetic compatibility*, 41(4):307–319.
- [Flintoft-2014] Flintoft, I. (2014). Aeg vulture: A finite-difference time-domain solver for electromagnetic applications.
- [Flintoft-2012] Flintoft, I., Dawson, J., Xia, R., Porter, S., and Marvin, A. (2012). Simulation of materials and joints in FDTD using digital filter macro-models. In *Proc. EUROEM European Electromagnetic*, Toulouse (France).
- [Flintoft-2007] Flintoft, I. D., Dawson, J. F., Marvin, A. C., and Porter, S. J. (2007). Development of time-domain surface macro-models from material measurements. In *23rd International Review of Progress in Applied Computational Electromagnetics (ACES)*.
- [Frickey-1994] Frickey, D. (1994). Conversions between S, Z, Y, H, ABCD, and T parameters which are valid for complex source and load impedances. *IEEE Transactions on Microwave Theory and Techniques*, 42(2):205–211.
- [Fusco-1990] Fusco, M. (1990). FDTD algorithm in curvilinear coordinates [em scattering]. *Antennas and Propagation, IEEE Transactions on*, 38(1):76–89.
- [Fusco-1991] Fusco, M. A., Smith, M. V., and Gordon, L. W. (1991). A three-dimensional ftdt algorithm in curvilinear coordinates [em scattering]. *IEEE Transactions on Antennas and Propagation*, 39(10):1463–1471.
- [Garcia-2002] Garcia, S., Lee, T.-W., and Hagness, S. (2002). On the accuracy of the ADI-FDTD method. *IEEE Antennas and Wireless Propagation Letters*, 1(1):31–34.

- [Garcia-2006] Garcia, S., Rubio, R., Bretones, A., and Martin, R. (2006). On the dispersion relation of ADI-FDTD. *IEEE Microwave and Wireless Components Letters*, 16(6):354–356.
- [Garcia-1994] Garcia, S. G. (1994). *Contribuciones al metodo de las diferencias finitas para la resolucion de las ecuaciones de Maxwell en el dominio del tiempo*. PhD thesis, Facultad de Ciencias - Universidad de Granada.
- [Garcia-2003] Garcia, S. G., Bretones, A. R., Olmedo, B. G., and Martín, R. G. (2003). Finite Difference Time Domain methods. In Poljak, D., editor, *Time Domain Techniques in Computational Electromagnetics*, pages 91–132. WIT Press.
- [Garcia-2000] Garcia, S. G., Garcia Olmedo, B., and Gomez Martin, R. (2000). A time-domain near- to far-field transformation for FDTD in two dimensions. *Microwave and Optical Technology Letters*, 27(6):427–432.
- [Gedney-1996] Gedney, S. D. (1996). An anisotropic perfectly matched layer-absorbing medium for the truncation of FDTD lattices. *IEEE Transactions on Antennas and Propagation*, 44(12):1630–1639.
- [Gil-2011] Gil, E. P. and Gutierrez, G. G. (2011). Simplification and cleaning of complex CAD models for EMC simulations. In *International Symposium on Electromagnetic Compatibility EMC Europe*, York (UK).
- [Glassner-1989] Glassner, A. S. (1989). *An introduction to ray tracing*. Elsevier.
- [Gonzalez-1996] Gonzalez, S., Materdey Bao-Hung, T., Garcia Olmedo, B., and Gomez Martin, R. (1996). Volume-conformation method to study scattering by pec objects with FDTD. *IEE Proceedings Microwaves, Antennas and Propagation*, 143(2):131–136.
- [Gottlieb-1987] Gottlieb, D., Lustman, L., and Tadmor, E. (1987). Stability analysis of spectral methods for hyperbolic initial-boundary value systems. *SIAM journal on numerical analysis*, 24(2):241–256.
- [Gottschalk-1996] Gottschalk, S., Lin, M. C., and Manocha, D. (1996). Obbtree: A hierarchical structure for rapid interference detection. In *Proceedings of the 23rd annual conference on Computer graphics and interactive techniques*, pages 171–180. ACM.
- [Gustavsen-1999] Gustavsen, B. and Semlyen, A. (1999). Rational approximation of frequency domain responses by vector fitting. *Power Delivery, IEEE Transactions on*, 14(3):1052–1061.
- [Gustavsen-2001] Gustavsen, B. and Semlyen, A. (2001). Enforcing passivity for admittance matrices approximated by rational functions. *Power Systems, IEEE Transactions on*, 16(1):97–104.
- [Gutierrez-2014] Gutierrez, G., Alvarez, J., Pascual-Gil, E., Bandinelli, M., Guidi, R., Martorelli, V., Fernandez Pantoja, M., Ruiz Cabello, M., and Garcia, S. (2014). HIRF virtual testing on the C-295 Aircraft: On the application of a pass/fail criterion and the FSV method. *IEEE Transactions on Electromagnetic Compatibility*, 56(4):854–863.

- [Gutierrez-2016] Gutierrez, G. G., Mateos, D., Cabello, M. R., Pascual-Gil, E., Angulo, L. D., and Garcia, S. G. (2016). On the design of aircraft electrical structure networks. *IEEE Transactions on Electromagnetic Compatibility*, 58(2):401 – 408.
- [Gutierrez-2012] Gutierrez, G. G., Romero, S. F., Alvarez, J., Garcia, S. G., and Gil, E. P. (2012). On the use of FDTD for HIRF validation and certification. *Progress In Electromagnetics Research Letters*, 32:145–156.
- [Han-2006] Han, M., Dutton, R., and Fan, S. (2006). Model dispersive media in finite-difference time-domain method with complex-conjugate pole-residue pairs. *IEEE Microwave and Wireless Components Letters*, 16(3):119 –121.
- [Hill-1998] Hill, D. A. (1998). Plane wave integral representation for fields in reverberation chambers. *IEEE Transactions on Electromagnetic Compatibility*, 40(3):209–217.
- [Holland-1983] Holland, R. (1983). Finite-difference solution of maxwell's equations in generalized nonorthogonal coordinates. *IEEE Transactions on Nuclear Science*, 30(6):4589–4591.
- [Holland-1993] Holland, R. (1993). Pitfalls of staircase meshing. *Electromagnetic Compatibility, IEEE Transactions on*, 35(4):434–439.
- [Holland-1994] Holland, R. (1994). Finite-difference time-domain (fdtd) analysis of magnetic diffusion. *IEEE Transactions on Electromagnetic Compatibility*, 36(1):32–39.
- [Holland-1981] Holland, R. and Simpson, L. (1981). Finite-difference analysis of EMP coupling to thin struts and wires. *Electromagnetic Compatibility, IEEE Transactions on*, EMC-23(2):88 –97.
- [Holloway-2005] Holloway, C., Sarto, M., and Johansson, M. (2005). Analyzing carbon-fiber composite materials with equivalent-layer models. *Electromagnetic Compatibility, IEEE Transactions on*, 47(4):833–844.
- [Hu-2010] Hu, F. G., Song, J., and Kamgaing, T. (2010). Modeling of multilayered media using effective medium theory. In *19th Topical Meeting on Electrical Performance of Electronic Packaging and Systems*, pages 225–228.
- [Hue-2005] Hue, Y.-K., Teixeira, F. L., Martin, L. S., and Bittar, M. S. (2005). Three-dimensional simulation of eccentric lwd tool response in boreholes through dipping formations. *IEEE Transactions on Geoscience and Remote Sensing*, 43(2):257–268.
- [Hwang-2011] Hwang, K. and Jotwani, N. (2011). *Advanced Computer Architecture*, 3e. McGraw-Hill Education.
- [Hwang-2001] Hwang, K.-P. and Cangellaris, A. C. (2001). Effective permittivities for second-order accurate FDTD equations at dielectric interfaces. *IEEE Microwave and Wireless Components Letters*, 11(4):158–160.
- [Hwang-1999] Hwang, K.-P. and Jin, J.-M. (1999). Application of a hyperbolic grid generation technique to a conformal PML implementation. *Microwave and Guided Wave Letters, IEEE*, 9(4):137 –139.

- [IEEE-1990] IEEE (1990). Ieee standard radar definitions. *IEEE Std 686-1990*.
- [J. F. Dawson-2017] J. F. Dawson, I. D. Flintoft, S. A. B., M. P. Robinson, M. R. C., and S. G. Garcia, J. A. (2017). Face centered anisotropic surface impedance boundary conditions in fdtd: Improved performance of staircased mesh for shielding problems,. *IEEE (Accepted)*.
- [Jauregui-2013] Jauregui, R., Aragon, M., and Silva, F. (2013). The role of uncertainty in the feature selective validation (fsv) method. *IEEE Transactions on Electromagnetic Compatibility*, 55(1):217–220.
- [Jauregui-2014] Jauregui, R., Pous, M., and Silva, F. (2014). Use of reference limits in the feature selective validation (fsv) method. In *Electromagnetic Compatibility (EMC Europe), 2014 International Symposium on*, pages 1031–1036. IEEE.
- [J.Boissin-2012] J.Boissin (2012). In-flight lightning measurements and reconstruction on a metallic and composite aircraft. *ESA Workshop Aerospace EMC*.
- [Junkin-2011] Junkin, G. (2011). Conformal FDTD modeling of imperfect conductors at millimeter wave bands. *IEEE Transactions on Antennas and Propagation*, 59(1):199–205.
- [Junkin-2007] Junkin, G. and Parron, J. (2007). A robust 3D mesh generator for the dey-mitra conformal FDTD algorithm. In *Proc. Second European Conf. Antennas and Propagation EuCAP 2007*, pages 1–6.
- [Junqua-2007] Junqua, I., Guibert, L., and Parmantier, J. P. (2007). Assessment of high frequency coupling in a generic object by the power balance method. In *2007 18th International Zurich Symposium on Electromagnetic Compatibility*, pages 397–400.
- [Junqua-2011] Junqua, I., Parmantier, J. P., and Ridet, M. (2011). Modeling of high frequency coupling inside oversized structures by asymptotic and pwb methods. In *2011 International Conference on Electromagnetics in Advanced Applications*, pages 68–71.
- [Jurgens-1993] Jurgens, T. and Taflove, A. (1993). Three-dimensional contour FDTD modeling of scattering from single and multiple bodies. *IEEE TRANSACTIONS ON ANTENNAS AND PROPAGATION*, 41(12).
- [Jurgens-1992] Jurgens, T., Taflove, A., Umashankar, K., and Moore, T. (1992). Finite-difference time-domain modeling of curved surfaces [em scattering]. *Antennas and Propagation, IEEE Transactions on*, 40(4):357–366.
- [Kaneda-1997] Kaneda, N., Houshmand, B., and Itoh, T. (1997). FDTD analysis of dielectric resonators with curved surfaces. *IEEE Transactions on Microwave Theory and Techniques*, 45(9):1645–1649.
- [Kantartzis-2001] Kantartzis, N. V., Kosmanis, T. I., Yioultis, T. V., and Tsiboukis, T. D. (2001). A nonorthogonal higher-order wavelet-oriented fdtd technique for 3-d waveguide structures on generalized curvilinear grids. *IEEE transactions on magnetics*, 37(5):3264–3268.

- [Kantartzis-2000] Kantartzis, N. V., Prokopidis, K. P., Tsiboukis, T. D., and Kriezis, E. E. (2000). A nonorthogonally-oriented higher-order fdtd technique for 3-d waveguide and antenna structures on curvilinear grids. In *Antennas, Propagation and EM Theory, 2000. Proceedings. ISAPE 2000. 5th International Symposium on*, pages 65–68.
- [Kantartzis-2008a] Kantartzis, N. V. and Tsiboukis, T. D. (2008a). Modern emc analysis techniques volume i: time-domain computational schemes. *Synthesis Lectures on Computational Electromagnetics*, 3(1):1–224.
- [Kantartzis-2008b] Kantartzis, N. V. and Tsiboukis, T. D. (2008b). Modern emc analysis techniques volume ii: models and applications. *Synthesis Lectures on Computational Electromagnetics*, 3(1):1–238.
- [Karkkainen-2003] Karkkainen, M. (2003). Subcell FDTD modeling of electrically thin dispersive layers. *Microwave Theory and Techniques, IEEE Transactions on*, 51(6):1774–1780.
- [Keller-1962] Keller, J. B. (1962). Geometrical theory of diffraction. *JOSA*, 52(2):116–130.
- [Kim-2010] Kim, H.-J. and Tautges, T. J. (2010). Ebmesh: An embedded boundary meshing tool. In *Proceedings of the 19th International Meshing Roundtable*, pages 227–242. Springer.
- [Kobidze-2010] Kobidze, G. (2010). Implementation of collocated surface impedance boundary conditions in FDTD. *Antennas and Propagation, IEEE Transactions on*, 58(7):2394–2403.
- [Kouyoumjian-1974] Kouyoumjian, R. G. and Pathak, P. H. (1974). A uniform geometrical theory of diffraction for an edge in a perfectly conducting surface. *Proceedings of the IEEE*, 62(11):1448–1461.
- [Kunz-1993] Kunz, K., Steich, D., and Luebbers, R. J. (1993). Low frequency shielding effects of a conducting shell with an aperture: Response of an internal wire. *IEEE Transactions on Electromagnetic Compatibility*, 34(3):370–373.
- [Lax-1956] Lax, P. D. and Richtmyer, R. D. (1956). Survey of the stability of linear finite difference equations. *Communications on pure and applied mathematics*, 9(2):267–293.
- [Lee-2011] Lee, R. T., Maloney, J. G., Baker, B. N., and Landgren, D. W. (2011). Fdtd in curvilinear coordinates using a rectangular fdtd formulation. In *Antennas and Propagation (APSURSI), 2011 IEEE International Symposium on*, pages 2326–2329.
- [Leontovich-1948] Leontovich, M. (1948). Investigation of propagation of radio waves, part ii. *Printing House of the Academy of Sciences, Moscow, USSR*.
- [Lewis-1969] Lewis, R. M. and Boersma, J. (1969). Uniform asymptotic theory of edge diffraction. *Journal of Mathematical physics*, 10(12):2291–2305.
- [Li-2015] Li, P., Shi, Y., Jiang, L. J., and Bağcı, H. (2015). DGTD analysis of electromagnetic scattering from penetrable conductive objects with ibc. *Antennas and Propagation, IEEE Transactions on*, 63(12):5686–5697.

- [Lorensen-1987] Lorensen, W. E. and Cline, H. E. (1987). Marching cubes: A high resolution 3d surface construction algorithm. *SIGGRAPH Comput. Graph.*, 21(4):163–169.
- [Luebbers-1991] Luebbers, R., Kunz, K., Schneider, M., and Hunsberger, F. (1991). A finite-difference time-domain near zone to far zone transformation [electromagnetic scattering]. *IEEE Transactions on Antennas and Propagation*, 39(4):429–433.
- [M. Apra-2008] M. Apra, M. D’Amore, K. G. M. S. V. V. (2008). Lightning indirect effects certification of a transport aircraft by numerical simulation. *IEEE Trans. On EMC, Special Issue “EMC in Aerospace”*.
- [M. R. Cabello-2017] M. R. Cabello, L. D. Angulo, A. R. B. R. G. M. S. G. G. J. A. (2017). A novel subgridding scheme for arbitrarily dispersive thin-layer modeling,. In Conference, I. M.-S. I., editor, *Numerical Electromagnetic and Multiphysics Modeling and Optimization for RF, Microwave, and Terahertz Applications (NEMO)*.
- [Maloney-1992] Maloney, J. and Smith, G. (1992). The efficient modeling of thin material sheets in the finite-difference time-domain (FDTD) method. *Antennas and Propagation, IEEE Transactions on*, 40(3):323–330.
- [M.Apra-2001] M.Apra (2001). Vam-life: Virtual aircraft electromagnetic lightning indirect effect evaluation. *SAE Trans*.
- [Merewether-1980] Merewether, D., Fisher, R., and Smith, F. (1980). On implementing a numeric Huygen’s source scheme in a finite difference program to illuminate scattering bodies. *Nuclear Science, IEEE Transactions on*, 27(6):1829–1833.
- [Meyer-2008] Meyer, M., Flourens, F., Rouquette, J. A., and Delnevo, A. (2008). Modeling of lightning indirect effects in cfrp aircraft. In *2008 International Symposium on Electromagnetic Compatibility - EMC Europe*, pages 1–5.
- [Mezzanotte-1995] Mezzanotte, P., Roselli, L., and Sorrentino, R. (1995). A simple way to model curved metal boundaries in fdtd algorithm avoiding staircase approximation. *IEEE Microwave and Guided Wave Letters*, 5(8):267–269.
- [Miller-1997] Miller, E. K. (1997). Computational electromagnetics. In *The Electrical Engineering Handbook, Second Edition*. CRC Press.
- [Minami-2014] Minami, T., Hibino, M., Hiraishi, T., Iwashita, T., and Nakashima, H. (2014). Automatic parameter tuning of three-dimensional tiled fdtd kernel. In *International Conference on High Performance Computing for Computational Science*, pages 284–297. Springer.
- [Moglie-2006] Moglie, F. and Pastore, A. P. (2006). Fdtd analysis of plane wave superposition to simulate susceptibility tests in reverberation chambers. *IEEE Transactions on electromagnetic compatibility*, 48(1):195–202.
- [Morton-2005] Morton, K. W. and Mayers, D. F. (2005). *Numerical Solution of Partial Differential Equations*. Cambridge University Press.

- [Mur-1998] Mur, G. (1998). The fallacy of edge elements. *Magnetics, IEEE Transactions on*, 34(5):3244–3247.
- [Nadobny-2003] Nadobny, J., Sullivan, D., Wlodarczyk, W., Deuflhard, P., and Wust, P. (2003). A 3-D tensor FDTD-formulation for treatment of sloped interfaces in electrically inhomogeneous media. *IEEE Transactions on Antennas and Propagation*, 51(8):1760–1770.
- [Nayyeri-2013] Nayyeri, V., Soleimani, M., and Ramahi, O. (2013). Modeling graphene in the finite-difference time-domain method using a surface boundary condition. *Antennas and Propagation, IEEE Transactions on*, 61(8):4176–4182.
- [Nielson-1991] Nielson, G. M. and Hamann, B. (1991). The asymptotic decider: Resolving the ambiguity in marching cubes. In *Proceedings of the 2Nd Conference on Visualization '91, VIS '91*, pages 83–91, Los Alamitos, CA, USA. IEEE Computer Society Press.
- [Nieter-2009] Nieter, C., Cary, J. R., Werner, G. R., Smithe, D. N., and Stoltz, P. H. (2009). Application of dey–mittra conformal boundary algorithm to 3d electromagnetic modeling. *Journal of Computational Physics*, 228(21):7902–7916.
- [Oh-1995] Oh, K. S. and Schutt-Aine, J. (1995). An efficient implementation of surface impedance boundary conditions for the finite-difference time-domain method. *Antennas and Propagation, IEEE Transactions on*, 43(7):660–666.
- [Okoniewski-1997] Okoniewski, M., Mrozowski, M., and Stuchly, M. (1997). Simple treatment of multi-term dispersion in fdtd. *IEEE Microwave and Guided Wave Letters*, 7(5):121–123.
- [Orlandi-2006a] Orlandi, A., Antonini, G., Ritota, C., and Duffy, A. (2006a). Enhancing Feature Selective Validation (FSV) interpretation of EMC/SI results with Grade-Spread. In *Proc. IEEE Symposium on Electromagnetic Compatibility*, Portland (USA).
- [Orlandi-2006b] Orlandi, A., Duffy, A. P., Archambeault, B., Antonini, G., Coleby, D. E., and Connor, S. (2006b). Feature selective validation (FSV) for validation of computational electromagnetics (CEM). Part II - assessment of FSV performance. *IEEE Transactions on Electromagnetic Compatibility*, 48(3):460–467.
- [Parmantier-2013] Parmantier, J. (2013). Indirect effects of lightning on aircraft and rotorcraft. *Journal Aerospace Lab., ONERA*.
- [Pereda-1998] Pereda, J. A., Enrique Fernández del Río, J., Wysocka–Schillak, F., Prieto, A., and Vegas, A. (1998). On the use of linear–prediction techniques to improve the computational efficiency of the FDTD method for the analysis of resonant structures. *IEEE Transactions on Microwave Theory and Techniques*, 46(7):1027–1032.
- [Perrin-2013] Perrin, E., Guiffaut, C., Reineix, A., and Tristant, F. (2013). Using a design-of-experiment technique to consider the wire harness load impedances in the fdtd model of an aircraft struck by lightning. *IEEE Transactions on Electromagnetic Compatibility*, 55(4):747–753.

- [Rachidi-2012] Rachidi, F. (2012). A review of field-to-transmission line coupling models with special emphasis to lightning-induced voltages on overhead lines. *IEEE Transactions on Electromagnetic Compatibility*, 54(4):898–911.
- [Radasky-2004] Radasky, W. A., Baum, C. E., and Wik, M. W. (2004). Introduction to the special issue on high-power electromagnetics (hpem) and intentional electromagnetic interference (iem). *IEEE Transactions on Electromagnetic Compatibility*, 46(3):314–321.
- [Railton-1995] Railton, C. and Craddock, I. (1995). Analysis of general 3-D PEC structures using improved CPFDTD algorithm. *Electronics Letters*, 31(20):1753–1754.
- [Ramadan-2015] Ramadan, O. (2015). On the equivalence of the stability of the de and je ade-fdtd schemes for implementing the modified lorentz dispersive model. *IEEE Microwave and Wireless Components Letters*, 25(7):487–488.
- [Rasek-2008] Rasek, G. and Loos, S. (2008). Correlation of direct current injection (DCi) and free-field illumination for HIRF certification. *IEEE Transactions on Electromagnetic Compatibility*, 50(3):499–503.
- [Rasek-2011] Rasek, G. A. and Gabrišák, M. (2011). Wire bundle currents for high intensity radiated fields (hirf) and indirect effects of lightning (iel) with focus on bulk current injection (bci) test. In *Radioelektronika (RADIOELEKTRONIKA), 2011 21st International Conference*, pages 1–10. IEEE.
- [Rasek-2015] Rasek, G. A., Schröder, A., Tobola, P., Řezníček, Z., Loos, S. E., Tischler, T., and Brüns, H.-D. (2015). Hirf transfer function observations: Notes on results versus requirements and certification approach. *IEEE Transactions on Electromagnetic Compatibility*, 57(2):195–202.
- [Remis-2000] Remis, R. F. (2000). On the stability of the finite-difference time-domain method. *Journal of Computational Physics*, 163(1):249–261.
- [Remis-2006] Remis, R. F. (2006). Stability of {FDTD} on nonuniform grids for maxwell's equations in lossless media. *Journal of Computational Physics*, 218(2):594 – 606.
- [Richtmyer-1967] Richtmyer, R. D. and Morton, K. W. (1967). *Numerical solution of partial differential equations*. Interscience Publishers a division of John Wiley & Sons.
- [Ritter-1997] Ritter, J. and Arndt, F. (1997). A generalized 3d subgrid technique for the finite-difference time domain method. In *Microwave Symposium Digest, 1997., IEEE MTT-S International*, volume 3, pages 1563–1566 vol.3.
- [Ritter-2015] Ritter, J., Benjes, M., Murso, M., Wulf, D., and Lange, S. (2015). A stable subgridding finite difference time domain method on multi-gpu cluster. In *2015 IEEE International Symposium on Electromagnetic Compatibility (EMC)*, pages 507–511.
- [Romero-2012] Romero, S. F., Gutierrez, G. G., Morales, A. L., and Cancela, M. A. (2012). Validation procedure of low level coupling tests on real aircraft structure. *International Symposium on Electromagnetic Compatibility EMC Europe*.

- [Rosa-2008] Rosa, I. M. D., Sarasini, F., Sarto, M. S., and Tamburrano, A. (2008). Emc impact of advanced carbon fiber/carbon nanotube reinforced composites for next-generation aerospace applications. *IEEE Transactions on Electromagnetic Compatibility*, 50(3):556–563.
- [Rouf-2009] Rouf, H., Costen, F., and Garcia, S. (2009). 3D crank-nicolson finite difference time domain method for dispersive media. *Electronics Letters*, 45(19):961–962.
- [Salvador G. Garcia-2005] Salvador G. Garcia, Rubio Bretones, A., Olmedo, B. G., and Martín, R. G. (2005). New trends in FDTD methods in computational electrodynamics: Unconditionally stable schemes. In *Recent Res. Development in Electronics*. Transworld Research Network.
- [Sarto-1999] Sarto, M. (1999). A new model for the FDTD analysis of the shielding performances of thin composite structures. *Electromagnetic Compatibility, IEEE Transactions on*, 41(4):298–306.
- [Sarto-2014] Sarto, M. S., Greco, S., and Tamburrano, A. (2014). Shielding effectiveness of protective metallic wire meshes: Em modeling and validation. *IEEE Transactions on Electromagnetic Compatibility*, 56(3):615–621.
- [Schmidt-2004] Schmidt, S. and Lazzi, G. (2004). Use of the fdtd thin-strut formalism for biomedical telemetry coil designs. *IEEE Transactions on Microwave Theory and Techniques*, 52(8):1952–1956.
- [Schneider-2010] Schneider, J. B. (2010). *Understanding the Finite-Difference Time-Domain Method*.
- [Schröder-2014] Schröder, A., Rasek, G. A., Brüns, H. D., Řezníček, Z., Kučera, J., Loos, S. E., and Schuster, C. (2014). Analysis of high intensity radiated field coupling into aircraft using the method of moments. *IEEE Transactions on Electromagnetic Compatibility*, 56(1):113–122.
- [Schuster-2000] Schuster, C., Christ, A., and Fichtner, W. (2000). Review of FDTD time-stepping schemes for efficient simulation of electric conductive media. *Microw. Opt. Technol. Letters*, Vol. 25:pp. 16–21.
- [Sewell-2005] Sewell, P., Benson, T., Christopoulos, C., Thomas, D., Vukovic, A., and Wykes, J. (2005). Transmission-line modeling (tlm) based upon unstructured tetrahedral meshes. *Microwave Theory and Techniques, IEEE Transactions on*, 53(6):1919–1928.
- [Sherman-1995] Sherman, B. (1995). Md-90 transport aircraft lightning induced transient level evaluation by time domain three dimensional finite difference modeling. *ICOLSE*.
- [Singh-2010] Singh, G., Tan, E. L., and Chen, Z. N. (2010). A split-step FDTD method for 3-d maxwell's equations in general anisotropic media. *Antennas and Propagation, IEEE Transactions on*, 58(11):3647–3657.
- [Smartt-2013] Smartt, C., Christopoulos, C., Sewell, P., and Greedy, S. (2013). Efficient modelling of a reverberation chamber environment in the time domain. In *Electromagnetic Compatibility (EMC EUROPE), 2013 International Symposium on*, pages 354–358. IEEE.

- [Smith-2014] Smith, S. and Furse, C. (2014). A tutorial on stochastic fdtd. In *2014 IEEE Antennas and Propagation Society International Symposium (APSURSI)*, pages 1–2.
- [Steeds-1996] Steeds, M. W., Broschat, S. L., and Schneider, J. B. (1996). A comparison of two conformal methods for fdtd modeling. *IEEE Transactions on Electromagnetic Compatibility*, 38(2):181–187.
- [Sullivan-2000] Sullivan, D. M. (2000). *Electromagnetic Simulation Using The FDT Method*. IEEE Microwave Theory and Technique Society.
- [Taflove-1995] Taflove, A. (1995). *Computational Electrodynamics: The Finite-Difference Time-Domain Method*. Artech House, Boston.
- [Taflove-2005] Taflove, A. and Hagness, S. C. (2005). *Computational Electrodynamics The Finite-Differences Time Domain Method*. Artech House.
- [Taflove-2013] Taflove, A., Oskooi, A., and Johnson, S. G. (2013). *Advances in FDTD computational electrodynamics: photonics and nanotechnology*. Artech house.
- [Taflove-1983] Taflove, A. and Umashankar, K. (1983). Radar cross section of general three-dimensional scatterers. *IEEE Transactions on Electromagnetic Compatibility*, EMC-25(4):433–440.
- [Tesche-2008] Tesche, F.-M. (2008). Electromagnetic field shielding of a spherical shell—revisited. *Forum for Electromagnetic Research Methods and Application Technologies (FERMAT)*.
- [Thiele-1975] Thiele, G. and Newhouse, T. (1975). A hybrid technique for combining moment methods with the geometrical theory of diffraction. *IEEE Transactions on Antennas and Propagation*, 23(1):62–69.
- [Thomas-1949] Thomas, L. H. (1949). Elliptic problems in linear difference equations over a network. *Watson Sci. Comput. Lab. Rept., Columbia University, New York*, 1.
- [T.Hubing-2008] T.Hubing (2008). Survey of current computational electromagnetics techniques and software. *Clemson Univ.Tech.Report*.
- [Triverio-2007] Triverio, P., Grivet-Talocia, S., Nakhla, M. S., Canavero, F. G., and Achar, R. (2007). Stability, causality, and passivity in electrical interconnect models. *IEEE Transactions on Advanced Packaging*, 30(4):795–808.
- [Ufimtsev-1971] Ufimtsev, P. Y. (1971). Method of edge waves in the physical theory of diffraction. Technical report, DTIC Document.
- [Ufimtsev-1991] Ufimtsev, P. Y. (1991). Elementary edge waves and the physical theory of diffraction. *Electromagnetics*, 11(2):125–160.
- [Ufimtsev-2007] Ufimtsev, P. Y. (2007). *Fundamentals of the physical theory of diffraction*. John Wiley & Sons.

- [Volski-2009] Volski, V. and Vandenbosch, G. A. (2009). Full-wave electromagnetic modelling of fabrics and composites. *Composites Science and Technology*, 69(2):161–168.
- [VonNeumann-1950] VonNeumann, J. and Richtmyer, R. D. (1950). A method for the numerical calculation of hydrodynamic shocks. *Journal of applied physics*, 21(3):232–237.
- [Wait-1955] Wait, J. R. (1955). Reflection at arbitrary incidence from a parallel wire grid. *Applied Scientific Research, Section A*, 4(1):393–400.
- [Wang-2014] Wang, J., Zhou, B., Shi, L., Gao, C., and Chen, B. (2014). A novel 3-D HIE-FDTD method with one-step leapfrog scheme. *Microwave Theory and Techniques, IEEE Transactions on*, 62(6):1275–1283.
- [Wang-2002] Wang, S., Teixeira, F. L., Lee, R., and Lee, J.-F. (2002). Optimization of subgridding schemes for FDTD. *IEEE Microwave and Wireless Components Letters*, 12(6):223–225.
- [White-1997] White, M., Iskander, M., and Huang, Z. (1997). Development of a multigrid FDTD code for three-dimensional applications. *Antennas and Propagation, IEEE Transactions on*, 45(10):1512–1517.
- [Woo-1993] Woo, A., Wang, H., Schuh, M., and Sanders, M. (1993). Em programmer's notebook-benchmark radar targets for the validation of computational electromagnetics programs. *Antennas and Propagation Magazine, IEEE*, 35(1):84–89.
- [Xiao-2005] Xiao, K., Pommerenke, D. J., and Drewniak, J. L. (2005). A three-dimensional fdttd subgridding method with separate spatial and temporal subgridding interfaces. In *Electromagnetic Compatibility, 2005. EMC 2005. 2005 International Symposium on*, volume 2, pages 578–583. IEEE.
- [Xiao-2004] Xiao, T. and Liu, Q. (2004). Enlarged cells for the conformal FDTD method to avoid the time step reduction. *Microwave and Wireless Components Letters, IEEE*, 14(12):551–553.
- [Xiao-2008] Xiao, T. and Liu, Q. H. (2008). A 3-D enlarged cell technique (ECT) for the conformal FDTD method. *Antennas and Propagation, IEEE Transactions on*, 56(3):765–773.
- [Yee-1966] Yee, K. (1966). Numerical solution of initial boundary value problems involving Maxwell's equations in isotropic media. *IEEE Transactions on Antennas and Propagation*, 14(3):302–307.
- [Yu-2005] Yu, W., Liu, Y., Su, T., Hunag, N.-T., and Mittra, R. (2005). A robust parallel conformal finite-difference time-domain processing package using the MPI library. *IEEE Antennas and Propagation Magazine*, 43(3):39–59.
- [Yu-2000] Yu, W. and Mittra, R. (2000). A conformal FDTD algorithm for modeling perfectly conducting objects with curve-shaped surfaces and edges. *Microwave and Optical Technology Letters*, 27(2):136–138.

- [Yu-2001] Yu, W. and Mittra, R. (2001). A conformal finite difference time domain technique for modeling curved dielectric surfaces. *Microwave and Wireless Components Letters, IEEE*, 11(1):25–27.
- [Yu-2006] Yu, W., Mittra, R., Su, T., Liu, Y., and Yang, X. (2006). *Parallel Finite-Difference Time-Domain Method*. Artech House, Inc.
- [Yu-2011] Yu, W., Yang, X., Liu, Y., Mittra, R., and Muto, A. (2011). *Advanced FDTD Methods (Parallelization, Acceleration, and Engineering Applications)*. Artech House.
- [Zagorodnov-2003] Zagorodnov, I., Schuhmann, R., and Weiland, T. (2003). A uniformly stable conformal FDTD-method in cartesian grids. *International Journal of Numerical Modelling: Electronic Networks, Devices and Fields*, 16(2):127–141.
- [Zagorodnov-2007] Zagorodnov, I., Schuhmann, R., and Weiland, T. (2007). Conformal FDTD-methods to avoid time step reduction with and without cell enlargement. *Journal of Computational Physics*, 225(2):1493 – 1507.
- [Zemanian-1963] Zemanian, A. (1963). An n-port realizability theory based on the theory of distributions. *IEEE Transactions on Circuit Theory*, 10(2):265–274.

Curriculum Vitae

Developer in numerical methods in engineering, with special focus in computational electromagnetism and computational geometry methods. Deep experience in the design and development of large scale, high performance and cross platform numerical simulation tools. In-depth knowledge of the complete problem solving cycle: modeling, simulation, validation and post-processing, with emphasis in Electromagnetic Compatibility. The aforementioned tasks have been developed and applied within the framework of several aeronautical projects.

Personal Information

Name: Miguel D. Ruiz-Cabello Núñez

Email miguelrcn@gmail.com

Nationality: Spanish

Technical Skills

- **Programming Languages:** C/C++, Python, Python/Django, FORTRAN, MATLAB, Unix shell.
- **High Performance Computing libraries:** MPI, OpenMP, OpenCL, OpenMP, C++11 (<threads>).
- **Operating Systems:** Linux (Debian, Ubuntu), Windows.
- **IDE:** MS Visual Studio, Eclipse, NetBeans
- **Tools:** L^AT_EX, CMake, make, Git, Subversion, mahematica, valgrind, FreeCad, Paraview.
- **Strong background in algorithm implementation.**

Professional Experience

Project Research Associate

2011 - Present

University of Granada

Granada, Spain

- **Numerical simulators:** Research, development and validation of numerical techniques in FDTD simulations for EMC problems. Part of the development team of the UGRFDTD tool.
- **Geometrical Meshers:** Design, development and testing of light and fast cartesian/conformal mesh generation methods for complex geometries.
- **Post-processing and visualization techniques** (Paraview, mayavi, vtk, matplotlib)
- **Expertise in python, Matlab and parallel C++11 & FORTRAN with MPI and OpenMP** (applied to the development of the previous tools).

Research Internship

January 2013 - April 2013

University of Roma: Dipartimento di Ingegneria Astronautica, Elettrica ed Energetica (DIAEE)

Rome, Italy

Supervisor: Professor Maria Sabrina Sarto.

During this period (3-month) I developed a new computational techniques for the treatment of aeronautical materials.

Instructor 2013 - 2015

University of Granada Granada, Spain

Co-taught undergraduate level courses. Shared responsibility for lectures, lab sessions, exams, coursework assignments, and grades. table **PhD-student Scholarship** 2011 - 2015

University of Granada Granada, Spain

Granted by Secretariat of state for research, development and innovation (4-years).

Patent

- **OpenSEMBA**: Coauthor of the open source project OpenSEMBA for the definition of data structures for electromagnetic simulations, downloadable from <https://github.com/OpenSEMBA/OpenSEMBA>.

Education

Ph.D. in Physic 2017

University of Granada Granada, Spain

Dissertation Topic: *Subcell FDTD Techniques for Electromagnetic Compatibility Assessemnt in Aeronautics*.

Advisor: Professor Salvador Gonzalez Garcia

M.Sc., Physics and Mathematics 2011

University of Granada Granada, Spain

Thesis: Electromagnetic Models for Thin Panels in FDTD

Advisors: Professor Salvador Gonzalez Garcia

With special focus on numerical methods and discrete mathematics.

Bachelor's in Physics 2004 - 2011

University of Granada Granada, Spain

With special focus on electromagnetic, optics, and electronic devices.

Publications

1. **Ruiz-Cabello, Miguel**; Fernandez, S.; Pous, M.; Pascual-Gil, E.; Angulo, L. D.; Lopez, P.; Riu, P. J.; Gutierrez, G. G.; Mateos, D.; Poyatos, D.; Fernandez, M.; Alvarez, J.; Fernandez, M.; Añón, M.; Silva, F.; Bretones, A. R.; Trallero, R.; Nuno, L.; Escot, D.; Martin, R. G.; Garcia, S. G.
A benchmark for EMC Simulations of UAVs including composite materials.
IEEE Transactions on Electromagnetic Compatibility, **2017**.
2. Gutierrez, G. G. ; Mateos, D.; **Ruiz-Cabello, Miguel**; Pascual-Gil, E.; Angulo, L. D.; Garcia, S.

- On the design of Aircraft Electrical Structure Networks.
IEEE Transactions on Electromagnetic Compatibility, **2016**.
3. **Ruiz-Cabello, Miguel**; L. D. Angulo; J. Alvarez; I. D. Flintoft; S. Bourke; J. Dawson; R. G. Martin; S. G. Garcia,
A hybrid Crank-Nicolson FDTD subgridding boundary condition for lossy thin-layer modeling *IEEE Transactions on Microwave Theory and Techniques*, **2016**.
 4. **Miguel Ruiz-Cabello**; Luis D. Angulo; J. Alvarez; A. Rubio Bretones; Salvador G. Garcia.
A New efficient and stable 3D Conformal FDTD.
IEEE Microwave and Wireless Components Letters, **2016**.
 5. Gutierrez, G. G.; Mateos, D.; **Ruiz-Cabello, Miguel**; Pascual-Gil, E.; Angulo, L. D.; Garcia, S.
On the design of Aircraft Electrical Structure Networks.
IEEE Transactions on Electromagnetic Compatibility, **2015**.
 6. E. Moreno, M. F. Pantoja; A. R. Bretones; **Miguel Ruiz-Cabello**, and S. G. Garcia.
A Comparison of the Performance of THz Photoconductive Antennas. *IEEE Antennas and Wireless Propagation Letters*, **2014**.
 7. Alvarez, J.; Alonso-Rodriguez, J. M.; Carbajosa-Cobaleda, H.; **Ruiz-Cabello, Miguel**; Angulo, L. D.; Gomez-Martin, R.; Garcia, S. G.
DGTD for a Class of Low-Observable Targets: A Comparison with MoM and (2,2) FDTD.
IEEE Antennas and Wireless Propagation Letters, **2014**.
 8. Guadalupe G. Gutierrez; Jesus Alvarez; Enrique Pascual-Gil; Mauro Bandinelli, Rodolfo Guidi, Valerio Martorelli, Mario Fernandez Pantoja; **Miguel Ruiz-Cabello**; Salvador G. Garcia.
HIRF Virtual Testing on the C-295 Aircraft: On the Application of a Pass/Fail Criterion and the FSV Method
IEEE Transactions on Electromagnetic Compatibility, **2014**.
 9. Jesus Alvarez; Luis Diaz Angulo; Amelia Rubio Bretones; **Miguel Ruiz-Cabello**; and Salvador G. Garcia;
A Leap-Frog Discontinuous Galerkin Time-Domain Method for HIRF Assessment
IEEE Transactions on Electromagnetic Compatibility, **2013**.

Conference Presentations

1. **Ruiz-Cabello, M.**; Angulo, L. D.; A. R. Bretones; R. G. Martin; S. González-Garcia; J. Álvarez
A Novel Subgridding scheme for Arbitrarily Dispersive Thin-Layer Modeling
IEEE MTT-S International Conference on NEMO (Sevilla, Spain), **May-2017**.
2. J. F. Dawson, I. D. Flintoft, S. A. Burke, M. P. Robinson, **Ruiz-Cabello, M.**, S. González-García, J. Álvarez

- Face Centered Anisotropic Surface Impedance Boundary Conditions in FDTD: Improved performance of staircased mesh for shielding problems
IEEE MTT-S International Conference on NEMO (Sevilla, Spain), May-2017.
3. García, S. G.; Angulo, L. D.; **Ruiz-Cabello, M.**; Mateos, D.
SEMBA: A broadband electromagnetic simulator.
Convention of Advances and Applications of GiD, 2016.
 4. **Ruiz-Cabello, M.**; L. D. Angulo; A. R. Bretones.; R. G. Martin; S. G. Garcia.
A new FDTD subgridding boundary condition for FDTD subcell lossy thin-layer modeling.
IEEE AP-S/URSI (Fajardo, Puerto Rico), 2016.
 5. **Ruiz-Cabello, M.**; L. D. Angulo; A. R. Bretones.; R. G. Martin; S. G. Garcia.
SEMBA: Broadband simulator for EMC.
New technological developments at EMC (Zaragoza, Spain), 2015.
 6. Angulo, L. D.; Greco, S.; **Ruiz-Cabello, M.**; García, S. G.; Sarto M. S.
FDTD techniques to simulate composite air vehicles for EMC.
AES Symp (Paris, France), 2012.

Research projects

A-UGRFDTD

August 2012 - December 2016

This project consists on the development of a fully functional geometrically conforming FDTD simulator. It is being funded by the Airbus Group and the University of Granada.

UAVEMI

January 2014 - December 2017

This project analyses the electromagnetic immunity of Unmanned Air Vehicles (UAV) under the effect of lightning and High Intensity Radiated Fields (HIRF). It is being developed by a partnership between the Polytechnical University of Catalonia (UPC), the National Institute for Aerospace Technique (INTA) and the University of Granada. Granted by Secretariat of state for research, development and innovation.

UAVE3

January 2017 - December 2019

This project is a continuation of the UAVEMI project, more focused in lightning indirect effects. It is being developed by a partnership between the Polytechnical University of Catalonia (UPC), the National Institute for Aerospace Technique (INTA) and the University of Granada. Granted by Secretariat of state for research, development and innovation

MORFEO

September 2014 - December 2015

The MORFEO project aimed the assessment of the viability of new braiding techniques for the EMC protection of wires in aircrafts. It was co-funded by Airbus and the Andalusian regional government.

MANIAS **December 2014 - December 2015**

The MANIAS project aims the development, fabrication and evaluation of multifunctional antennas integrated into aerodynamic surfaces. It was developed in partnership with the Airbus Group.

Teralab **November 2009 - November 2013**

The TeraLab project aims to develop a numerical laboratory for the design and simulation of Ter- ahertz technology. To do so, physical models of materials in that range of frequency are being developed and integrated in the numerical solvers.

UGRFDTD_MN **September 2013 - December 2017**

The aim of this project is to maintain and give technical support for the UGRFDTD software. The project is being funded by the Instituto Nacional de Técnica Aeroespacial (INTA).

HIRF-SE **December 2008 - June 2013**

The High Intensity Radiated Fields: Synthetic Environment aims to develop a computer framework to simulate electromagnetic phenomena during the development phase. This project is funded by the European Commission and 44 other partners from the EU. The contribution by our group consisted in a fully functional FDTD volumic solver to be integrated within the framework. More information in: <http://www.hirf-se.eu>

HPC numerical techniques for millimeter-wave antennas **2011-2014**

Devoted to the development of numerical techniques for the design of MMW antennas in time domain. Granted by Secretariat of state for research, development and innovation

